Development and Characterization of Improved Red Fluorescent Protein Variants

by

Premashis Manna

M.Sc., Indian Institute of Technology Kanpur, 2012

A thesis submitted to the

Faculty of the Graduate School of the

University of Colorado in partial fulfillment

of the requirements for the degree of

Doctor of Philosophy

Department of Chemistry & Biochemistry

2017

This thesis entitled:
Development and Characterization of Improved Red Fluorescent Protein Variants
written by Premashis Manna
has been approved for the Department of Chemistry & Biochemistry

_____

Prof. Ralph Jimenez

_____

Prof. Amy E. Palmer

Date _____

The final copy of this thesis has been examined by the signatories, and we find that both the content and the form meet acceptable presentation standards of scholarly work in the above mentioned discipline.

Manna, Premashis (Ph.D., Chemistry & Biochemistry)

Development and Characterization of Improved Red Fluorescent Protein Variants

Thesis directed by Prof. Ralph Jimenez

Aequorea victoria-based green fluorescent proteins and their blue, cyan and red counterparts offer unprecedented advantage as biological markers owing to their genetic encodability and straightforward expression in different organisms. Fluorescent proteins are characterized with complex photo-kinetics due to the presence of light-induced non-fluorescent or dark states which are responsible for their fluorescence intermittency or 'blinking'. We developed time- and frequency-domain techniques for probing the kinetics involving dark state conversion (DSC) and ground state recovery (GSR) in red fluorescent proteins (RFPs). Ensemble-level DSC and GSR kinetics in FPs were presented in the context of their single molecule fluorescence behaviors. Although significant advancements have been made towards improving the key photo-physical properties of the red fluorescent proteins (RFPs), they continue to perform sub-optimally compared to their green or cyan counterparts. We developed a high-throughput microfluidic screening and sorting platform to generate improved RFP variants by engineering their excited state lifetimes. Using this microfluidic system, mCherry and FusionRed mutants were developed with higher *in-vivo* brightness and fusion efficiency. We employed a novel rational design for the enhancement of brightness in RFPs through engineering of their radiative rates and extinction coefficients. This enabled us to produce bright mutants those out-performed the existing red fluorescent proteins.

Dedication

To Ma, Baba, Ritu

&

all the beautiful corals and jellyfishes

Acknowledgements

In Bengali, there is a famous poem by Sunirmal Basu, titled as 'I am a Learner of Nature'. In that poem, the poet describes how the vastness of sky teaches him to be open-minded, the powerful wind inspires him to be industrious *etc.* and how all of Nature helps him towards an all-round development. Similarly, at my graduate school, I have learned different qualities from a diverse range of friends, colleagues, teachers, advisors without whom I would not be what I am today.

Special thanks to Prof. Amitava Bagchi for encouraging me to stay in the field of Chemistry. I acknowledge the contributions of Nabakumar Bera, SS Riaz, Debasis Jana for developing my solid background in physical chemistry and specially introducing me to the Jablonski diagram which helped me a lot to perform some of the work presented here. Thanks to Prof. Madhav Ranganathan for teaching me to solve chemical and biological problems with advanced mathematics. I am deeply indebted to Prof. Nisanth N. Nair, Prof. Pratik Sen, Prof. S. Manogaran for teaching me the fundamentals of quantum mechanics, fluorescence spectroscopy and NMR.

I am really fortunate to have Dr. Ralph Jimenez as my thesis advisor. I recognize his endless support and encouragement in pursuing new ideas, grooming me for the scientific world and teaching me: "Science is not a sprint. It's a marathon". Thanks to Prof. Amy Palmer for guiding our RFP development project in proper direction and answering my stupid questions regarding biology with patience. I have been lucky to work with many talented post-doctoral researchers in my lab. Kevin Dean helped me in my early days at the graduate school introducing me to the fluorescent proteins and the microfluidics. Special thanks to Prof. Lloyd Davis for educating me with laser

alignment and optical trap. Felix Vietmeyer was very helpful building different electronics those were invaluable in my project. Sheng Ting Hung continues to be my friend, philosopher and guide. Pia Friis tolerated our endless demands of protein purifications and library constructions. I am thankful to Brett Fiedler for he patiently answered all of my technical questions and gave invaluable tips for the grad school. Special thanks to Sheng Ting Hung, Samantha Allen, Srijit Mukherjee, Richard Erickson, Emma Simmerman, Josh Slocum for helping me professionally and emotionally with scientific inputs, proof-reading this thesis and saying 'hi', day in and day out. Thanks to David Simpson & Maria Lo for handling the mammalian cells, Gary Mo & Prof. Jin Zhang for a fruitful collaboration. JILA is a wonderful place with all the people very cooperative and helping each others. I recognize the contribution of the staffs working in the Electronic shop and Machine shop at JILA in achieving my doctoral degree.

During my graduate research I got continuous mental and emotional supports from my father, mother and other family members. Special mention to my elder brother, Raj Kumar Manna, as he was always ready to help me when needed, be it with mental guidance or LaTeX formatting. I acknowledge the support of all of my friends, here at CU and in India, including Shirong, Nirmal, Shanti, Abir who motivated me all the time with positive words. Thanks to Snehashis Da for endless scientific and political discussions. Many thanks to Amitava Da & Manika Di for illuminating my week-ends with card games and recreational chitchat.

No appreciation would be sufficient in describing Ritu's role in my journey here at graduate school. Being wife of a graduate student she faced all the challenges that I faced and supported me all the way no matter how hard it was for her.

Contents

Chapter

List of Tables

Table

Chapter 1

Introduction

"I've always been attracted to colors. Color helps make the work more interesting and endurable. It helps when things aren't going well." -Roger Tsien (Recipient of Nobel Prize in Chemistry, 2008)

1.1 Fluorescent Proteins: A Historical Perspective

The story of fluorescent proteins started in 1962 when Osamu Shimomura identified and purified green fluorescent proteins (GFP) from the jellyfish *Aequorea Victoria* (avGFP) [1]. He was intrigued by the beautiful blue and green colors from jellyfish and was curious about their chemical origin. Eventually, he was able to purify the proteins responsible for the blue color of jellyfish, aequorin. GFP was a byproduct of the purification of aequorin. It was later found that upon binding to Ca^{2+} (abundant in sea water), aequorin emits blue light (λ_{max}, 465 nm). This blue light triggers the excitation in GFP and subsequently it fluoresces green [2]. In 1979, Shimomura reported the optical properties and chemical structure of the GFP chromophore [3, 2]. At that time, it was conjectured that the post-translational modifications to form the chromophore in GFP required specific enzymatic machineries and therefore it was not suitable for bio-marker applications. So, Shimomura stopped working on GFP and continued his work on bio-luminescence. Fluorescent proteins came back to life in the early 90s, when Martin Chalfie and Douglas Prasher cloned the GFP gene [4] and expressed it in *E. coli* and *C. elegans*, a roundworm [5]. To their

surprise, both of these organisms fluoresced green when excited with blue light. This proved that for the formation of functional GFP, no additional cofactors or exogenous substrates were necessary. It required only molecular oxygen for the formation of the chromophore [6]. Expression of GFP in *C. elegans* by Chalfie *et al.* [5] clearly revealed the touch receptor neurons and the localization pattern agreed well with previous studies. This eventually opened the floodgate of research in understanding and using fluorescent proteins for myriad applications.

Following the initial expression of GFP in bacteria and worms, Roger Tsien's lab at the University of California at San Diego pioneered the engineering of fluorescent proteins. Tsien and co-workers were able to modify avGFP to produce a palette of colors [7, 8]. The first red fluorescent protein, DsRed, was derived from a coral *Discosoma sp.* [9]. But it was characterized to be an obligate tetramer and with very slow maturation [10]. By changing the chromophore-forming tripeptide and manipulating the immediate chromophore environment of DsRed, Tsien and coworkers generated several monomeric, fast-maturing FP variants with emission maxima ranging from 537 to 610 nm [11, 12, 13]. Together with blue fluorescent proteins (BFP), cyan fluorescent proteins (CFP), green fluorescent proteins, yellow fluorescent proteins (YFP) and red fluorescent proteins (RFP), FP technology ushered in a new era in live-cell imaging. Researchers from all around the world started using GFP and its homologue fluorescent proteins as markers to illuminate hidden biological activities, sensing metal ions, temperature, pH *etc* [14]. Later, harnessing the 'blinking' property of FPs, super-resolution technologies were developed to break the diffraction-limited spatial resolution in optical imaging [15, 16, 17]. Consequently, FPs became part and parcel for the broader community of chemists, biologists and physicists. Figure 1.1 proves this point. It displays how literature of the fluorescent proteins increased over the years. The figure has been generated by searching the keyword "green fluorescent proteins" in Web of Science (www.webofknowledge.com). For their contribution to the development of fluorescent protein technology, Shimomura, Chalfie and Tsien were awarded Nobel prize for chemistry in 2008.

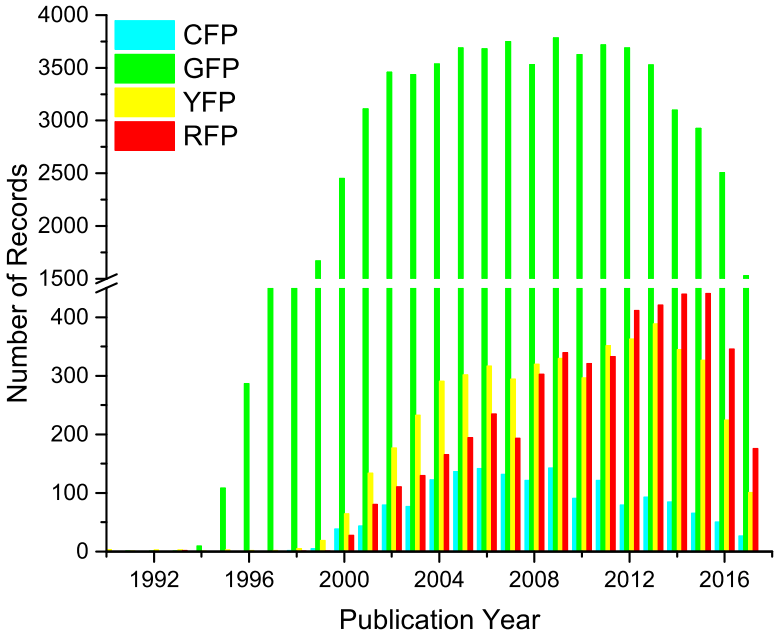

Figure 1.1: Number of articles that mentioned cyan, green, yellow and red fluorescent proteins over the years. The data were generated by searching Web of Science with the key word "Green Fluorescent Protein" *etc.*

1.2 Structural and Photo-physical Properties of Fluorescent Proteins

Despite having large dissimilarity in genetic sequences, the basic structure of green fluorescent proteins and its homologues are very similar. It consists of a 11-stranded β-barrel or β-can. An α-helix spirals down into the interior of β barrel and holds the chromophore [18]. The top and bottom portions of the structure are characterized with numerous short loops. Figure 1.2 represents the generic structure of a monomeric FP (mCherry, PDB 2H5Q). A typical monomeric FP contains $\sim$ 230 amino acids with molecular weight in the range of 25-30 kDa [19]. Although the basic structure is similar for all of the FPs, structural heterogeneity can also be found. For instance, unlike many FP variants from avGFP family, a monomeric RFP from DsRed family, mCherry, was characterized with large intra-strand dynamics between β-7 and β-10 strand that has been

implicated to correlate with higher photobleaching from mCherry [20]. Figure 1.3 [19] shows the heterogeneity in structure of the FP β-barrel and chromophore of 202 fluorescent proteins taken from the protein data bank. It is notable that most of the chromophores in the reported literature are in *cis* form. The 11-stranded β-barrel plays a huge role by minimizing the non-radiative pathways and thereby increasing fluorescence quantum yield (ϕ).

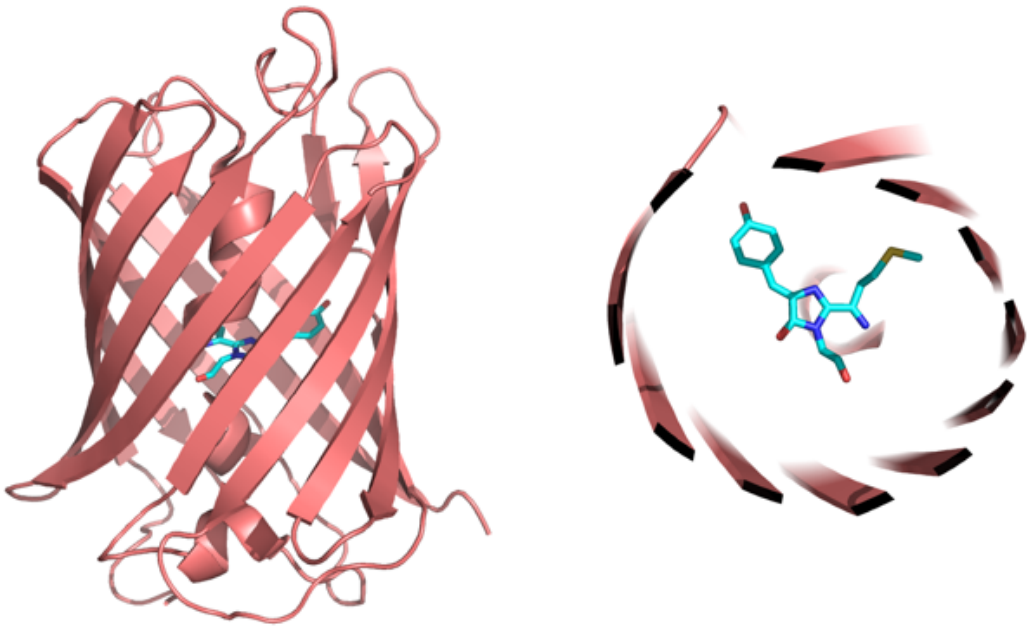

Figure 1.2: (Left) The generic structure of a monomeric fluorescent proteins (mCherry, PDB:2H5Q). It consists of a 11 stranded β-barrel with an α-helix co-axially spiraling down into the barrel. The chromophore is formed autocatalytically through post-translational modification of the tri-peptide 66-67-68 (mCherry numbering). The dimension of the barrel is $\sim$ 2 nm in diameter and $\sim$ 4 nm in length. (Right) The top-down view of mCherry structure focusing the chromophore structure.

The post-translational modification of the tri-peptide (X66-Z67-G68, mCherry numbering ; X65-Z66-G67, avGFP numbering) is responsible for formation of the FP chromophore. Of the X-Z-G trio, G (glycine) is always conserved across the fluorescent proteins because it is required for the cyclization of the chromophore. Z can be any amino acid with aromatic side-chain. Although for wild-type GFP and DsRed, Z is tyrosine, it can be phenylalanine (mBlueberry), tryptophan (CFP) *etc.* As found in the literature, X can be serine (avGFP), methionine (dsRed, eqFP578,

mHoneydew), threonine (CFP), glycine (YFP, EGFP), lysine (ZFP528), histidine (Kaede) *etc.* In spite of the diversity in sequences, there are some conserved residues in FPs that indicate their importance in proper folding of the β barrel or formation of the chromophore. For example, Arg96 and Glu222 are highly conserved across the different types of FP. Wood *et al.* [21] studied the importance of R96 residue in GFP by mutating it to several other non-charged or charged residues. From their studies it was revealed that the maturation of R96M mutant was severely slowed down (from hours to months) while R96K restored the maturation speed. This indicates the importance of a charged residue at the position 96 for the fast formation of GFP-like chromophores.

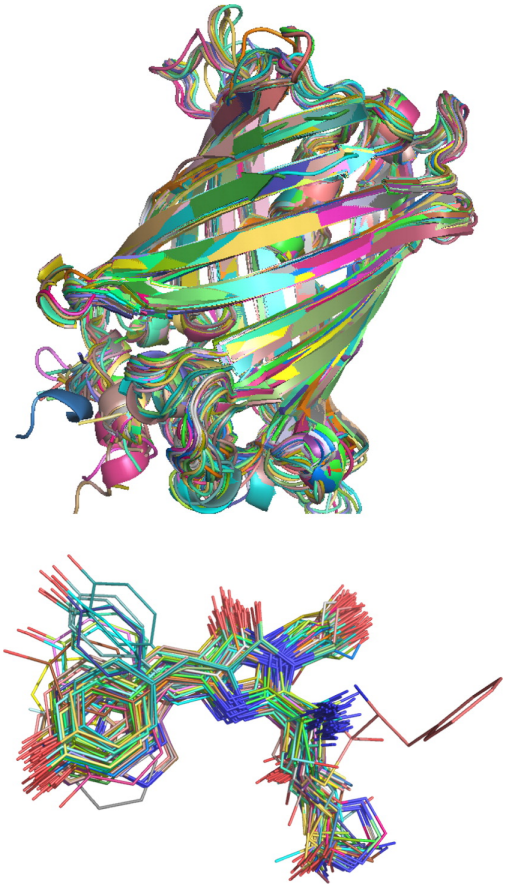

Figure 1.3: Structure of 202 different fluorescent proteins from protein data bank. From this analysis, it is obvious that most of the reported fluorescent proteins prefer *cis* conformations. The Figure has been taken from Dedecker *et al.* [19].

For the proper formation of the chromophore, folding into a 3-dimensional β barrel-like structure is essential. An early study by Reid *et al.* showed that improper folding of avGFP

arrested the formation of the characteristic chromophore [22]. After folding, the post-translation modification in the above mentioned tri-peptide occurs to form a functional chromophore. This process is called **chromophore maturation**. For constitutively fluorescent proteins, the post-translational reactions can be categorized into two different mechanisms:

- GFP-like chromophore: In GFP-like proteins (*e.g.* avGFP), the formation of the chromophore occur in the following sequences: cyclization-oxidation-dehydration [23, 24]. Figure 1.4 demonstrates the mechanism of GFP chromophore formations in detail. First, cyclization happens by the nucleophilic attack by the N_{67} of the Gly67 residue on the C-O π^* orbital on C_{65}. This process is reversible. Next the cyclized intermediate trapped *via* oxidation and followed by dehydration to form a double bond between $C\alpha_{66}$ and $C\beta_{66}$ carbons. The functional GFP chromophore contains an imidazolinone group conjugated to the side-chain of Tyr66 through a double bond. Kinetic isotopic effect revealed that the removal of hydrogen atom of $C\beta_{66}$ did not happen in the oxidation step but in the dehydration step. This oxidation step was found to be rate-determining [22].

- DsRed-like chromophore: There had been a considerable amount of debate on the formation of chromophore in red fluorescent proteins *e.g.* DsRed [25, 26, 27, 28]. A functional DsRed-like chromophore contains an additional N-acylimine conjugated to the GFP-like chromophore. This extended conjugation de-localizes the electrons and lowers the energy gap between highest occupied molecular orbital (HOMO) and lowest unoccupied molecular orbital (LUMO) resulting in a bathochromic shift the spectra. Initial studies by Gross *et al.* [25] suggested that DsRed chromophore formation happens with additional oxidation of a GFP-like intermediate chromophore. But this mechanism could not explain the residual green fluorescence in DsRed and the presence of a blue-intermediate ($\sim$ 408 nm) during the DsRed chromophore maturation process [26]. Hence, Verkhusha *et al.* [26] proposed that the formation of red chromophore happens through formation of a protonated GFP-like chromophore (blue intermediate) and subsequent oxidation. But this model unrealistically

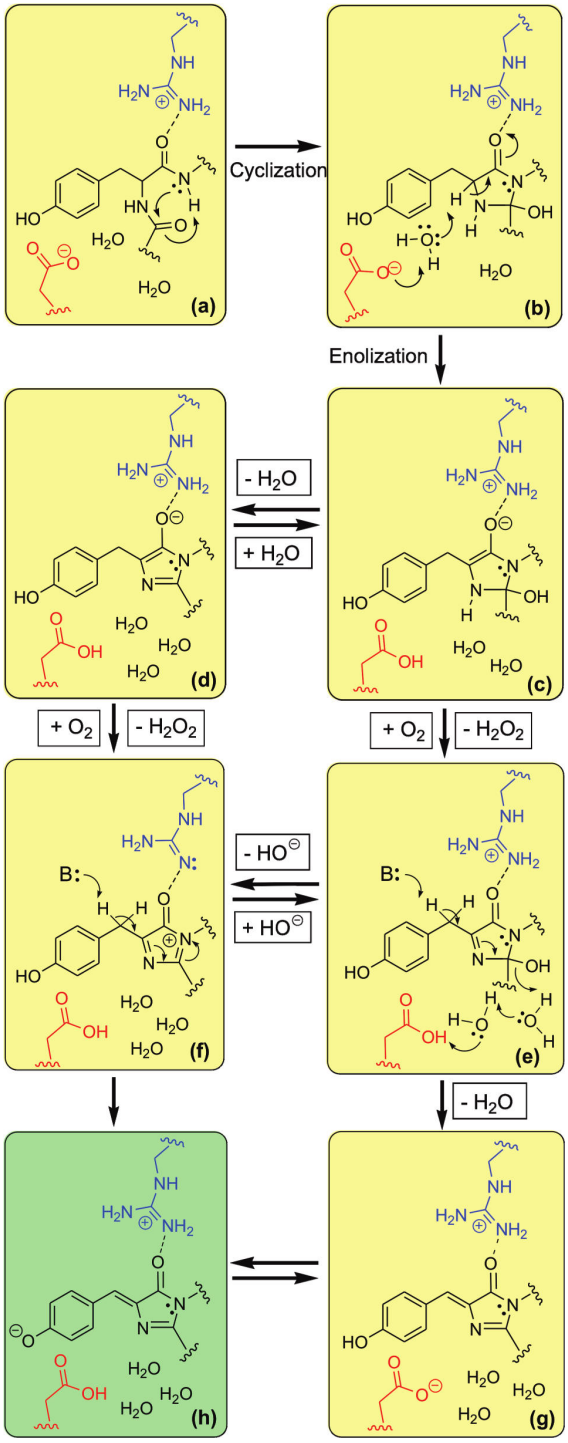

Figure 1.4: Chromophore formation in GFP-like FPs: First, nucleophilic attack by the lone pair of N_{67} of Gly67 generate the cyclized product **a**. Subsequent enolization forms **c** which establishes a hydration-dehydration equilibrium between **c** & **d**. Next, oxidation happens by molecular oxygen to generate cyclic imine formation either in hydrated (**e**) or dehydrated (**f**) form and releases hydrogen peroxide (H_2O_2). Finally hydrogen is abstracted from the β carbon (tyrosine-derived) and subsequent bond re-arrangements forms fluorescent chromophore either in its neutral (**g**) or anionic form (**h**). The Figure has been taken from Wachter *et al.* [24].

assumes that de-protonation is strictly irreversible. A branched mechanism proposed by Strack *et al.* [27] solved some of the previous inconsistencies of red chromophore formation mechanism. According to this mechanism, after the initial cyclization process, the cyclized intermediate formed an hydroxylated cyclic imine through oxidation by molecular oxygen. This is in rapid equilibrium with cyclic imine and represents the branched point for the GFP/RFP chromophore formation. From this point, a GFP chromophore can be formed by dehydration and further protonation-deprotonation equilibrium. Alternatively, another oxidation could lead to the generation of a cationic blue intermediate where N-acylimine and the imidazolinone ring is conjugated. Finally, dehydration from this blue intermediate and subsequent additional rearrangements lead to the formation of a functional RFP chromophore.

In 2012, the computational and experimental studies of TagRFP and TagBFP by Bravaya *et al.* further refined this branched pathway model [28]. In particular, this study argued that the blue intermediate formed in the way of forming red chromophore is anionic in nature, unlike the mechanism by Strack *et al.* where it was described as cationic [27]. This anionic structure of blue intermediate is supported by its computational absorption energy that agrees with the experiment (408 nm, 3.04 eV). The proposition of anionic blue intermediate required that dehydration precedes oxidation. This mechanism also explained the role of Lys70 and Arg95 residues in stabilizing the blue intermediate. Figure 1.5 elucidates the mechanism of red chromophore formation by Bravaya *et al.* [28]. This mechanism suggests that at the branching point the propensity of the reaction to form GFP/RFP chromophore is controlled by two different dehydration mechanisms. In first mechanism, if the dehydaration happens due to removal of H^+ and OH^- from methylene bridge and imidazolinone respectively, a GFP-like chromophore forms. On the other hand, if the H^+ is abstracted from the peptide bond of Phe65 for dehydration, it leads to a formation of blue intermediate which eventually forms the RFP chromophore with an additional oxidation. According to this study, the blue intermediate formed during the formation of DsRed-like chromophore forma-

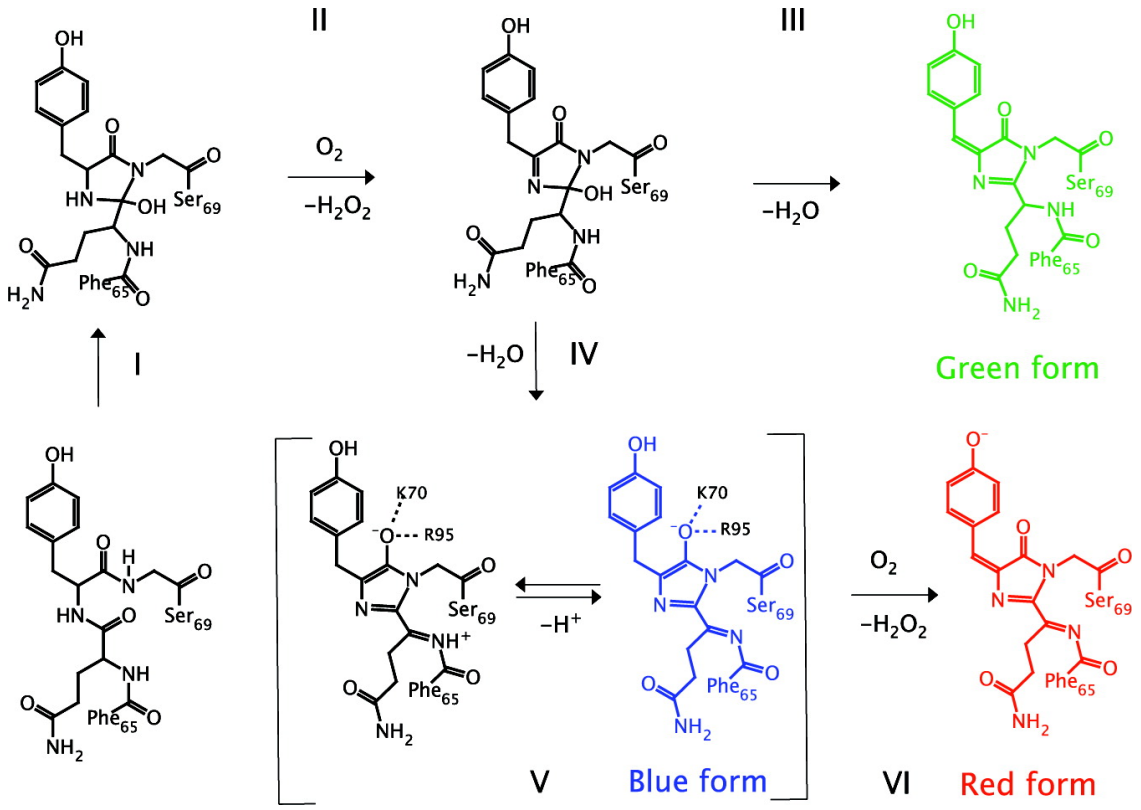

Figure 1.5: The mechanism of chromophore formation in DsRed-like RFPs as outlined by Bravaya *et al.* [28]. The initial cyclization due to nucleophilic attack by N atom of Gly is followed by a oxidation reaction to produce a cyclic imine. This forms the branching point to form either GFP-like or RFP-like chromophore. GFP-like chromophore can be formed by dehydration through proton abstraction from C_β (derived) from Tyr67. On the other hand, if dehydration happens through de-protonation of Phe65 peptide bond and subsequent rearrangement, an anionic blue intermediate is formed. Further oxidation of this blue intermediate is required to form the functional red chromophore. The Figure has been adopted from the reference [28].

tion, in fluorescent timer [29], TagBFP [30], PAmCherry [31] is probably similar in structure if not identical.

To be an efficient bio-marker, fast chromophore maturation is necessary. In Chapter 5 the formation of immature mCherry chromophore and mutations associated with incomplete maturation is described.

Upon excitation with light, the FPs show complex photo-physics. Some fraction of the excited molecule returns to the ground state in a radiative fashion, leading to fluorescence. The molecules, once excited, can also become trapped in long-lived non-fluorescent or dark states (*via* Dark State

Conversion or DSC). At the single molecule level this is manifested in the form of fluorescent intermittency or 'blinking'. Dickson *et al.* [32] first reported the on/off blinking behavior of GFP mutants at time scale of seconds with 488-nm excitation. According to their report, the 'blinking' kinetics depended on the illumination intensity and the off state molecule could be reverted back to their emissive states by 405-nm irradiation. We have shown that RFPs can spontaneously return from the long-lived dark states to the ground state (*via* Ground State Recovery or GSR) in the time-scale of sub-ms [33]. The 'blinking' or reversible switching properties of various fluorescent proteins have been studied by fluorescence correlation spectroscopy [34, 35, 36]. The chemical nature of dark state can be context dependent. It can be associated with different isomeric forms of the chromophore (*cis-trans*) [37], protonation state or radical form [38] *etc.* In Chapter 2, time and frequency-domain measurements techniques for measuring DSC and GSR have been discussed in detail. DSC & GSR dynamics are presented in the context of single molecule 'blinking' of the fluorescent proteins in Chapter 3.

Other than constitutively fluorescent proteins, there are classes of FP that can switch between dark and bright states or change the absorption/emission wavelength. These FPs can be classified in three categories:

- Reversibly photo-switchable FPs (RSFP): These proteins can be reversibly switched between ON (bright) or OFF (dark) states. Dronpa [39], rsTagRFP [40], asFP595 [41], Skylan-NS [42] falls into this category. The mechanism behind the ON/OFF switching in RSFP is presumably *cis-trans* isomerization, protonation-deprotonation or both. The photo-switching in Dronpa and its mutants have been widely studied by X-ray crystallography [37, 43, 44], fluorescence correlation spectroscopy (FCS) [34] and molecular dynamics simulations [45]. Dronpa forms the bright state upon excitation with 408-nm light (*cis* state) and it can be converted into a dark state by 488 nm illumination [37]. Crystal structure analysis of the dark and bright state of Dronpa reveals that once excited with 488-nm light the chromophore adopts a *trans* configuration with increased non-planarity and a re-

duced number of electrostatic interactions with neighboring residues. Consequently, this makes the *trans*-configuration non-fluorescent by opening various non-radiative pathways [37]. Similarly, the first red version of RSFP, rsTagRFP, can be switched on/off by blue and yellow light respectively. The switching properties of these proteins have been used in different modalities of super-resolution microscopy, *e.g.* **RE**versible **S**aturable **O**ptica**L** **F**luorescence **T**ransition (RESOLFT) microscopy [17].

- Photo-activatable FPs (PAFPs): This class of proteins, *e.g.*, PA-GFP [46], PAmCherry1 [47] *etc.* show light-induced conversion from dark to bright states. Upon photo-activation with 413 nm light, PA-GFP shows $\sim$ 100 fold enhancement in fluorescence when excited with 488 nm light. The mechanism of photoactivation, as studied with the fluorescent and non-fluorescent states of PAmCherry1, involves decarboxylation-mediated configurational changes of the chromophore [31]. PAFPs have been extensively used in photoactivated localization microscopy (PALM) for achieving diffraction-unlimited resolution in biological samples [15, 48].

- Irreversibly photo-switchable FPs: Dendra2 [49], Kaede [50], EosFP [51] change the wavelength of fluorescence when excited with high-energy illumination. This change in color has been employed in PALM, stochastic optical reconstruction microscopy (STORM) [52] for diffraction-unlimited imaging.

The gradual loss fluorescence due to illumination is known as 'irreversible photobleaching' or photodegradation. The molecule, in this scenario, goes off the excitation-emission cycle. FPs are characterized with higher photobleaching tendency than their small molecule counterparts *e.g.* organic dyes. The exact mechanism of photo-degradation in fluorescent proteins is still unclear but probably it varies in different FPs and depends on the illumination and environment conditions. For instance, a structure-based study on mIrisFP [53] revealed that at low illumination intensity, the FP became non-fluorescent by photo-induced oxidation of sulfur-containing residues while at higher illumination intensity the mechanism of photo-bleaching involves decarboxylation of con-

served Glu212 moiety. The photobleaching rates also depend on the modality of imaging. This is evidenced by comparing photostability of FusionRed [54] and mCherry [12]: with wide-field imaging mCherry and FusionRed have comparable photostability but with confocal imaging FusionRed bleaches several fold faster than mCherry. This is probably due to the fact that FusionRed has a higher tendency for dark state conversion and with higher illumination energy in confocal imaging the FP is forced it to be trapped in those dark states and subsequently photobleach. Photobleaching may proceed *via* formation of radical ions, as observed in the KillerRed series of FPs [38]. We have discovered that there is a correlation between the excited state lifetime of the chromophore and its photodestruction [55]. This can be explained by the fact that with longer lifespan of the FPs in the excited state, it enhances the probability of various excited state reactions *e.g.* dark state conversion (DSC) [56]. Although molecular oxygen is necessary for the formation of a functional chromophore in FP, oxygen can enhance the photobleaching by reacting with the chromophore. This is supported by reduction of photobleaching of TagRFP-T and Kriek in anaerobic conditions [11, 57].

1.3 Application of Fluorescent Proteins

Fluorescent proteins have become an extremely useful tool in cellular biology for imaging cell-cycle progression [58], cellular trafficking [59] and architecture [60, 61], to name a few. Each year, the armada of FPs is finding novel and innovative ways to illuminate the inner workings of Nature. FPs offer a genetically-encodable platform for targeted localization that is essential for illuminating the cellular architecture at unprecedented level of spatial and temporal resolution. Although organic fluorophores have better photostability and brightness, FPs are superb for specific localization. Again, as they are protein-based, most FPs impart minimal photo-toxicity which is always advantageous for long-term live-cell imaging. As the red fluorescent proteins can be excited with longer wavelength lights, they are particularly useful for long-term imaging to suppress photo-induced toxicity [62]. Also, as the scattering of light by molecules is inversely proportional of its

wavelength, live-cell imaging with RFPs suffers minimally from scattering. As, light with longer wavelength are not significantly absorbed by water, lipid and hemoglobin, RFPs, far-red FPs and infrared FPs (iRFP) show negligible auto-fluorescence making them excellent markers for deep-tissue imaging. This drives the engineering of bright and photostable far-red and iRFPs [63]. Multi-photon microscopy, light-sheet microscopy partly ameliorate the photobleaching in FPs owing to their intrinsic confocal effect or selective plane illumination and thereby removing out-of-focus light contribution.

Thanks to the dark states in FPs, they can be used in various diffraction-unlimited microscopies, *e.g.*, PALM [15] or RESOLFT where routinely 20-50 nm spatial resolution is achieved. Although PALM, STED, RESOLFT and STORM microscopies give higher spatial resolution, structured illumination microscopy (SIM) or stochastic optical fluctuation imaging (SOFI) can give higher temporal resolutions, albeit with lower spatial resolution (only $\sim$ 2-3 fold improvement from diffraction-limited resolution). These techniques reveal biological architectures that were not seen previously with diffraction-limited imaging [64, 65]. For example, the high-resolution mapping of phosphoinositide (PI) had been possible using the photo-switchable FP, mEos2, in conjunction with photo-activated localization microscopy [66]. By and large, FPs are playing a big role in the success of super-resolution imaging. Although, in theory, these techniques can have unlimited resolution capability, practically the resolution is limited due to the photo-bleaching and photo-fatigue of the FPs. More photostable fluorescent proteins are urgently needed for further proliferation of this field.

The change in fluorescence of FPs due to variations in environmental conditions has led to the development of sensors for quantification of ions [67, 68, 69], pH [70], temperature [71], cAMP [72] *etc.* Baird *et al.* reported the first FP-based ion indicators where circular permutation and insertion of calmodulin or zinc finger domain in EYFP led to several fold change in fluorescence upon binding of metal ions [67]. Subsequent improvement of Ca^{2+} sensors generated the so-called GCaMP series, which is now routinely employed to monitor calcium ions and action potentials in neuronal cells [73, 74, 75]. Other FP-based ion sensors *e.g.* Zn^{2+} [76, 77], Mg^{2+} [78], Cd^{2+} [79]

etc. have been developed for assessing the roles of those metal ions in cellular biology. The sensors based on FPs can be classified in two categories: ratiometric or intensiometric. In ratiometric sensors the FRET efficiency from a blue-shifted donor to a red-shifted acceptor changes several fold depending on the concentration of a particular metal ion. For example, the Zn^{2+} sensors developed by Dittmer *et al.* [76] where CFP and YFP are connected with a zinc finger domain that remains unstructured with low Zn^{2+} and therefore exhibits a minimal FRET response. But, upon increasing the concentration of Zn^{2+} and its resultant binding of Zn^{2+} to the zinc finger domain, CFP and YFP are brought into close proximity which results in several fold enhancement of FRET. On the other hand, intensiometric sensors depend on the change in fluorescence of a single FP upon changing the environment, resulting in chromophore re-arrangement or a shift in pH stability. In the single FP based GaMP6m sensor, Ca^{2+} binding to CaM stabilizes the anionic state of the FP chromophore through electrostatic interaction, thereby enhancing the fluorescence several fold [80]. Although FP-based calcium indicators have been tuned to report Ca^{2+} ions very efficiently, the other FP based sensors, *e.g.* Zn^{2+} or voltage sensors are still in sub-optimal stage and could stand significant improvements in temporal resolution, improvement in dynamic range, pH resistance and optimal expression in mammalian cells. Dedicated strategies to screen large FP-based Zn^{2+} sensor libraries and selection based on improved performance are a right step in this direction [81].

Apart from conventional fluorescence imaging, nanoscopy or sensors, FPs can be used in optogenetics where light dependent conformational changes lead to the control of specific protein functions. In chromophore-assisted light inactivation (CALI), following excitation, the chromophore produces reactive oxygen species which can diffuse and oxidize nearby proteins and thereby altering their activities [82]. KillerRed [83] or its monomeric version SuperNova [84] produce superoxide radical anion upon green light excitation, which is ideal for optogenetic controls. Optogenetic control of protein activity has also been demonstrated using light-dependent dimerization of a Dronpa mutant [85].

1.4 Directed Evolution of Red Fluorescent Proteins

Several properties of FPs have been engineered to make them more efficient as a bio-marker. Monomericity, brightness, cyto-toxicity and pH-resistance are a few properties of FPs that have been heavily evolved to cater to the ever-growing need of biologists. Fluorescent proteins from natural sources are mostly oligomeric and suffer from slow maturation. The oligomeric structures compromise the usefulness of FPs by perturbing the native function of the targeted proteins. In spatially confined cellular compartments, *e.g.* the secretory pathway, proteins tend to mis-fold and aggregate presumably due to oxidative nature of those organelles [86]. The brightness of a fluorescent protein improves the signal-to-noise of the image and offers a clear insight into the relevant biological processes. Bright FPs also require lower irradiation illumination to obtain acceptable image quality. This lower illumination ultimately reduces the photo-toxicity of the biological specimen and photo-destruction of FPs. Also, RFPs and far-red FPs are excited with longer wavelength light where the absorption of water, hemoglobin, deoxy-hemoglobin is minimal and hence such FPs are well-suited for deep-tissue imaging [87]. Consequently, in the last decade, there has been an incredible amount of effort to engineer bright, monomeric, photo-stable RFP mutants with lower cyto-toxicity, and fast maturation kinetics [88, 89, 90]. In spite of this effort, RFPs routinely show sub-optimal performance relative to their green, yellow or cyan counterparts. Hence, the biological community is eagerly waiting for a drastic improvement in the photo-physics of RFPs.

A particular phenotype of a FP is largely controlled by few key residues and some additional supporting residues. For directed evolution of a particular phenotype, conventionally, site-directed mutagenesis is performed based on some hypothesis, previous findings or less commonly some simulation guided residues. Residues close to chromophore mainly control the key photo-physics of FPs but distal mutations have also been reported to control maturation kinetics, barrel fluctuations *etc.* After the initial site-directed mutagenesis, normally the FPs become completely non-fluorescent or weakly fluorescent. Additional mutagenesis is generally required to restore the brightness through improving folding/maturation or improvement of extinction coefficient (ϵ) of the FPs. By and large,

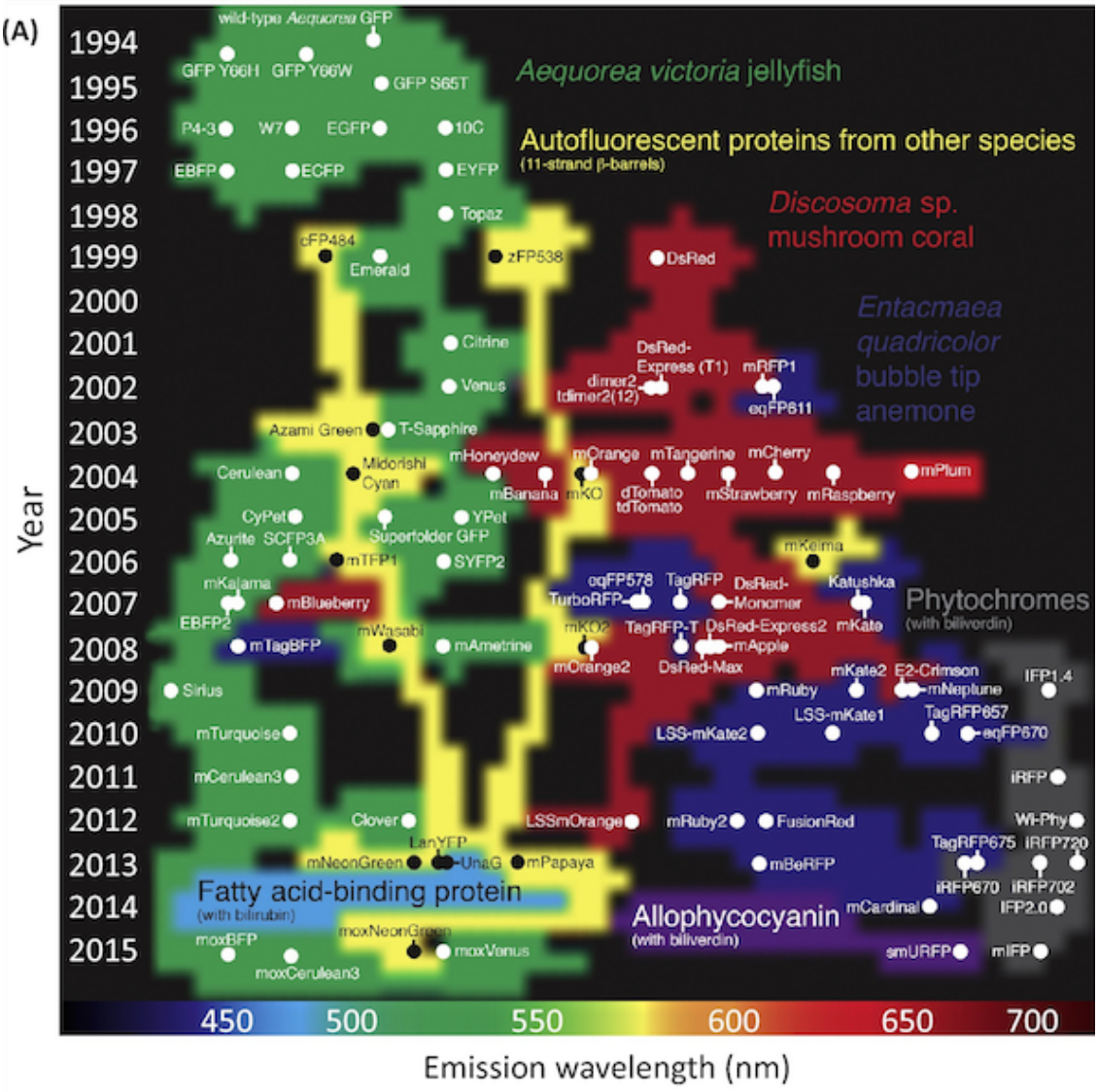

Figure 1.6: Evolution of avGFP homologues of FP with 11 stranded β barrel and bacteria-phytochrome based FP over the years. The x-axis displays their wavelength emission wavelength. It is notable that FP derived from *A. victoria*, *Discosoma sp.* and *E. quadricolor* have been heavily mutagenized and evolved while Allophycocyanin and FPs from other species have not been largely explored that might have untapped potential. The Figure has been adopted from Rodriguez *et al.* [80].

this restoration process is performed using random mutagenesis. However, computation guided approaches based on PHONEIX and FASTER [91] have also been reported [92]. Generally, *in vitro* mutagenesis and subsequent expression in *E. coli* is the preferred cellular host platform for directed evolution of the FPs. However, *in-vivo* mutagenesis *e.g.* viral mutagenesis [93], somatic

hypermutation [94, 95] *etc.* have also been used for evolution of FP. Although *in vivo* mutagenesis might be a laborious process, it can be used to create library in mammalian cells which ultimately promise efficient expression in the host organism and minimal cyto-toxicity. On the other hand, mutagenesis in *E. coli* or yeast is easy to perform but the evolved FPs might have expression issues in mammalian cells. A number of good reviews account for the directed evolution of red fluorescent proteins and discussed pros and cons of different approaches [88, 89, 90].

After the initial round of mutagenesis, the libraries are subjected to selection of desired phenotypes. Traditionally, fluorescence activated cell sorter (FACS) and subsequent expression in plates (for yeast or bacterial mutagenesis) is the common choice of selection. However selection based on FACS is limited by fluorescence intensity and wavelength. Also, bacterial colony-based screening restrict the library size and thereby mutational space of the FPs. Microfluidic-based sorting is an alternate option which can incorporate additional selection parameters, *e.g.*, excited state lifetime, photo-stability, polarization, anisotropy etc [96, 97, 98, 55, 57]. Also rapid screening and sorting would allow study of larger combinatorial libraries, to explore the mutational space efficiently. In Chapter 5, 6 and 7 of this thesis, the utilization of a multi-parametric microfluidic sorter for directed evolution of FPs have been discussed in detail.

Historically, **monomerization** of RFPs has been undertaken as a first approach to optimize their functionality [13, 99]. DsRed, the first RFP from *Anthozoa sp.* was obligate tetramer and suffered from slow maturation. In order to produce a monomeric variant, Campbell *et al.* first disrupted the A/B interface with replacing the non-polar group by large positively charged residues (Arg, Lys) [13]. This modification introduces electrostatic repulsion at the oligomeric interface and renders formation of higher-order oligomer thermodynamically unfavorable. Next, the disruption of A/C interface was performed by substituting charged residues as done previously. It was observed that Anthozoa FPs had higher tolerance of disruption of A/B interface (involving non-poplar residues) than A/C interface which involves replacing polar residues [90]. However, the disruption of dimeric interface 'cripples' the FP by slow maturation which then becomes nearly non-fluorescent. With several round of targeted mutagenesis, brightness had been restored to pro-

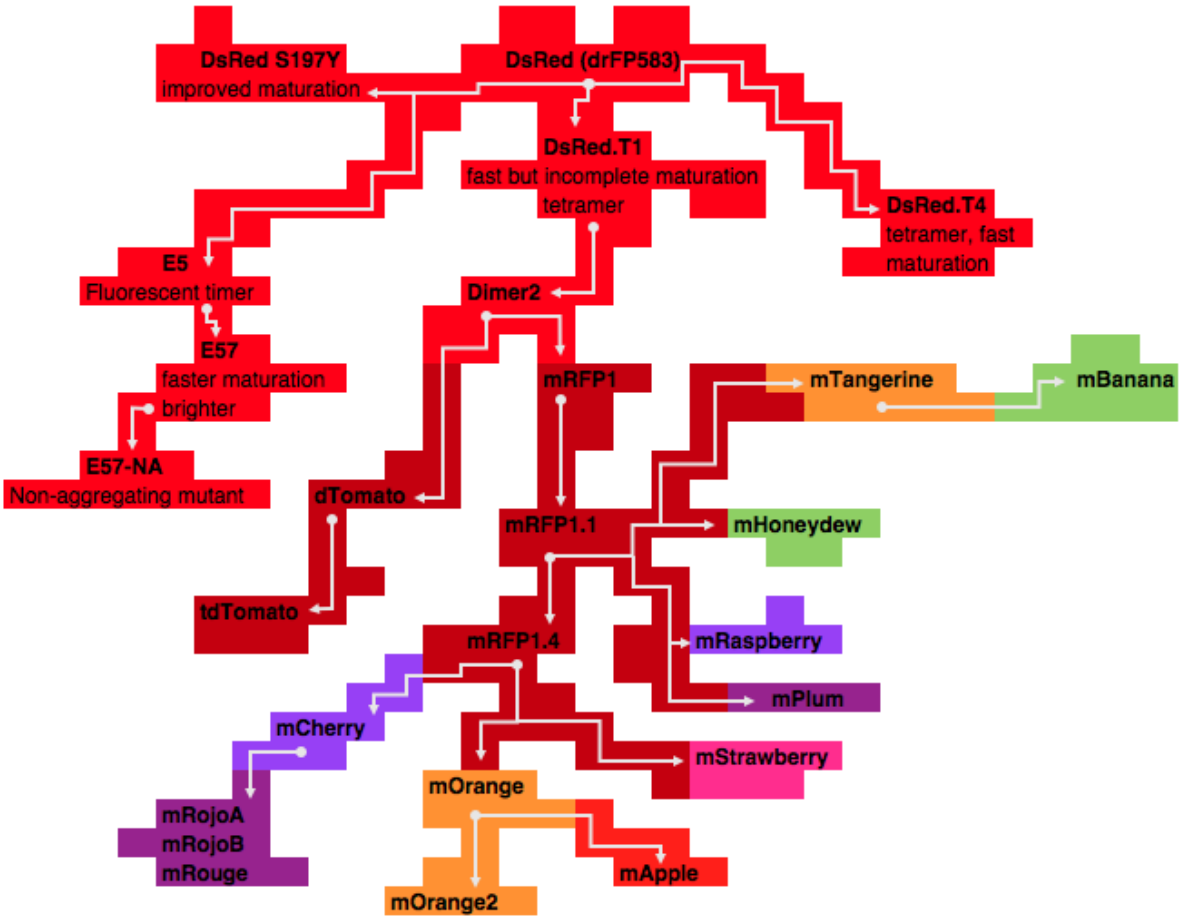

Figure 1.7: Evolution of DsRed to form the mFruit series of RFPs and others.

duce the first monomeric RFP, named mRFP1 [13]. Further site-directed mutagenesis of mRFP1 produced the 'mFruit' series of mutants with diversification of colors [12]. Similarly, the formation of monomeric TagRFP [99] was produced by destabilizing oligomeric interface of TurboRFP, a dimeric, fast maturing variant of eqFP578. Although, recently it was observed that TagRFP tends to dimerize in some specific cellular environments *e.g.* in endoplasmic reticulum [100, 101]. Figure 1.7 demonstrates the evolution of DsRed.

As discussed earlier, **Brightness** in fluorescent proteins is a very desirable property. Although theoretically, brightness is related to extinction coefficient ($\propto$ absorption cross-section) and fluorescence quantum yield (ϕ) ($\propto$ excited state lifetime) of the FPs, practically, it depends on folding/maturation kinetics, completeness of maturation, expression efficiency in host organism and the optics (wavelength of excitation, profiles of dichroics and detection filter). Evolution of bright mApple was achieved from several rounds of random and site-directed mutagenesis by the selection of brightness and maintaining higher photo-stability [11]. The higher brightness of mApple can be attributed to its higher ϕ than mCherry (0.49 *vs.* 0.22). For generation of bright mRuby3 variants, Bajar *et al.* executed multiple round of mutagenesis on mRuby2 and subsequent selection based on brightness [102]. Although the authors claimed that the improved brightness in mRuby3 was due to tighter packing of chromophore and reduction of non-radiative channel, it was not verified and most of the mutations were facing outward or in the loop region of the protein barrel. Very few studies have been reported in the literature that are based on a strict rational hypothesis. In a recent study by Pandelieva *et al.* [103], the chromophore of mRojoA was sandwiched between two Tyr residues creating a rigid chromophore environment. This eventually leads to an increase in ϕ by ~ 3 fold and increased rigidity of the chromophore was validated by its B-factor or temperature factor. As the excited state lifetime of FPs is proportional to the ϕ, the engineering of lifetime is a viable option for enhancing the brightness of red fluorescent proteins. This idea has been employed by our group to generate brighter versions of mCherry. Recently, Bindels *et al.* generated a bright RFP, mScarlet, using a synthetic gene by selecting mutants with improved lifetime [104]. mScarlet was reported to have a 70% quantum yield which is the highest for a monomeric RFP

to date. Screening and selecting based on lifetime could also be used to generate mutants with nearly mono-exponential decays which is advantageous in fluorescence lifetime imaging microscopy (FLIM).

Engineering efforts to improve the **photostability** of RFPs have largely been performed based on random mutagenesis owing to a lack of clear mechanistic understanding of photobleaching decay pathways. Photostable versions of TagRFP and mOrange have been generated by a cohort of targeted and random mutagenesis followed by colony-based based screening with irradiation under the arc lamp and subsequent selection of mutants to generate TagRFP-T and mOrange2 respectively [11]. Interestingly, Liu and coworkers proposed an explanation for the improved photostability of TagRFP-T based on four available states of its chromophore: *trans*-protonated, *trans*-deprotonated, *cis*-protonated, *cis*-deprotonated. According to their "circular restoration model", the light excitation drives efficient conversion between dim and bright states in a dynamic loop and thereby decreasing photo-degradation [105]. As discussed previously, molecular oxygen is necessary for the maturation process of chromophore. But oxygen is also implicated in the process of photobleaching as evidenced by the fact that TagRFP-T and other proteins show a reduced rate of bleaching in anaerobic conditions [11, 57]. Recently, Ren et al. produced a photostable version of mKate2 by introducing cysteine residues in the vicinity of the chromophore [106]. mStable, which is reported to be ~ 12 times more photo-stable than its precursor undergoes a photo-induced reaction to produce sulfinic and sulfonic acids making it more photo-stable.

A significant amount of rational designing has been employed for tuning the spectral properties of RFPs [107, 108]. Essentially, the emission maximum of a FP depends on the energy gap between the ground and excited chromophore electronic states. There have been several hypothesis presented in literature to reduce this gap in order to achieve a bathochromic shift in the spectra. In the DsRed-like chromophore, GFP-like chromophore is further conjugated with a N-acylimine moiety. From a number of theoretical studies it was shown that during the excitation process, electron density from the phenol-ring was transferred to the N-acylimine region of the chromophore. So, introducing new H-bonding at the N-acylimine part of the RFP chromophore would potentially

stabilize the excited state and thereby decreasing the HOMO-LUMO gap in a FP. Indeed it has been shown that direct or water mediated H-bonding with the N-acylimine and Glu16 has been crucial for longer wavelength emission of mNeptune, mPlum and mCardinal [108]. Introduction of Tyr above or below the chromophore facilitates π-stacking interactions that leads to red-shifted emission. This is due to increased dipole moment of Tyr at the excited state and preferential stabilization of its excited state in a polar solvent [109]. In fact, the introduction of Tyr above the chromophore of GFP and mCherry leads to development of YFP and mRojoA those emit longer wavelength than their precursors [109, 92]. Grigorenko *et al.* proposed that a triple-decker motif where the traditional GFP chromophore is sandwiched between two Tyr residues would emit at a lower energy wavelength [110]. Another proposed mechanism for reducing the HOMO-LUMO gap, was to introduce a bulky group at the phenolate-end of the RFP chromophore and thereby de-stabilize the ground state. This has not been validated though. Hense *et al.* [107] described how altering the fraction of *cis-trans* conformations could lead red-shifting of eqFP611.

Chromophore maturation in RFPs is slower than GFPs and often it leads to incomplete maturation by forming both green and red chromophores [95]. As both GFP and RFP chromophore formation occurs through a branched pathway, a detailed understanding of roles of different amino acids need to be investigated in order to differentially slowing down or accelerating certain reactions [111]. Engineering of FPs that withstand extreme conditions *e.g.* oxidizing conditions have been achieved [86]. The cytotoxicity and dimerization tendency of mKate2 have been alleviated by generating the FusionRed variant. FusionRed is discussed in detail in Chapter 6.

It has been revealed that the key photo-physical parameters of FPs are largely inversely correlated. For instance, with increasing the excited state lifetime of FPs, ϕ is increased but at the cost of reduced photostability. To improve ϕ, rigidity of the chromophore is paramount, which can be achieved by increased interaction of the chromophore with the surrounding residues. However, flexibility around the chromophore-forming tri-peptide is essential for fast maturation process. Also, increase in emission wavelength requires longer conjugation within the chromophore that is associated with enhanced vibrational motions and non-radiative decays. This is detrimental

for fluorescence quantum yields of the FPs. Innovative and creative approaches are essential for bypassing these fundamental limitations. For example, directed mutagenesis to achieve a non-native chromophore within the β-barrel with a higher number of double bonds could be attempted. Engineering radiative lifetime of the chromophore is a viable strategy for simultaneous improvement in quantum yield and photostability of the FPs as discussed in Chapter 7.

1.5 Thesis Objectives & Outlines

Even two decades after the introduction of RFPs, their performance is not comparable to that of their green, cyan and yellow counterparts. Several laboratories around the globe are engaged in developing the key photo-physical properties of RFPs, *e.g.*, brightness, maturation, photo-stability, quantum yield *etc.* The complex photo-physics have yet to be discerned at a molecular level so that FPs with any desired phenotype could be produced at will. This thesis describes different photo-physical events with a molecular focus so that in the near future we can proceed into that direction. For simultaneous enhancement of different photo-physical properties of RFPs, the use of a multi-parametric microfluidic platform was established presented along with some novel alternative approaches for library design and selections. This thesis is a repository of large number of RFP mutants produced by the evolution pressure to engineer the excited state properties of the RFPs. These mutants could significantly advance the optical imaging with RFPs and provide a bedrock to unravel some key questions in this field.

Chapter 2 describes the measurement of dark state conversion and ground state recovery of the RFPs. Time and frequency-domain methods for DSC/GSR measurements for mCherry, TagRFP-T and Kriek are discussed in this chapter. The connection between ensemble level DSC/GSR and single molecule level 'blinking' is elucidated in Chapter 3. This chapter also deals with the increased blinking of Dronpa-linker-TagRFP-T (DpTT) compared to wild-type TagRFP-T. The methods and instrumentation for microfluidic screening and sorting are discussed in Chapter 4. Chapter 5 describes the evolution of mCherry from a RFP with low quantum yield ($\sim$ 20 %)

to a mutant with 71 % quantum yield. In this chapter, I discuss how systematic engineering of excited state lifetime of fluorescent proteins could lead to improvement in quantum yield. The evolution of brighter variants of FusionRed is discussed in Chapter 6. This represents the result of directed evolution in fluorescence lifetime and maturation of FusionRed. Chapter 7 describes how engineering of radiative lifetime of the FPs could be an alternative and novel approach for enhancing the fluorescence quantum yield. The final Chapter 8 explores the future developments of the RFP engineering project.

Chapter 2

Dark State Conversion and Ground State Recovery in Red Fluorescent Proteins

2.1 Publication Note

This Chapter has been adopted from Manna *et al.*, Time and frequency-domain measurement of ground-state recovery times in red fluorescent proteins, *The Journal of Physical Chemistry B*, 119 (15):4944-4954, **2015** [33] and the corresponding Supplementary Information of the article.

2.2 Introduction

The discovery of green fluorescent proteins (GFP) from the jellyfish *Aequorea victoria* and its subsequent expression in living cells without exogenous substrates or cofactors had a revolutionary impact on the field of *in vivo* bioimaging, biosensors, and super-resolution microscopy [5]. The genetic encodability of the GFPs and their mutated homologous forms, blue, cyan, and yellow FPs, makes them particularly advantageous in biosensing and live cell imaging [14, 19]. Red fluorescent proteins (RFPs) are particularly useful because they require low energy excitation ($\lambda > 550$ nm) to fluoresce and therefore impart less phototoxicity and reduce fluorescence from endogenous fluorophores. Despite these advantages, low brightness and low photostability compromise the usefulness of existing RFPs, and the continued development of monomeric RFPs with increased brightness, complete chromophore maturation, long lifetime, photostability, and pH-stability is an ongoing challenge [11, 99, 90].

The low brightness and quantum yield of the FPs are generally attributed to various non-radiative pathways including reversible and irreversible photobleaching mechanisms. Experimental evidence on green and yellow FPs revealed the existence of long-lived non-fluorescent or dark states (lifetimes ranging from μs to s) responsible for the reversible photobleaching [32, 112, 113]. RFP molecules are trapped in these dark states via dark state conversion (DSC), which reduces the fluorescence quantum yield. In addition, permanent photobleaching or photodestruction may take place from these dark states. These rich photo-dynamics have motivated various *in vitro* and *in vivo* analyses characterizing these dark states and elucidating the mechanism involved in photobleaching using X-ray crystallography, fluorescence correlation spectroscopy (FCS), single molecule spectroscopy (SMS), two-photon laser scanning microscopy (TPLSM), NMR, and other techniques [114, 115, 116, 38, 117, 118]. These dark states may be triplet states, different geometric isomers, or different protonated forms of the chromophore [37, 119]. For example, a crystallographic study of mKate (mutant of eqFP578) revealed that in an acidic environment the chromophore of the FP is in a non-fluorescent, *trans* configuration, whereas at high pH it is in a fluorescent, *cis* configuration [117]. In general the ground-state recovery (GSR) times for FPs vary from millisecond to sub-millisecond time scales. Knowledge of the GSR time can be used to inform the optimal choice of FP for a particular imaging method, which may have an associated excitation intensity, scan rate, and duty cycle. For example, by employing pulsed excitation with pulse separation times longer than the GSR time, Donnert *et al.* observed considerable increase in fluorescence output from GFP and the dye Atto532 [119]. Beyond this report, however, there are few instances in which pulsed excitation has been used to mitigate the contribution of dark states to reduction of the fluorescence output.

Super-resolution microscopy has taken *in vivo* imaging to new heights by surpassing the diffraction-limited spatial resolution of traditional optical microscopy [120, 121]. Several of these techniques rely on manipulating the DSC process. In particular, single molecule localization-based super-resolution techniques such as photoactivated-localization microscopy (PALM), stochastic optical reconstruction microscopy (STORM), and direct STORM (dSTORM) employ the spontaneous

blinking or photo-switching properties of fluorescent proteins and organic dyes [122]. The resulting demand for well-characterized blinking, photo-activatable, photo-convertable, and photoswitchable FPs has led to the generation of multiple FPs covering a wide range of excitation and emission windows [47, 123, 40, 124]. Measurement of the switching rates and elucidating the underlying mechanism of blinking is helpful in engineering these FPs for system-specific applications. Flow cytometry is a promising technique for high-throughput screening and sorting of FP libraries generated by random or site-directed mutagenesis. Recent efforts have been made to incorporate photostability and fluorescence lifetime as sorting parameters for developing new FPs [125, 98, 97]. New methods to measure the GSR times or switching rates of the RFPs would provide another dimension to these cytometry-based selection procedures and would therefore promote broader application of super-resolution microscopies.

Permanent photobleaching is one of the main drawbacks of FPs. The mechanism of photobleaching is still poorly characterized and seems to vary among FPs, yet a detailed mechanistic understanding along with methods to quantify the rate of these processes would be useful for generating improved fluorophores. The DSC process is closely related to the permanent photobleaching, which can occur from dark states as well as from the initially excited state and may act to increase or decrease the photostability of an FP [56]. Although several reports in the literature described the nature of dark states, to the best of our knowledge few detailed studies of DSC and GSR kinetics and analysis of the measurement techniques have been reported [32, 112, 113, 114, 36, 126].

Here we examine approaches for the measurement of GSR times of RFPs based on time- and frequency-domain techniques. In the time-domain technique, the sample is excited with 2 ms pulses at a varying inter-pulse delay, to populate the dark states. The time constant of the subsequent fluorescence recovery directly quantifies the relaxation rate. The frequency-domain technique is based on phase fluorimetry [127, 128]. In conventional frequency-domain fluorescence lifetime measurements, the sample is excited with a sinusoidally modulated laser beam with a modulation frequency comparable to the reciprocal of the excited-state lifetime. The intensity of fluorescence from this sample oscillates at the same frequency but the signal is time-delayed if the

molecules spend a finite amount of time in the excited state [129]. The oscillating emission signal shows a negative phase-shift (*i.e.*, phase lag) and a modulation amplitude lower than that of the excitation waveform. For a two-state system, this phase shift (ϕ) and reduction in modulation amplitude (m, modulation) are directly related to the lifetime of the sample as,

$$\phi = arctan(\omega\tau) \tag{2.1}$$

$$m = \frac{1}{\sqrt{1+\omega^2\tau^2}} \tag{2.2}$$

where, ω and τ are the modulation frequency and the excited-state lifetime, respectively. Recent experiments and calculations by Zhu and co-workers [127, 128] show that this phase shift can be positive if the chromophore has a dark state (*i.e.*, for a three-state or higher state system) and if the modulation frequency employed in the measurement is comparable to the inverse of the GSR time. Under these conditions, the emission waveform seems to precede the excitation waveform. This "fluorescence anomalous phase advance" (FAPA) can be explained in the following way: After excitation to S1 (Figure 2.6a), a fraction of the excited-state population is trapped in the dark state. When the modulation frequency is very low compared to the GSR rate, the fluorescence closely follows the excitation, giving $\phi \sim 0$. At high frequency compared to the GSR rate, the dark state is unresponsive and $\phi < 0$. But if the two frequencies are comparable, the rising half of the oscillation populates a fraction of the molecule in the dark state. But due to the long lifetime of the dark states, the falling half of the waveform will excite a smaller population resulting in decreased fluorescence. This effect makes the waveform asymmetric (Figure 2.1) and causes the apparent phase advance [128].

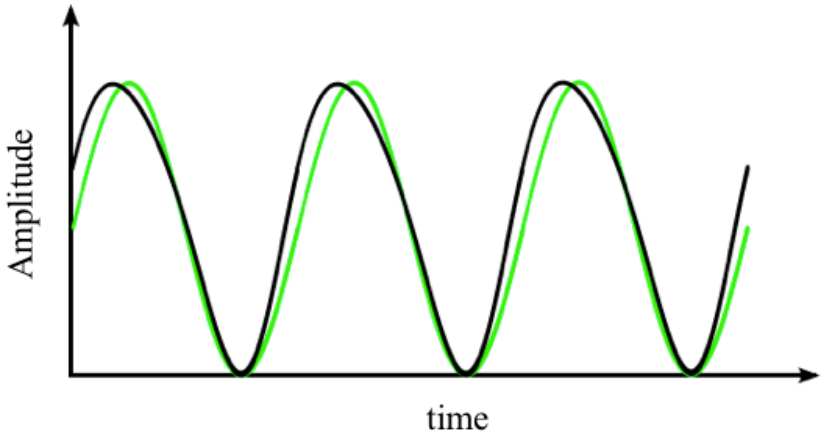

Figure 2.1: Schematic diagram displaying phase advance. When molecules having dark or non-fluorescent states are excited with sinusoidally modulated laser (green) and the frequency of the modulation is comparable to its dark-state dynamics (DSC/GSR), distortion of the fluorescence (black) signal causes anomalous phase advance.

2.3 Experimental Methods

2.3.1 Time-Domain Measurement

For the time-domain method the sample was excited with laser pulses from a 532-nm diode-pumped solid-state laser (Laser Quantum, Opus-2.0W). The laser pulses had a rectangular time profile with a 2 ms exposure and varying inter-pulse dark times (zero laser intensity) ranging from 5 μs to 50 ms. Some samples, especially TagRFP-T showed a kindling effect upon first exposure to light, resulting unusually high fluorescence for a few microseconds (data not shown). To remove this artifact, all the samples were pre-illuminated at very low laser intensity (<500 W/cm^2) for 2 ms duration before the measurement pulse-sequence. An acousto-optic modulator (AOM, Gooch & Housego, 35210-BR) was used to obtain this pulse profile. The RF input to the AOM driver (Gooch & Housego, R31210-6ADS) was delivered by a function-generator (Agilent, 33250A) controlled by custom-made software. The modulated light enters a custom-built inverted

microscope and is focused on the sample with a 100X 0.8 NA air-immersion objective (Olympus). The measured FWHM of the beam profile was 3 μm. The average power at the focal point of the lens was measured with a power meter. Scattered light from the sample was focused onto a CMOS camera (ThorLabs, DCC1545M) for visualization of the sample. A 532-nm long-pass filter was used to separate the excitation from emission. The epifluorescence was collected using an Avalanche Photo Diode (APD, Advanced Photonics) or Photo-Multiplier Tube (PMT, Hamamatsu Photonics, R9880U-20). The PMT photocurrent was converted to voltage with a home-built trans-impedance operational amplifier to improve the signal to noise ratio. The signal from the PMT was digitized at a sampling frequency of 1 MHz with a data acquisition (DAQ) card (National Instruments). Typical fluorescence signals obtained from the RFPs are shown in Figure 2.2. The raw fluorescence data were spline/exponential fitted to get smooth traces. The ground state recovery or percent recovery (PR) for first three pulses were calculated from the fluorescence profiles as follows:

$$PR = \frac{FR - FB}{FL - FB} \times 100 \tag{2.3}$$

where FL, FB and FR are initial fluorescence, fluorescence after exposure and recovered fluorescence respectively as explained in Figure 2.2. The average percent recoveries from these three pulses were fitted against the dark times with a single-exponential function to extract the GSR time constant.

To extract the irreversible photobleaching time-constants in the time-domain measurements, we locate the peak intensities of the pulses and fit those intensities with a single exponential function (Figure 2.3). We have specifically chosen the time-domain data set having inter-pulse delay time as 10 ms between two successive 2 ms pulses. This allows most of the population trapped in the dark state to relax back in the ground state. Hence, these time-constants reflect the combined bleaching from bright and dark states (Figure 2.6a, k_{S1B} and k_{DB}).

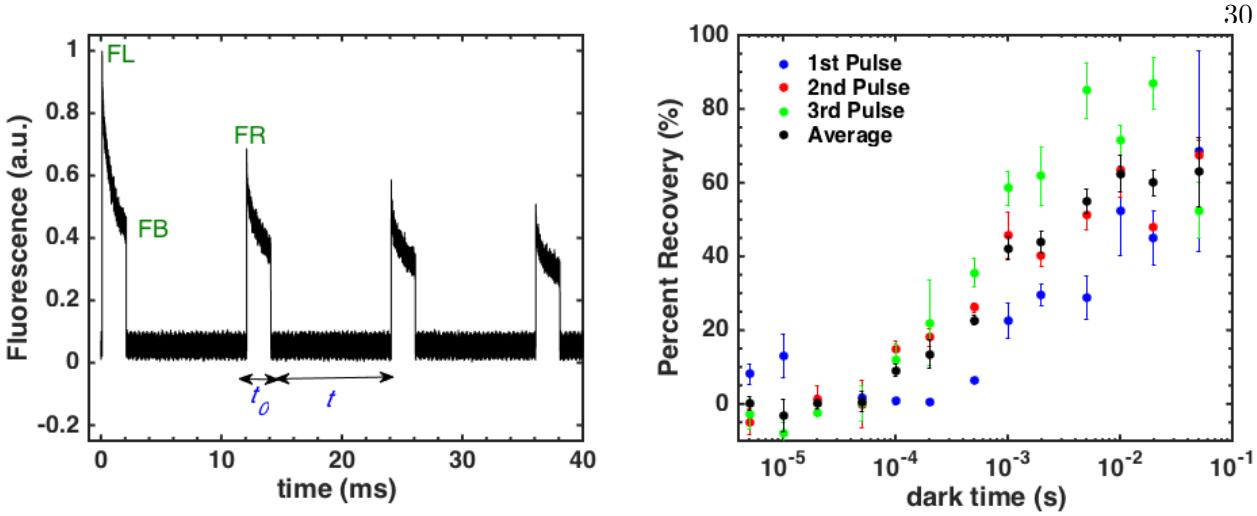

Figure 2.2: (left)Typical fluorescence signal obtained from RFPs in time-domain GSR experiment. The sample is excited with a pulse having constant exposure time (t_0), but the time between two pulses (t) varied from 5 μs to 50 ms. This figure shows the fluorescence intensity profile of mCherry at 25 kW/cm^2 for exposure and dark time 2 and 10 ms respectively. (right) Percent Recovery (PR) of the first 3 pulses and the average of the PR for mCherry at 25 kW/cm^2. Average PR is fitted against the dark time to extract the GSR time-constant.

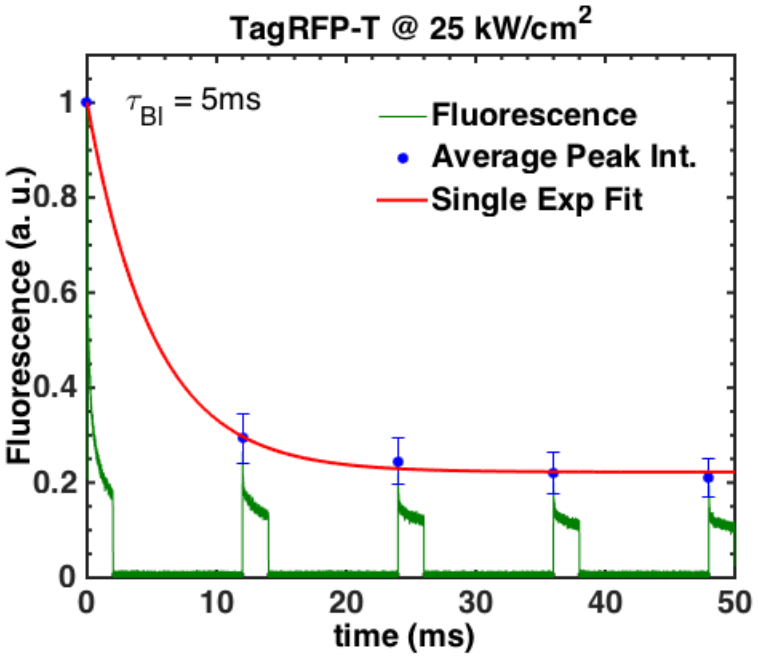

Figure 2.3: Peak intensities of the pulsed fluorescence traces are identified and fitted with a single exponential function to extract the pulsed photo-bleaching time-constants of the FPs. Fluorescent proteins were excited with pulses of 2 ms exposure time and 10 ms of inter-pulse delay.

2.3.2 Frequency-Domain Measurement

For frequency-domain measurements, purified proteins were excited with the same 532-nm laser as in time-domain measurements but with a light beam sinusodially modulated by the AOM driven by a function generator. The incoming beam from the AOM is split with a 50:50 beam splitter. Half of the modulated beam was sent to a photodiode (DET36A, ThorLabs) to provide a reference signal for a high-frequency lock-in amplifier (Zurich Instruments, UHF). The remainder of the beam used for sample excitation went through the same custom-built inverted microscope setup described as before. The fluorescence signal was collected by a PMT and further processed by the lock-in amplifier to obtain the phase-shift induced by the FPs. To eliminate any effect of varying photoelectron transit time on the measured phase, the PMT was operated with same gain (or voltage) for different sets of phase measurements. We use home-built software (Labview) for interfacing the laser, function generator, and lock-in amplifier. The sample was scanned from modulation frequency of 1 kHz to 200 kHz with an average 4 s of exposure and a 80 ms lock-in time constant. The last 1000 phase points from the lock-in output were averaged to obtain the phase shift. Phase values at each modulation frequency were obtained by focusing the laser at different spots on the coverslip to avoid any photo-bleaching. Phase shift values from the scattered signal by a blank coverslip were measured to provide an absolute phase shift value which accounts for time-delays induced by cables, optics, and electronics in the experimental setup. This absolute phase shift is subtracted from the sample phase shift to obtain the actual phase shift [129]. To ensure that phase measurements are not impacted by the free diffusion of the proteins, we verified that the same results were obtained from phase spectra on localized proteins expressed in *E. coli* and FPs measured in solution.

2.3.3 Sample Preparation

RFPs used in these experiments were either purified proteins (frequency-domain experiments) or expressed in *E. coli* (time-domain experiments). For the expression in *E. coli*, we used standard

molecular biology techniques. The competent cells (Top10) were transfected with plasmid DNA (pBAD vector) and cultured overnight on agar plates containing Lysogeny Broth (LB) media and ampicillin at 37°C. After the FPs were well-expressed in these bacteria, we picked a single colony and transferred it to 500 μL of Ca^{2+} and PO_4^{3-} free HEPES-buffered Hank's balanced salt solution (HHBSS, pH 7.4). Measurements were performed on a 20 μL volume of the buffer solution containing the bacteria placed on a coverslip with 20 μL of poly-L-lysine for cell immobilization. Purified RFPs were dissolved in 3-(N-morpholino)propanesulfonic acid buffer (15 mM MOPS, 100 mM KCl, pH 7.4), and measurements were performed on 25 μL volumes.

2.4 Results

Figure 2.4 shows the results of time-domain GSR measurement of RFPs expressed in *E. coli* excited at 4, 8, and 25 kW/cm^2. The fluorescence decay profiles were fit with multiexponential functions to extract the weighted photobleaching time constants of mCherry, TagRFP-T, and Kriek which are 3.5, 2.1, and 7.6 ms, respectively (Figure 2.4a). For mCherry and Kriek, the decay had been fitted with biexponential functions whereas a triexponential function was needed to fit the TagRFP-T profile. At 25 kW/cm^2 laser intensity, TagRFP-T bleaches ~1.7 times faster than mCherry during the course of a 2 ms exposure, in agreement with previous findings [125, 56]. The Kriek FP is a higher photostability variant of mCherry selected from a mCherry-based mutagenesis library after multiple rounds of microfluidic-based sorting based on photostability [57]. Accordingly, Kriek bleaches ~ 2 times slower than mCherry. In this 2 ms window, this decay of the fluorescence signal is the result of both irreversible and reversible processes. To isolate the irreversible photobleaching from the total photobleaching, we use a pulse sequence of 2 ms exposure and varying dark time as explained in Experimental Methods. We specifically used a 2 ms pulse train as it was observed (Figure 2.2a) that in this regime, a significant fraction of the population is bleached and therefore the dark state is significantly populated.

Figure 2.4 presents the percent recoveries (PR; calculated from 2.3) of the RFPs as a function

Table 2.1: Fitting Parameters for Time-Domain GSR Data to $a - be^{-t/\tau_{GSR}}$

RFP	Intensity (kW/cm^2)	$\tau_{Bl}(ms)$	$\tau_{GSR}(ms)$	a	b	$PR_{lim}(observed) = (a+b)/2$
TagRFP-T	25	5.0	0.22	44	43	44
TagRFP-T	8	14	0.20	35	35	33
TagRFP-T	4	17	0.26	41	38	40
mCherry	25	28	0.99	58	54	56
mCherry	8	250	1.2	73	74	74
Kriek	25	49	2.8	65	62	64

of dark time. The fitted GSR times are collected in Table 2.1. The value of PR does not reach 100 % even if the dark time is allowed to be sufficiently large to reach an asymptotic value. As shown in the kinetic modeling section (below), the limiting value falls below 100 % because some of the population is bleached during the 2 ms irradiation period. As expected, it is observed that the laser intensity does not have a pronounced effect on the GSR time scale. The recovery of mCherry at 4 kW/cm^2 and Kriek at 4 kW/cm^2 and 8 kW/cm^2 are not determined at these intensities, as there is not enough dark-state population to produce a reliable recovery curve (data not shown). The irreversible photobleaching or photodestruction time constants (τ_{Bl}), measured by fitting the peak intensities of the pulses with single-exponential functions (Figure 2.3), show strong intensity dependency (Table 2.1), indicating that the processes involved in photodestruction are light-induced rather than spontaneous. At 25 kW/cm^2, the irreversible photobleaching occurs from mCherry with a time constant (τ_{Bl}) of 28 ms, but at 8 kW/cm^2, it is almost $\sim$ 9 times more photostable with $\tau_B l$ of 250 ms. This photobleaching reflects the total photodestruction of the FPs out of both excited and dark states (Figure 2.6a). The relative order of irreversible photobleaching time constants of the three FPs studied here is Kriek > mCherry > TagRFP-T, in agreement with previous reports [56, 57].

Figure 2.5 depicts the results of frequency-domain GSR measurements for the three FPs *in vitro*, over the range from 1 kHz to 175 kHz. In this frequency window we observe positive phase shift or phase advance rather than a phase lag. Our results reveal (Figure 2.5) the existence of phase advance up to 2° at 25 kW/cm^2 in this frequency region. The maximum values of the

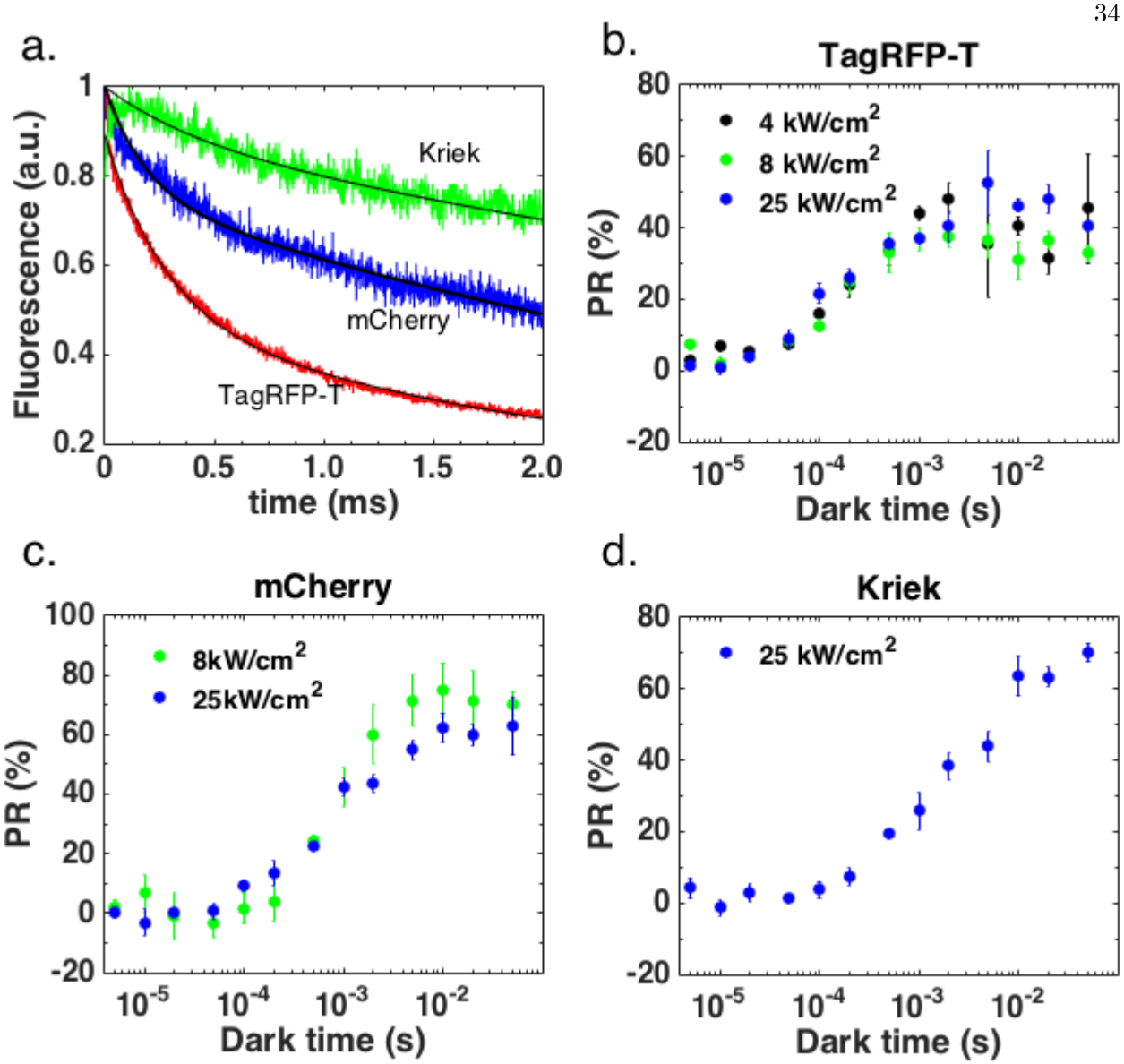

Figure 2.4: Fluorescence profiles of TagRFP-T (red), mCherry (blue), and Kriek (green) expressed in *E. coli* at 25 kW/cm^2. The solid black lines represent the biexponential (mCherry, Kriek) and triexponential (TagRFP-T) fit of the fluorescence decay. The weighted decay constants based on the fit are 2.1, 3.5, and 7.6 ms for TagRFP-T, mCherry, and Kriek, respectively. Plots b-d show the percent recovery of each FP as a function of dark time between the two pulses at different intensities.

phase advance observed by Min *et al.* [127] (∼10°) were significantly larger due to the higher laser intensities employed in that study (600 kW/cm^2) as well as the higher rate of DSC for the chromophores (Flavin adenine dinucleotide and fluorescein isothiocyanate). As explained by our

numerical simulations (below) the magnitude of the phase advance also decreases if the GSR rate is higher than or comparable to the DSC rate. Figure 2.5d presents the intensity dependence of phase advance of mCherry at 1 kHz modulation frequency. It is clear that with the increase of intensity, the phase advance also increases, which supports the fact that FAPA is an intensity-dependent phenomenon. At higher excitation intensity, a larger fraction of the population is trapped in these dark states, increasing the phase advance. As described in Introduction of this chapter, this phase advance is inherently related to the dark-state relaxation, and we modeled these data to extract the DSC time-constants (k_{S1D}, k_{DS1}).

2.5 Kinetic Modeling

2.5.1 Time-domain Measurement

The observed time-domain and frequency-domain results can be explained with a three-state kinetic model (Figure 2.6a) with S_0, S_1, and D as the ground electronic state, first excited state, and non-fluorescent (dark state) state, respectively. The population photo-excited to S_1 can either photobleach irreversibly or it can be transferred to the dark state and subsequently relax to the ground state. There is also a possibility of photobleaching from the dark state. The kinetic equations describing the populations of these states are:

$$\frac{d[S_0]}{dt} = -k_{ex}[S_0] + k_{em}[S_1] + k_{GSR}[D] \tag{2.4}$$

$$\frac{d[S_1]}{dt} = k_{ex}[S_0] - k_{em}[S_1] - (k_{S1D} + k_{S1B})[S_1] + k_{DS1}[D] \tag{2.5}$$

$$\frac{d[D]}{dt} = k_{S1D}[S_1] - (k_{DS1} + k_{GSR} + k_{DB})[D] \tag{2.6}$$

$$k_{ex} = \frac{I\sigma\lambda}{hc} \tag{2.7}$$

The excitation rate is calculated with Eqn. 2.7, where, I, σ, and λ are laser intensity, absorption cross-section, and excitation wavelength, respectively, and h and c are Planck's constant

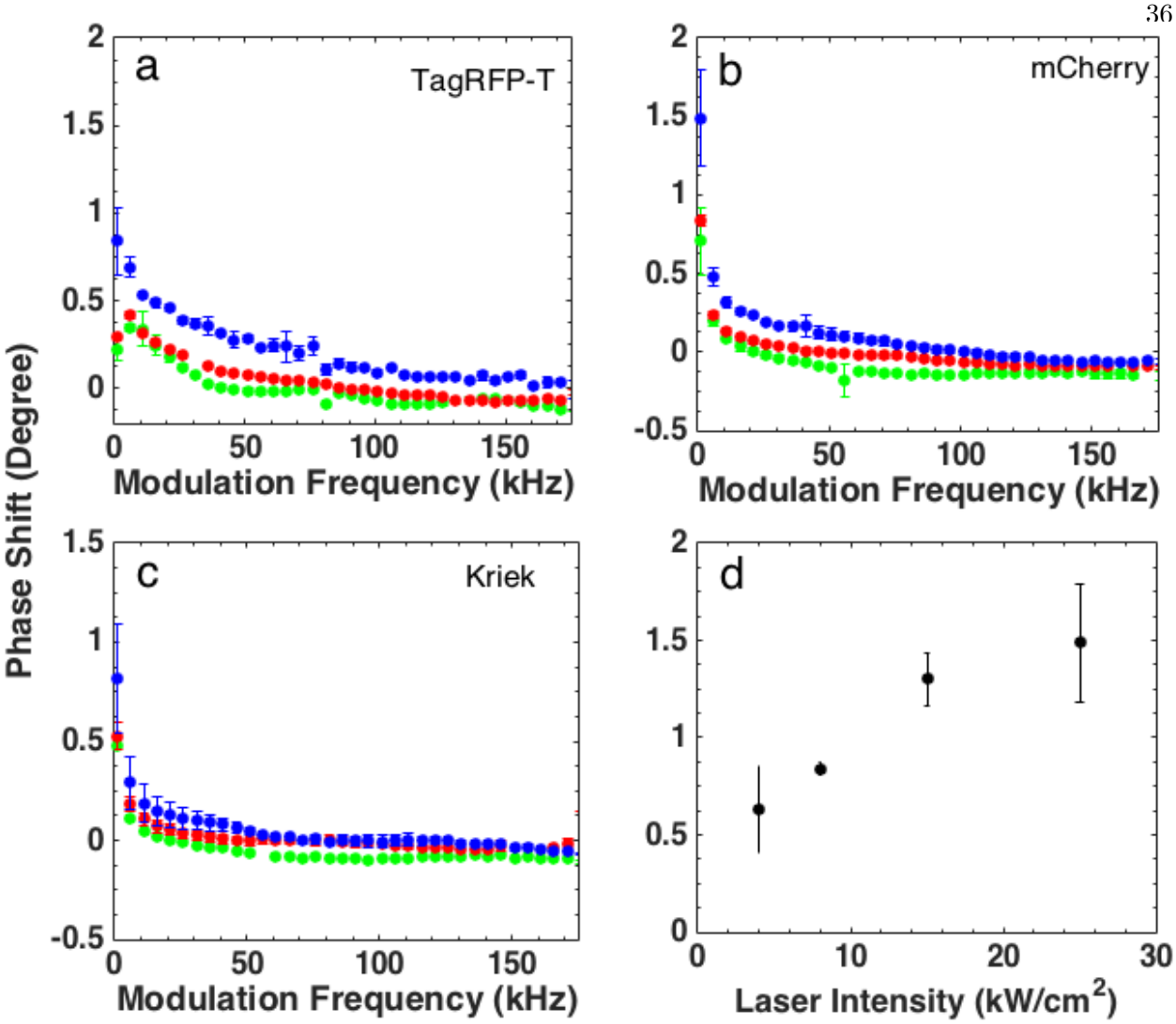

Figure 2.5: (a-c) Frequency-domain results for TagRFP-T, mCherry, and Kriek measured *in vitro*. Green, red, and blue dots represent the phase shift at 4 kW/cm^2, 8 kW/cm^2 , and 25 kW/cm^2 laser intensities, respectively. (d) The phase shift of mCherry at a modulation frequency of 1 kHz increases with the laser intensities.

and the speed of light. I and λ (532 nm) are known quantities in this experiment. The absorption cross-section at any arbitrary wavelength λ, σ_λ, has been calculated using the known molar extinction coefficient of the FPs using the following equations:

$$\sigma_\lambda = 2.303 \times \frac{\epsilon_\lambda}{N_A} \times 10^3 \tag{2.8}$$

where, σ_λ is the molar extinction coefficient at λ in M^{-1}cm^{-1}, N_A is the Avogadro's constant.

Table 2.2: Molar extinction coefficients and excited state lifetime of the RFPs used for the simulations.

RFP	ϵ_{max} ($mM^{-1}cm^{-1}$)	ϵ_{532} ($mM^{-1}cm^{-1}$)	Lifetime (τ, ns)
TagRFP-T	81	39	2.71
mCherry	72	29	1.87
Kriek	48	18	1.00

The molar extinction coefficient at 532 nm of the three RFPs used in the calculations has been given in Table 2.2.

In time-domain experiments, the sample was excited with rectangular pulses of duration t_0 (2 ms) with a variable inter-pulse delay time (t) (Figure 2.2a). After the exposure t_0, the populations of ground and dark states are denoted as $[S_0]_{t0}$ and $[D]_{t0}$, respectively. As the fluorescence is proportional to the ground-state population, $FL = 1$ and $FB = [S_0]_{t0}$. Now assuming that in the dark time period, molecules trapped in the dark state primarily relax to the ground state, the population of D after a dark time of t is given by $[D]_{t0}e^{-k_{GSR}t}$. Therefore, during this dark time, the population that returns to the ground state is $[D]_{t0} - [D]_{t0}e^{-k_{GSR}t} = [D]_{t0}(1 - e^{-k_{GSR}t})$. So, $FR = [S0]_{t0} + [D]_{t0}(1 - e^{-k_{GSR}t})$. Incorporating these expressions for the fluorescence signals into the expression for PR gives:

$$
\begin{aligned}
PR &= \frac{FR - FB}{FL - FB} && (2.9)\\
&= \frac{[S_0]_{t0} + [D]_{t0}(1 - e^{-k_{GSR}t}) - [S_0]_{t0}}{1 - [S_0]_{t0}} \times 100 && (2.10)\\
&= \frac{[D]_{t0}(1 - e^{-k_{GSR}t})}{1 - [S_0]_{t0}} && (2.11)\\
&= PR_{lim}(1 - e^{-t/\tau_{GSR}}) && (2.12)
\end{aligned}
$$

where, $\tau_{GSR} = \frac{1}{k_{GSR}}$ and

$$PR_{lim} = \frac{[D]_{t0}}{1 - [S_0]_{t0}} \times 100 \qquad (2.13)$$

PR_{lim} reflects the percent recovery of the sample at very long dark time when all population from the dark state has relaxed to the ground state. As Eqn. 2.13 shows, to obtain the limiting

percent recovery (PR_{lim}), $[S_0]_{t0}$ and $[D]_{t0}$ need to be calculated by solving the set of coupled differential equations (Eqn. 2.5-Eqn. 2.6), which cannot be done analytically for sinusoidally modulated excitation. The solutions are very complicated and difficult to interpret even for a constant exposure, so we solved the equations numerically. ODE45 solver in Matlab had been used to solve those coupled differential equations.

Figure 2.6b and 2.6c shows the dependence of PR_{lim} on the various kinetic parameters of the three-level system. As shown in Figure 2.6b, PR_{lim} decreases monotonically with the increase of the bleaching rate constant (k_{S1B}) whereas percent recoveries increase with the increase of k_{S1D}. This trend can be explained by the fact that, with an increase of bleaching rate constant (k_{S1B}), a larger fraction of the molecules are permanently bleached and therefore removed from excitation-emission cycle, thus lowering the limiting percent recovery. On the other hand, with an increase in the DSC rate constant (k_{S1D}), a larger fraction of the molecules are trapped in the photo-protective dark state ($k_{DB} = 0Hz$), leading the molecules to recover slowly and accordingly increasing the PR_{lim}. Figure 2.6c shows that, with increasing GSR rate constant (k_{GSR}), PR_{lim} reaches a maximum at intermediate GSR rate constant (~1 kHz) but subsequently decreases as k_{GSR} continues to increase. This can also be explained on same line of argument as Figure 2.6b: For small values of k_{GSR}, the molecules are photo-protected in the dark state, increasing the percent recovery, but with a continuing increase in k_{GSR}, this effect becomes less pronounced and causes high photobleaching due to a nonzero k_{S1B}, resulting a decrease in PR_{lim}. Percent recoveries presented in these figures have been calculated using exposure and dark time as 2 and 5 ms, respectively.

Figure 2.6d shows the simulations of our time-domain experiments. Percent recovery (PR) was calculated using numerical simulations based on the three-state model system with dark-state lifetimes ranging from 5 μs to 50 ms and 2 ms light exposure time. The simulated percent recovery vs time profiles were fitted with single exponential functions to extract the values of k_{GSR}. As expected, the k_{GSR} from fitting results (k_{GSR} fitting) match the actual k_{GSR} used in the simulations. Notably, with increasing k_{GSR} the limiting percent recovery decreases, which supports simulation results in Figure 2.6c and the experimental results as discussed later. As the above analytical and

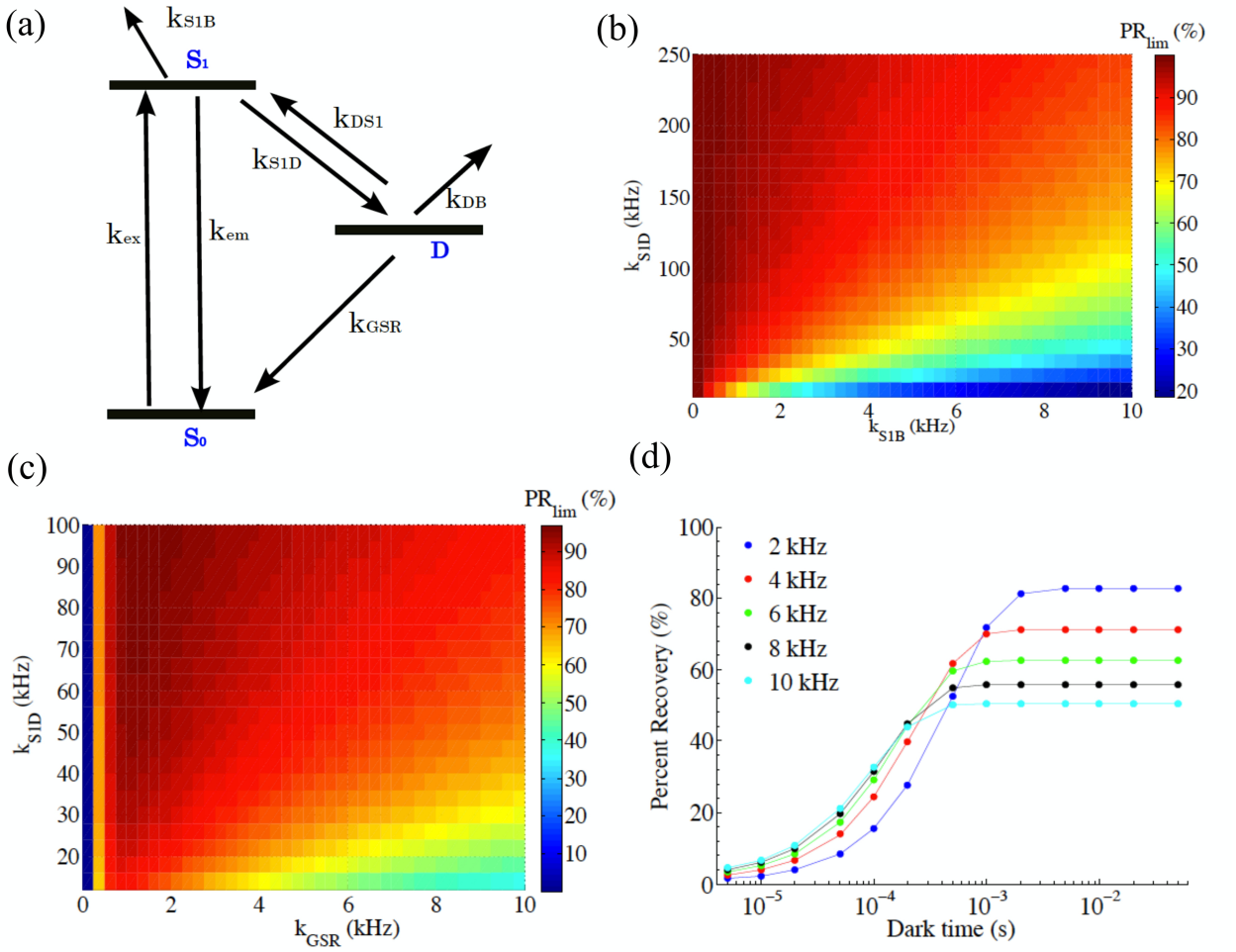

Figure 2.6: (a) Three-state photophysical model with ground state (S_0), excited state (S_1), dark state (D), and the relevant photokinetic parameters. (b) Numerical simulations based on the three-state model show the dependency of PR_{lim} on k_{S1D} and k_{S1B} rate constants. Parameters used in this study are, k_{ex}= 7.4 MHz ($\sim$ 25 kW/cm^2), k_{em}= 530 MHz (τ $\sim$1.87 ns), k_{S1D} = 10-250 kHz, k_{DS1}= 0 kHz, k_{GSR} = 2 kHz, k_{S1B} = 0-10 kHz and k_{DB} = 0 kHz. The limiting percent recovery (PR_{lim}) is calculated using exposure and dark time as 2 and 5 ms, respectively. Magnitudes of percent recoveries are given in the color bar. (c) Numerical results displaying the dependence of PR_{lim} on dark-state conversion rate constant (k_{S1D}) for and ground state recovery rate constants (k_{GSR}). Parameters used in this calculations were k_{ex} =7.4 MHz ($\sim$ 25 kW/cm^2), k_{em}= 530 MHz (τ $\sim$ 1.87 ns), k_{S1D}=12-100 kHz, k_{DS1}= 0 kHz, k_{GSR} = 0-10 kHz, k_{S1B} = 1 kHz, and k_{DB}= 0 kHz. The exposure and dark time used in these calculations were 2 and 5 ms, respectively. (d) Simulated percent recovery (dots) and single exponential fitting (lines) at different dark times ranging from 5 μs to 50 ms for different k_{GSR}. The exposure time used was 2 ms. The k_{GSR} extracted from single exponential fitting (k_{GSR} fitting) agrees well with the actual k_{GSR} used in the simulations (k_{GSR} input).

numerical analysis of percent recovery suggests that PR can be modeled as a single exponential

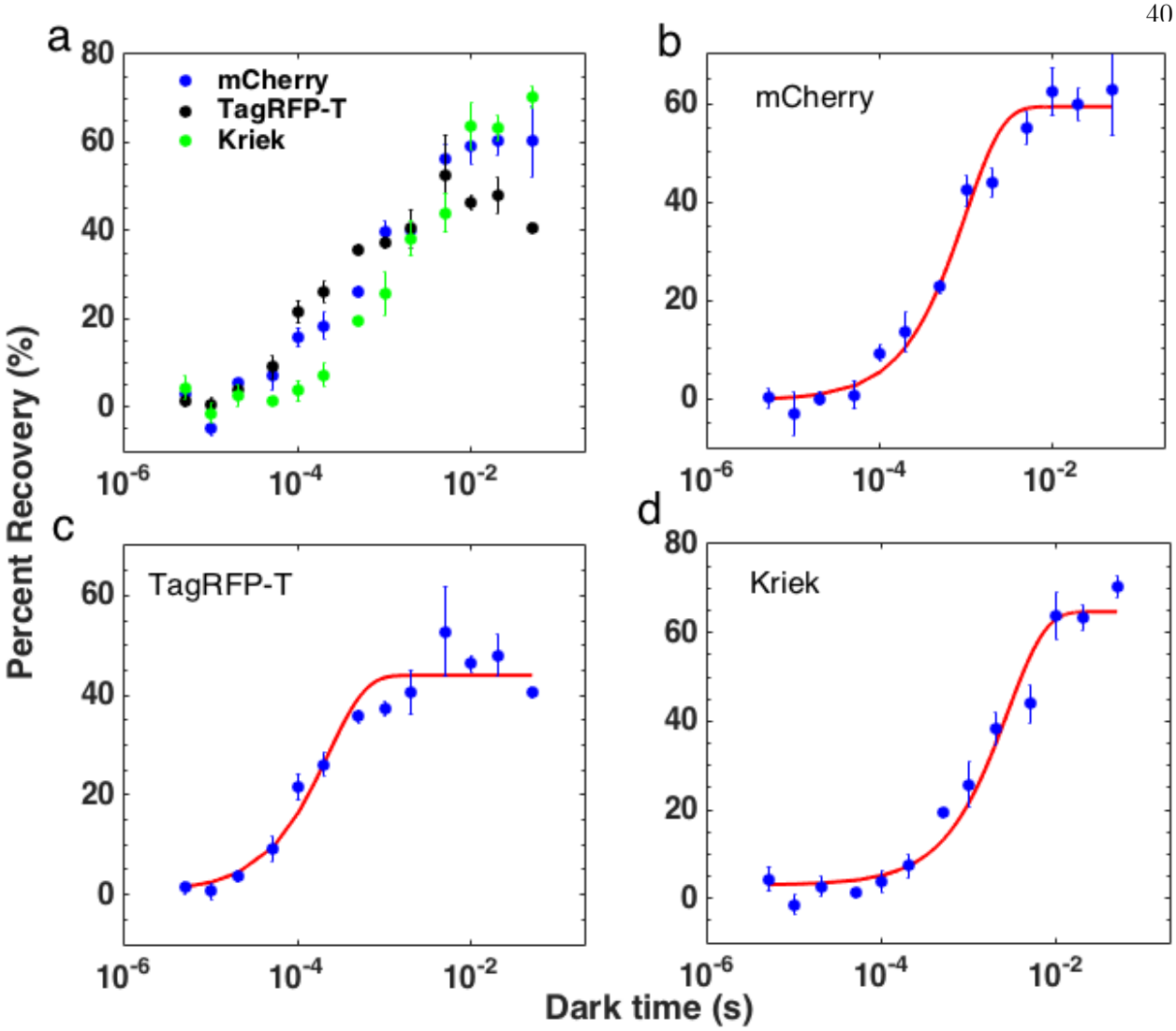

Figure 2.7: . (a) Results of time domain GSR experiments for different RFPs at 25 kW/cm^2 laser intensity. (b-d) Single exponential fitting (red lines) of the percent recovery (blue dot) measured at 25 kW/cm^2 in time-domain experiments. The plots are fitted with a function of $a - be^{-t/\tau_{GSR}}$ to extract the GSR time constants. The fit parameters are presented in Table 2.1. The order of the observed GSR time constant is Kriek > mCherry >TagRFP-T.

function of the dark time (Eqn 2.12), we fit the observed PR with a functional form of $(a-be^{-t/\tau_{GSR}})$ to extract GSR time constants. As shown in Eqn. 2.12, the parameters a or b can give the approximate PR_{lim}. Hence, we define the observed PR_{lim} as the average of a and b: (a + b)/2. Figure 2.7 shows the fitting of the percent recovery of the FPs at 25 kW/cm^2. Table 2.1 gives the fitted parameters, showing that TagRFP-T has the fastest and Kriek has the slowest ground-state

recovery.

2.5.2 Frequency-Domain Measurement

To extract the photokinetic parameters from our frequency domain measurements, numerical simulations were performed using the three-state model system (Figure 2.6a). We calculated the phase shift numerically by a home-built software that simulates the operation of a lock-in amplifier. We solved the three-state model kinetics numerically for a system excited with a sinusoidally varying intensity. In this analysis, the excited-state population $S_1(t)$, which is proportional to the fluorescence signal, was mixed with the modulated reference signal $sin(\omega t)$ and integrated to obtain the in-phase (I) component. Similarly, the in-quadrature (Q) component was obtained by mixing $S_1(t)$ with $cos(\omega t)$ and subsequent numerical integration. Finally, since I and Q are proportional to $cos(\phi)$ and $sin(\phi)$, respectively, for a sinusoidal excitation, the phase shift (ϕ) was calculated using, $tan^{-1}(Q/I)$. Technical details of the simulation and the Matlab code have been presented in Appendix A.

As direct least-squared fitting of the model parameters from the coupled differential equations is impractical, we systematically investigated the effect of various parameters on the phase shift in the frequency range in which the individual RFPs show phase advances and fit the parameters thereafter. From our simulations, it was found that the phase shift is insensitive to the bleaching rates from the excited state (k_{S1B}) or dark state (k_{DB}). Hence, we conclude that the frequency-domain measurement cannot be used effectively to resolve the rate of irreversible photobleaching. On the other hand, the simulations showed that the phase shift is sensitive to changes in k_{S1D} and k_{DS1}, which is unsurprising since these rate constants are directly responsible for equilibration of the excited state with the dark state, which in turn governs the phase advance. These two parameters were varied to obtain phase spectra with over a range of k_{S1D} and k_{DS1} values. Figure 2.8b and 2.8c demonstrates the effect of dark-state conversion rates (k_{S1D}, k_{DS1}) on phase shift for mCherry at 25 kW/cm^2. As expected, increasing the value of k_{S1D} results in an increasing positive phase shift because it corresponds to increasing population transfer to the dark state, which is

Table 2.3: Fitting Parameters for Frequency-Domain GSR Results.

RFP	Intensity (kW/cm^2)	$\tau_{GSR}(ms)$	$\tau_{S1D}(\mu s)$	$\tau_{DS1}(ms)$
TagRFP-T	25	0.22	15	0.017
TagRFP-T	8	0.20	14	0.031
TagRFP-T	4	0.26	15	0.058
mCherry	25	0.99	36	0.14
mCherry	8	1.2	40	0.50
Kriek	25	2.8	43	0.40

positively correlated to phase advance. Conversely, Figure 2.8c shows the phase shift decreases with increasing k_{DS1} as it corresponds to decreased dark-state population. By examining the effect of each parameter on the value of phase advance, it was possible to narrow down the initial range of kinetic parameters to permit fitting of the spectra.

The excitation rates (k_{ex}) were calculated using Eqn 2.7 and emission rates (k_{em}) were approximated as the reciprocal of the excited-state lifetime of the RFPs found in literature [56, 57]. The dark-state recovery times (k_{GSR}) were taken from the time-domain GSR rate constants. The best fit of the phase spectra was obtained after a few rounds of iterating the parameters k_{S1D} and k_{DS1}. Figure 2.8d shows the result for the best set of values for the mCherry phase spectra at 25 kW/cm^2 with k_{S1D} = 28 kHz and k_{DS1} = 7 kHz. Inability of the fit to perfectly capture both the low and high frequency range of the data may be due to the presence of multiple DSC pathways. Table 2.3 displays the best fitting results for other FPs at various laser intensities. The time constants, τ, for the different process in Table 2.3 are the reciprocals of the corresponding rate constants.

2.6 Discussion

The time-domain measurements were done on RFPs in *E. coli*, whereas the frequency-domain measurements were done on solutions with purified proteins. Time-domain measurements of the percent recovery require the proteins to be immobilized on the longest time-scale of the pulse sequence which is $\sim$ 260 ms. To mitigate the effects of diffusion, we tried to perform time-domain

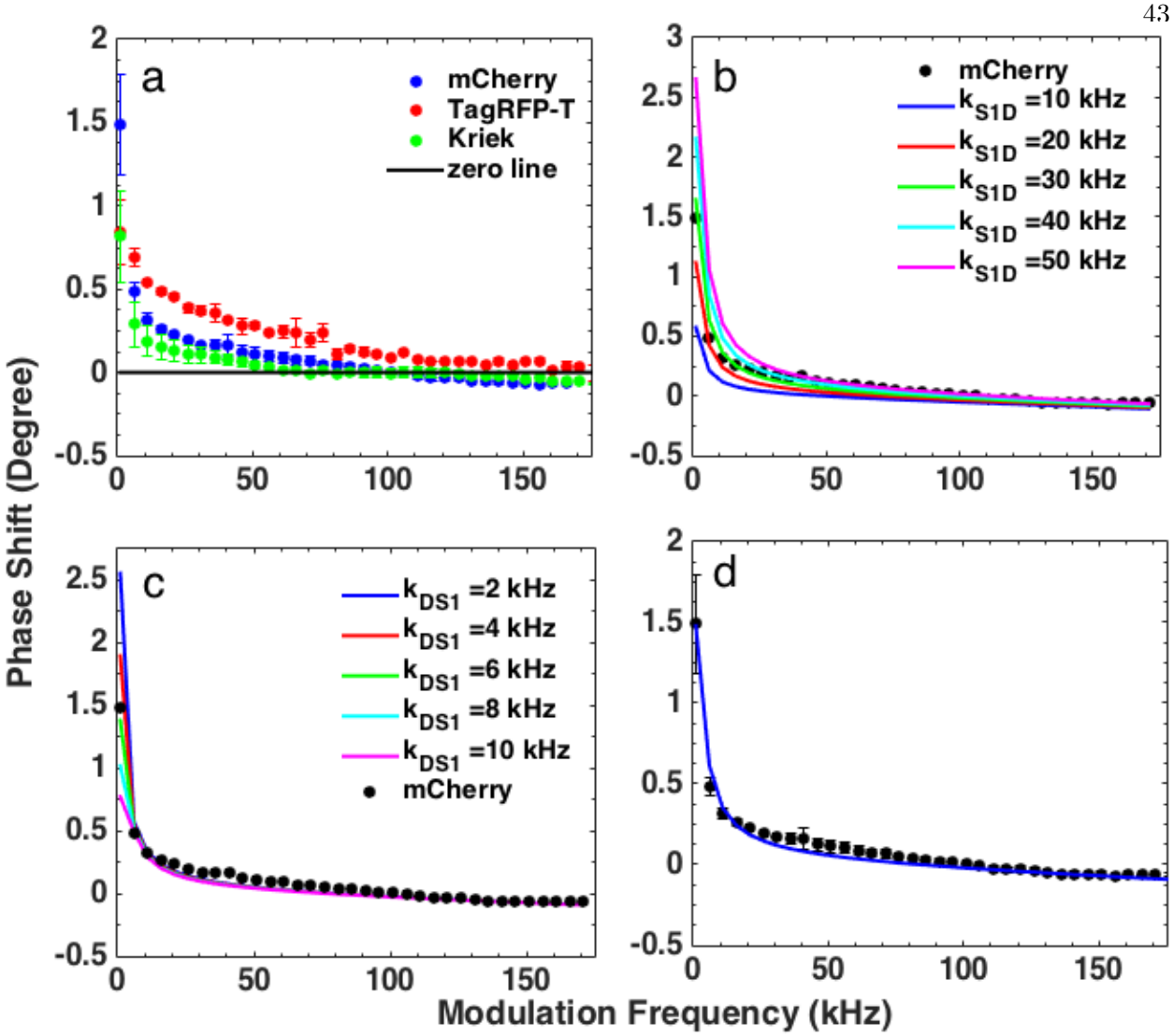

Figure 2.8: (a) Frequency-domain results comparing the region of phase advance for mCherry, TagRFP-T, and Kriek at 25 kW/cm^2. The solid black line represents the zero phase shift. (b) Simulated phase spectra showing the dependence of k_{S1D} at a fixed value of k_{GSR}. The value of k_{S1D} was varied from 10 kHz to 50 kHz with an interval of 10 kHz. Other parameters used were k_{ex}= 7.4 MHz ($\sim$ 25 kW/cm^2), k_{em} = 530 MHz ($\tau \sim$ 1.87 ns), k_{DS1} = 6 kHz, k_{GSR} = 1011 Hz, k_{S1B} = 100 Hz and, k_{DB}= 0 Hz. (c) Simulated phase spectra demonstrating that phase shift increases with decreasing of k_{DS1}.The values of the parameters were k_{ex} = 7.4 MHz ($\sim$ 25 kW/cm^2), k_{em} = 530 MHz ($\tau \sim$ 1.87 ns), k_{DS1} = 2-10 kHz, k_{S1D} = 25 kHz, k_{GSR} = 1011 Hz, k_{S1B} = 100 Hz and, k_{DB} = 0 Hz. (d) Best fit obtained for mCherry at 25 kW/cm^2 by systematic study of various relevant parameters gives τ_{S1D} = 36 μs and τ_{DS1} = 0.14 ms.

measurement of RFPs in 50 μm microdroplets prepared by mixing 1-octanol with the buffer containing purified RFPs in a 9:1 ratio according to a previously reported method [130]. As seen in

Figure 2.9, using the microdroplets, RFPs did not show the monotonic decay due to photobleaching (Figure 2.3), but instead it shows a rise in fluorescence intensity associated with diffusion of FPs into the excitation volume. Figure 2.2a shows that by using RFPs expressed in immobilized *E. coli*, this diffusion artifact can be avoided.

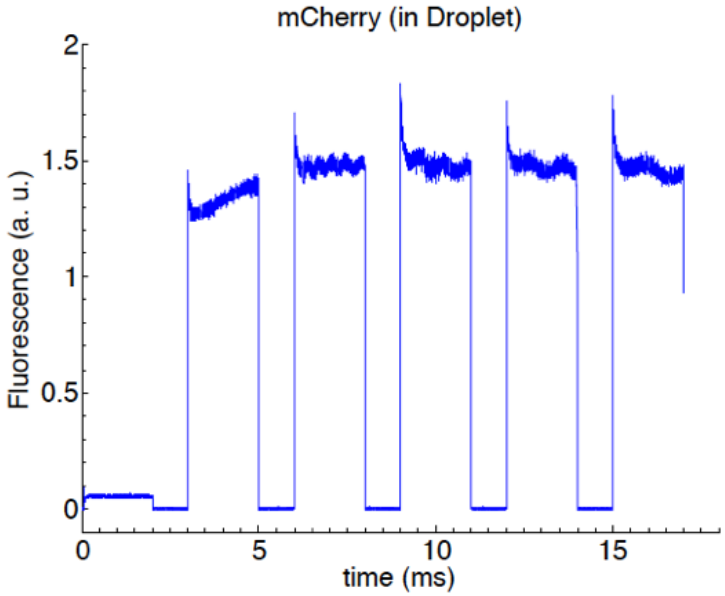

Figure 2.9: Time-domain fluorescence trace of mCherry in microdroplet showing that the decay is not monotonic due to diffusion-related artefacts. The exposure and dark time used in this experiment was 2 ms and 1 ms respectively.

On the other hand, the frequency-domain measurements in bacteria are tricky to perform because of two reasons: 1. In bacteria, due to low protein content, signal intensity was low resulting in noisy phase-shift and 2. Due to less ground state recovery times for the RFPs, it requires longer exposure that assists the FPs to bleach completely before the phase is measured. So, RFPs in solution is perfect for the frequency-domain measurements. To see whether the phase shift is influenced by the diffusion of the proteins in solutions, we compare the phase shift of purified mCherry in solution and mCherry expressed in *E. coli* attached to the cover-slip using poly-L-lysine. It was shown that phase-shift using purified proteins and immobilized bacteria did not differ by much [33] and within error limit. So it proves that the frequency-domain method does

not have the diffusional artifact in it which is also supported by the fact that phase shift is the property of bulk solution.

The experimental and simulation results show that the time- and frequency-domain measurements are complementary. The time-domain experiments give accurate measurements of photobleaching and GSR rate, whereas the frequency-domain experiments are more sensitive to the dark-state conversion rates (k_{S1D}, k_{DS1}). The intensity-dependent, time-domain measurements reveal that the k_{GSR} is nearly constant in the intensity range from 4 kW/cm^2 to 25 kW/cm^2. In these measurements, a correlation between the limiting percent recovery and k_{GSR} is also notable as displayed in Table 2.1. TagRFP-T has the highest GSR rate and the lowest PR_{lim} (∼44%) while Kriek has the slowest GSR rate but highest limiting percent recovery (∼64%) at 25 kW/cm^2 laser intensity. mCherry shows intermediate GSR rates and PR_{lim} (∼56%). This decrease in percent recovery with increase of GSR rate is also supported by our simulation results of time-domain experiments (Figure 2.6d).

The frequency-domain results are consistent with the expected intensity dependence of the phase advance [128, 127] (Figure 2.5d), which increases with intensity. Although the modulation frequencies at the maxima of the phase advances (∼1 kHz) are not widely different for the three RFPs, the shapes of the spectra are different at a particular laser intensity as shown by Figure 2.8a, where the solid black line represents the zero phase shift. It can be clearly observed that, at the same laser intensity, the crossover point from positive to negative phase shift happens in the RFPs in the order from lowest to highest frequency: Kriek, mCherry, and TagRFP-T, demonstrating that the region of phase advance in frequency space is larger for TagRFP-T than for mCherry and Kriek.

Our experiments and simulations of time- and frequency-domain measurements suggest that the rate constants of DSC and GSR are correlated. As it is demonstrated in Table 2.3, at 25 kW/cm^2, TagRFP-T has both fastest GSR and DSC time constants as 0.22 ms and 15 μs, respectively. On the other hand, Kriek has both slowest GSR/DSC rates (2.8 ms and 43 μs, respectively). This correlation between DSC and GSR time constant supports our previous findings [56]. We found

that the relative rate of the GSR/DSC of the three RFPs are as follows: TagRFP-T > mCherry > Kriek. The largest DSC and GSR rate constants of TagRFP-T among the three RFPs studied here suggests that it is more susceptible to blinking or has higher k_{S1D} and k_{DS1} compared to mCherry and Kriek, which is also in agreement with our previous photobleaching and DSC measurements of RFPs [56].

Interestingly, from our measurements of GSR/DSC and previously reported photobleaching tendencies of the FPs, a correlation between the photostability and DSC or GSR rates can be noted. From our time-domain irreversible photobleaching study we observe that, at 25 kW/cm^2, TagRFP-T (τ_{Bl}, 5 ms) has almost 6 times higher photodestruction rate compared to mCherry (τ_{Bl}, 28 ms), whereas Kriek (τ_{Bl}, 49 ms) bleaches ~2 times slower than mCherry. Our previous study of closely related RFPs indeed shows a weak correlation between percent dark-state conversion and irreversible photobleaching [56]. Although this trend needs to be examined more broadly, the available data suggest that GSR/DSC measurements may serve as a proxy for susceptibility to photobleaching. Therefore, selection of FPs based on their DSC/GSR kinetics can be performed to generate photostable FP variants. The correlation between DSC/GSR and photostability indicates that dark state involved in the FP studied here is photo-protective. However, if the dark state is photo-destructive and susceptible to higher order excitation, this trend of DSC/GSR and photostability may not exist. To employ a selection strategy based on DSC/GSR, intensity-dependence of DSC/GSR kinetics should also be considered. A fluorescent protein, selected based on DSC/GSR using high illumination intensity may posses different dark state dynamics at low irradiation.

For the three RFPs examined here, the 10^{-3} to 10^{-4} s GSR time scales and the 10^{-5} s DSC time scales fall within the range of "flickering" time scales observed by FCS and single molecule fluorescence techniques [112, 115, 36, 35]. For example, an FCS study of yellow FPs by Schwille *et al.* revealed conversion to a dark state populated on the ms to μs time scale, with a flickering rate that varies linearly with laser intensity [36]. The current results indicate the values of k_{GSR} and k_{S1D} are nearly constant at intensities from 4 kW/cm^2 to 25 kW/cm^2 , whereas the rate from dark state to excited state (k_{DS1}) increases with intensity. This variation in k_{DS1} explains the intensity

dependence of the flickering observed in FCS. Similar intensity-dependent sub-ms flickering was obtained in FCS measurements of dsRed and mCitrine by Heikal *et al.* [112] and in a FCS study of solution-phase and immobilized eqFP611 and drFP583 by Schenck *et al.* [35]. The similarity of these time scales suggests that although some tuning occurs due to the specific structural context of a particular FP, the flexibility of the chromophore environment is maintained across a wide range of monomeric, dimeric, or tetrameric FPs, regardless of whether they are derived from GFP, DsRed, or other wild-type species.

For photo-switchable FPs, dark-state structural changes, including formation of radicals or triplet states, *cis-trans* isomerization, different protonation states of the chromophore, and changes in the chromophore hydrogen bonding, may serve as modulators of biochemical activity [38, 37, 131, 132]. For example, crystal structures of the photo-switchable FPs Dronpa and Padron reveal that switching is due to *cis-trans* chromophore isomerization [37, 133, 44]. An NMR study on Dronpa switching relates the loss of fluorescence in the trans chromophore isomer to the disruptions of hydrogen bonds and β-barrel flexibility [134]. Isomerization can be coupled to the exterior of the barrel and the solvent, as demonstrated by the viscosity-dependent photo-switching kinetics of Dronpa and the Dronpa-3 variant [135] or it can be coupled to the interaction between β-barrel subunits, as exemplified by tetrameric Dronpa K145N mutant, which shows photo-switching rates slower than that of monomeric Dronpa [43]. Apparently, oligomerization decreases β-barrel flexibility hence slowing the isomerization. A molecular dynamics simulation study of Dronpa mutants supports the notion of a positive correlation between flexibility and increased cis-trans isomerization rates [45]. Isomerization is not the only important structural change in the dark state. In particular, studies of IrisFP suggest that the formation of the dark-state chromophore with a distorted structure is due to the protonation of the chromophore methylene bridge by neighboring side chain of residue Arg66 [136, 137]. In addition, the photo-switchable FP Dreiklang shows a unique blinking mechanism in which dark-state formation is due to hydration-dehydration reactions [124]. Hence, it is clear that the formation of the dark state can be due to the flexibility of the β-barrel interior to accommodate a range of ms and sub-ms time scale structural dynamics.

The measurement techniques presented here could be useful for high-throughput screening and sorting of FP clones with a diverse range of switching mechanisms and rates, which could be pivotal in the generation of improved photo-switching FPs with useful bio-photonic functionality for sensing and actuating biological processes. For this purpose, the frequency-domain technique is most suited because it only involves measurement of phase advance from a lock-in amplifier output using sinusoidally modulated excitation. One drawback of this technique is that it might need high laser intensity to observe an appreciable amount of positive phase shift which might be detrimental to viability in cell-based library screening. Time-domain GSR measurement can be helpful for off-chip GSR time analysis of various FPs.

2.7 Conclusion

In this chapter, we report two methods of measuring the ground state recovery and dark-state conversion rates of fluorescent proteins and compare the results we obtained. We found that the switching rates of the three RFPs (mCherry, TagRFP-T, and Kriek) fall in the range of ms to μs time-scale, which is consistent with previous observations on similar FPs. It has been observed that the time- and frequency-domain methods described here are complementary to each other. While accurate GSR times can be obtained using the time-domain technique, phase-shift-based frequency-domain method is most-suited for measurements of the rates of DSC processes. We also found a correlation between GSR and DSC time constants of the RFPs studied here. Our results show that the GSR rate and rate from excited state to the dark state (k_{S1D}) are almost constant for 4 kW/cm^2 to 25 kW/cm^2, although rate from dark state to excited state (k_{DS1}) shows slight intensity dependence in this intensity range. This type of measurement can shed light into the various photophysical processes in FPs and rates associated with them. Based on the speed of the measurement and the direct experimental readout of the phase advance, the frequency-domain method is more suitable for the implementation of high-throughput screening and sorting on the basis of ground-state recovery times and dark-state conversion rates.

Chapter 3

Single Molecule Fluorescence & Dark State Dynamics in Red Fluorescent Proteins

3.1 Publication Note

A portion of this Chapter has been adopted from Mo *et al.*, Genetically encoded biosensors for visualizing live-cell biochemical activity at super-resolution, *Nature Methods*, 14(4):427-434, **2017** [65] and the corresponding Supplementary Information of the article.

3.2 Introduction

Using single molecule measurements, a variety of photo-physical dynamics have been investigated in the previous decades. Protein folding-unfolding, spectral diffusion, triplet state blinking, multichromophoric assemblies *etc.* are few notable examples of that [138, 139, 140, 141]. Various dynamical features in a system are obscured in the ensemble-level measurements through statistical averaging of its molecular properties. On the other hand, single molecule-based techniques generate the distribution of certain photo-physical parameters, such as fluorescence off and on-times, thus revealing the heterogeneity of the system. This provides unprecedented insights into the dynamics of the system under investigation which are otherwise not possible with bulk-scale measurements. Single molecule techniques can shed light on very rare processes in the molecules which might be overshadowed by more frequent or abundant processes [138]. Two main requirements of this tech-

nique are: 1) use of very dilute sample so that single molecules are under investigation and 2) a high signal to noise ratio.

The first single molecule study of fluorescent proteins was carried out by Dickson *et al.* [32]. The authors observed "blinking" in GFP mutants and revealed the intensity dependence of the fluorescence fluctuation. This study found that GFP-mutants could be trapped in very long-lived dark states with 488-nm illumination and could be recovered back to the bright states with 405-nm excitation. After this initial finding, several other groups contributed to unraveling the hidden dynamics of FPs at single molecule level [142, 143, 144, 145, 146, 147]. Single molecule studies by Garcia-Parajo *et al.* and others revealed the intra-molecular energy transfer process in DsRed between different monomer subunits [144, 114]. The sequential bleaching mechanism of DsRed was observed by Lounis *et al.* using single molecule spectroscopy [114]. Intensity and pH-dependent single molecule experiments on GFP mutants by Peterman *et al.* revealed that the "blinking" is correlated with the time-scale of cis-trans isomerization of the chromophore in those FPs and was not associated with protonation-deprotonation of the chromophore [143]. Recently, the fluorescence fluctuation and photo-activation properties of FPs have been harnessed to generate a large pool of super-resolution microscopy techniques [15, 17, 122]. The photostability of the related FPs needs to be enhanced in order to improve the performance of these diffraction-unlimited microscopies. A detailed understanding of the single-molecule dynamics of the FPs in the context of its immediate chromophore environment, pH, illumination intensity is still missing. A mechanistic understanding of the fluorescence dynamics in FP is required for the suppression of fluctuation to create bio-markers for regular fluorescence-based approaches or to induce efficient "blinking" imparting high image contrast and the generation of super-resolution probes with reduced photobleaching and photo-fatigue [42, 148]. A holistic view of single molecule properties and their ensemble-level manifestation is of utter importance for achieving this goal.

In this Chapter, we explore the connection between single-molecule fluctuation of red fluorescent proteins and their dark state conversion (DSC)/ ground state recovery (GSR) processes measured at the bulk scale. In particular, we studied the **F**luorescence f**L**uctuation **I**ncrease by

Nanometer **C**ontact (FLINC) phenomenon discovered by our collaborators [65] . We have measured GSR/DSC and excited state lifetime of these FLINC constructs as a function of irradiance. Finally, Monte-Carlo based simulation were performed to explain the dark state dynamics of those constructs with a 3-state model system consisting of ground, excited and dark state.

3.3 Fluorescence fLuctuation Increase by Nanometer Contact (FLINC)

Dronpa [39], a photo-switchable GFP, is routinely used in various super-resolution based techniques including PALM, STORM, RESOLFT *etc.* It can be switched between on and off states with 405-nm and 488-nm laser illuminations, respectively [37]. On the other hand, TagRFP-T [99, 11], is an RFP derived from eqFP578 used as a bio-marker in fluorescence microscopy. TagRFP-T has been reported to show "blinking" or fluorescence fluctuation that was used to implement Super-resolution Optical Fluctuation Imaging (SOFI) [149]. Recently, the study by Mo *et al.* reported that the "blinking" behavior of TagRFP-T varies in a distance-dependent manner when fused to Dronpa with a short flexible linker (comprising of 8 amino acid) and expressed at the plasma-membrane [65]. This proximity-based effect resembles to Fluorescence Resonance Energy Transfer (FRET) in which a blue-shifted donor transfers its energy to a red-shifted acceptor in a non-radiative manner. Here, in the vicinity of another FP (Dronpa), the the amplitude of fluorescence fluctuations of TagRFP-T are increased several fold. This phenomenon had been termed **F**luorescence f**L**uctuation **I**ncrease by **N**anometer **C**ontact (FLINC) which has been coupled with SOFI to study enzymatic activities in live-cells at a $\sim$ 3 fold higher spatial resolution than the diffraction-limit.

Figure 3.1a shows the representative fluorescence images of TagRFP-T (TT), co-targeted Dronpa/TagRFP-T (Dp+TT), Dronpa-linker-TagRFP-T (DpTT) and EGFP-linker-TagRFP-T expressed in plasma-membrane of HeLa cells *via* a myristoylatedpalmitoylated sequence (lyn). Upon 561-nm illumination, the DpTT construct showed $\sim$10 fold decrease in mean fluorescence intensity and $\sim$ 5 fold increase in the amplitude of fluctuation (see Figure 3.1c & d) compared to wild-type

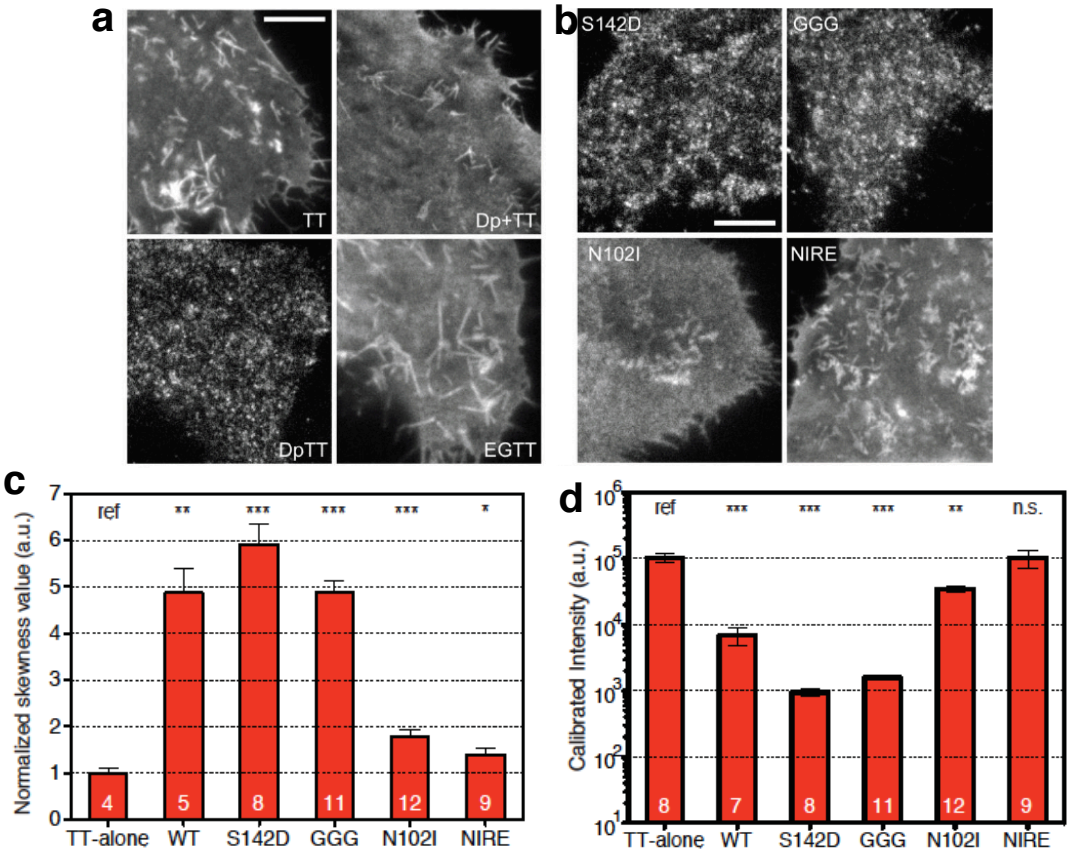

Figure 3.1: (a) Representative fluorescence images of TagRFP-T (TT), co-targeted Dronpa and TagRFP-T (Dp+TT), Dronpa-linker-TagRFP-T (DpTT), EGFP-linker-TagRFP-T (EGTT) expressed in plasma-membrane of HeLa cells. The images have been acquired by 561-nm illumination and 35 ms exposure time. Scale bar: 10 μm. (b) Representative images of Dronpa S142D-linker-TagRFP-T (S142D), Dronpa C62G Y63G -linker-TagRFP-T (GGG), Dronpa N102I-linker-TagRFP-T(N102I) and Dronpa N102I R149E-linker-TagRFP-T (NIRE) expressed in plasma-membrane of HeLa cells. 561-nm illumination and 35 ms exposure had been used to acquire the images. Scale bar: 10 μm. (c) Normalized skewness values of TagRFP-T (TT), WT (DpTT), S142D and other constructs as quantified from the time-series Total Internal Reflection Fluorescence (TIRF) images (Eqn 3.1). In S142D & GGG constructs Dronpa was non-fluorescent and fluctuation was still observed as observed from their relatively high normalized skewness. In N102I and NIRE constructs mutations were introduced in outer-side of the barrel and this suppressed the fluctuations observed in DpTT construct. (d) Mean fluorescence intensities of the constructs. DpTT (WT) had $\sim$ 10 fold reduction in the mean fluorescence intensity compared to TagRFP-T. Pair-wise t-test results are marked where data were compared with the construct marked "ref"; n numbers are marked in the corresponding bars. n.s.: not-significant; *: $p<0.05$; **:$p<0.01$; ***: $p<0.001$ where applicable.

TagRFP-T.

It was assumed that fluorescence fluctuations arise from the reversible transition of the TagRFP-T chromophore between an emissive (bright) and non-emissive (dark) state and denoted the lifetime of these two states as τ_{on} and τ_{off}, respectively [150]. In observing N identical but fluctuating fluorophores, the probability that emission from n fluorophores will be detected at any given time is given by a binomial distribution with probability of success $p_{on} = \frac{\tau_{on}}{\tau_{on}+\tau_{off}}$ (bright-state probability) and number of trials n. In principle, the distribution of the fluorescence recorded in each detector pixel over time could be used to estimate the degree of fluorescence fluctuations. We considered two statistical parameters as being appropriate: skewness (defined below) and normalized variance σ^2_{norm}. From a series of Monte Carlo simulation, it was found that skewness approximated the fluctuations of the fluorophore well and displayed a close correspondence with p_{on}. A decrease in p_{on} (*i.e.*, more fluctuations) unambiguously corresponds to an increased skewness. In contrast, normalized variance is strongly dependent on imaging conditions and is non-monotonic, making it unsuitable. Skewness is also only marginally sensitive to changes in fluorophore brightness and essentially independent of fluorophore diffusion. We therefore considered skewness to be a good metric for estimating the degree of fluorescence fluctuations. The normalized skewness (g) of a sample is defined as:

$$g = \frac{\frac{1}{j}\sum_{i=1}^{j}(x_i - \bar{x})^3}{(\frac{1}{j}\sum_{i=1}^{j}(x_i - \bar{x})^2)^{3/2}} \tag{3.1}$$

where, $\bar{x}$ is the sample mean and j is the number of the sample. This calculation was performed on the time series from each pixel within a cell. To account for possible photobleaching of the fluorescent probe, the average skewness of each time series (840 to 1700 in size) in intervals of 50, 100, and 170 images was measured. The mean skewness over different interval sizes is displayed in Figure 3.1c.

Figure 3.2a shows the distance-dependence of the FLINC phenomenon. A series of Dronpa-linker-TagRFP-T were generated by inserting rigid helical linkers (H1, H2 *etc.*) of known lengths [151]. It is obvious from the Figure 3.2a that normalized skewnesses of the constructs approach the

value of the skewness of that of Dp+TT after H5. This indicated that FLINC is functional in the 5-6 nm range. In the Dp+TT construct, where Dronpa and TagRFP-T were expressed together in plasma-membrane, the fluctuation presumably reduced due to larger distance between them compared to the DpTT construct.

It was shown that the FLINC phenomenon was induced by the β-barrel of Dronpa and not by its chromophore. The S142D & "GGG" (C62G/Y63G) variants of Dronpa which show no fluorescence due to absence of a functional chromophore were used to create DpTT-like constructs. This constructs showed identical fluorescence fluctuation as the DpTT constructs. Further random-mutagenesis on Dronpa revealed mutations involved in the interaction between Dronpa and TagRFP-T. It was reported that a combination of N102I & R149E mutations that point outside of the β-barrel were enough to restore the brightness of TagRFP-T and showed reduced fluctuation (see Figure 3.1). This proves that the FLINC is induced by a charge-charge interaction between the barrels of TagRFP-T and Dronpa. In fact the electrostatic interactions between the those FPs had been corroborated by the basic pocket and acidic patch in the surface of Dronpa and TagRFP-T respectively (Figure 3.2d). Size-exclusion chromatography shows the presence of a small hetero-dimer peak of Dronpa and TagRFP-T [65].

The *in-vitro* spectral analysis of DpTT constructs showed the presence of immature TagRFP-T. This indicates that the charge-charge interactions between the barrel of TagRFP-T and Dronpa might divert the maturation process of the TagRFP-T to produce immature proteins. Presumably the over-expression of TagRFP-T in the plasma-membrane obscure the "blinking". Due to the generation of a fraction of immature proteins, the effective label-concentration might be reduced for the DpTT construct, thereby enhancing the fluorescence fluctuation. The generation of immature proteins also explained the $\sim$ 10 fold decrease in brightness in DpTT constructs compared to TT.

Figure 3.2c displays the results of the single molecule experiments with purified TagRFP-T & DpTT *in vitro* at 561-nm with 24 W/cm^2 irradiance. Values of τ_{on} and τ_{off} measured from the single molecule traces showed that DpTT had 21 % faster τ_{on} compared to wild-type TagRFP-T (111.3 ms vs 141.3 ms respectively). The values of τ_{off} were similar for both of the proteins ($\sim$ 80

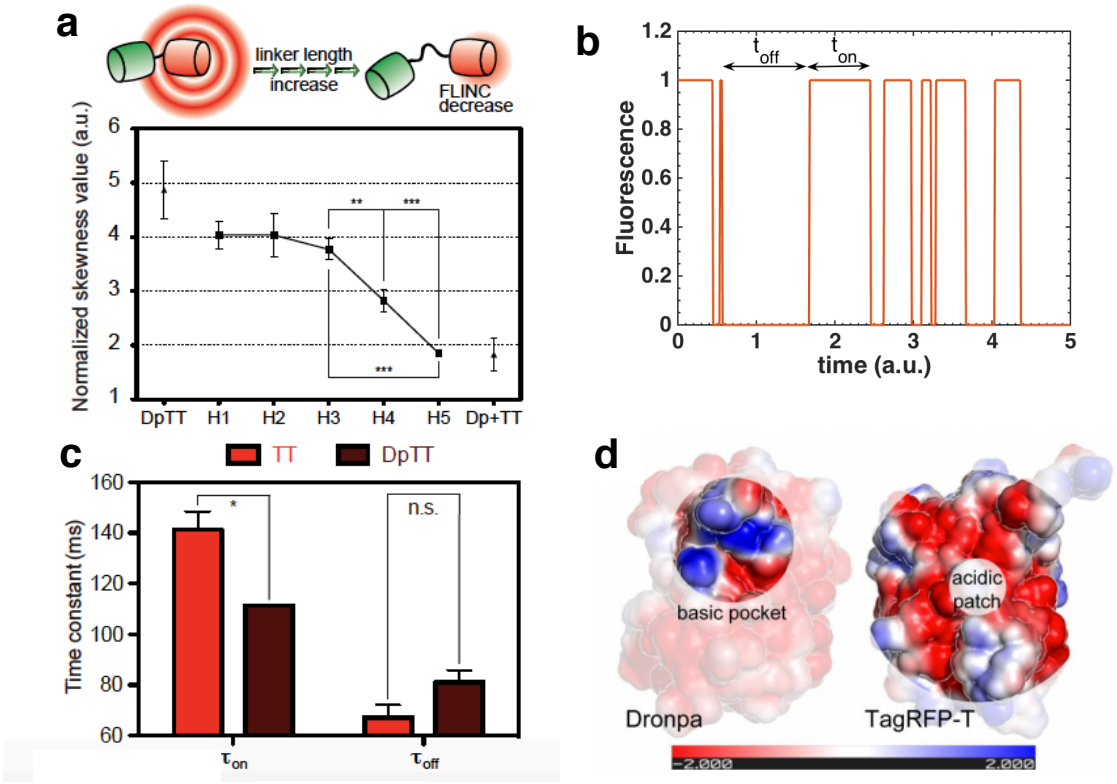

Figure 3.2: (a) The distance dependence of FLINC shown by introducing rigid helical linker with known distance between Dronpa and TagRFP-T. Fluorescence fluctuations (quantified by normalized skewness) of constructs practically reduced to wild-type TagRFP-T after H5. (b) Schematic of the fluorescence trace obtained in a single molecule measurement. The dwell time of the molecules in the ON/fluorescent states (t_{on}) and OFF/non-fluorescent states (t_{off}) are collected from the fluorescence trace. From the distribution of t_{on} and t_{off}, the value of the ON and OFF time-constants, *i.e.*, τ_{on} and τ_{off} are obtained. (c) Single molecule fluorescence traces of TagRFP-T and Dronpa-linker-TagRFP-T (DpTT) revealed that the later had faster τ_{on} (141.3 ms in TagRFP-T; 111.3 ms in DpTT) while τ_{off} was similar for both of the constructs ($\sim$ 80 ms). (d) Electrostatic surfaces of Dronpa and TagRFP-T calculated by the Adaptive Poisson-Boltzmann Solver (APBS) plug-in in PyMOL. The basic pocket in Dronpa and the acidic patch around the chromophore in TagRFP-T, both features believed to be important for FLINC, have been highlighted. Pair-wise t-test results are marked where data were compared with the construct marked "ref"; n.s.: not-significant; *: p<0.05; **:p<0.01; ***: p<0.001 where applicable.

ms). Now, it is known that τ_{on} and τ_{off} due to single molecule blinking are related to the trapping of the molecule in a long-lived dark states [139]. In particular, τ_{on} is related to the conversion rate from bright state to the dark state (*i.e.* dark state conversion, DSC) and τ_{off} is related to the

transfer rate of dark state population in the bright state (*i.e.* ground state recovery) (see Figure 3.10a). In a 3 state model consisting of two bright states (S_0 & S_1) and a dark state (D), τ_{on} and τ_{off} are related in the following way [139]:

$$\frac{1}{\tau_{on}} = k_{ex}\frac{k_{dsc}}{k_r + k_{ic} + k_{gsr}} \tag{3.2}$$

$$\frac{1}{\tau_{off}} = k_{gsr} \tag{3.3}$$

where, k_{ex}, k_r, k_{ic}, k_{dsc} and k_{gsr} are rate-constants involving excitation, radiation (emission), internal conversion, DSC and GSR respectively (Figure 3.10a). The derivation of the above equations assumes that k_{ex} is very small compare to the combined rate of radiative, DSC and internal conversion processes, i.e., $k_{ex} << (k_r + k_{ic} + k_{dsc})$. This assumption will be explained later in detail (Section 3.5.2).

We carried out experiments to quantify the kinetics of DSC and GSR processes of TagRFP-T and DpTT. We also measured the excited state lifetime of those constructs.

3.4 Photo-physical Measurements of TagRFP-T & DpTT Constructs

3.4.1 Cell culture and transfection

For DSC and GSR measurements HeLa cells expressing nuclear-localized TagRFP-T and DpTT were used. HeLa cells were cultured in DMEM medium with FBS (Fetal Bovine Serum), Penicillin/Streptomycin to ∼100% confluency in 100 mm dish. Next they were split cells into 60 mm imaging dishes 24 hrs prior to transfection. Typically 40-70% of confluency was targeted at time of transfection, which generally translates to a seeding density of 1.5-2 $\times 10^5$ cells per dish. Cells were transfected using Lipofectamine 3000 reagent, following a standard protocol using Opti-MEM media for diluting reagents and DNA. 1.5 μg of plasmid DNA was used per transfection. DNA/Lipofectamine mixture was incubated for 20 min at room-temperature. The mixture was

added drop-wise to cells in the imaging dish and the dish was rocked to mix. Cells were incubated at 37°C & with 5% CO_2 for 48 hours prior to measuring DSC/GSR kinetics. Purified proteins were used for excited state lifetime measurements. For intensity dependence of GSR time-constants, TagRFP-T expressed in yeast was used.

3.4.2 Instrumentation & Analysis

HeLa cell expressing TagRFP-T/DpTT were irradiated with a 561-nm solid-state diode-pumped laser (Genesis MX, Coherent) through a custom-built inverted microscope at an irradiance of $\sim$ 8-10 kW/cm^2. A 629/56-nm band-pass filter (Semrock) was used to remove excitation from emission. Epifluorescence from the cells was collected using a PMT (Hamamatsu Photonics) and subsequently the PMT photo-current was converted to voltage using a custom-built trans-impedance operational amplifier for a better signal to noise ratio. Fluorescence signal was digitized using a data acquisition card (DAQ, National Instruments) at a rate of 1 MHz. Pulsed illumination was achieved using an acousto-optic modulator (AOM, Gooch & Housego, 35210-BR). For DSC measurement, cells expressing FPs were irradiated continuously for 0.1 s and fluorescence traces were collected for further analysis.

The raw fluorescence data collected for DSC measurements were background-corrected and spline-fitted for smoothing. The fluorescence traces had three distinct features: a rapid decay up to 100 μs time-scale, a flat region in 100-1000 μs region and finally a slow decay on a ms time-scale. Hence, the fluorescence traces were fitted with a 3-exponential function using equi-distant time-points in log scale. The fastest time-constant and its corresponding weight from the fitting results were taken as the DSC time-constant and percent DSC respectively [56].

To measure the GSR time-constants, FPs were excited with pulse-trains having 2 ms exposure time and varying inter-pulse delays (dark time) ranging from 5 μs to 10 ms. Typical fluorescence traces for this measurement are displayed in Figure 3.3. Fluorescence traces collected using the pulsed excitations were used to compute percent recoveries without further processing using the

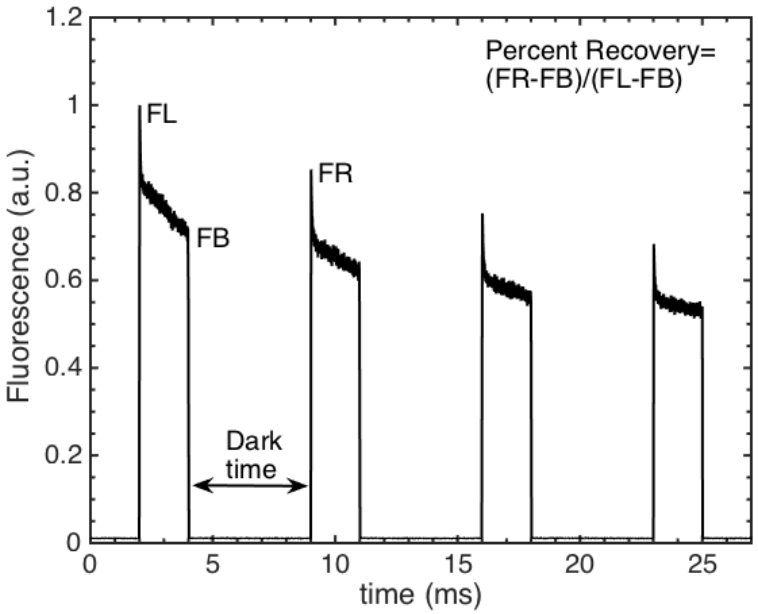

Figure 3.3: Typical pulsed fluorescence trace in Ground State Recovery rate measurements. This figure shows fluorescence trace of TagRFP-T with 5 ms dark time and 2 ms exposure time at ~ 10 kW/cm^2.

following equation:

$$PR = \frac{FR - FB}{FL - FB} \times 100 \tag{3.4}$$

where, PR is the percent recovery; FL, FB, FR are initial fluorescence intensity, fluorescence intensity after 2 ms exposure and fluorescence recovered between pulses, respectively (Figure 3.3). Home-built software (Matlab) was used to compute percent recoveries of the fluorescence and finally percent recovery *vs.* dark time plots were fitted with single exponential to extract GSR time-constants [33].

Excited state lifetimes of mCherry, TagRFP-T, DpTT were measured with a commercial TCSPC system (Fluro Time 100, PicoQuant) using 560-nm laser excitation with a repetition rate of 2.5 MHz. Lifetime measurements were performed with purified proteins and PBS buffer (pH=7.4) was used for necessary dilutions. The fluorescence transients of the FPs were fitted with iterative reconvolution with a bi-exponential function and using the measured instrument function (IRF) of the system.

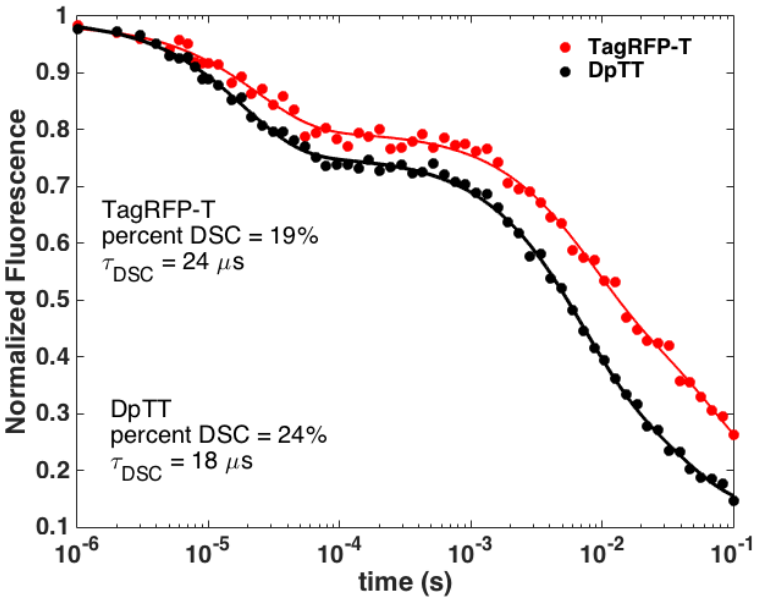

Figure 3.4: Fluorescence traces of TagRFP-T (red dot) and DpTT (black square) with their corresponding fits (red and black lines respectively) measured at $\sim$ 8 kW/cm^2 illumination intensity. DpTT shows higher dark state population and faster DSC time-scale than TagRFP-T.

3.4.3 Results

Fluorescence decays of TagRFP-T and DpTT with their fits are depicted in Figure 3.4. These decays are the average of traces from 5 individual HeLa cells.

Table 3.1 gives DSC time-constants and percent DSC of TagRFP-T and DpTT in a "mean $\pm$ standard deviation" format. The results show that DpTT has 25% faster DSC time-constant than TagRFP-T whereas percent DSC (or dark state population) of DpTT is 26% higher than TagRFP-T.

Figure 3.5 depicts percent recovery *vs.* dark time plot for the constructs. Single exponential fitting of percent recovery gives GSR time-constants of TagRFP-T and DpTT as 50 μs and 51 μs respectively. We therefore conclude that TagRFP-T and DpTT have similar GSR kinetics.

The intensity-dependence of the GSR time-constants is demonstrated in Fig 3.6. The measurements were done with TagRFP-T expressed in yeast cells. The GSR time-constants extracted from the corresponding dark time and percent recovery are revealed as 150 μs and 96 μs at 2 kW/cm^2 and 5 kW/cm^2 illumination irradiances respectively. The results clearly show that ground

Table 3.1: Time-constants of different photo-physical processes for TT and DpTT.

Constructs	Percent DSC (%)	$\tau_{DSC}(\mu s)$	$\tau_{GSR}(\mu s)$	Lifetime (ns)
TagRFP-T	19 ($\pm$ 4.0)	24 ($\pm$ 5.8)	50	2.45
DpTT	24 ($\pm$ 1.8)	18 ($\pm$ 1.4)	51	2.40

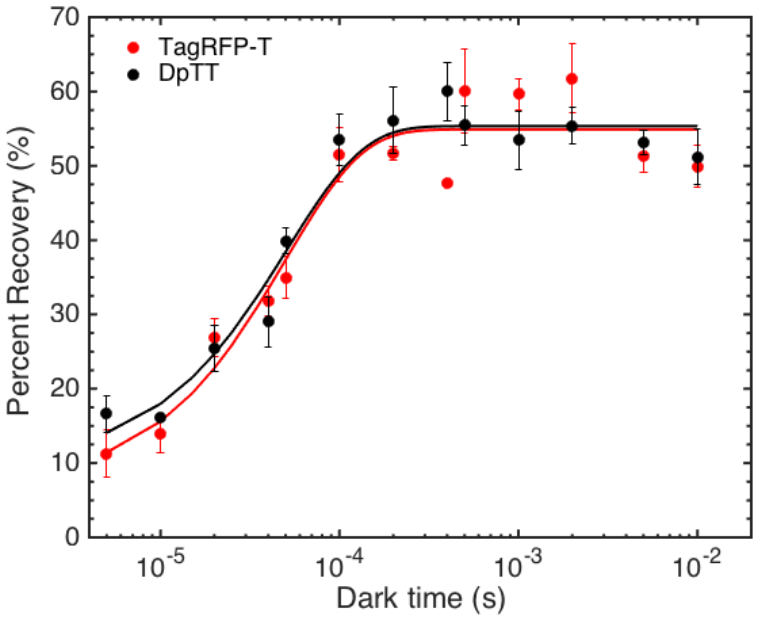

Figure 3.5: Percent recovery vs. dark time plot for TagRFP-T and DpTT constructs measured at 10 kW/cm^2. Single exponential fitting of the percent recoveries give GSR time-constants of TagRFP-T and DpTT as 50 μs and 51 μs respectively.

state recovery process is an intensity-dependent phenomenon. At higher illumination intensity, the recovery process is faster. The intensity dependence might originate from higher order absorption of the dark states and subsequent relaxation. Alternatively, a light-driven transition can happen from dark state to bright state in a non-radiative fashion, thus accelerating the recovery processes. These different mechanisms are discussed in the Simulation section (Section 3.5) of this Chapter.

The intensity-weighted average excited state lifetime of mCherry, TagRFP-T and DpTT were measured as 1.70 ns, 2.45 ns and 2.40 ns respectively. This shows that TagRFP-T and DpTT have almost same excited-state lifetimes and they have similar fluorescence dynamics in ns time-scale. Figure 3.7 displays the fluorescence decays of the FPs and instrument response function (IRF).

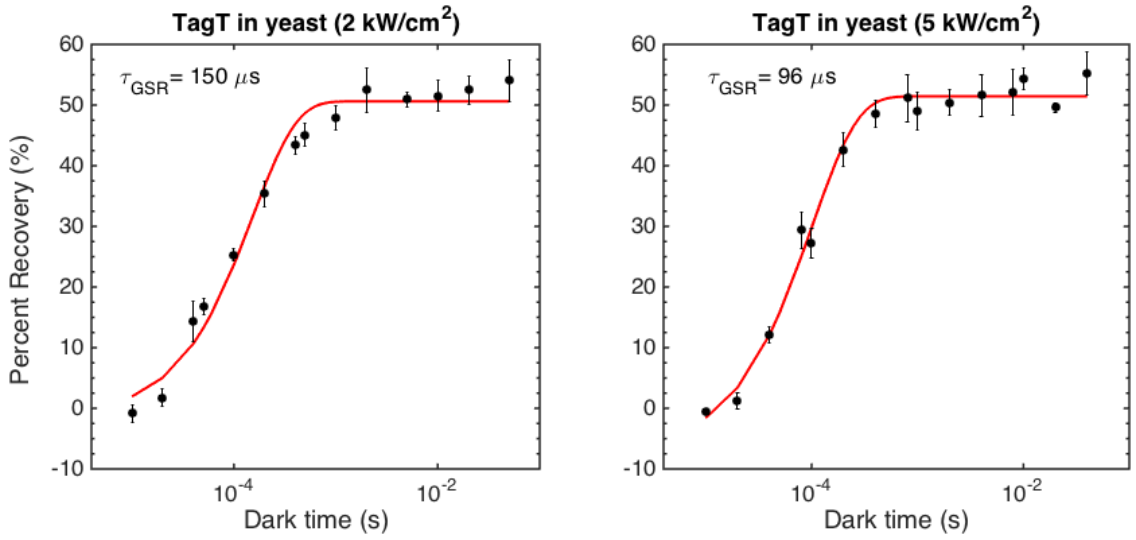

Figure 3.6: The intensity-dependence of GSR time-constants for TagRFP-T expressed in yeast. It is obvious that with higher illumination intensity, τ_{GSR} decreases, indicating that the recovery process is associated with excitation of dark state population or transition from dark state to bright state *via* non-radiative process.

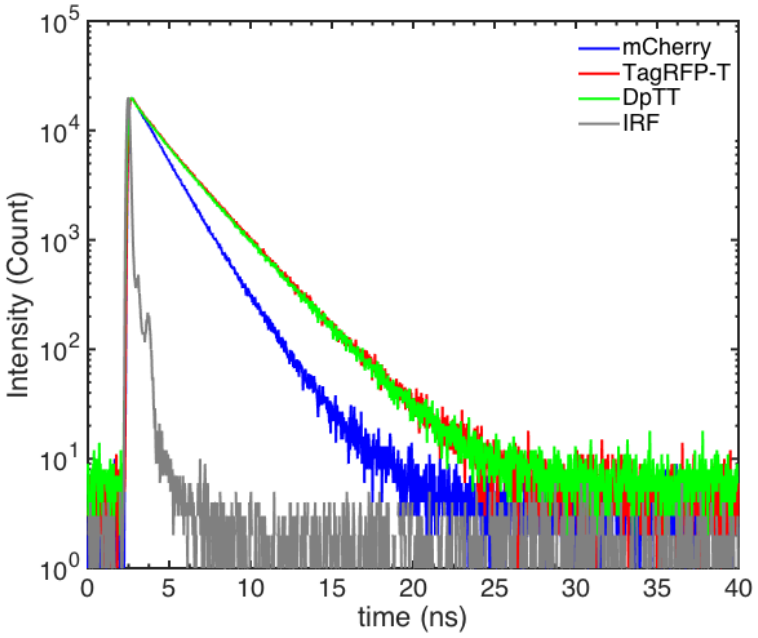

Figure 3.7: Fluorescence decays of the FPs and instrument response function (IRF). Iterative reconvolution fits give average excited state lifetime of of mCherry, TagRFP-T and DpTT as 1.70 ns, 2.45 ns and 2.40 ns respectively. The measurement were performed on purified proteins.

3.5 Simulation of Single Molecule Fluorescence

To investigate the single molecule "blinking" and dark state dynamics more closely, we performed Monte Carlo based simulation using different model systems. First, we used a simple 2 state model system consisting of bright and dark state to understand the underlying influence of different rate-constants into the ON and OFF dwell-times of the system. Next we moved to a 3 state model that consist of ground state (S_0), excited state (S_1) and a dark state (D_0). This is a more realistic model system to describe the FP dynamics. With this model, the intensity-dependence of τ_{on} can be nicely explained as reported by various authors [32, 143, 142]. However, this model fails to justify the intensity-dependence of GSR and hence associated τ_{off} constants. So, we proposed a modified 3 state model system that accounts for the light-driven recovery of dark state population into the ground state.

3.5.1 2 State Model

In this 2 state model, the molecule can be either in fluorescent/bright state (ON, A) or non-fluorescent/dark state (OFF, B). The rates of their inter-conversions are given by k_1 and k_2. k_1 is the forward reaction rate from A (ON) to B (OFF), whereas k_2 is the backward reaction rate from B (OFF) to A (ON).

$$\mathrm{A} \underset{\mathrm{k_2}}{\overset{\mathrm{k_1}}{\rightleftharpoons}} \mathrm{B}$$

Now for a time-window of Δt, the probability of the molecule of leaving the state A is given by:

$$p(A) = 1 - e^{-k_1 \Delta t} \tag{3.5}$$

similarly, the probability of leaving the state B is given by:

$$p(B) = 1 - e^{-k_2 \Delta t} \tag{3.6}$$

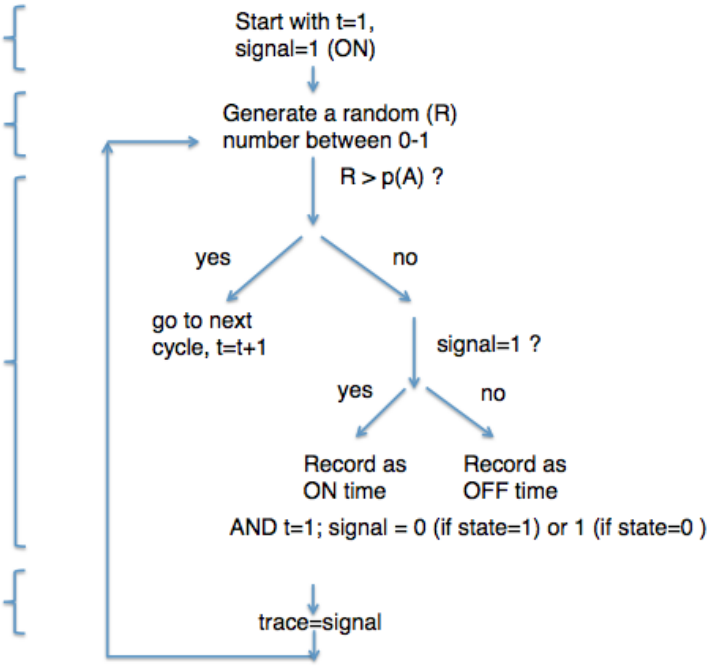

Figure 3.8: Algorithm to generate single molecule fluorescence trace from a 2 state model system consisting of ON and OFF states.

For a sufficiently small Δt, $p(A)$ and $p(B)$ can be approximated as $k_1\Delta t$ and $k_2\Delta t$ respectively. From the above-mentioned probabilities, one can compute the average dwell time of the system in ON and OFF states and subsequently fluorescence traces can be calculated. The algorithm is depicted in Figure 3.8.

Figure 3.2b shows the representative single molecule fluorescence traces obtained by using this algorithm. The dwell times for ON and OFF states are collected from these traces to generate a series of t_{on} and t_{off}. The histograms for t_{on} and t_{off} are shown in Figure 3.9. Finally the distribution of t_{on} and t_{off} are fitted with a single exponential function to extract τ_{on} and τ_{off} respectively.

In this simulation, time-step (Δt), k_1 and k_2 of 0.01 s, 5 s^{-1} 3 s^{-1} respectively were used. The simulation was run to generate the fluorescence signal for 200 s. As Figure 3.9 displays, τ_{on} and τ_{off} calculated from these histograms were 0.19 s and 0.30 s respectively which is almost equal to the reciprocal of the forward and backward reaction rates (5 s^{-1} and 3 s^{-1}).

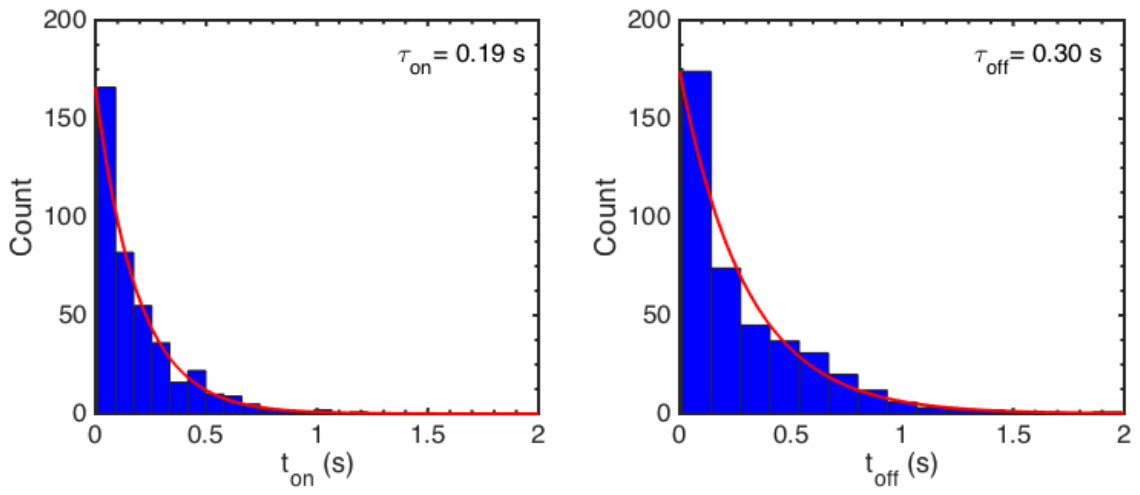

Figure 3.9: Distribution of t_{on} and t_{off} and single exponential fitting (red lines) to extract τ_{on} and τ_{off}.

Additional simulations were performed varying the backward and forward reaction rates and subsequently computing the τ_{on} and τ_{off} from the single molecule fluorescence traces. It was found that τ_{on} and τ_{off} were always the reciprocal of k_1 and k_2. So, it can be concluded that for a simple two state model, τ_{on} and τ_{off} are related with k_1 and k_2 in the following ways:

$$\tau_{on} = \frac{1}{k_1} \tag{3.7}$$

$$\tau_{off} = \frac{1}{k_2} \tag{3.8}$$

This result makes sense as k_1 is the rate-constant for bright state to dark state and hence dictates dwell time in ON states or τ_{on}. On the other hand, k_2 is the rate constant for dark to bright state conversion and consequently it is related to τ_{off}. This initial idea gained in 2 state model system was propagated into a 3 state model system to obtain τ_{on} and τ_{off} consisting of multiple bright and dark states. For such a complex system, the "blinking" dynamics can be computed if various model parameters (k_{gsr}, k_{dsc}, k_r, k_{ex} etc.) are known.

3.5.2 3 State Model

Now we use a 3 state model system (Figure 3.10a) to explain the single molecule kinetics of TagRFP-T and DpTT constructs. In this model, the molecule once excited into S_1 can emit fluorescence by radiative transition into ground state (S_0) or become trapped in a long-lived dark state (D). The molecule can return to the ground state from dark state through non-radiative decay. The necessary parameters for this model *e.g.* k_{dsc} ($1/\tau_{DSC}$), k_{gsr} ($1/\tau_{GSR}$) and excited state lifetime of those constructs were measured and displayed in Table 3.1.

Assuming the excitation rate-constant is very small compared to ($k_r + k_{ic} + k_{dsc}$), the population in S_1 ($[S_1]$) is very small and constant at a given time. Therefore, a steady-state approximation can be applied on $[S_1]$:

$$\frac{d[S_1]}{dt} = k_{ex}[S_0] - (k_r + k_{ic} + k_{dsc})[S_1] = 0 \tag{3.9}$$

The above equation can be re-arranged to give,

$$[S_1] = \frac{k_{ex}}{k_r + k_{ic} + k_{dsc}}[S_0] \tag{3.10}$$

Now in analogy to the 2 state model, for a 3 state model τ_{on} and τ_{off} can be given by:

$$k_{on} = \frac{1}{\tau_{on}} = \frac{k_{ex}}{k_r + k_{ic} + k_{dsc}} k_{dsc} \tag{3.11}$$

&

$$k_{off} = \frac{1}{\tau_{off}} = k_{gsr} \tag{3.12}$$

Again,

$$\frac{1}{k_r + k_{ic} + k_{dsc}} = \tau \tag{3.13}$$

where, τ is excited state lifetime. Substituting Eqn. 3.13 into Eqn. 3.11 we find that,

$$\frac{1}{\tau_{on}} = k_{ex} k_{dsc} \tau \tag{3.14}$$

k_{ex} in the above equation can be obtained by the following way,

$$k_{ex} = \frac{I\sigma\lambda}{hc} \tag{3.15}$$

where, I, σ, λ are illumination irradiance ($\sim$ 24 W/cm^2), absorption cross-section of the FP and wavelength of the excitation (561 nm). σ can be calculated from the extinction coefficient of the FPs:

$$\sigma_\lambda = 2.303 \times \frac{\epsilon_\lambda}{N_A} \times 10^3 \tag{3.16}$$

where, ϵ_λ is the molar extinction coefficient at λ (71 M^{-1} cm^{-1}), N_A is the Avogadro's constant. Using the τ_{DSC}, τ_{GSR} and excited state lifetime of TagRFP-T and DpTT (from Table 3.1) into Eqn 3.14 and Eqn 3.12, we can calculate values of τ_{on} and τ_{off}. The values of τ_{on} calculated from this model for TagRFP-T and DpTT are 532 ms and 408 ms respectively. The value of τ_{off} for both of the constructs was $\sim$ 50 μs. So this model predicts that DpTT has $\sim$ 23% faster τ_{on} than TagRFP-T which agrees well with the single molecule experiment where we observed that DpTT showed 21% faster τ_{on} relative to TagRFP-T (141.3 ms, TagRFP-T; 111.3 ms, DpTT). However, it is notable that although these analytical expressions predict the relative τ_{on} for the constructs qualititatively, the absolute values are far off. Also, τ_{off} calculated from these analytical expressions was $\sim$1000 fold faster than the experimentally observed τ_{off}. Hence, in order to justify these discrepancies, we performed Monte Carlo based numerical simulations using a modified 3 state model system (Figure 3.10b).

3.5.3 Modified 3 State Model

In this modified 3 state model (Figure 3.10b), following the light-induced transition from the ground state (S_0) to the excited state (S_1), molecules can enter into the dark state (D). The rate of this transition from bright state (S_1) to the non-fluorescent or dark state (D) is governed by the DSC rate constant, k_{dsc}. From D, the molecule can relax to the ground state *via* ground

state recovery. This model assumes that recovery can be thermally-driven or induced by light with corresponding rate constants k_{gsr} and $\Phi_g * k_{ex}$. Here, k_{ex} is the excitation rate which depends on laser intensity (Eqn 3.15) and Φ_g is an adjustable constant.

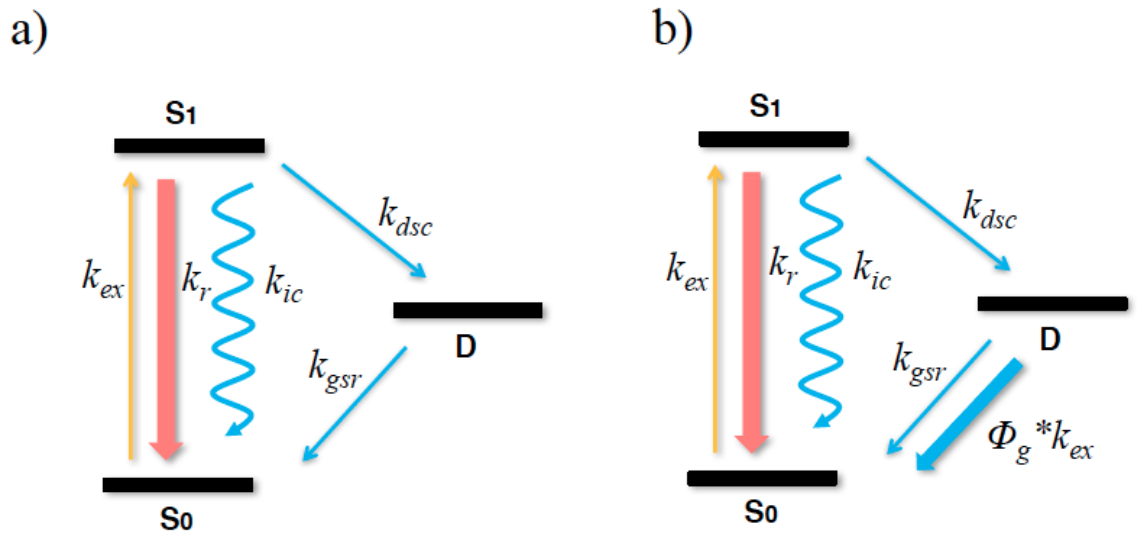

Figure 3.10: (a) 3 State model consisting of ground state (S_0), excited state (S_1) and dark state (D). Upon laser illumination, the molecules can be excited to S_1. From S_1, the molecules can decay in a radiative manner or can get trapped into a dark state (D, *via* dark state conversion) with subsequent radiationless transition into ground state (S_0, *via* ground state recovery). This model can explain the intensity-dependence of τ_{on} observed in single molecule experiments but fails to account for intensity-dependence of τ_{off}. (b) In this modified 3 state model, the ground state recovery process is considered to be both thermally and light-driven process with the corresponding rate constants of k_{gsr} and $\Phi_g * k_{ex}$ respectively. This is the minimal model to explain the intensity-dependence of τ_{on} and τ_{off}.

This model is justified by the observation that the recoveries of the dark state populations in many FPs and organic dyes were found to be intensity-dependent as revealed by several FCS and modulation-based fluorescence studies [36, 112, 35, 152]. For instance, Schwille *et al.* [36] measured intensity dependent "flickering rate" of YFP mutants in the intensity range of 50 kW/cm^2 to few W/cm^2. Similar intensity-dependent flickering was observed by the FCS studies in DsRed [112]. Schenk *et al.* [35] observed that the "flickering rate" and dark fraction in eqFP611 and drFP583 depends on excitation rate and explained the observation invoking a light-dependent as well as spontaneous recovery from the dark states. More recently, Mahoney *et al.* [152] used modulation

based techniques to enhance fluorescence intensity in cyanine dyes by relying on light-dependent recovery of the molecules from the dark states. Based on these observations, we modeled DSC as a thermally driven process from excited state S_1 to D but GSR as both a spontaneous and light-driven phenomenon. Intensity-dependence of the recovery process can be explained by excitation of dark state (D) into an excited state and relaxation to the ground state thereafter. This model is basically a 4 state system comprising of 2 bright state and 2 dark state as given by Schwille *et al.* [36]. Alternatively, the light-dependent recovery can happen through a stimulated transition of dark state population into the ground state in a non-radiative fashion as described by Schenk *et al.* [35]. Our model (Figure 3.10b) closely resembles the model given by Schenk *et al.* [35]. We prefer this model, as this is the minimal model to explain all the experimental observations.

Based on this 3 state model (Figure 3.10b), the molecule can switch between bright (S_0, S_1) and dark state (D). The probability of leaving a particular state depends on the reaction rates out of that state and the time-step. For example, the probability of leaving the state S_1 is given by,

$$p(S_1) = 1 - e^{-(k_{dsc}+k_r+k_{ic})*\Delta t} \tag{3.17}$$

where, Δt is the time-step of the simulation. The probabilities of leaving the other states can be obtained in similar way. Now the probabilities of changing the conformational states (i.e from S_0 to S_1 or vice verse) relies on the weightage of the process leading to the conformational change compared to other processes. For instance, probability of changing the state S_1 to S_0 can be expressed as,

$$cProb(S_1) = \frac{k_r + k_{ic}}{k_{dsc} + k_r + k_{ic}} \tag{3.18}$$

All these probabilities can be used to estimate the duration of time the molecule spends in a particular state. Considering that the molecule would fluoresce (signal=1) only when it resides in state S_0 or S_1 (bright states), we can generate the fluorescence traces of the system. Finally from these fluorescence traces, τ_{on} and τ_{off} can be extracted by fitting ON and OFF dwell-time

respectively. Each simulation was run for 100,000 ms of time with a step-size of 1 μs. The algorithm for these simulations and the corresponding Matlab code is presented in Appendix A.

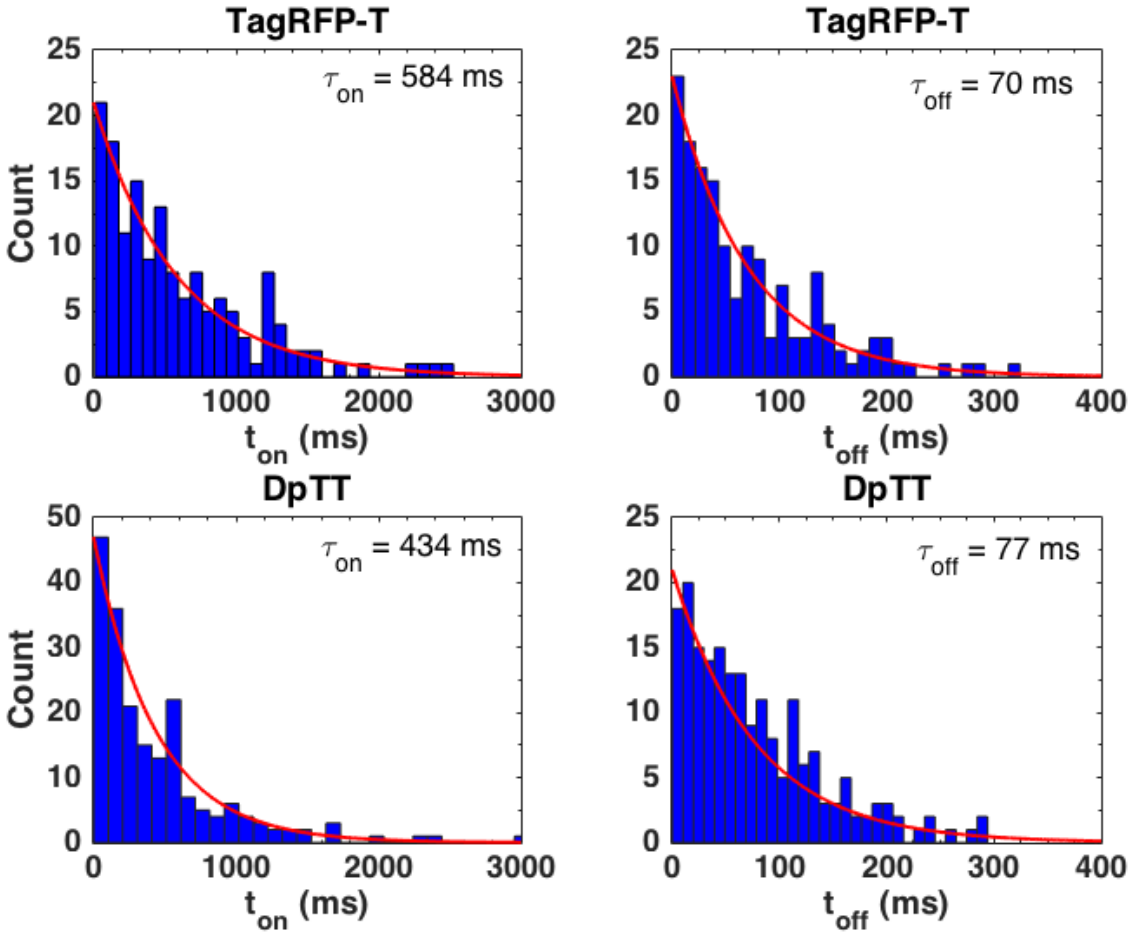

Figure 3.11: Histograms displaying distributions of t_{on} and t_{off}. Single exponential fits of the histograms are shown by the solid red lines.

Figure 3.11 shows the histograms of t_{on} and t_{off} and the single exponential fittings. τ_{on} of TagRFP-T and DpTT are given by 584 ms and 434 ms respectively which is similar to that obtained from the analytical expression (Eqn 3.14). τ_{off} of TagRFP-T and DpTT are found to be 70 ms and 77 ms respectively. The relative τ_{on} and τ_{off} values of TagRFP-T and DpTT are in good agreement with the experimental values. In the single molecule experiments, we observe 21% faster ON time of DpTT compared to TagRFP-T whereas in the simulation we find 26% faster ON time of DpTT. Also in the experiments, no significant changes was observed in experimental τ_{off}

values for the two constructs. The simulated τ_{off} times show a similar trend.

3.6 Discussion

The measurements of dark state dynamics of TagRFP-T and DpTT constructs reveal that they have similar GSR time-constants but DSC time-constants of DpTT constructs was 25% shorter than TagRFP-T (τ_{DSC} 24 μs in TagRFP-T and 18 μs in DpTT). This faster dark state conversion in DpTT results a higher fraction of dark state in this construct. Indeed we observe 26% higher dark state fraction in DpTT compared to wild-type TagRFP-T (Table 3.1).

The ensemble level measurement of GSR and DSC of TagRFP-T and DpTT can explain the single molecule kinetics measured *in vitro*. τ_{on} and τ_{off} measured from individual fluorescence traces showed 21% faster ON time for DpTT while OFF time was similar for both of those constructs. With the input from DSC/GSR, excited state lifetime measurements and using numerical simulation based on a 3 state model, we were able to show that the faster DSC kinetics in DpTT was responsible for its shorter τ_{on}.

The 3 State model used in the simulations assumes an intensity-dependence of GSR which is supported by the previous studies [35, 112, 147]. From our GSR measurements of TagRFP-T at different intensities (Figure 3.6), we have observed that τ_{GSR} tends to be shorter at higher intensities. In a previous study (Chapter 2, Figure 2.6a) [33], we presented a kinetic model for RFP, where population from dark state (D) can relaxes back to the ground state (S_0) or can go the excited state (S_1). This later process could be termed as "reverse DSC" and we have found the corresponding rate constant (k_{DS1}) to be slightly intensity-dependent. So, that model is equivalent to the model presented here (Figure 3.10b).

It is worth noting that although numerical simulation was able to account for the relative τ_{on} of TagRFP-T and DpTT, the absolute value of τ_{on} measured from simulation was far off. In fact, the τ_{on} values obtained from simulation were higher than the experimental ones. While the experimentally observed τ_{on} for TagRFP-T and DpTT was 141.3 and 111.3 ms respectively, the

numerical simulations results produced τ_{on} of TagRFP-T and DpTT as 584 ms and 434 ms. This discrepancy could be due to the fact that photo-bleaching from excited (S_1) and dark states (D) have not been taken into account in our model. With additional bleaching from S_1 and D, τ_{on} calculated from the model system would be lower. Using a more refined model, better agreement with the experiments could be achieved.

From the photo-physical and single molecule measurements, it is clear that Dronpa-linker-TagRFP-T showed $\sim 25\%$ faster blinking and higher dark state conversion. But, by measuring the skewness of the image, ~ 5 fold higher fluorescence fluctuation was observed in DpTT construct. So, dark state conversion alone can not account for the visibly different fluctuations in DpTT compared to TagRFP-T. It has been discussed earlier that the purification of DpTT construct revealed a fraction of immature TagRFP-T. It is possible that due to charge-charge interactions between Dronpa and TagRFP-T, the maturation pathway in TagRFP-T was affected resulting in the formation of non-functional chromophores. Thus the effective TagRFP-T concentration would be reduced when expressed in plasma membrane and as a consequence the fluctuations in TagRFP-T would be more prominent which is otherwise obscured by high FP-concentration. This could also explain ~ 10 fold reduction in brightness for DpTT construct. In essence, it can be concluded that the increased fluctuations in DpTT is the result of increased dark state conversion and inefficient maturation pathway of TagRFP-T leading to a lower label-concentration.

The charge-charge interactions in Dronpa and TagRFP-T is supported by the presence of basic and acidic patches on the surface of the β-barrel. These interactions can introduce barrel-flexibility that in turn can change the photo-physical behavior in FPs *e.g.* non-radiative decay or photo-switching kinetics [153, 135]. Kao *et al.* reported that the viscosity of the medium can exert hydrodynamic effect to slow down the photo-switching kinetics in Dronpa [135]. So, it is possible that the interactions between basic and acidic patches of Dronpa/TagRFP-T produce the similar protein-flexibility mediated coupling altering dark state conversion process.

Currently, FLINC is limited to only Dronpa and TagRFP-T. Generations of EGFP-linker-TagRFP-T or Dronpa-linker-mCherry constructs did not show the characteristics fluctuations ob-

served in DpTT. During our engineering of improved red fluorescent proteins, we generated a mCherry mutant (C4PB-12) showing higher dark state fraction upon 561 nm illumination. We used this RFP to create DpTT-like construct. Although the resulting constructs showed high fluorescence fluctuations, due to the its fast photo-bleaching, the construct could not be used as a PKA activity sensor. A complete mechanistic and theoretical understanding of the FLINC process is lacking for the future development of FLINC-based sensors.

3.7 Conclusion

In this Chapter, we explored the dynamics of dark state conversion (DSC) and ground state recovery (GSR) processes of the FPs and present them in the context of their impact on single molecule characteristics *e.g.* τ_{on} and τ_{off}. We discussed a novel class of fluorescent-based bio-sensor which works by altering the fluorescence fluctuation of an RFP in a distance-dependent manner. When Dronpa is within 5-6 nm of TagRFP-T, the fluorescence fluctuations in red fluorescence signal of TagRFP-T increases dramatically enabling it as a smart reporter of *in-vivo* enzymatic activities at super-resolution. Characterization of DSC, GSR kinetics of nuclear-localized TagRFP-T and DpTT (Dronpa-linker-TagRFP-T) in HeLa cells reveals a 25% increased rate of dark state conversion in DpTT. This increase can explain the kinetics that partly accounts for the enhanced fluctuations. Monte Carlo based numerical simulations were performed in different model systems to quantify the τ_{on} and τ_{off} of the constructs. The intensity-dependence of τ_{on} and τ_{off} was explained by this model.

Chapter 4

Multi-parametric Microfluidic Platform for Directed Evolution of the Red Fluorescent Proteins

4.1 Publication Note

Part of this Chapter has been adopted from Dean et al., High-speed multiparameter photophysical analyses offluorophore libraries, *Analytical Chemistry*, 87(10):5026-5030, **2015** [55] and the corresponding Supplementary Information of the article.

4.2 Introduction

The key photo-physical properties of FPs, *e.g.* brightness, photostability, spectral shift *etc.*, are largely inter-connected. For this reason, the engineering of a particular property of an FP often leads to inevitable changes in its other important photo-physical parameters. In many cases, these changes are undesirable. For example, with a selection based on excited state lifetime and using a synthetic RFP gene template, Bindels *et al.* [104] developed mScarlet which has a long lifetime (3.9 ns) and high quantum yield (70 %). However, this mutant lacks photostability compared to mCherry [12], the most commonly used RFP. mScarlet also shows slower maturation which is manifested in its lower than predicted *in-vivo* brightness based on its high extinction coefficient (ϵ) and quantum yield (ϕ). In fact, mScarlet-I, the faster-maturing version of mScarlet, displays higher brightness when expressed in mammalian cells although its theoretical brightness ($\epsilon * \phi$) is lower than mScarlet. In the process of generating mScarlet-H, the more photostable version of

mScarlet, the brightness was compromised. Similarly, far-red FPs with lower photo-toxicity and greater contrast over cellular auto-fluorescence tend to have lower QY and thus reduced brightness [95, 154]. Hence, for all-around improvement of FPs, the simultaneous monitoring of multiple photo-physical parameters is important. A multi-parametric selection of FP library is a viable option to achieve this goal.

Development of most FPs has been achieved by a combination of targeting the chromophore-forming residues, its immediate environment [12, 11] or dimeric interfaces [54] and subsequent random mutagenesis. However, further attempts to tune the photo-physical properties of FPs, particularly RFPs, have usually not been satisfactory. For example, to engineer mCherry, mutations in the residues surrounding the chromophore led to mutants with more pronounced dark state conversion (and therefore enhanced photobleaching) or immature chromophore as described in Chapter 5. This indicates that all the "low lying fruits" may have been procured through conventional RFP engineering and selection methods. Therefore, unconventional, inclusive and advanced engineering strategies need to be taken to overcome this deadlock. There is evidence in the literature that mutations in the distal part of the β-barrel can also modulate the photo-physical properties of the FPs in unique ways, *e.g.* through barrelfluctuations [135, 155]. These residues could be targeted to enhance the diversity and improve the FP photo-physics.

Also, some mutations are known to be context-dependent or to co-evolve with other residues in an FP. Inclusion of these new target residues could eventually increase the library size exponentially. To explore libraries of a large number of genetically distinct mutants requires high-throughput screening and sorting platforms. Traditionally, FPs are selected by plate-based techniques [11] or throughfluorescence activated cell sorting (FACS) or combinations of both. However, plate-based screening is slow and therefore incapable of covering large mutational space. Furthermore, although FACS is suitable for fast sorting and screening, FACS based selection is limited to only fluorescence intensity and wavelengths.

To enable simultaneous selection for evolution of the FP photo-physics and production of FPs with novel functionalities from a large library, we designed a multi-parametric microfluidic-

based platform [55]. Using phasefluorimetry and photobleaching through multiple laser beams, this microfluidic platform is capable of characterizingfluorescence intensity, excited state lifetime and photostability of the RFP mutants. This Chapter discusses the methodologies, instrumentation and operation of this microfluidic sorter. The use of this multi-parametric sorter leads to the generation of various RFP variants that are presented in Chapter 5, 6, 7.

4.3 Microfluidic Design and Manifold Assembly

To employ the multi-parametric sorting on RFP libraries, we adopted a microfluidic design from our previous work [98, 125]. The details of the microfluidic design are depicted in Figure 4.1a. The microfluidic is entirely made of borosilicate glass that can withstand the high intensity laser power used for optical sorting. The microfluidic chip consists of three inlets (sheath, sample, sheath) and two outlets (collection and waste). Cell suspensions are flowed through the middle channel. Two sheath channels hydrodynamically focus the middle channel to narrow the stream and thereby improve the coefficient of variation (CV) of the optical measurements. CV is measured as the ratio of mean and standard deviation of the measured values.

The microfluidic is sealed by a manifold through o-rings (Figure 4.1b). The manifold is made of polytetrafluoroethylene (PTFE) that minimize the non-specific adsorption of cells [125]. Three inlets of the manifold are connected with and regulated by three pressure-controllers (Pneutronics, OEM, EPS10-5-0-2) for independent control of theflow of each channel. The microfluidic chip is fitted in the middle of the manifold, allowing the delivery of light for epi- and trans-illumination. The inlet reservoirs of the manifold can be filled with up to 150 μl of sample or sheath buffers. Following the addition of buffer/sample into the inlets, the reservoirs are sealed with stoppers and a metal plate. The two outlets (collection and waste) are left open.

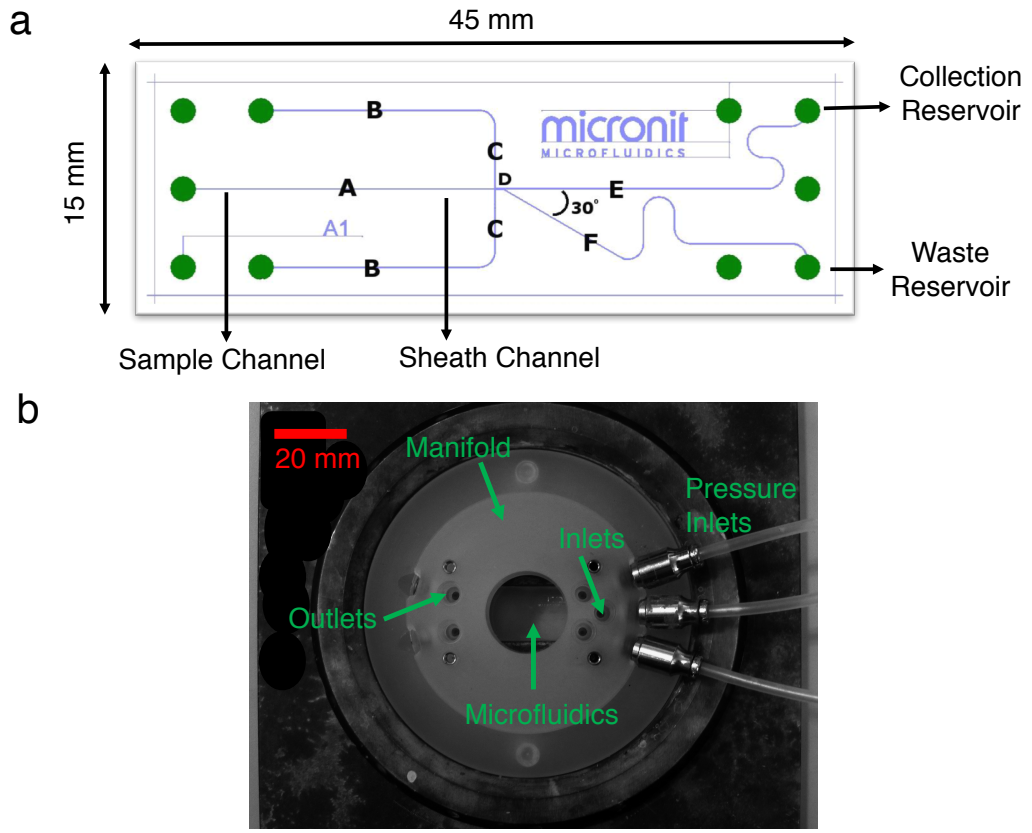

Figure 4.1: **Microfluidic Design and Manifold Assembly**: (a) Design of the microfluidic chip. The chip is custom fabricated by Micronit Microtechnologies B.V., The Netherlands. The length and width of different portion of the channels are: A [20 mm, 100 μm], B [15 mm, 130 μm], C [5 mm, 130 μm], D [0.5 mm, 150 μm], E [27 mm, 125 μm], F [27 mm, 125 μm]. The height of all channels is wet-etched to 25 μm. Solutions with cells are flowed in the middle channel (A). Sheath channels (B) hydrodynamically focus the sample channel to produce a narrow stream that improves the coefficient of variation (CV) of the measurements. (D) is the interrogation region where multiple laser beams are focused. (E) and (F) are collection and waste channels respectively. (b) Microfluidic and manifold (made of ploytetrafluoroethylene, PTFE) assembly consisting of three inlets (sheath, sample, sheath) and two outlets (waste and collection). The pressure of each channel is independently controlled by pressure controllers (Pneutronics, OEM, EPS10-5-0-2) within 0-2 psi range. The microfluidic chip is entirely made of borosilicate glass and fits in the middle of the manifold allowing delivery of light for epi- and trans-illuminations [98, 125].

4.4 Optical Set-up and Detection Electronics

The optical set-up for the microfluidic sorter is presented in Figure 4.2. In previous work, for in-flow photobleaching measurement of RFPs, a microfluidic platform with multiple beams was

used [98]. The multiple beams with appropriate spacing would allow us to achieve higher resolution in photobleaching and eliminate the reversible bleaching contributions of the mutants originating from dark state conversion [33].

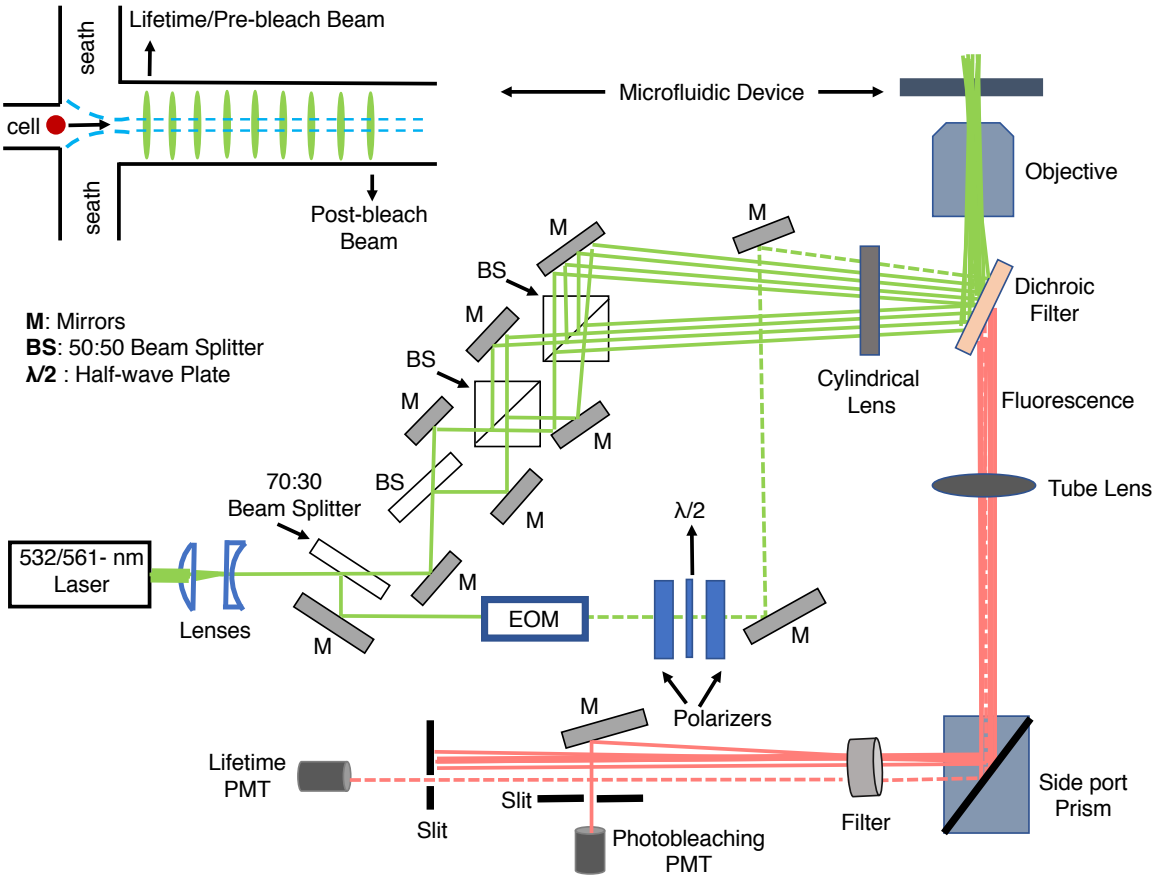

Figure 4.2: **Schematic of the Optical Layout**: A beam from 532-nm or 561-nm laser is passed through multiple lenses, mirrors, beam splitters and focused onto the microfluidic chip. The epifluorescence from the RFP-expressing cells upon their passage through the beams are collected using two PMTs. The details can be found in the text.

A 532-nm (Coherent Verdi, 5W) or 561-nm laser (Genesis MX, Coherent, 1W) laser beam is split with a 70:30 beam splitter. 30% of the beam power is directed through an electro-optic modulator (EOM, ThorLabs, EO-AM-NR-C4) that amplitude-modulates the beam at a frequency of 29.5 MHz. Before the beam enters the EOM, it is focused with a lens to fit into the EOM aperture. Two polarizers (Newport) and a half-wave plate (Newport) are introduced after the EOM to control the power of the lifetime beam. The remaining 70% of the beam is split into 9

beams with the help of multiple mirrors and 50:50 beam splitters (Figure 4.2). All these beams together with the modulated lifetime beam are passed through a plano-convex cylindrical lens (f = 150 mm), transforming the circular beams into elliptical ones. This minimizes the alignment sensitivity of the laser beams and reduces thefluctuations offluorescence signals that arises due to variations of the cell trajectories perpendicular to the direction of flow in the microfluidic channel [125]. The elliptical beams from the cylindrical lens enter the side-port of a commercial inverted microscope (Olympus IX71) and are reflected through a dichroic mirror (Semrock, FF573-Di01-25x36, for 561-nm laser). The reflected beams are finally focused into the microfluidic chip through an air-objective (Olympus, 20x, NA 0.45). The FWHM of the lifetime beam is measured to be 9 $\mu m$and 56 μm in the minor and major axes of the elliptical beam, respectively. The other beams have similar dimension as the lifetime beam. Epifluorescence from cells expressing RFPs is separated from the excitation beams using a band-pass filter (Semrock, FF01-629/56-25, for 561 nm laser). Subsequently, the lifetime and post-bleach beams are spatially separated from each other and other intervening beams using mirrors and slits and collected by two red-wavelength sensitive photo-multiplier tubes (PMT, Hamamatsu R9880U-20) as illustrated in Figure 4.2.

The electronic components for detection, amplification and processing of the fluorescence signals are schematically illustrated in Figure 4.2. A function generator (Agilent, 33520B) is used to provide a sinusoidally modulated electrical signal with 10 V peak-to-peak at 29.5 MHz to drive the EOM, and also send a 1 V peak-to-peak reference signal to the lock-in amplifier. Thefluorescence signal obtained from the lifetime PMT is split into two components (high and low frequencies) using a biased-tee. The high frequency component ($>$ 1 MHz) is directed to a custom-made amplifier and then sent to a lock-in amplifier (Zurich Instruments, UHF) for frequency-domain lifetime measurements. The lock-in amplifier is controlled by a web-based LabOne user interface. The low frequency components ($<$ 1 MHz) from the biased-tee (pre-bleach), along with the signal from post-bleach beam are further amplified with a home-built trans-impedance amplifier for improving the signal-to-noise ratios. The pre- and post-bleach signals are further smoothed with a custom-built 5 kHz low-pass filter. Electronic amplification of the pre-bleach beam is achieved by either

a linear or logarithmic trans-impedance amplifier. The logarithmic amplifier has higher dynamic range and thus helps to resolve the brightness of a mixture of mutants better than the linear amplifier. Finally, the pre-bleach, post-bleach, in-phase and quadrature-phase signals are digitized at 125 kHz, 16-bit resolution by a data acquisition card (DAC, National Instruments BNC-209a, PCI-6251 with NI-SCX). The DAC board communicates with a Target computer that runs the LabView RealTime module to analyze the digitized data streams, identify the isolated non-overlapping bursts of peaks due to the passage of cells through the laser beams, and make selection decisions based on user-defined thresholds of lifetime,fluorescence intensity, transit time of the cells through the microfluidics or photostability of the mutants. The Target computer is connected to a Host computer that controls the operation of the sorter and used for real-time data display. The design of the biased-tee, trans-impedance amplifiers and filters is provided in the Appendix.

Various methods for cell sorting have been reported [156, 157, 158, 159], including electro-osmosis, generation of explosive vapor bubbles [157], optical force [158, 160], and acoustic wave-based [156, 161] sorting. We employ optical force gradient based sorting that does not require a high-NA objective and is compatible with live-cells and the microfluidic chip we use. Our implementation of this technique is schematically shown in Figure 4.4 and has been described in detail in reference [98].

The 1064-nm laser can deliver up to 20W power but only 30-40% of it (6 - 8 W) is required to generate force for the deflection of the cells. Although higher trap-laser intensity increases the selection efficiency, it reduces the viability of the sorted cells [98]. Higher intensity of the trap-laser also increases the risk of damage to the microfluidic chip.

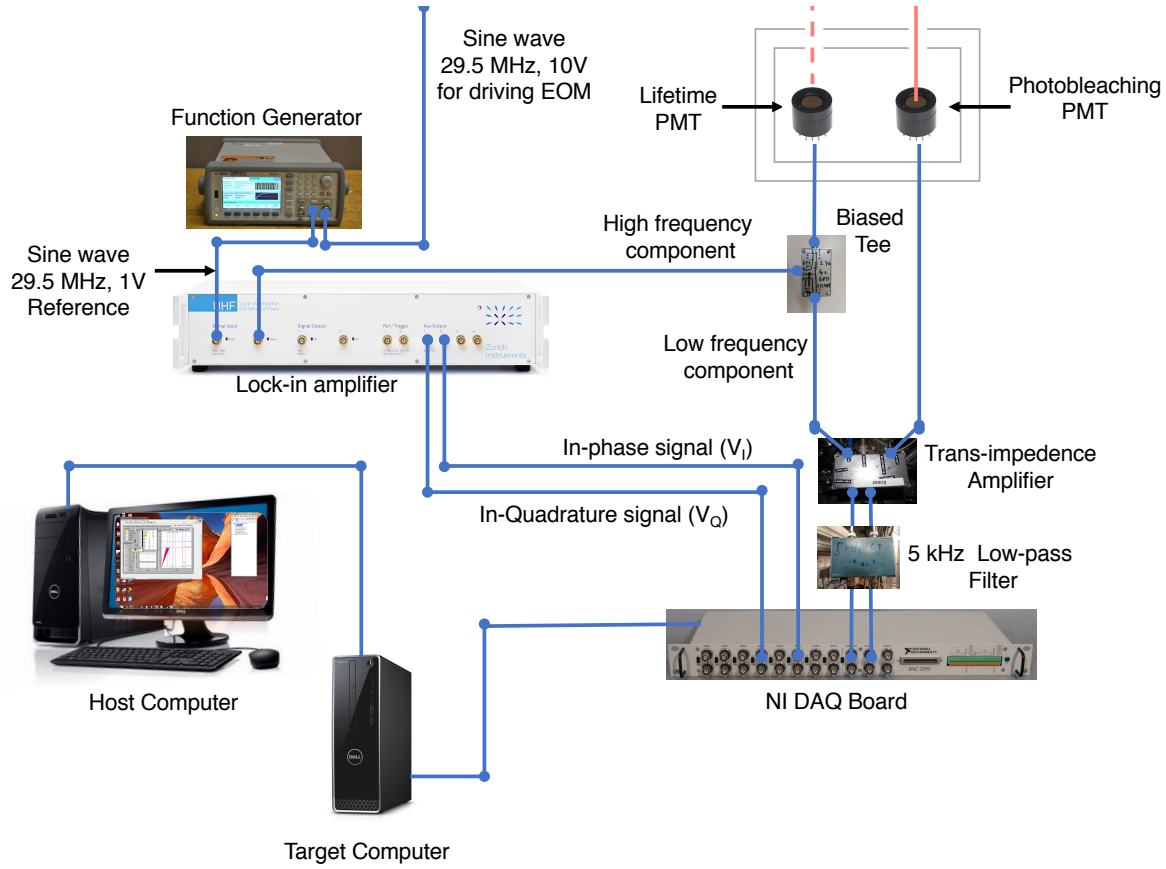

Figure 4.3: **Schematic of the Electronics and Signal Processing**: Following the collections of red fluorescence from lifetime and post-bleach beams by two red-sensitive PMTs (Hamamatsu R9880U-20), further processing of the signals is conducted by multiple electronics components as described in the text.

4.5 Theory of Frequency-Domain Lifetime Measurements in Flow Cytometry

The intensity ($I(x, y)$) of a Gaussian laser beam focused to an elliptical spot with $1/e^2$ intensity radii σ_x and σ_y is given as [55]

$$I = I_0 e^{(-\frac{2x^2}{\sigma_x^2} - \frac{2y^2}{\sigma_y^2})} \tag{4.1}$$

where I_0 is the intensity at the center of the Gaussian beam.

In flow-cytometry, the fluorescence signal generated due to the passage of cells through the laser

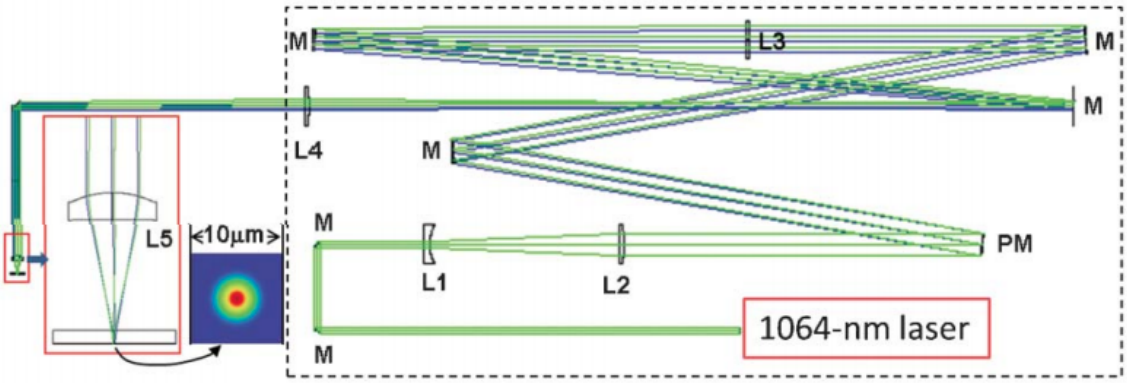

Figure 4.4: **Schematic of the Components for Optical Force Switching**: A 1064-nm laser (IPG Photonics Laser, YLR-20-1064-LP, 20W) beam is expanded 3.5 times using a [L1 (Plano-concave, f = -50 mm, ThorLabs LC1715-C) & L2 (Plano-convex, f = 175 mm, ThorLabs LA1229-C)] lens assembly and focused on a piezo-tilt mirror (PM, Physik Intrumente, S-315). Laser reflected from the PM is further directed through [L3 (Plano-convex, f =1000 mm, ThorLabs LA1464-C) & L4 (Plano-convex, f = 300 mm, ThorLabs LA1484-C)] and focused into the microfluidic chip from top using an aspheric lens (f = 11 mm, ThorLabs A397TM-C). PM is used to translate the focus laser spot with a scan range of 88 μm. It is driven by a 3-channel 100V amplifier (Physik Intrumente, E-663 LVPZT amplifier) controlled by 0-10 V input signals. (inset) The Huygens point-spread function of the laser beam focus. The Figure has been adopted from reference [98].

beam has a Gaussian profile in temporal coordinate. The peak fluorescence intensity ($F(t)$) of a cell with radius r and velocity v_x across the laser beam is given by

$$F(t) = F_0 e^{(-\frac{t^2}{\sigma_t^2})} \tag{4.2}$$

where, $\sigma_t = \frac{\sqrt{\omega_x^2 + r^2}}{2v_x}$ and the flow is along the x-direction. The fluorescence intensity, F_0, is proportional to the excitation intensity ($I(x, y)$). Using σ_x as 9 μm, r as 3 μm and v_x as 10 mm/s, σ_t is found to be 0.5 ms. In our measurements, the passage time of the cells in each beam is in the range of 200 μs -1 ms.

For frequency-domain lifetime measurements, the sample is excited with an amplitude modulated sinusoidal excitation with a period typically on the order of its excited state lifetime. The fluorescence signal emitted by the sample has the same frequency but is phase delayed due to a finite excited state lifetime. So, if the excitation has the form of $Asin(\omega t)$, then the corresponding

fluorescence signal would be [129]:

$$A * m * sin(\omega t - \phi) \tag{4.3}$$

where A is the amplitude of the signal, m is the modulation, ϕ is the phase shift, and ω is the angular frequency of the excitation ($\omega = 2\pi\nu$), ν is the modulation frequency). It can be shown that and m are related to the excited state lifetime (τ) and angular frequency of the system in the following way [129]:

$$\tau = \frac{1}{\omega} tan(\phi) \tag{4.4}$$

$$m = \frac{1}{\sqrt{1 + \omega^2 \tau^2}} \tag{4.5}$$

In frequency-domain flow cytometry, the fluorescence signal is the a product of Eqn 4.2 and 4.3. *i.e.* $\propto sin(\omega t - \phi) e^{\frac{-t^2}{2\sigma_t^2}}$. Now, the fluorescence signal is further delayed due to the optics and the electronics used to amplify the signal. The detected signal can be represented as:

$$F(t) \propto sin(\omega t - \phi - \delta) e^{\frac{-t^2}{2\sigma_t^2}} \tag{4.6}$$

where, δ is the phase shift induced by optics and electronics [162].

Before the fluorescence signal reaches the lock-in amplifier, the low frequency component ($e^{\frac{-t^2}{2\sigma_t^2}}$ ~kHz) is separated from the high frequency component ($sin(\omega t - \pi - \delta)$, ~ MHz) using a biased-tee. In the lock-in amplifier, the fluorescence signal is demodulated by multiplying with the reference signal, $sin(\omega t)$ and $cos(\omega t)$, to give V_I and V_Q, respectively. The in-phase signal is then given by:

$$V_I \propto sin(\omega t - \phi - \delta) sin(\omega t) \tag{4.7}$$

$$\propto \frac{1}{2} cos(2\omega t - \phi - \delta) - \frac{1}{2} cos(\phi + \delta) \tag{4.8}$$

The first part of the voltage contribution in the above equation with high frequency can be eliminated using a low-pass filter to give,

$$V_I = Bcos(\phi + \delta) + V_{BI} \tag{4.9}$$

where B is a constant and V_{BI} is the background signal for the detection of V_I. Similarly, it can be shown that the in-quadrature phase signal (V_Q) would be:

$$V_Q = Bsin(\phi + \delta) + V_{BQ} \tag{4.10}$$

Eqn. 4.9 and 4.10 can be rearranged to give,

$$\phi = tan^{-1}(\frac{V_Q - V_{BQ}}{V_I - V_{BI}}) - \delta \tag{4.11}$$

Using Eqn. 4.4 and Eqn. 4.11 we get,

$$\tau = \frac{1}{\omega} tan(tan^{-1}(\frac{V_Q - V_{BQ}}{V_I - V_{BI}}) - \delta) \tag{4.12}$$

Further simplification of the above equations gives

$$\tau = \frac{1}{2\pi\nu} \frac{\bar{V_Q} cos(\delta) - \bar{V_I} sin(\delta)}{\bar{V_I} cos(\delta) + \bar{V_Q} sin(\delta)} \tag{4.13}$$

where $\bar{V_I}$ and $\bar{V_Q}$ are background corrected in-phase and quadrature-phase signal ($\bar{V_I} = V_I - V_{BI}$, $\bar{V_Q} = V_Q - V_{BQ}$). Eqn. 4.13 is used for the in-flow quantification of the excited state lifetime of the system. $\bar{V_I}$ and $\bar{V_Q}$ are directly obtained from the lock-in amplifier. The modulation frequency, ν, is 29.5 MHz. The parameter δ is obtained by using a FP with known fluorescence lifetime. We use mCherry (τ = 1.87 ns) as a reference for the adjustment of δ.

4.6 Cell Culture, Library Generation, and Sample Preparation

For the RFP engineering project, we use yeast (*Saccharomyces cerevisiae*) as the host organism. Conventionally, bacteria (*E. coli*) or mammalian cell-lines are preferred choices of host

organisms for library generation. However, we choose yeast rather than bacteria or mammalian cell-lines for the following reasons. (1) Using yeast as a host organism makes the library generation, screening, sorting and the recovery of cells after sorting much faster, since the doubling time is only 90 minutes for yeast cells comparing to 20 hrs for mammalian cells. Also, mammalian cell-lines require more maintenance than yeast cells which are more robust to the change in pH or temperature. (2) Unlike bacteria, yeast cells are eukaryotic and have a proper nucleus. In this respect, they are more similar to the mammalian cell-lines where eventually the engineered proteins would be targeted. So, ideally, the phenotypes shown in the yeast cells are expected to be more comparable to the phenotype shown in mammalian cells. However, as will be discussed in Chapter 5, 6 and 7, the fluorescence intensity of some RFPs in yeast is not comparable to the mammalian cells.

The engineering of RFP mutants involves incorporation of point mutations within the protein and library generation. To generate point mutations, a particular amino acid in FP is changed to a different one. The accumulation of many protein variants with different mutations is what leads to the creation of library. To create mutations, we use either Quick Change or g-Block protocols as described in Appendix D. Library generation is associated with changing a defined (site-directed mutagenesis) or a random (random mutagenesis) amino acid residue with multiple other amino-acids or nucleotides (for synonymous mutations). For the microfluidic screening of yeast cells containing RFPs, the corresponding library or the culture is freshly grown from a stored stock and expressed transiently. A 0.5 ml volume of stored culture media is added to 10 ml solution of growth media (yeast nitrogen base, ammonium sulphate, dextrose) and grown for 8 hrs. in a 50 ml tube. Next, 0.5 ml of this freshly grown cell culture is added to 10 ml solution of induction media (yeast nitrogen base, ammonium sulphate, galactose, raffinose) in an Erlenmeyer flask. Cells are screened or sorted 17-20 hrs post-induction. During growth and expression, the cultures are incubated at 30°C and constantly shaken at 250 rpm. For the expression of the FPs, oxygen is necessary. Hence, care is taken so that the flasks containing yeast cultures are sufficiently exposed to the air. The stock yeast culture is stored in a 4°C fridge and passaged twice a month. For long-term use of the yeast cultures or libraries, a glycerol-stock is prepared and stored in a -80°C freezer.

For screening in the microfluidics, the expressed yeast cells are diluted (10-20 fold) with the blank media (yeast nitrogen base, ammonium sulphate) containing 14% OptiPrep (60% weight/volume iodixanol in water), and subsequently filtered using a 40 μm filter to discard the cell debris. OptiPrep increases the specific density of the media making the cells buoyant inside the microfluidic channel. Also, OptiPrep modifies the refractive index of the solution, which is advantageous for tracking the flow of the sample channel and alignment of the trap-laser beam.

4.7 Multi-parametric Screening

Microfluidic screening reveals the fluorescence intensity, excited state lifetime and photostability profiles of the individual mutants or RFP libraries. Based on the initial screening results of a library, decision is made to sort some sub-population of the library for further enrichment and selection. Screening is also carried out to quantify the properties of individual mutants with large number of cells (∼10,000). The detailed, step-by-step protocol for using the microfluidic for the screening and sorting purpose are presented in Appendix B and C. In brief, 150 μl of ultra-pure water (milli-Q water filtered with a 2 μm filter) and the cell media (blank solution with 14% OptiPrep) is added in the two sheath and sample channels of the microfluidic respectively and run for 10 minutes at high pressure (10 psi). This step eliminates the dirt or cell-debris that is present in the microfluidic channels from the previous sorting/screening. As the sample channel and the sheath channels are running two different media with different refractive index, theflow originating from each channel can be visually distinguished and ideally the flow focus would be symmetric. Next, a blank solution is run in all of the three channels for 30 minutes at 2 psi. This step stabilizes the flow and eliminates any bubbles present in the channels. Finally, if the flow is stable, the sample is loaded in the sample reservoir (the middle inlet) and blank solution is loaded into the two side-inlets for hydrodynamic focusing of the sample.

At different stages of the project, different combinations of the optical set-up (Figure 4.2) were used. However, the basic configuration remained the same. For the development of C4LT

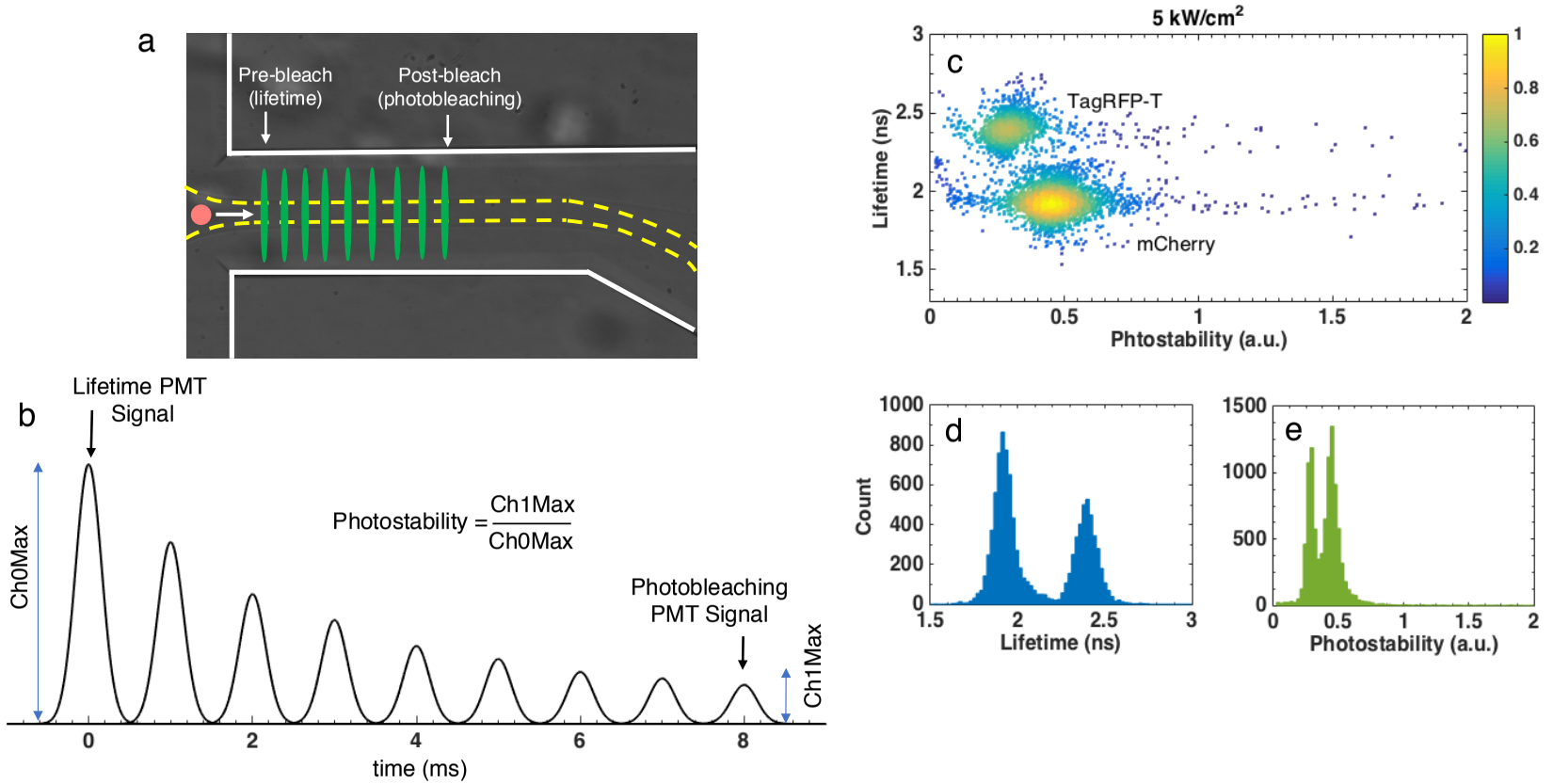

Figure 4.5: **Multi-parametric Microfluidic Screening**: (a) Cells expressing RFPs are passed through the laser beams focused on the microfluidic chip for rapid in-flow determination of brightness, photostability and lifetime. (b) The first beam is amplitude modulated at 29.5 MHz. PMT signal from this beam is used to determine the excited state lifetime and also produce pre-bleach fluorescence intensity (Ch0Max). Ratio of the fluorescence intensity from last beam (Ch1Max) and first beam (Ch0Max) is defined as the photostability of the mutants. Transit time between first and last beam is $\sim$ 8 -10 ms. (c) Screening results of a mixture of cells expressing mCherry and TagRFP-T at 5 kW/cm^2 illumination intensity (lifetime beam). (d, e) Distribution of excited state lifetime and photostability, showing clearly-resolved peaks for mCherry and TagRFP-T.

and C4PB mutants that will be described in Chapter 5, a 532-nm laser (Coherent Verdi, 5W) was used with all the lifetime and photobleaching beams (*i.e.* 1 lifetime beam + 8 photobleaching beams). Here, simultaneous evolution of excited state lifetime and photostability was carried out using mCherry as a template. On the other hand, for the development of SDC, SLT (Chapter 5), FusionRed mutants (Chapter 6) and Radiative Rate mutants (Chapter 7), the photostability parameter was dropped. In these cases, evolution pressure was applied for the generation of mutants with bright mutants having high quantum yield. Here, a 561-nm laser (Genesis MX, Coherent, 1W) was used and the 8 photobleaching beams were blocked. Only the lifetime beam (which measures the brightness and excited state lifetime of the mutants) and one timing beam was used. The timing beam was required for the computation of cell velocity in the microfluidic channel that is required for the efficient sorting.

When the photostability parameter is included, as a cell passes through different laser beams, the FPs photobleach and the fluorescence signals from the lifetime and post-bleach beams are detected in two different PMTs. After processing by several electronics components, the digitized data from the PMTs are analyzed by a custom-made LabView software. The software quantifies the excited state lifetime of the mutants from the in-phase (V_I) and in-quadrature phase (V_Q) values provided by the lock-in amplifier using the Eqn. 4.13. The LabView software also pair-matches the bursts of signals arises due to the passage of the cells based on their transit time between lifetime and post-bleach beams (Figure 4.5a). This pair-matching recognizes the fluorescence signals from the lifetime and photobleaching beams which are Gaussian in nature (see Figure 4.5b). The maximum of the lifetime and photobleaching beams are denoted as Ch0Max and Ch1Max respectively. The photostability of is quantified as:

$$Photostability = \frac{Ch1Max}{Ch0Max} \tag{4.14}$$

Figure 4.5c demonstrates typical screening results obtained by mixing yeast cells expressing mCherry and TagRFP-T. The x and y-axis of the plot displays the photostability and the lifetime of the

mutants. Figure 4.5d and e show the distribution of lifetime and photostability of these two RFP mutants. The distributions clearly demonstrate two peaks due to the presence of two mutants in the sample.

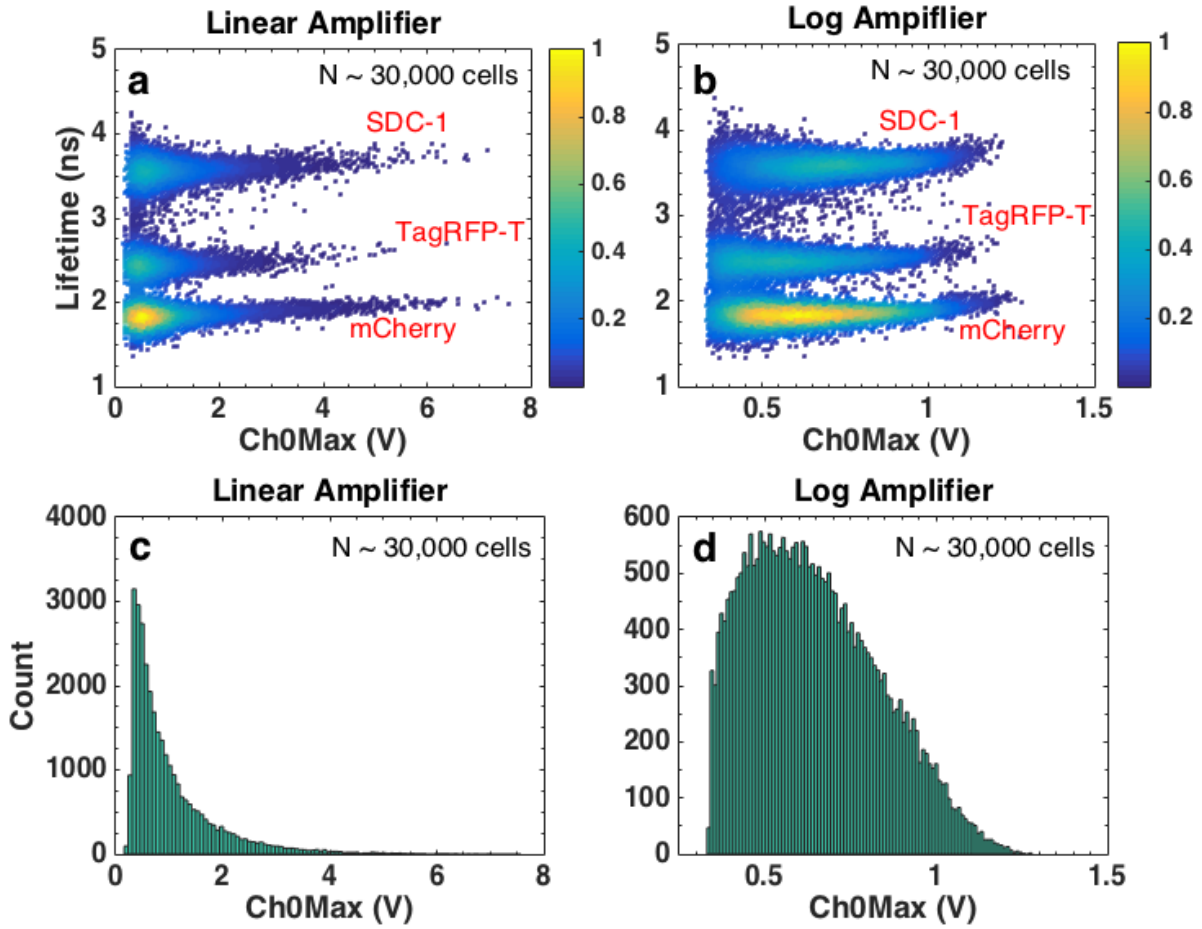

Figure 4.6: **Microfluidic Screening with Linear and Logarithmic Amplifier**: (a) Microfluidic screening displaying the profile of fluorescence intensity (Ch0Max) and the excited state lifetime of a sample containing mCherry, TagRFP-T and SDC-1. Linear amplifier was used for the amplification of lifetime PMT signal. (b) Screening results of the same sample using logarithmic amplifier. (c & d) Histogram of Ch0Max of the sample containing mCherry, TagRFP-T and SDC-1 using linear and logarithmic amplifier respectively. ~ 30,000 cells were screened for each run.

It should also be noted that the lifetime measured from the frequency-domain flow cytometry is approximate in nature. The lifetime results are accurate when the fluorescence lifetime decays of the FPs are purely mono-exponential. For the FPs that display multi-exponential fluorescence decays, only the major component is captured by the frequency-domain lifetime measurements. For

instance, fluorescence decay of mCherry (in purified proteins) when measured in a Time Correlated Single Photon Counting (TCSPC) system shows a bi-exponential decay with a major (73%) 1.74 ns component and a minor (27%) 1.05 ns component. However, in the microfluidic screening of mCherry (in yeast) using the frequency-domain technique, it shows a lifetime of 1.87 ns. This value is close to the value of the major component (1.74 ns) as measured by TCSPC. The slight discrepancy of the values may be attributed to the different environment of the mCherry in two different measurement systems (mCherry in yeast for microfluidic and mCherry in purified proteins for TCSPC).

For assessing the brightness of the mutants, thefluorescence intensity from the lifetime beam (Ch0Max) was used. During the microfluidic screening, either a linear or logarithmic amplifier was used for the amplification of lifetime PMT signal. Figure 4.6 a & b present the lifetime *vs.* Ch0Max plots of a sample containing three RFPs: mCherry, TagRFP-T and SDC-1 with linear and logarithmic amplifier respectively. Although, both amplifiers clearly resolve the excited state lifetime of the three mutants, owing to its higher dynamic range, only the logarithmic amplifier captures the peak of thefluorescence intensity. This is obvious from the Figure 4.6 c & d.

4.8 Sorting of the Improved Red Fluorescent Protein Variants

Once the lifetime, brightness and photostability profiles of a RFP library are revealed through the microfluidic screening, the logical next step is to sort the mutants with desired phenotypes. As described previously, the sorting of cells is done with optical force using a 1064-nm pulsed laser operated by a custom-made LabView software.

The sorting process is illustrated in Figure 4.7. For the sorting purpose, the flow of the sample is biased to direct the cells into the waste channel. The trap-laser is focused to a place close the junction of collection and waste channels and slightly below the sample stream. The LabView software measures the distance between A and B when the pixel positions of lifetime and post-bleach beams are entered. From the transit time of cells from A to B (T_{AB}) and the physical

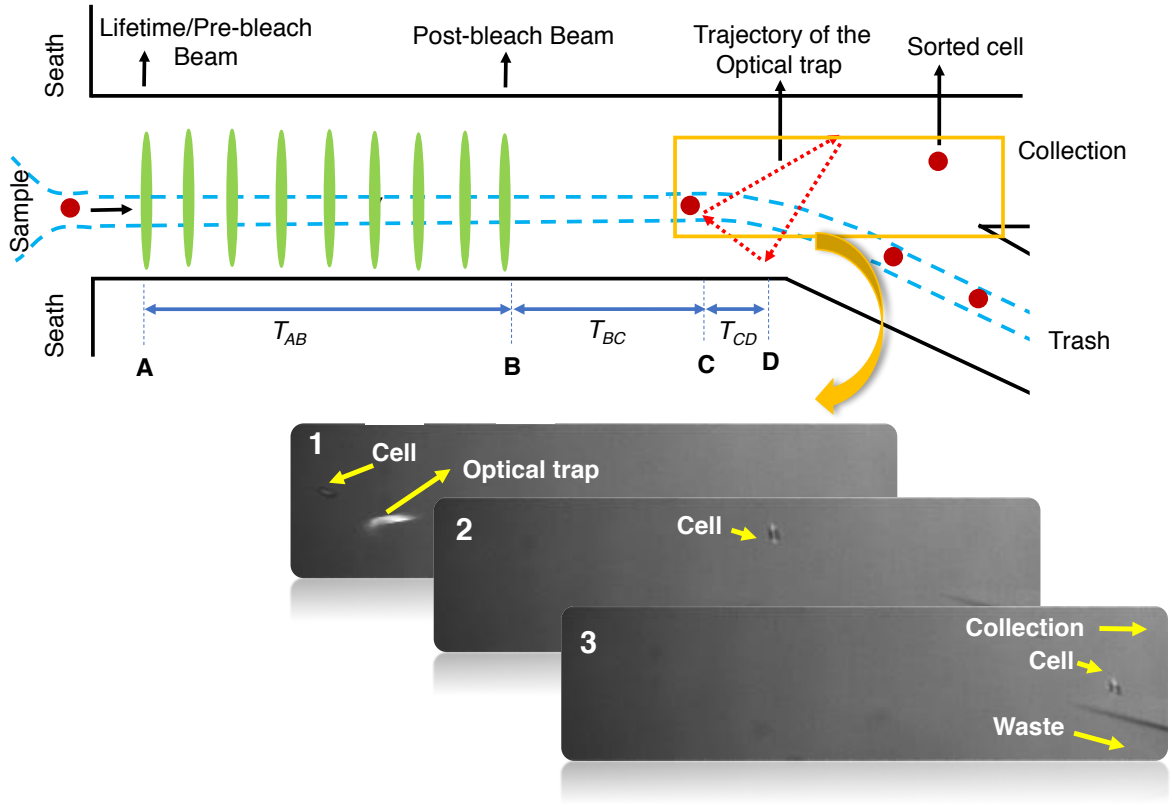

Figure 4.7: **Sorting of Improved RFP Variants with Optical Gradient Force Switching**: (above) The flow in the microfluidic is biased to direct the cells to the waste channel. Once a mutant shows improved phenotype based on some pre-defined thresholds, the optical sorter is turned on to sort the corresponding cell. Based on the physical distance between lifetime and post-bleach beams and the transit time associated with it (T_{AB}), the cell velocity is computed. From the cell velocity, the time delay from position B to C (T_{BC}), and the transit time from C to D (T_{CD}) for sweeping velocity for the firing of trap laser are determined so that the trajectory of the optical trap intercepts with the cell to deflect the cell into the collection channel. (below) A portion of the microfluidic is zoomed to display a set of images showing a yeast cell being captured into the collection channel.

distance between them, the velocity of the cells in the microfluidic channel is computed. From the measured cell velocity and the distance from B to C and C to D, the transit time of the cell to travel BC (T_{BC}) and CD (T_{CD}) is measured. T_{BC} and T_{CD} determine the delay time and the sweeping velocity of the trap laser so that the trap laser intercepts the cell and deflects it to the collection channel. However, the speed of the cells is not uniform in the microfluidic channel and

tends to decrease in the sorting junction. To account for this effect, another adjustable parameter (Extra Delay) was added in the software. The value of the Extra Delay parameter is optimized to increase the sorting efficiency through visual inspection of the cell trajectory in the camera. Once the sorting efficiency is optimized, mutants with improved photo-physical properties can be sorted based on user-defined thresholds.

A detailed step-by-step sorting protocol and the instructions for operation of the LabView software are provided in the Appendix C.

Chapter 5

Directed Evolution of Photostability and Excited State Lifetime in mCherry

5.1 Introduction

The brightness of the red fluorescent proteins (RFPs) is relatively lower than their green or cyan counterparts. The main reason behind the significantly low brightness of RFPs is their lower quantum yield (ϕ) compared to GFPs or CFPs. For instance, mTurquoise2 [155] and mNeonGreen [163] are two bright green and cyan fluorescent proteins with 93% and 80% quantum yield respectively. On the other hand, mCherry [12], the most widely-used RFP, has only a 22% quantum yield. The mKate2 RFP [164] has a higher quantum yield (40%) than mCherry but still significantly lower than other green and cyan FPs. TagRFP-T is another bright and photostable RFP derived from TagRFP with high ϕ (41%) and extinction coefficient (ϵ_{max}, 81,000 $M^{-1}cm^{-1}$) [11]. Unfortunately, fusion-constructs of TagRFP-T are reported to aggregate in the cellular environment [101, 100]. Similarly, mRuby2 [165] and mRuby3 [102], RFPs derived from eqFP611 aggregate when expressed in mammalian cells [104]. Recently, Bindels *et al.* reported mScarlet, a bright red fluorescent protein developed through excited state lifetime-based screening [104]. Based on its *in-vitro* properties, mScarlet is the brightest, monomeric RFP so far with its 70% fluorescence quantum yield and high ϵ_{max} value (100,000 $M^{-1}cm^{-1}$). However, it photobleaches faster than mCherry and matures more slowly. In fact, due to its slower maturation kinetics, mScarlet shows lower in-vivo brightness than its mScarlet-I variant which has significantly lower QY (54%) but matures $\sim$ 5-fold faster than mScarlet. We have also observed that mScarlet tends to mis-localize when expressed in Golgi *e.g.*

with GalT-mScarlet constructs (see Chapter 6).

In order to develop RFP mutants with higher brightness and reduced photobleaching, we started with mCherry as a template. mCherry displays high photostability, excellent pH-resistance, fast maturation and a moderate extinction coefficient. However, mCherry is significantly dimmer than other more recently developed RFPs, *e.g.* mRuby3 or mScarlet, due to its lower ϕ. Hence, we set out to improve the brightness of mCherry by improving its quantum yield. As the ϕ of a chromophore is directly proportional to its excited state lifetime (τ), enhancing the lifetime holds the promise of improving its quantum yield. Based on this concept, several site-directed and random mutagenesis libraries were created and screened for higher excited state lifetime and photostability. In this Chapter, the directed evolution of mCherry is discussed. Several mCherry mutants with improved photo-physical properties were selected and characterized. Figure 5.1 describes the genealogy of the mCherry mutants generated in the course of this work. Targeted mutagenesis of mCherry and subsequent photostability and excited state lifetime-based selections resulted in the generation of C4, C9 and C12 mutants. The C4 mutant was further evolved through multiple rounds of error-prone and FACS-based selection to produce C4PB and C4LT mutants. SDC and SLT mutants were generated through site-directed and random mutagenesis of C9 and C12 following the enrichment of populations with higher fluorescence lifetimes. The multi-parametric microfluidic platform presented in Chapter 4 was used for the screening and sorting of the FP libraries.

5.2 Evolution of mCherry: C4 and C12 Mutants

In order to achieve simultaneous improvement in brightness and photostability of mCherry, first we took a targeted mutagenesis approach. We decided the positions of the residues based on studies from our lab and from the literature.

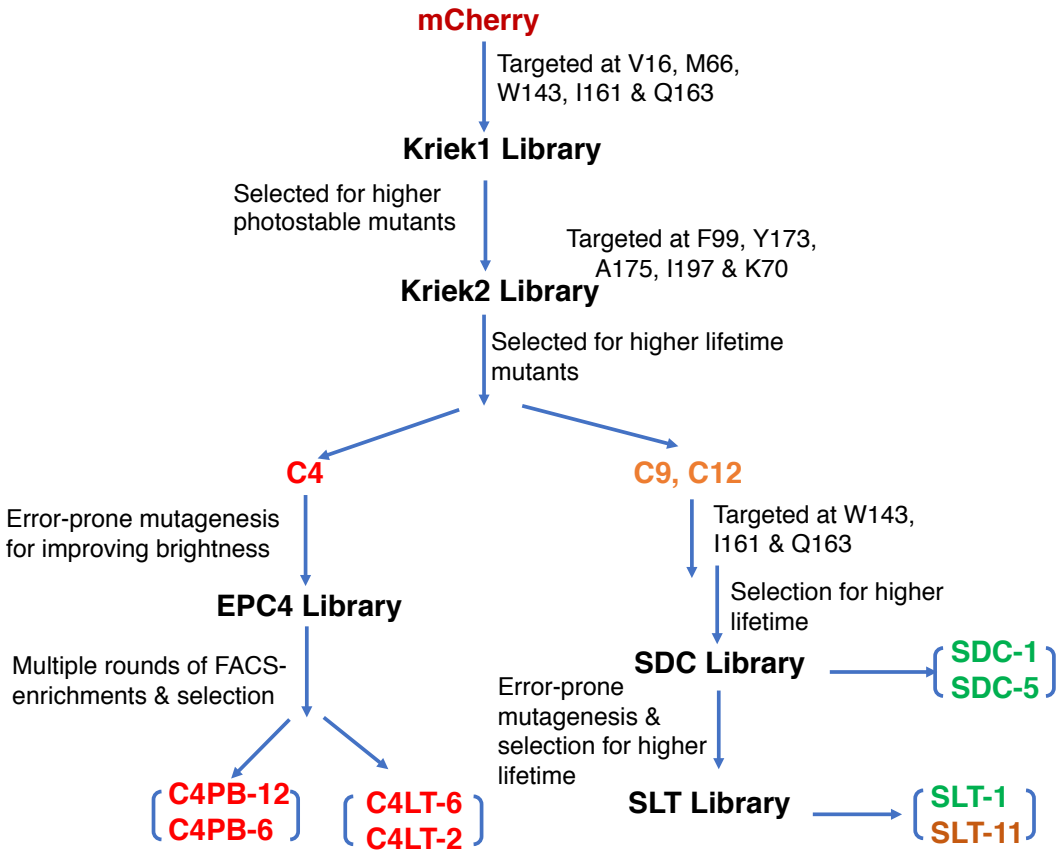

Figure 5.1: Genealogy of the mutants derived from mCherry through photostability and excited state lifetime-based selections.

5.2.1 Targeted Mutagenesis: Kriek1 Library

In first round of targeted mutagenesis, we tried to improve the photostability of mCherry. Although molecular oxygen (O_2) is essential for the auto-catalytic formation of chromophore in FPs [27, 28], it can also enhance the rate of irreversible photobleaching by reacting with the excited state chromophore [11, 57]. Chapagain *et al.* performed MD simulations on mCherry and Citrine (a yellow fluorescent protein) and suggested that the inferior photostability of mCherry might be due to its increased inter-strand dynamics between β-7 and β-10 [20]. According to this study, in Citrine, entry of molecular oxygen from the bulk solvent to the interior of the FP is energetically unfavored. On the other hand, the dynamics of mCherry are such that oxygen can easily enter into the inside of FP barrel to enhance its photo-degradation. Their MD simulations also predicted that

Table 5.1: Targeted Mutagenesis in mCherry: Kriek1 Library

Residues	Amino acids targeted	Rationale
V16	E/D/A/K/N/T/V	common target
M66	K/E/Q/V/M/L/N/D/H/Y/I/F	common target
W143	All 20	MD
I161	L/M/V/I/F	common target
Q163	All 20	MD

the W143K, Q163R, and R164E mutations could improve the photostability of mCherry by closing the major low-energy pathways for oxygen entry. We found that incorporation of these mutations into mCherry resulted in a non-fluorescent variant, presumably due to poor folding. In order to restore the brightness, we looked for commonly mutated residues in the mFruit series of FPs [12] and identified V16, M66, W143, I161, Q163, I197, and A217 as candidates for mutagenesis. Two of these residues (W143 and Q163) were also identified as highly dynamic in the MD simulations. Based on further literature analysis, we selected the following residues to target in our first round of site-directed mutagenesis: V16, M66, W143, I161, Q163. The resulting library was called Kriek1. Residue R164 was not included as it was reported that the presence of charged side-chains at this position disrupt dimer formation in mFruit RFPs [13], and it would be undesirable to compromise the monomeric character. Positions I197 and A217 were excluded in the first round to limit the size of the library. Table 5.1 displays the residues targeted in Round 1 site-directed library and the rationale for choosing those positions. All the numbering of the residues used in this Chapter and Chapter 7 was based on the numbering used in a reported mCherry crystal structure (PDB 2H5Q) [166] . The size of Kriek1 library was: $7 \times 12 \times 20 \times 5 \times 20 = 168000$ members. Fluorescent colony screening of the library in *E. coli* showed that ~10% of the library was fluorescent.

Figure 5.2 displays the screening results of Kriek1 with its precursor mCherry. Both mCherry and Kriek1 were screened for 15,000 cells. It was evident from the screening results that Kriek1 contained a population of higher photo-stability. We sorted the library to enrich the population with higher photostability with sort criteria set according to the pink box in Figure 5.2b. This sorter-enriched population served as the template for our next round of targeted mutagenesis.

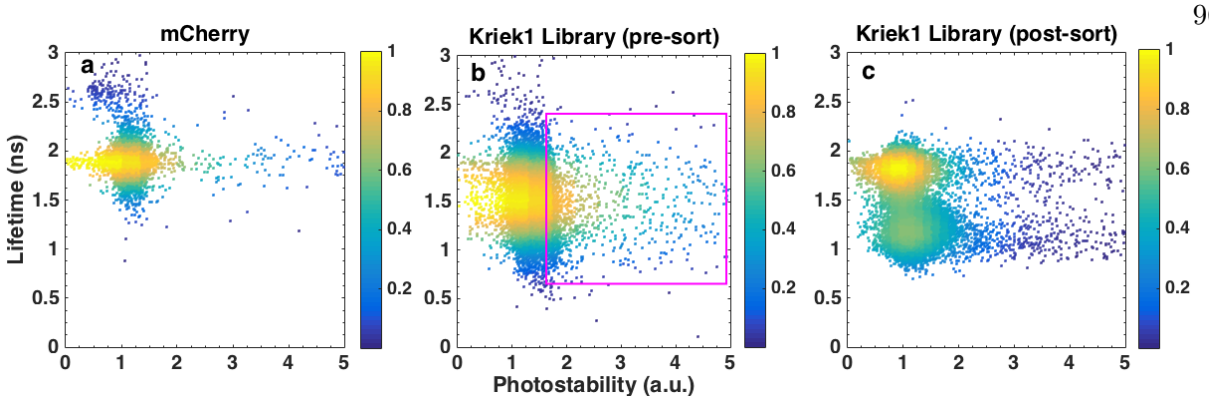

Figure 5.2: Screening results showing the excited state lifetime and photo-stability of mCherry (a), Kriek1 library before (b) and after (c) the microfluidic sorting. ~15,000 cells were screened for each panel. Kriek1 library displayed some mutants with higher photostability (population in the pink box; b) those were further enriched by the microfluidic sorter.

5.2.2 Targeted Mutagenesis: Kriek2 Library

After the first round of targeted mutagenesis and subsequent enrichment of the photostability, we produced a population of lower photobleaching tendency (Figure 5.2c). Unfortunately, the excited state lifetime of these mutants was significantly shorter than the parent mCherry, and therefore we suspected they would be of lower quantum yield. To improve the lifetime of those populations, we targeted the I197 residue, whose side-chain is reported to be capable of a π-π stacking interaction with the chromophore [109]. For example, in mRojoA, sandwiching the chromophore between two aromatic residues at 197 and 63, along with a few other mutations, resulted in a 3-fold improvement of quantum yield over mCherry and a 22 nm red-shift of the emission spectrum [103, 92]. Mutation at this position in GFP also red-shifted its spectra to produce YFP [109]. Hence, we speculated that introducing a stacking interaction with the residue at 197 might rigidify the chromophore and thereby reduce rate of non-radiative processes. Also, it was reported that mutations at position 70 are correlated with those at 197 (*i.e.* K70 "co-evolved" 197) [99]. We therefore chose I197 and K70 as target residues for 2nd round of mutagenesis. Additional residues targeted in this phase of library generation were suggested by the MD simulations of mCherry by Regmi *et al.* [167] who explored the oxygen diffusion pathways into the β-barrel and identified F99, Y173, A175 as 'gateway' residues. We hypothesized that rigidifying the barrel by

Table 5.2: Targeted Mutagenesis in mCherry: Kriek2 Library

Residues	Amino acids targeted	Rationale
F99	All 20	gatekeeper
Y173	All 20	surrounding gatekeeper
A175	All 20	surrounding gatekeeper
I197	All 20	stacking residue
K70	K/R	co-evolved with stacking residue

reducing the motions of these dynamic residues would have a beneficial effect on the fluorescence quantum yield.

Table 5.2 summarizes the positions targeted in this round of library generation. The total size of this library, which was named Kriek2, is $20 \times 20 \times 20 \times 20 \times 2 \sim 320,000$ members. Figure 5.3 shows the results of screening Kriek2. We observed mutants with increased lifetime (population in the pink box), whose population we enriched with the microfluidic sorter.

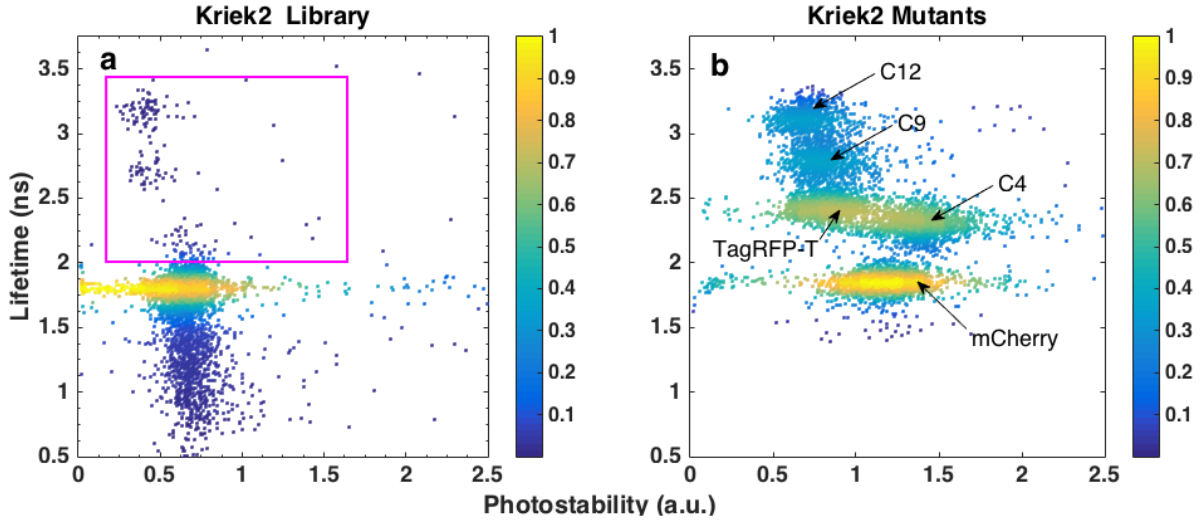

Figure 5.3: (a) Microfluidic screening results of Kriek2 library. In this library, we observed some clusters with higher excited state lifetime (population in the pink box) which were selected to identify Kriek2 mutants: C4, C9, C12 *etc.* (b) Screening results demonstrating the lifetime and photostability of a mixture containing mCherry, TagRFP-T, C4, C9 and C12 at 6 kW/cm^2. All of the mutants displayed improved lifetime relative to mCherry. The C4 mutant showed higher photostability and longer lifetime than mCherry.

5.3 Selection of Mutants after 2nd Round of Mutagenesis

To isolate the mutants with higher lifetime, we grew our lifetime-enriched library on galactose-containing (for inducing expression in yeast) plates. Resulting yeast colonies were fluorescent and the lifetime for each colony was measured in a fashion similar to the in-flow phase fluorimetry, as described below. To pick colonies according to their lifetimes, all beams except for the modulated lifetime beam were blocked (see Chapter 4). This excitation beam was focused onto single colonies at a low excitation intensity to avoid saturation of the PMT. The PMT signal was demodulated by the lock-in amplifier (Zurich Instruments, UHF). The resulting in-phase and in-quadrature outputs were digitized and processed to extract fluorescence lifetime values. To verify the performance of this technique, mCherry and TagRFP-T colonies were used as references.

Table 5.3: Sequences and excited state lifetime of the mutants picked from Kriek2 library. mCherry had lifetime of 1.9 ns as measured by phase fluorometry.

Clone	LT (ns)	V16	H17	K70	F99	W143	I161	Q163	Y173	A175	I197
C4	2.5	T	R	R	S		M	M		W	R
C9	3.0	A	R						L	T	R
C11	2.4	A	R		L	L	V	L		S	H
C12	3.4										R
C15	2.6	T	R	R	S		M	L		W	R
K2C	~ 1					I	M	V			

We picked 16 colonies from the sorted Kriek2 library, and DNA sequencing showed that only 5 of them were genetically distinct clones. Table 5.3 displays the sequence differences among the mutants, which were named C4, C9, C12, C11 and C15. It was found that mutations at position 16 were linked to a H17R (pointing outwards of β-barrel) mutation. This was not an intentional part of the Kriek2 library and was due to an error in the primer design. Clones C4 and C15 only differed by a single mutation at 163 (M/L). Figure 5.3b shows the lifetime and photostability screening results of the mutants measured individually, together with mCherry and TagRFP-T, plotted all together in one dot plot. The C4 mutant showed improved excited state lifetime and photostability. It was found to have a Kriek-like I161M mutation [57]. The C9 and C12 clones had

significantly longer lifetime than mCherry but lower photostability. It is interesting to note that C12 is only a single mutation (I197R) away from mCherry but has an 82% improvement in lifetime (1.87 ns *vs.* 3.4 ns). The L173 residue found in C9 also appeared in mRuby2 [165], TagRFP-T [11], FusionRed [54], mKate, Katuschka, mNeptune, mCardinal [154] and eqFP578. An R70 residue is found in TagRFP-T, mRuby2 and FusionRed.

5.4 Evolution of C4 mutant

The C4 mutant was promising as it showed improved excited state lifetime and photostability in the microfluidic screening (Figure 5.3b). However, as Figure 5.4a demonstrates, this clone was dimmer (lower Ch0Max) than the parent mCherry. This dimness may be due to its lower extinction coefficient (ϵ) or slower chromophore maturation in the cellular environment. Owing to the lack of a mechanistic understanding of the residues involved in chromophore maturation or EC enhancement, we opted for multiple rounds of random (*i.e.* "error-prone" PCR) mutagenesis to increase the brightness of the C4 mutant.

Figure 5.4 shows the evolution of the lifetime and brightness of the C4 libraries tracked for each round of FACS and error-prone PCR mutagenesis. The initial error-prone PCR library generated from C4 (called EPC4) contained few mutants with higher brightness (Figure 5.4b). Two and three rounds of FACS-based selection and subsequent random mutagenesis on EPC4 resulted in EPC4-FACS-R2 and EPC4-FACS-R3 respectively, which are brighter than the initial C4 clone (Figure 5.4c).

Multiple mutants were selected from EPC4-FACS-R2 and EPC4-FACS-R3. Figure 5 shows the lifetime *vs.* brightness dotplots of these two libraries. The major population in these libraries had slightly higher photostability and lifetime $\sim$ 2.3 ns. However, there was also a minor population with a lifetime with $\sim$ 3 ns. Individual mutants were isolated from these two libraries by picking colonies on plates according to their fluorescence lifetimes, as described in the previous section. The subpopulations selected with $\sim$ 2.3 ns and $\sim$ 3 ns lifetimes were named C4PB and C4LT

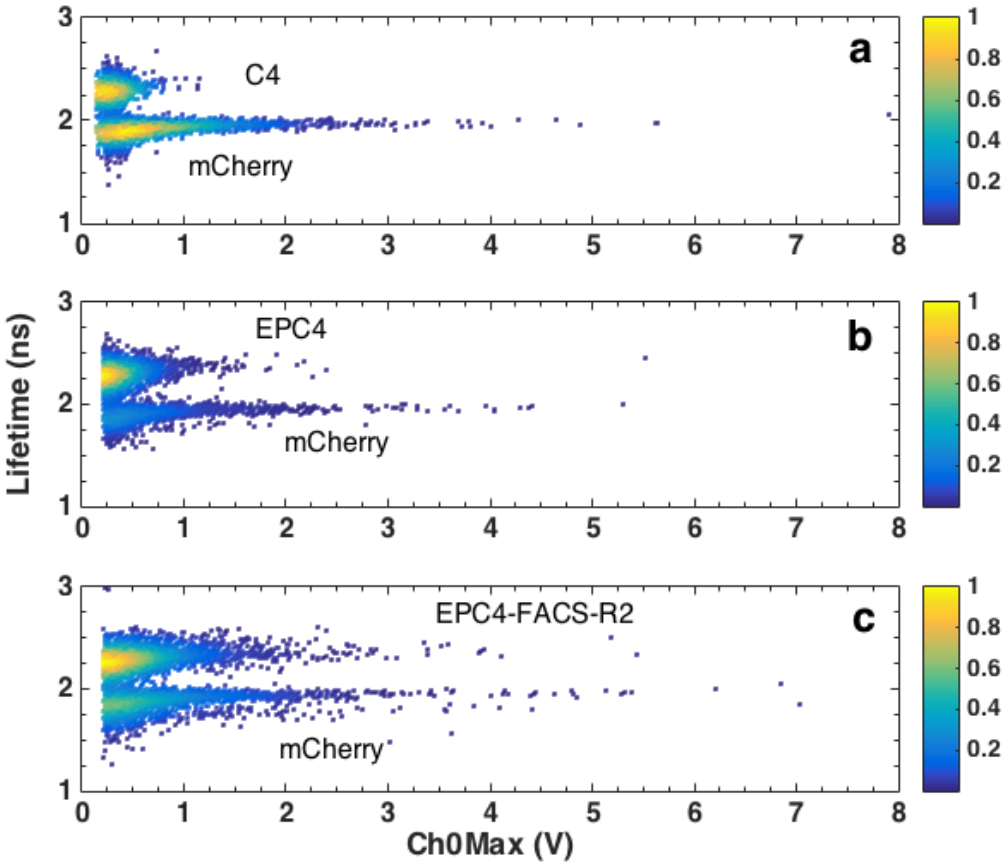

Figure 5.4: **Evolution of C4 mutant**: (a) Although C4 mutant displayed higher excited state lifetime and photostability, the brightness (Ch0Max) was lower than the parent mCherry. (b, c) Three rounds of error-prone mutagenesis and subsequent FACS-based selection were carried out to enhance the brightness of C4 mutant.

respectively. The "C4" indicates their parental origin. The "PB" and "LT" stands for Photo-Bleaching and LifeTime, respectively.

The photo-physical properties of the individual C4PB and C4LT clones expressed in yeast were characterized by screening in the microfluidic and by FACS. The results revealed that although the lifetimes of all the C4PB mutants were similar, the following mutants showed improved brightness relative to mCherry: C4PB-3, 5, 6 and 12. Sequence analyses of all the C4PB mutants showed the presence of K166R mutation indicating its involvement in improving the brightness of the mutants. C4LT-2 and 6 showed improved brightness and photostability respectively.

Figure 5.6 shows microfluidic screening results for C4PB-12 along with mCherry [12], Fu-

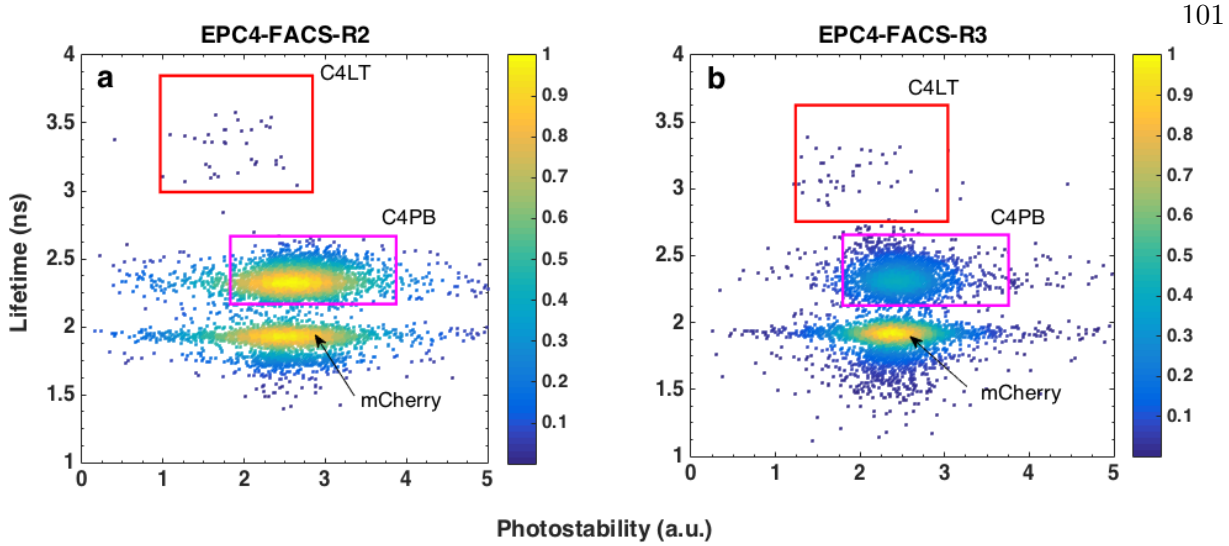

Figure 5.5: **C4PB and C4LT mutants**: Microfluidic screening results displaying lifetime and photostability profiles of 2nd (EPC4-FACS-R2) (a) and 3rd round (EPC4-FACS-R3) (b) of FACS-enriched error-prone C4 libraries. C4PB mutants were selected randomly from EPC4-FACS-R2 and EPC4-FACS-R3 libraries. C4LT was selected from the small populations in those libraries having longer excited state lifetime.

sionRed [54], mRuby2 [165] and TagRFP-T [11] expressed in yeast at different illumination intensities. At lower intensity (2.5 kW/cm2), all the RFPs show similar photostability. However, at higher intensities (5-10 kW/cm^2), C4PB-12 displays significant increase in photostability. From these results, we hypothesize that C4PB-12 would perform better in confocal imaging conditions where higher irradiances are employed.

The C4PB mutants were expressed in *E. coli* and purified and detailed *in-vitro* and *in-vivo* characterizations were carried out. Table 5.4 displays their photo-physical properties. All the in-vitro measurements were performed using PBS 10x (pH=7.4 buffer). Lifetime measurements were performed in a TCSPC set-up (Pico-quant) and the fluorescence traces were fitted with a bi-exponential function. For measurement of the quantum yield, Cresyl Violet (ϕ=0.54 in methanol) was used as a reference. Extinction coefficients of the purified proteins were measured using alkali denaturation protocol described in reference [12]. Quantification of *in-vivo* brightness in yeast was performed in a FACS set-up using 561-nm laser excitation. Photostability measurements were carried out with 532 nm laser excitation in the DSC/GSR set-up described in Chapter 2. Detailed

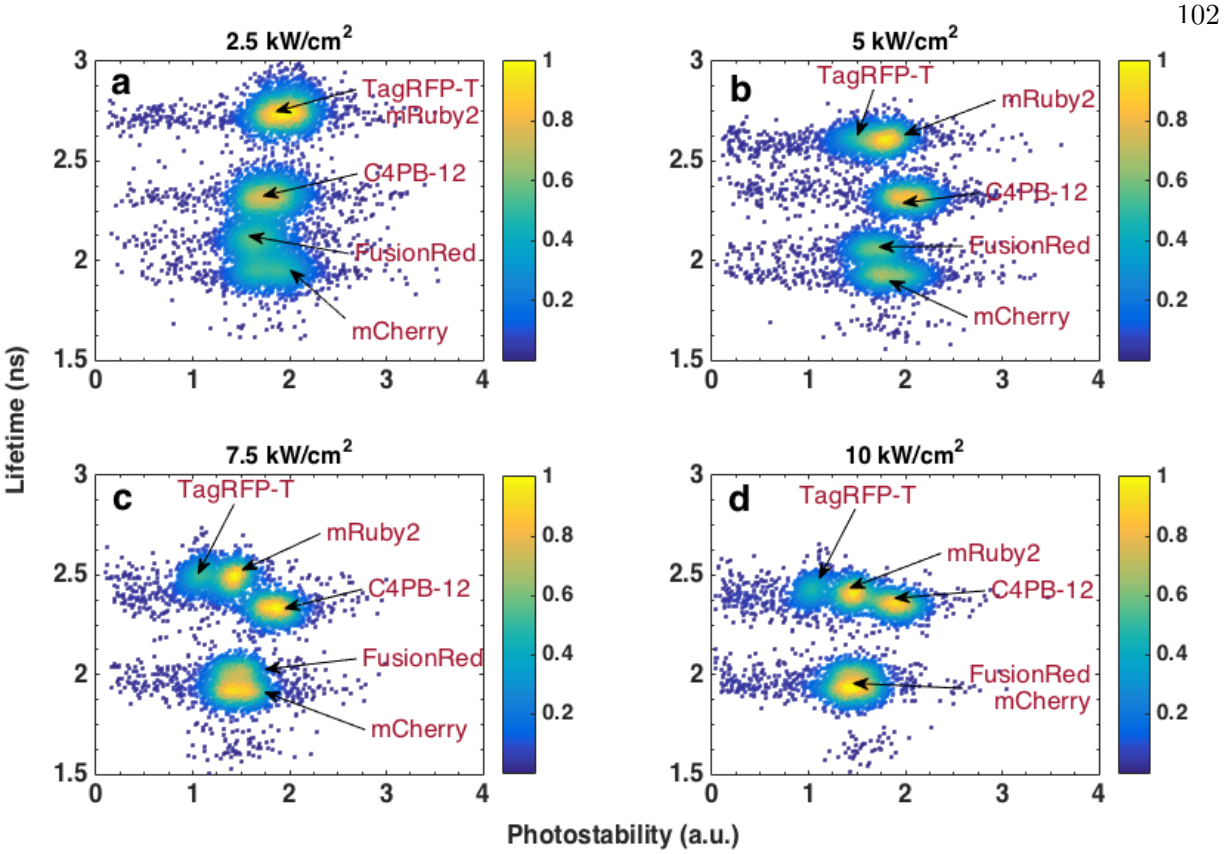

Figure 5.6: The lifetime and photostability profiles of yeast cells expressing mCherry, FusionRed, mRuby2, TagRFP-T and C4PB-12 at (a) 2.5 kW/cm^2 (b) 5 kW/cm^2 (c) 7.5 kW/cm^2 and (d) 10 kW/cm^2 illumination intensities. All the RFP mutants tend to show similar photostability at 2.5 kW/cm^2 (a) but at higher illumination intensities, C4PB-12 performs significantly better photostability than rest of the RFPs. With increasing illumination intensities, lifetime of the mutants tends to be lower due to ground state depletion as described in the reference [55].

procedures for the in-vitro characterization of the RFPs are presented in the Appendix.

As Table 5.4 shows, all the C4PB mutants were blue-shifted in absorption and emission compared to mCherry. The excited state lifetimes of all the mutants were longer than that of the parent mCherry. This was expected as the mutants were selected for higher lifetime. However, it is interesting to note, even after significant improvement in lifetime, the enhancement of the quantum yield was only marginal for C4-derived mutants. For instance, C4PB-12 had 29 % (2.22 ns *vs.* 1.72 ns) increase in lifetime relative to mCherry but only 8 % (0.27 *vs.* 0.25) improvement in ϕ. We found that this apparent discrepancy was due to the reduction of radiative rate constants for the C4PB mutants as discussed below.

Table 5.4: Photo-physical properties of the C4PB, SDC and SLT mutants.

Mutants	λ_{abs} (nm)	λ_{ems} (nm)	τ (ns)	ϕ	ϵ_{max} (M^{-1} cm^{-1})	Brightness ($\epsilon_{max} * \phi$)	Brightness (in yeast)	Photostability (in yeast)
mCherry	587	610	1.7	0.25	74,000	100	100	100
mScarlet	569	594	3.9	0.70	96,000	402	-	-
C4PB-12	572	608	2.2	0.27	55,000	80	135	103
C4PB-6	573	606	2.3	0.27	57,000	83	117	89
C4PB-5	572	604	-	-	64,000	-	105	88
C4PB-3	573	604	2.2	0.22	61,000	76	79	86
SDC-1	570	599	3.6	0.55	-	-	-	-
SDC-5	560	592	3.6	0.50	-	-	-	-
SLT-1	562	592	3.8	0.68	-	-	-	-
SLT-11	559	588	3.8	0.71	56,000	238	-	-

The radiative rate constant (k_r) of a fluorophore can be obtained from the following equation:

$$k_r = \frac{\phi}{\tau} \tag{5.1}$$

where, ϕ and τ are fluorescence quantum yield and the excited state lifetime of the fluorophore. Using the observed ϕ and τ of C4PB-12, we found that it had 17% reduction in radiative rate constant compared to mCherry. To investigate further the origin of this decrease in k_r, we computed the contributions of the emission spectra and the extinction coefficient to the radiative rate constant using the Strickler-Berg equation [168]:

$$A_{21} = k_r = \frac{8 \times 2303\pi n^2}{c^2} < \nu_f^{-3} >^{-1} \int \epsilon_\nu d ln \nu \tag{5.2}$$

where, c, n, ν and ϵ_ν are speed of light, refractive index of media, frequency and extinction coefficient at the frequency ν. ν. $< \nu_f^{-3} >$ is given by:

$$< \nu_f^{-3} > = \frac{\int \nu^{-3} I(\nu) d\nu}{\int I(\nu) d\nu} \tag{5.3}$$

where, $I(\nu)$ is the fluorescence intensity spectrum.

Our analysis of the different components of the Strickler-Berg equation (Eqn. 5.2) showed that although the contribution due to the emission spectra ($< \nu_f^{-3} >$) was similar for mCherry and C4PB-12, there was 16% decrease in the EC component ($\int \epsilon_\nu dln\nu$) of the C4PB-12. This accounted for the 17% decrease in radiative rate of this mutant. Therefore, it can be concluded that the decrease in ϵ reduced the radiative rate of the mutants which eventually resulted in a decreased ϕ.

The decrease in ϵ_{max} of the C4PB mutants resulted in a reduction of the molecular brightness which is quantified as the product of ϵ_{max} and ϕ. The slight increase in brightness measured *in-vivo* was due to 561-nm laser excitation in the FACS screening that resulted in more effective absorption of the light by the C4PB mutants compared to mCherry due to the hypsochromic shift of their absorption spectra.

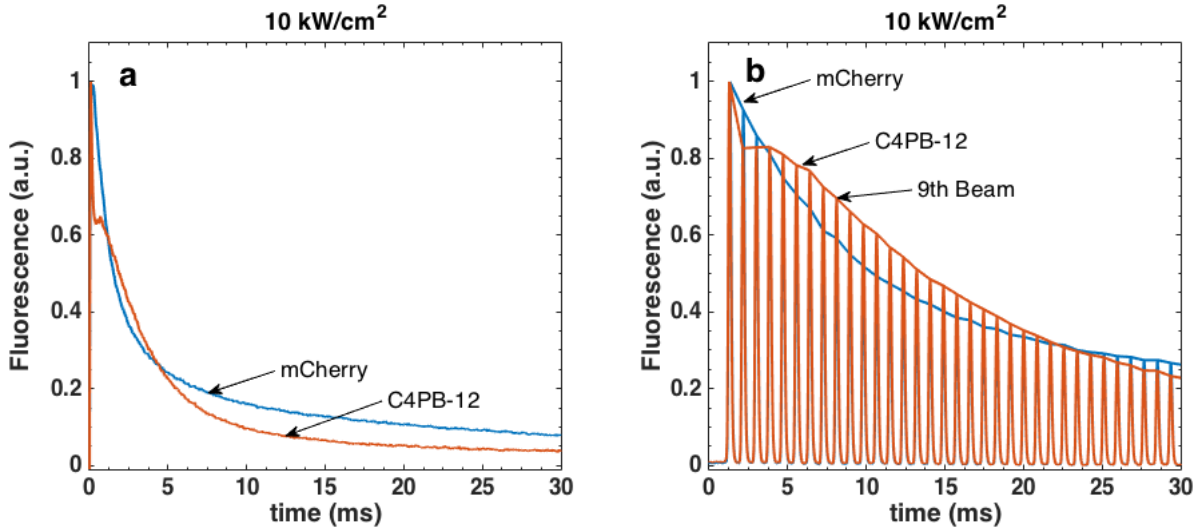

Figure 5.7: **Photobleaching decays of mCherry and C4PB-12**: (a) Normalized photobleaching decays of mCherry and C4PB-12 upon continuous illumination from a 532-nm laser at 10 kW/cm^2. C4PB-12 displayed faster photobleaching compared to mCherry. (b) Fluorescence decays of mCherry and C4PB-12 when excited with pulsed-laser beams with Gaussian profile (0.20 ms FWHM, 0.65 ms inter-pulse delay) similar to as experienced by the cells in the microfluidic.

In-vivo photostability of the mutants in yeast cells was measured by continuous 532-nm laser irradiation. The area-under the fluorescence curve was then computed from the normalized fluorescence decay of the mutants to quantify the photobleaching. Figure 5.7a showed the fluores-

cence traces of mCherry and C4PB-12 at 10 kW/cm^2 532-nm illumination. Although the mutants showed improved photostability in the microfluidic screening, we found that the photostabilities of the C4PB mutants were similar to or lower than that of mCherry. To investigate the discrepancy between the photostability measured in microfluidic *vs.* off-chip, we excited the mutants with similar illumination pattern as the mutants experienced in the microfluidic. The yeast cells expressing the mutants were excited with Gaussian pulses having 0.2 ms FWHM and 0.65 ms inter-pulse delays with 10 kW/cm^2 peak intensity. The resulting normalized fluorescence traces for mCherry and C4PB-12 are shown in Figure 5.7b. It clearly showed that C4PB-12 mutants bleached slower than mCherry only in the 4-20 ms time-window. This was within the interrogation time-regime in the microfluidic for measuring the photostability of the mutants by the ratio of the fluorescence signals from 9th beam and the first beam. It appeared that the improved photostability of the C4PB mutants in the microfluidic was due to their unique fluorescence decay behavior upon high-intensity pulsed illuminations. Presumably, at high illumination intensity, a significant portion of the C4PB mutants is trapped in photo-protective dark states reducing the photobleaching only in 4-20 ms time window. DSC measurements of the C4PB mutants indeed revealed a higher percentage of DSC compared to mCherry (23% in mCherry *vs.* 64% in C4PB-12; Figure 5.8a and b). The C4LT mutants were also found to have a high propensity for DSC and poor off-chip photostability (Figure 5.8c and d).

As the mutants derived from C4 did not show significant improvement in brightness or photostability, we focused attention on C9 and C12 mutants, aiming to enhance their brightness.

5.5 Evolution of C9 and C12 Mutants

The C9 and C12 mutants were found to have longer lifetimes than mCherry or C4 mutants. However, their brightnesses were lower than that of mCherry. In order to restore the brightness while maintaining their increased lifetimes, at first, we performed random mutagenesis. However, the random mutagenesis on C9 and C12 did not produce any bright mutants. Hence, we performed

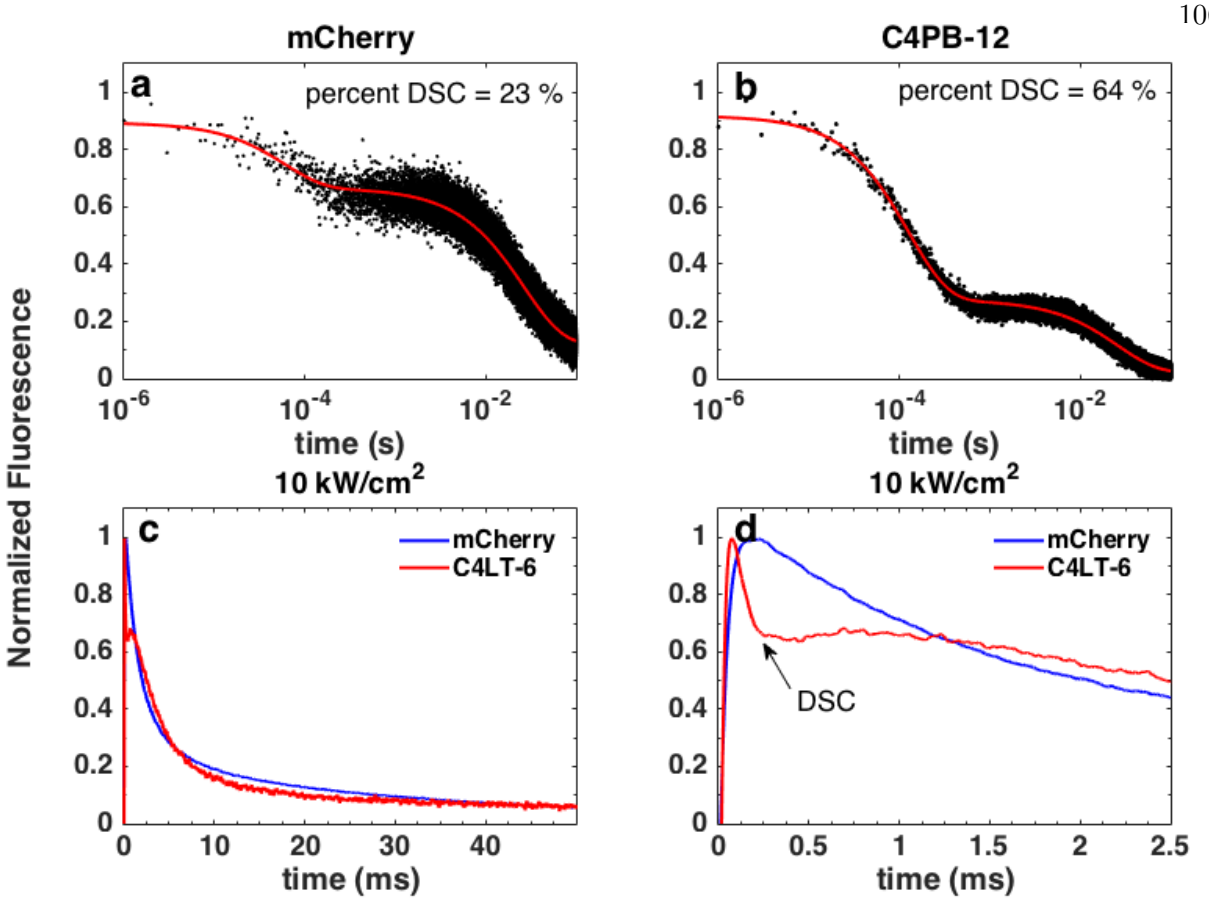

Figure 5.8: Fluorescence traces (black dots) of mCherry (a) and C4PB-12 (b) displaying high percent dark state conversion (DSC) of C4PB-12 compared to mCherry. The fluorescence traces were fitted with three exponential functions (red lines) and DSC time-constants and percent DSC were extracted as described in reference [56] and Chapter 3. Percent DSC of mCherry and C4PB-12 were found to be 23% and 64% respectively. DCS time-constants of mCherry and C4PB-12 were 59 μs and 138 μs respectively. Yeast cells expressing the RFPs were irradiated with 561-nm laser at $\sim$ 5 kW/cm^2 to obtain the fluorescence traces. (c) Fluorescence decays showing similar photostability of mCherry and C4LT-6 when expressed in yeast and excited with 532-nm laser at 10 kW/cm^2. (d) C4LT-6 displayed rapid drop of fluorescence upon 532-nm laser irradiation indicating higher DSC compared to mCherry.

targeted mutagenesis on those mutants. We specifically targeted W143, I161 and Q163 (Figure 5.9a) positions because of their sequence diversity in mFruit series of FPs [12].

Figure 5.9 b, c and d showed the lifetime, brightness and photostability profiles of C9, C12 and site-directed library of C12 generated by full saturation mutagenesis at the above-mentioned residues. Both the site-directed C9 and C12 libraries contained mutants with high lifetime and brightness. With the microfluidic platform, we sorted the mutants to enhance the populations with

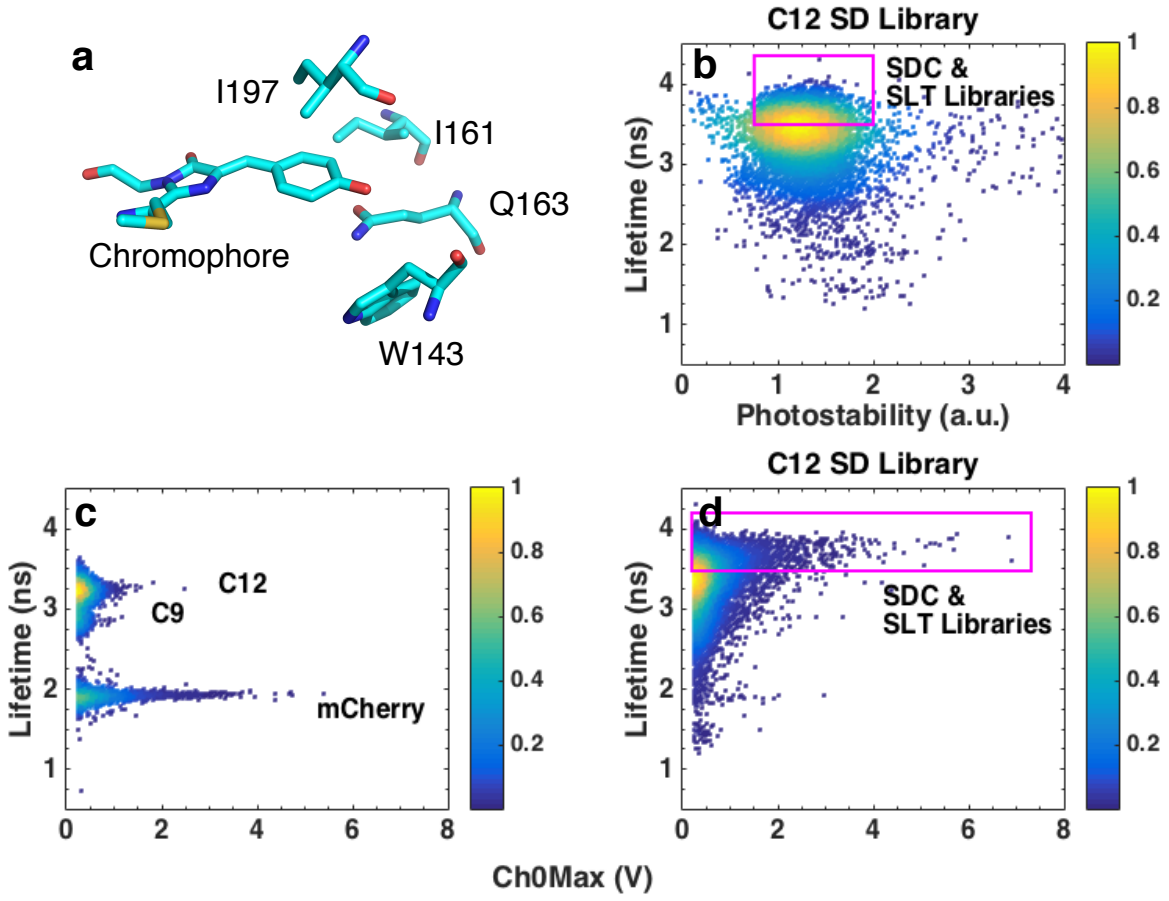

Figure 5.9: **Evolution of C9 and C12 mutants**: (a) Site-directed libraries were generated targeting W143, I161 and Q163 positions of C9 and C12. (b, c, d) Lifetime, Ch0Max (brightness) and photostability profiles of the resulting C12 SD (site-directed) library along with mCherry, C9 and C12 mutants. The mutants with higher lifetimes (population in the pink box) were enriched in the microfluidic sorter to generate SDC and SLT libraries. Subsequent selection from SDC and SLT libraries produced SDC and SLT mutants respectively.

lifetime higher than $\sim$ 3.5 ns. This library was called Site-Directed C9 and C12 library or simply SDC. We selected a few mutants from this library and called them SDC mutants. Two further error-prone mutagenesis and subsequent selection for higher lifetime mutants (with selection gate, lifetime$>$ 3.7 ns) were carried out to generate the SLT library. Mutants selected from the SLT library were called SLT mutants.

Table 5.5 shows the mutations in the SDC and SLT mutants and the microfluidic screening results. All of the mutants had I197R which indicated that C12 (mCherry I197R) mutant was the precursor of the SDC and SLT mutants. As expected, the SLT mutants were found to have

Table 5.5: Mutations and the screening results of the SDC and SLT mutants. Lifetime and brightnesses (in yeast) of the mutants were obtained from the screening in the microfluidic. The brightness was quantified as the average of Ch0Max signals from different mutants.

Mutants	143	161	163	197	Error-prone mutations	τ (ns)	Brightness (in yeast)
mCherry	W	I	Q	I		1.87	100
SDC-1	M	V	L	R		3.58	115
SDC-5	L	T	C	R		3.57	145
SLT-1	L	V	I	R	E10G	3.68	82
SLT-11a	S	V	Y	R	N98S, R125H, F129L, Q137L	3.74	83

slightly longer lifetimes than SDC mutants, and contained few mutations that appeared during the error-prone mutagenesis. The brightnesses of those mutants was quantified as the average of lifetime-PMT signal (Ch0Max, see Chapter 4) obtained from the microfluidic screening and normalized with the Ch0Max for mCherry. SDC-5 was the brightest mutant while SLT-11a had the longest lifetime.

All the SDC and SLT mutants were expressed and purified for detailed in-vitro photo-physical investigation. However, attempts to purify SLT-11a failed in *E. coli* even after prolonged incubation at 28C. As SLT-11a did not show higher brightness even with its long lifetime, we performed further mutagenesis to enhance its brightness. The N98S, F129L, Q137L mutations were sequentially reverted back to the mCherry-like residues with the QuickChange protocol discussed in the Appendix. It was observed that a combination of S98N and L129F was necessary for the successful expression of SLT-11a mutant in *E. coli* leading to its purification. Position 125 was fully saturated and mutants were selected with improved red fluorescence upon expression on galactose-containing plates. This led to the generation of the SLT-11 mutant with the following mutations relative to mCherry: W143S, I161V, Q163Y, I197R and H125K.

Figure 5.10 displays the absorption spectra of the SDC and SLT mutants. Similar to C4PB mutants, these mutants also showed blue-shifted spectra relative to mCherry. Along with RFP absorption peak around $\sim$ 560 nm, SDC-1, SDC-5 and SLT-1 mutants were also found to have an additional peak at $\sim$ 490 nm (green peak). This extra absorption peak indicates the chromophore

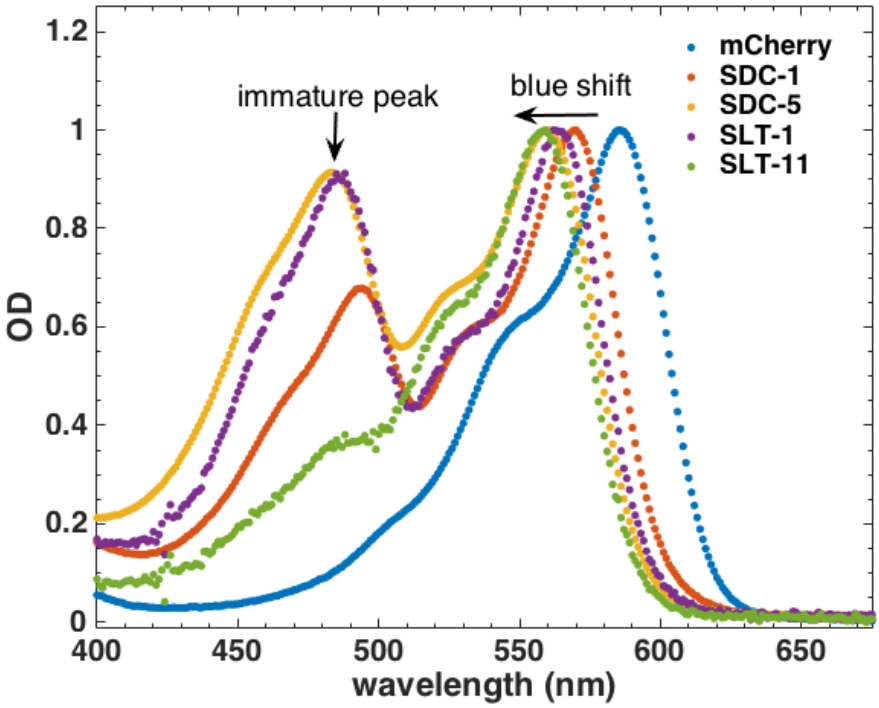

Figure 5.10: Absorption spectra revealed that all the mutants were blue-shifted relative to mCherry. SDC-1, SDC-5 and SLT-1 were characterized with green peak with maxima at $\sim$ 490 nm which corresponds to GFP-like immature chromophores. SLT-11 had negligible amounts of immature peak indicating a complete maturation in that mutant.

maturation process in these mutants was not complete and that some fraction of the population forms a GFP-like chromophore. This is a serious drawback for these mutants as the immature peak restricts their use in multi-color fluorescence imaging with multiple green and red fluorescent proteins. Attempts were made to assist complete maturation by introducing new mutations but without any success (described later). On the other hand, absorption spectra of SLT-11 showed no 'green peak' with a small shoulder at $\sim$ 490 nm.

Table 5.4 displays the photo-physical measurements of the SDC and SLT-1 mutants measured in purified proteins. All the mutants showed significant improvement in their quantum yield. Fluorescence quantum yield of SLT-11 was very high (71%) and similar to mScarlet (ϕ, 70%). Due to the presence of immature peak in the absorption spectra of SDC-1, 5 and SLT-1, measurement of ϵ was not possible in those mutants. ϵ_{max} of SLT-11 was measured as 56,000 $M^{-1}cm^{-1}$ which was significantly lower than that of mCherry (76,000 $M^{-1}cm^{-1}$).

The *in-vitro* brightness ($\epsilon_{max} * \phi$) of mCherry, mScarlet and SLT-11 are presented in Table 5.4. The brightness of SLT-11 was higher than mCherry due to its high quantum yield but it was lower than mScarlet because of its lower extinction coefficient. mCherry, mScarlet, SLT-11 were also expressed in nuclear-localized mammalian cells (HeLa) and the *in-vivo* brightness was measured through FACS screening. The screening results were also in qualitative agreement with the *in-vitro* brightness measurements: STL-11 displayed higher brightness than mCherry but the brightness was lower than mScarlet.

5.6 Discussion

Engineering of mCherry with brightness and photostability as selection pressures resulted in a large number of mutants with interesting photo-physical properties. In order to achieve the brighter mutants from C4 and C12 mutants, 532-nm and 561-nm laser were used for the excitations. As a result, all spectra of the resulting mutants were blue-shifted. For instance, the C12 mutant was characterized with hypsochromic shift compared to mCherry (572 nm *vs.* 587 nm). Further selection based on brightness with 561-nm laser excitation resulted in brighter SDC-5 and SLT-1 mutants with 560 and 559 nm absorption peak respectively. These absorptions are very close to 561 nm and excited very efficiently at this laser line thus resulting in bright fluorescence.

The improvement in lifetime of the C4PB mutants did not ensure the enhancement of quantum yield. As our analysis results showed, this is due to the reduction in the radiative rate constants of these mutants. Further analysis of radiative rate constants with the Strickler-Berg equation (Eqn. 5.2) suggested that reduction in extinction coefficient of those mutants was responsible for their lower radiative rate constants. While this result proves that enhancement of excited state lifetime does not always ensure the increase in ϕ, it indicates that the radiative rate constants of the FPs can also be modified through mutations. These findings created the bedrock of our next library generation for engineering the radiative rate constants of the RFPs as discussed in Chapter 7.

In the microfluidic screening, C4PB mutants showed lower photobleaching tendency relative

to mCherry. Intensity-dependent screening results (Figure 5.6) demonstrated that C4PB-12 had higher photostability than mCherry, FusionRed, mRuby2 and TagRFP-T, particularly at higher illumination intensities. However, C4PB-12 photobleached faster in wide-field and confocal imaging conditions. We speculated that this discrepancy was due to the enhanced dark state conversion of the C4PB mutants and the presence of photo-protective dark states. This outcome indicated that photostability screening of the mutants should be performed employing exact imaging conditions for consistency of chip and off-chip photobleaching measurements. For instance, LED-based screening with illuminating the entire path of the cells through microfluidic channel at low irradiation intensity can be implemented to generate mutants with higher photostability under wide-field illumination conditions. Complex photobleaching kinetics of the mutants indicates that screening based on the rate or quantum yield of the photobleaching could be more effective than the simple ratio-metric measurement of photobleaching to isolate mutants with improved photostability. In our future work, we intend to implement these advanced screening techniques for the directed evolution of the photostability of the mutants.

A fraction of the SDC and SLT mutants showed a 'green peak' at $\sim$ 490 nm indicating incomplete maturation of the chromophore. This peak suggests that amino acid residues at 143, 161 and 163 play significant roles in the formation of a functional RFP chromophore. Indeed, M163Q mutation eliminated the green peak (at $\sim$ 510 nm) observed in RFP1.4 and other DsRed mutants [12]. mRojoB, a RFP derived from mCherry, showed similar green peak at $\sim$ 500 nm which contained Q163M mutation [92]. As the 163 position is also responsible for high quantum yield and the residues at this position were selected through multiple round of sorting, we did not saturate this position to attain complete maturation of the mutants. Instead we searched for alternative pathways to assist the maturation in our SDC/SLT mutants. The mutational analysis of mRojoA, mRojoB and mRouge indicated that residues at 177, 195 and 217 positions could also improve maturation of the chromophore. However, library generation with saturation mutagenesis at these residues failed to eliminate the 'green peak' observed in SDC/SLT mutants. Generating multiple single mutants by replacing residues at 161 with non-polar residues (Ala, Ile, Leu) reduced

the 'green peak' but at the cost of lower brightness and shorter lifetime of the mutants.

The unsuccessful attempts to eliminate the green peak in SDC-1, SDC-5 and SLT-1 indicated that it might be a dead-end for the evolution of these mutants. We therefore focused on SLT-11 which had excellent quantum yield and complete chromophore maturation. However, the brightness of this mutant was compromised due to lower extinction coefficient. In our next level of library generation, we attempted to improve the extinction coefficient and radiative rate-constant of this mutant for improved brightness. This effort is discussed in Chapter 7.

5.7 Conclusion

In this Chapter, directed evolution of mCherry was discussed. Employing photostability and excited state lifetime as selection pressures, multiple mCherry mutants were generated with improved photo-physical properties. Although C4PB mutants displayed improved photostability in the microfluidic screening presumably due to their pronounced dark state conversion, the mutants showed faster photobleaching compared to mCherry in the confocal and wide-field imaging platforms. The C4PB mutants were characterized with reduced radiative rate constants. Consequently, the improvement in their excited state lifetime resulted in only marginal increase of quantum yield. On the other hand, mutants derived from C9 and C12 displayed higher fluorescence quantum yield and brightness relative to mCherry. Few SDC and SLT mutants were characterized with in-complete chromophore formations resulting in immature peaks in their absorption spectra. The SLT-11 mutant, owing to its higher quantum yield (71%) and complete chromophore maturation, was selected as a template for the next round of library generation to achieve further improvement in its brightness.

Chapter 6

Engineering of Excited State Lifetime in FusionRed for Improved *in-vivo* Brightness

6.1 Introduction

High monomericity and low cytotoxicity upon cellular expression are important properties of fluorescent proteins (FPs) for live-cell imaging. Although some assays those involving cell-type identification, do not require monomeric FPs, monomericity is of utter importance in experiments involving the fusion of FPs in sub-cellular compartments. Absence of dimerization in the FPs is essential for reliable interpretations of the underlying biological phenomena. FRET efficiency between GFP and YFP was found to have artifacts due to the weak dimerization tendencies of the related FPs [169]. Oligomerization of FPs was also reported to cause non-specific protein interaction or reorganization of cell organelle structure [170]. On the other hand, cytotoxicity of the FPs is a drawback for long-term imaging experiments [54]. Significant efforts have been made to generate monomeric variants of RFPs, *e.g.* mRFP1 [13], mCherry [12], TagRFP [99], mKate2 [164] *etc.*, by disrupting the oligomeric interfaces of their natural ancestors. Although these RFPs were successfully employed in a myriad of applications, they were found to perform sub-optimally compared to GFPs [54, 104]. For instance, TagRFP was reported to cause structural reorganization of endoplasmic reticulum (ER) when expressed in a protein located at the cytoplasmic-end of the ER (CytERM) [100] and mCherry was found to be functionally perturbing for *in-vivo* imaging of fission yeast [171].

To address the dimerization and cytotoxicity issues in RFPs, FusionRed was developed [54]. The precursor of FusionRed, mKate2, was characterized as having low cytotoxicity in transgenic *Xenopus laevis* embryos [164]. However, mKate2 displayed monomer-dimer equilibrium in high-pressure liquid chromatography (HPLC) due to some residual dimerization tendency. By targeting the residues involving dimeric interfaces and replacing the hydrophobic C-terminal with a flexible glycine-rich linker, the dimer formation in mKate2 was reduced. These changes were followed by few more mutations to produce FusionRed, which displays better fusion efficiency than mCherry. FusionRed was also characterized with low cytotoxicity, as shown by the degree of optic fissure closure when expressed in the eyes of *Xenopus laevis* embryos. Recently, the photo-switching behavior of FusionRed was employed to obtain super-resolution images [149]. FusionRed was also used to develop a genetically encodable voltage sensor [172] and fluorescent proteins with yellow (535 nm)/orange (565 nm) emission [173].

With its reduced dimerization tendency [101], improved fusion efficiency and low cytotoxicity [54], FusionRed has potential to be an excellent bio-marker for live-cell imaging. However, we found that *in-vivo* brightness is the 'Achilles heel' of FusionRed. Theoretically, the *in-vitro* brightness of FusionRed, which is reported to have a 19% quantum yield (ϕ) and high extinction coefficient (ϵ_{max}= 94,500 $M^{-1}cm^{-1}$) is similar to mCherry (ϕ, 22%; ϵ_{max} =72,000 $M^{-1}cm^{-1}$) [12]. However, we observed decreased brightness of FusionRed compared to mCherry upon expression in mammalian cell-lines (HeLa). Hence, we focused on developing a new version of FusionRed with improved *in-vivo* brightness in particular by improving its low fluorescence quantum yield. As improvement in excited state lifetime (τ) holds promise to improve quantum yield in FPs [155], we opted for improving the lifetime of FusionRed. This Chapter discusses the excited state lifetime engineering of FusionRed to enhance the brightness while retaining its good fusion properties. Figure 6.1 displays the genealogy of the mutants we generated in the course of these studies. FusionRed was first subjected to error-prone mutagenesis. The resulting error-prone library was sorted in the microfluidic system to produce two mutants with longer lifetimes: FR-1, FR-13. The *in-vivo* brightness of FR-13 was increased by multiple rounds of random mutagenesis and subsequent

selection in the microfluidic. This process resulted in the FRX mutants. In a separate evolutionary route, a site-directed mutagenesis library of FusionRed was generated by targeting residues known to have significant effects in the mCherry mutants. Two rounds of FACS and multiple rounds of selection based on lifetime generated FSD-9 and FSD-11 mutants. The photo-physical properties of the FusionRed mutants are also presented in this Chapter.

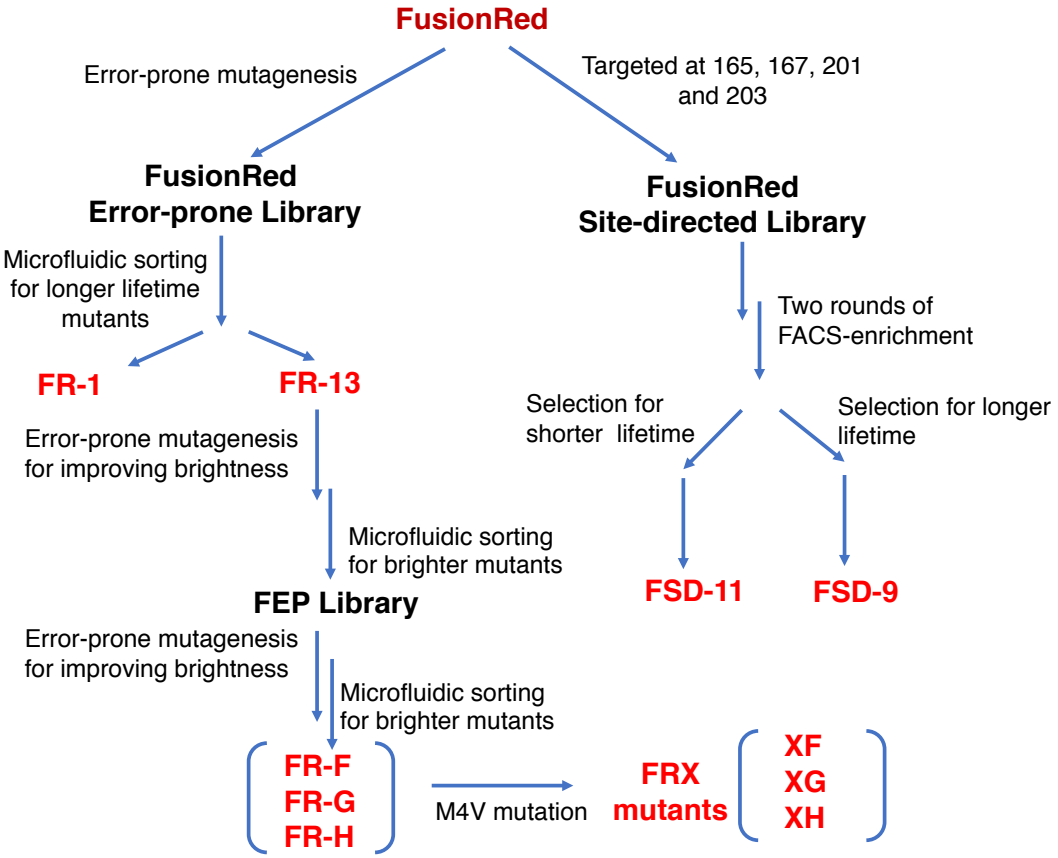

Figure 6.1: Genealogy of the FusionRed mutants.

6.2 Error-prone FusionRed Library

In order to improve the brightness of FusionRed, first we generated a random mutagenesis library (EP-PCR library). Figure 6.2 demonstrates the microfluidic screening results of FusionRed (wild-type) and the EP-PCR library expressed in yeast. The library was found to have a small

population with longer excited state lifetime than FusionRed. Multiple rounds of microfluidic sorting were performed to enrich this population (Figure 6.2b; population in the pink box) with lifetime greater than 2.2 ns. Following the microfluidic enrichment, the library was expressed on galactose-containing plates. Several mutants of FusionRed were selected from these plates, guided by the excited state lifetime of the colonies. The resulting mutants are called FR mutants. Out of several FR mutants, the excited state lifetime of FR-1 and FR-13 were characterized to be 2.48 ns and 2.82 ns (measured in microfluidic screening) respectively, which was significantly higher than the lifetime of FusionRed (τ; 2.05 ns). As the lifetime of FR-13 was longer than FR-1, we chose this mutant as a template for further engineering.

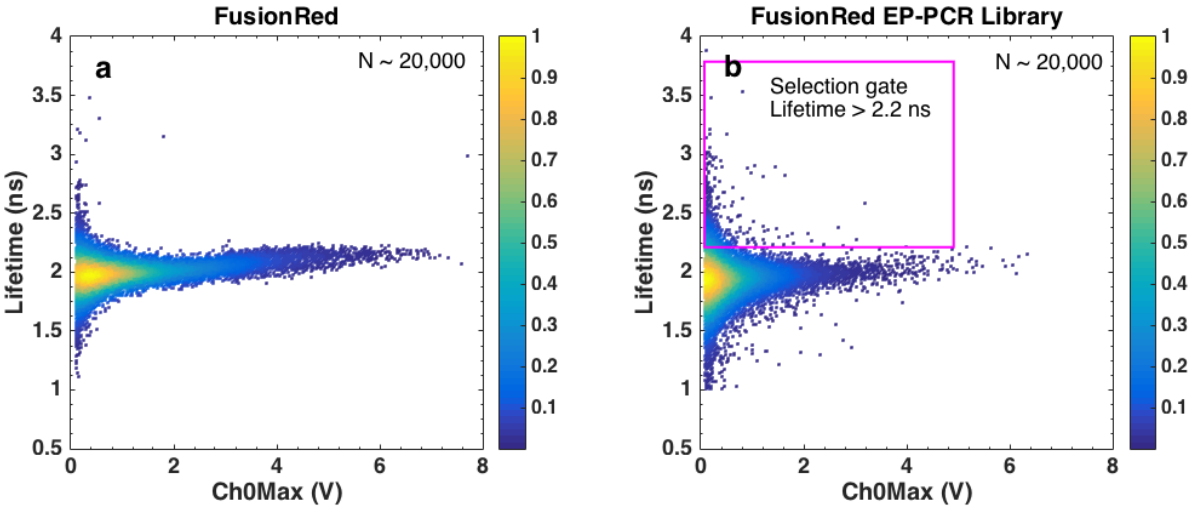

Figure 6.2: Microfluidic screening dotplots displaying lifetime and brightness (Ch0Max) profiles of FusionRed and the FusionRed EP-PCR library generated by random mutagenesis. The library contained a population with longer lifetime (enclosed in the pink box) which was enriched to produce the FR mutants.

6.3 Evolution of FR-13 Mutant: FRX Mutants

With the promising improvement in lifetime, FR-13 was expressed in and purified from *E. coli* and photophysical measurements were carried out. Table 6.1 displays the *in-vitro* photo-physical properties of FR-13 and FusionRed. The brightness calculated from the values of ϵ_{max} and ϕ of

this mutant is $\sim$ 2.6 fold higher than FusionRed wild-type. However, the *in-vivo* brightness of FR-13 measured by microfluidic screening in yeast showed that it was dimmer than FusionRed (Figure 6.3b & c). We speculated that the sub-optimal *in-vivo* brightness of FR-13 might be due to its slow maturation as was observed during its purification in *E. coli*. Both site-directed and random mutagenesis approaches were therefore undertaken to improve the *in-vivo* brightness of this mutant.

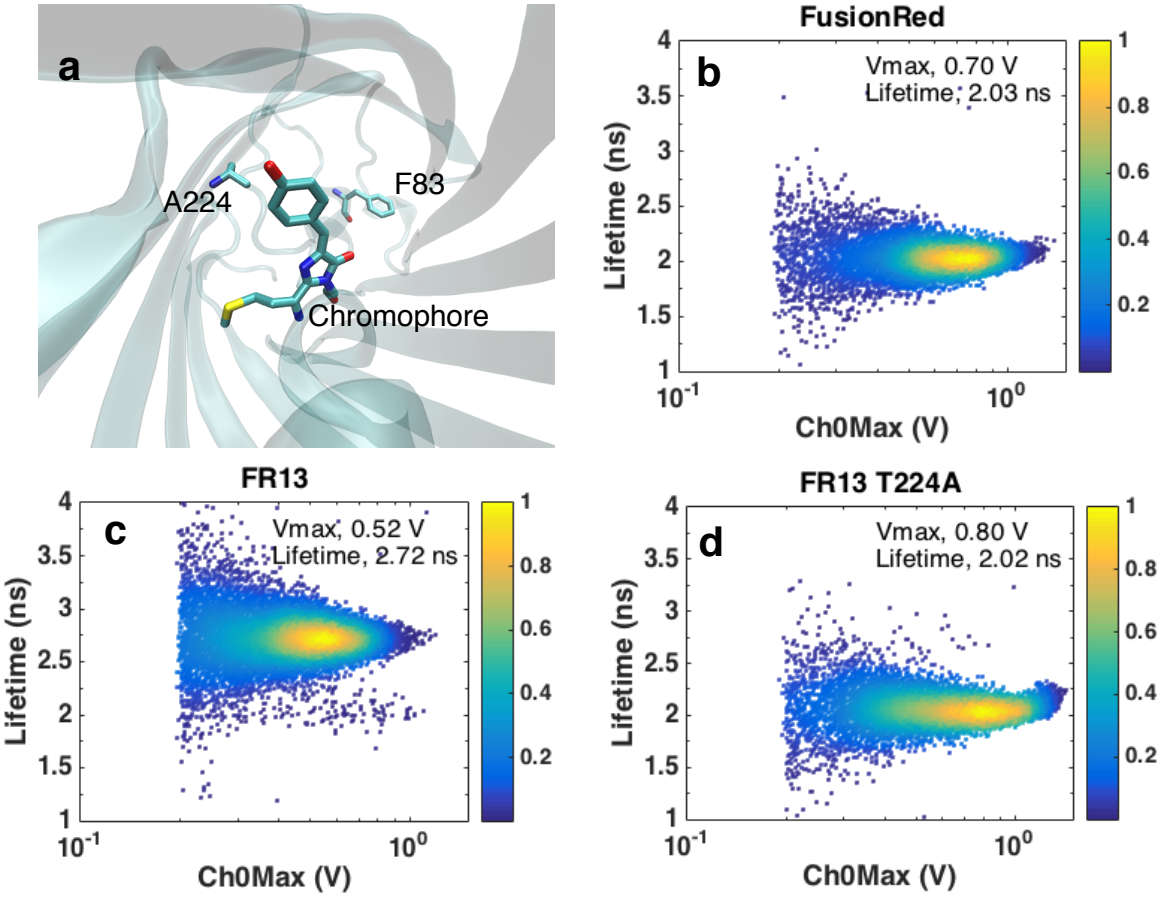

Figure 6.3: (a) FR-13 was found to have the following mutations: H25Y, V47I, F83Y and A224T (avGFP numbering). Position of A224 displayed in the mKate (precursor of FusionRed) crystal structure (3BXB). (b, c, d) Microfluidic screening results displaying lifetime and brightness of FusionRed, FR13 and FR13 T224A mutants. The T224A mutation improved the brightness of FR-13 (Ch0Max 0.53 V $\rightarrow$ 0.80 V) while reducing the lifetime (2.72 ns $\rightarrow$ 2.02 ns).

The DNA sequence of the FR-13 mutant revealed the following mutations relative to FusionRed: H25Y, V47I, F83Y and A224T. The amino acid residues were numbered by aligning the

sequence of the FR mutants with avGFP sequence as done in the original FusionRed article [54]. The sequence alignment is presented in the Appendix G.

Table 6.1: Photophysical properties of the mutants derived from FusionRed.

Mutants	λ_{abs} (nm)	λ_{ems} (nm)	τ (ns)	ϕ	ϵ_{max} $(M^{-1}cm^{-1})$	Brightness $(\epsilon_{max} * \phi)$	pKa
FusionRed	575	596	1.79	0.26	87,300	100	4.5
mCherry	587	611	1.72	0.22	72,000	70	-
FR-13	571	591	2.89	0.48	123,500	262	4.4
FR-F	571	591	2.36	0.36	104,300	167	4.7
FR-G	572	591	2.73	0.42	104,900	192	4.6
FR-H	572	592	2.73	0.42	90,100	165	4.7
FR-1	569	594	2.25	0.34	84,900	127	-
FR L177M	571	594	2.14	0.34	71,100	107	-
FR-1 C165V	569	589	2.55	0.39	91,100	157	-

To improve the brightness of FR-13, we first investigated the roles of each mutation that appeared in the mutant. Of the four mutations observed in FR-13, only position 224 was internal (the residue facing inward of the β-barrel) while others were located either in the α-helix (F83) or facing outward of the barrel (H25 and V47). Four mutants were generated from FR13 by reverting back the mutations to FusionRed-like residues one by one: FR-13 Y25H, FR-13 I47V, FR-13 Y83F and FR-13 T224A. From the microfluidic screening of yeast cells expressing these mutants, we observed that position 224 controlled both lifetime and brightness in FR-13. As it is evident from the Figure 6.3b, c and d, introduction of T224A mutation in FR-13 resulted in improved brightness with reduction of excited state lifetime. From these analyses, we concluded that the longer lifetime and lower brightness of FR-13 originated from the same mutation: A224T.

These photo-physical studies on FR-13 mutants led us to target position 224 with full saturated mutagenesis, in the hope of finding FR-13 mutants with similar or higher lifetime and improved brightness. However, the site-directed libraries generated by targeting only A224 or in combination with H25, V47 and F83 did not produce variants with higher brightness or longer lifetime. As several attempts of site-directed mutagenesis failed to improve the brightness of FR13, we took the random mutagenesis approach.

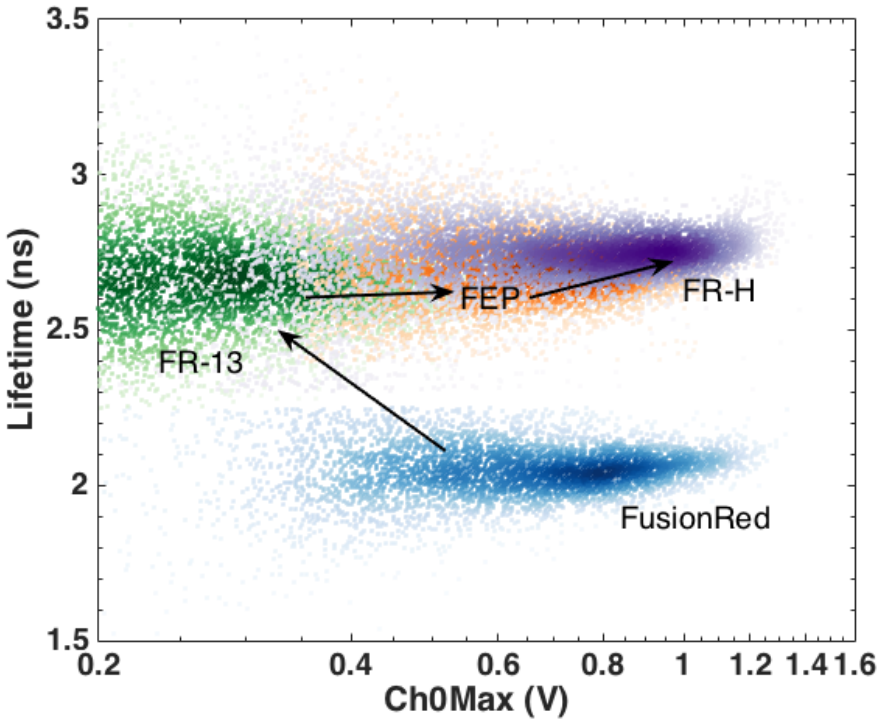

Figure 6.4: **Evolution of FusionRed through random mutagenesis**: FR-13 was generated from the error-prone mutagenesis library of FusionRed and subsequent selection based on excited state lifetime of the mutants. Two rounds of random mutagenesis on FR-13 and selection based on brightness produced FR-F, G and H mutants with improved brightness and lifetime. Individual mutants were screened with same number of cells and the results were overlaid with different color maps to generate this plot.

Figure 6.4 displays the evolution of FR-13 through several random mutagenesis libraries. A first round of EP-PCR mutagenesis and subsequent enrichment of brighter mutants through microfluidic sorting generated the FEP library. One of the mutants selected from the FEP library, FR-13 G160R, showed improved brightness relative to FR-13 and brightness similar to that of FusionRed. Further random mutagenesis on top of the FEP library generated multiple mutants brighter than FusionRed wild-type: FR-F, FR-G and FR-H. The *in-vitro* photophysical properties of these mutants are given in Table 6.1. The mutants were found to have improved ϵ_{max} and ϕ, resulting in higher *in-vitro* brightness. The pKa values of the mutants were similar to FusionRed. Sequencing of these mutants revealed the following mutations relative to FR-13: FR-F (V4M, Q115H, L142M); FR-G (V4M, G160R, T230S); FR-H (V4M, G160R, T230R).

Table 6.2: Photophysical properties of the mutants derived from FusionRed. The mutations involved in FR-13 and other FusionRed mutants are presented in Appendix G.

Mutants	Fl. Intensity (Trial 1)	Fl. Intensity (Trial 2)	Fl. Intensity (Mean)	Relative Brightness
HeLa	56	-	56	-
mCherry	448	461	455	229
FusionRed	175	223	199	100
FR-F	163	200	182	91
FR-G	184	192	188	94
FR-H	208	340	274	138
XF (FR-F M4V)	252	272	262	131
XG (FR-G M4V)	285	340	313	157
XH (FR-H M4V)	415	375	395	198

Although FR-F, G and H mutants showed higher brightness in yeast, when expressed in mammalian cells they displayed poor brightness relative to FusionRed. The sequence analyses showed the presence of a V4M mutation in all of the mutants. During the evolution of mKate2 from mKate, the M4V mutation was introduced to create an optimal Kozak sequence and efficient expression in the mammalian cells [164]. Another study based on FACS-seq indicated that multiple initiation sites, as observed in these mutants, could be detrimental for the effective expression of the proteins in the mammalian cells [174]. From these analyses, we speculated that reversing the V4M mutations in these mutants could improve their expression efficiency and brightness in mammalian cells. Hence, we generated the FRX mutants: XF (FR-F, M4V); XG (FR-G, M4V); XH (FR-H, M4V).

Figure 6.5 and Table 6.2 displayed the FACS screening results of the nuclear-localized FRX mutants and their precursors FR-F, G & H upon transient expression in HeLa cells. FRX mutants showed higher brightness than FusionRed and their precursors. For instance, XG showed a brightness of 157 which is significantly higher than FusionRed (100) or FR-G (94). However, it is notable that the brightness of these mutants is still lower than mCherry, which is inconsistent with expectations based on the *in-vitro* brightness (Table 6.1). Although these FRX mutants showed improved brightness compared to FusionRed upon transient expression in HeLa cells, when the mu-

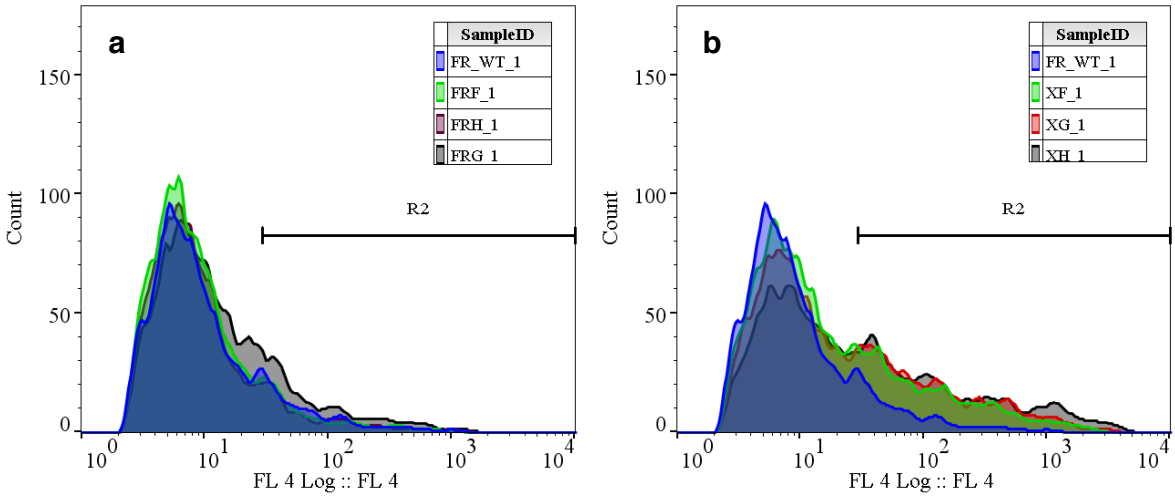

Figure 6.5: **FACS screening results of the FusionRed mutants**: (a) Distribution of the brightness (FL4 Log:FL4) of nuclear-localized FusionRed (FR-WT), FR-F, FR-G and FR-H upon transient expression in the mammalian cells (HeLa). Brightness was quantified by the mean of fluorescence intensity of cells within R2 region. FusionRed mutants displayed similar brightness relative to the wild-type FusionRed in mammalian cells. (b) FRX mutants (XF, XG and XH) showed improved brightness in mammalian cells.

tants were expressed stably in the MCF10A cell-line, their brightnesses were lower than FusionRed. This inconsistency in brightness results suggest that the slow maturation of FusionRed continues to play a role in reducing the *in-vivo* brightness.

6.4 *In-vivo* Oligomerization and Labeling Efficiency of the FRX Mutants

Next, we moved to investigate the *in-vivo* dimerization tendency and labeling efficiency of these FRX mutants. For the quantification of *in-vivo* dimerization propensity of the RFP mutants, the organized smooth endoplasmic reticulum (OSER) assay [100] was used. FPs were fused to the cytoplasmic-end of endoplasmic reticulum (ER) signal anchor membrane protein (CytERM) and

expressed in HeLa cells. The FPs having *in-vivo* oligomeric tendencies, tend to interact with each other, driving the restructuring of the reticular architecture of ER. This leads to the formation of OSER, which is manifested by small, bright puncta or whorls in fluorescence imaging. (Figure 6.6b). The OSER score, defined as the percentage of cells expressing CytERM-RFP constructs displaying no whorl, can be used to quantify the *in-vivo* dimerization tendency, *i.e.* an OSER score of 100 or 0 refers to a completely monomeric or oligomeric FP, respectively.

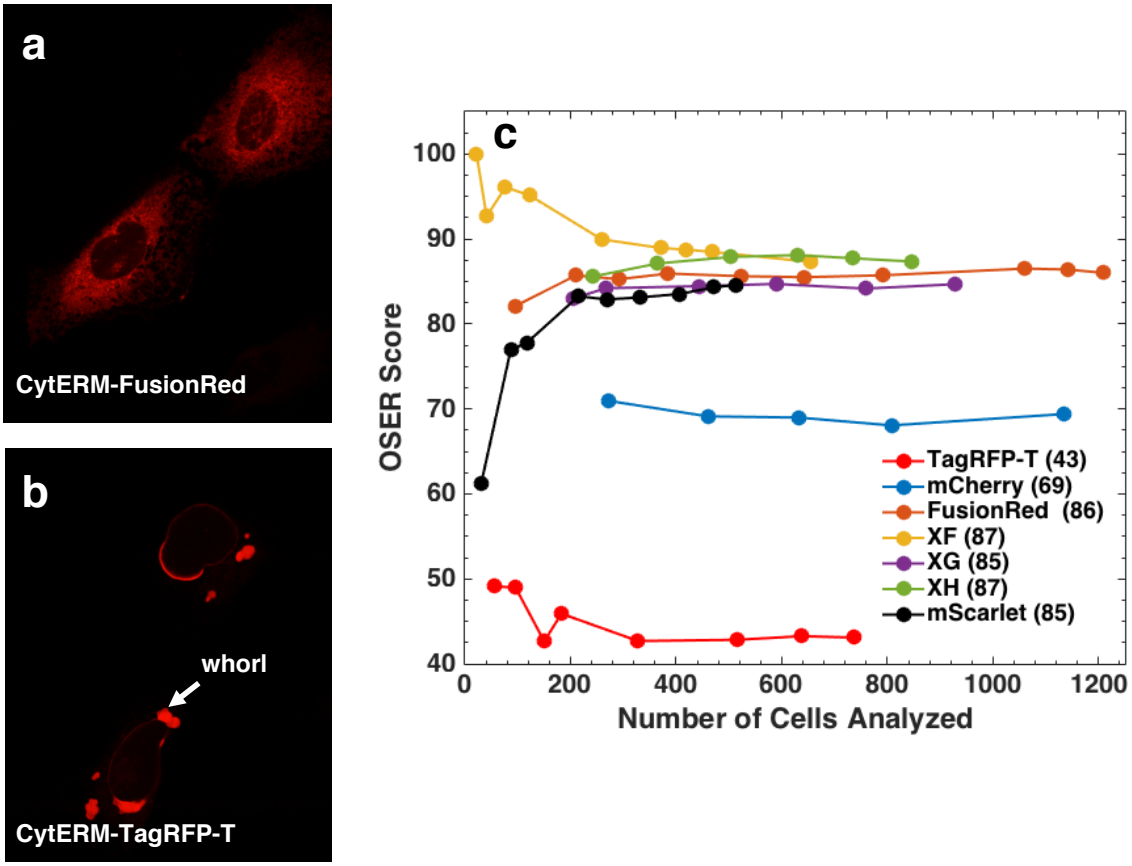

Figure 6.6: **OSER assay of the FusionRed mutants**: (a, b) HeLa cells expressing CytERM-FusionRed and CytERM-TagRFP-T constructs. Most of the cells expressing CytERM-FusionRed constructs displayed proper localization with reticular-like structures while TagRFP-T, owing to its *in-vivo* oligomerization tendencies, showed small (1-7 μm), bright puncta (whorl), upon fusion to CytERM. (c) OSER score of FRX mutants indicating their low *in-vivo* oligomerization tendencies.

The identification of whorls from a large number of cells is required to obtain a statistically robust OSER score. This process is tedious and subject to human bias and errors. To account

for these issues, we developed a custom-based image analysis program based on CellProfiler [175]. The functioning of this program has been explained in detail in Appendix H. Briefly, first, from a given image, the program identifies the cells expressing CytERM-RFP based on their size and fluorescence intensity. Next, the bright structures or whorls inside the cells are identified using thresholds based on size and fluorescence intensity. Shape-based filtering is done to remove the false-positive whorls. Finally, the whorls and cells are related based on their position and an OSER score is computed. An OSER score, analyzing thousands of cells can be obtained within an hour in an objective manner.

Figure 6.6c displays the OSER score of different mutants as a function of number of cells analyzed. From Figure 6.6c, it is evident that analysis of $\sim$ 400 cells was sufficient to obtain a stable OSER score. Different parameters and thresholds of the image analysis program were adjusted with the known OSER score of TagRFP-T (positive control) and FusionRed (negative control) [101]. As shown in Figure 6.6, TagRFP-T and FusionRed showed an OSER score of 43 and 86 respectively, which is close to the value obtained by Cranfill *et al.* by analyzing $\sim$ 10,000 cells for each FP (41.2 and 91.5 for TagRFP-T and FusionRed respectively) [101]. In our hands, mCherry showed a low OSER score which contradicts previous results [104, 101]. mScarlet, FusionRed and FRX mutants showed high OSER score indicating low *in-vivo* oligomerization tendencies.

To investigate the fusion efficiency of the mutants, FusionRed, mCherry, mScarlet and the FRX mutants were fused to Connexin-43 (Cx43, gap junction), Rab5a (endosome) & GalT (Golgi complex) and transiently expressed in mammalian cells (HeLa). Cells expressing these constructs were imaged on a commercial spinning disc microscope (Nikon) 48 hrs post transfection. Although localization of Cx43 was optimal for all the FPs, mCherry and mScarlet showed several instances of mis-localization with GalT constructs. Unlike FusionRed and FRX mutants, a significant fraction of the cells expressing GalT-mCherry and GalT-mScarlet constructs showed mobile vesicles that did not resemble the stack of perinuclear membranes characteristic of the Golgi complex (Figure 6.7d, e). Similar vesicles were observed by Kaberniuk *et al.* with GalT-Dendra2 constructs [176]. We quantified the fusion efficiency of mutants expressing GalT-RFP constructs with $\sim$150-250 number

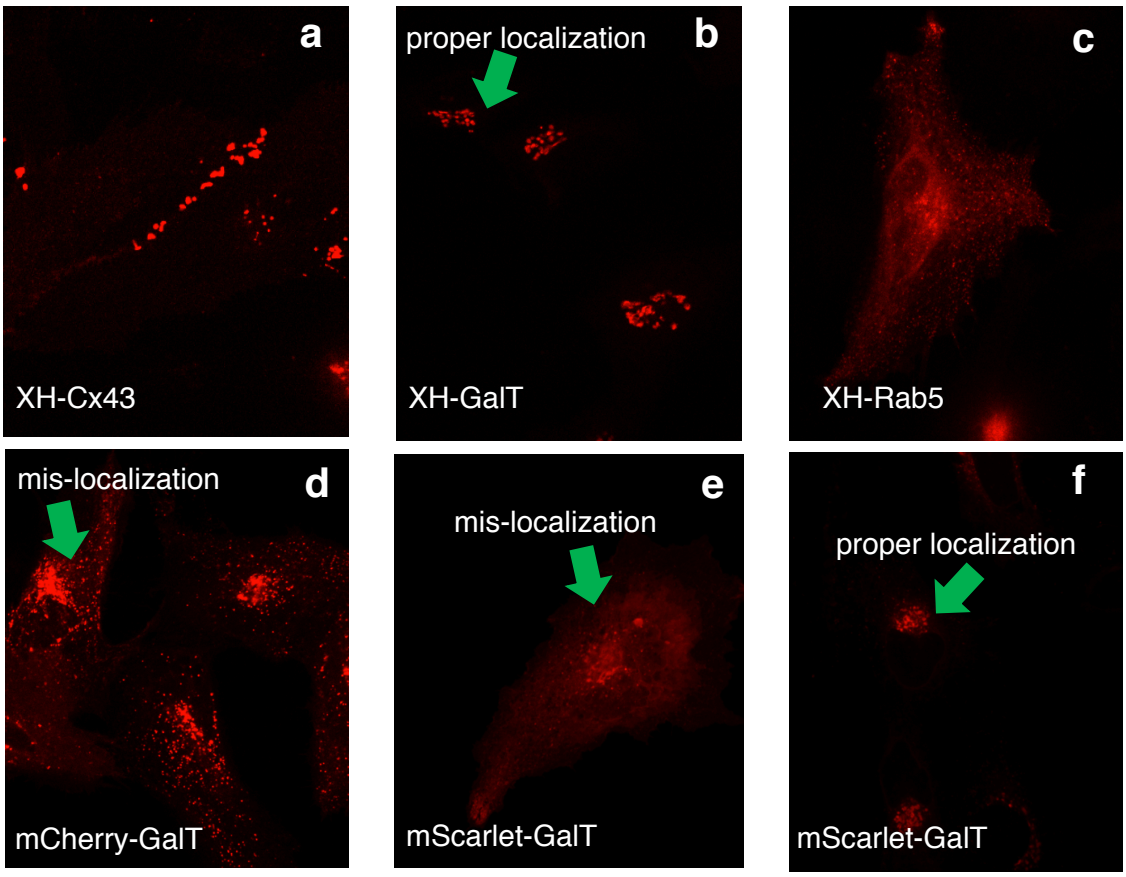

Figure 6.7: Localization efficiency of the FusionRed mutants: (a, b, c) Representative images displaying localization of XH in Cx43, GalT and Rab5. (d, e, f) mCherry and mScarlet showed poor performance when fused with GalT.

of cells. It was observed that the GalT fusion efficiencies of mCherry, mScarlet and XG were 17%, 57% and 87% respectively. This result is consistent with the high fusion efficiency of FusionRed relative to mCherry, as reported in the original FusionRed article [54].

FRX mutants showed improved *in-vitro* brightness and upon expression in yeast cells. These mutants displayed higher OSER score than mCherry, indicating lower *in-vivo* oligomerization tendencies. FRX mutants were characterized with excellent localization efficiency. However, transient and stable expression in the mammalian cells did not produce the anticipated high brightness presumably due to their slow maturation. The *in-vivo* brightness of these mutants was low compared to mScarlet and mCherry. On the other hand, FR-1 showed faster maturation when expressed in

E.coli and also had a longer lifetime than FusionRed. Hence, we focused on further mutagenesis of this variant to develop a brighter FusionRed mutant.

6.5 FR-1 Mutant

As discussed previously in section 6.2, FR-1 was generated by random mutagenesis on FusionRed and subsequent selection of longer lifetime mutants. Indeed, FR-1 was characterized with longer τ and higher ϕ compared to FusionRed as displayed in Table 6.1. Although the *in-vitro* brightness of FR-1 was found to be only $\sim$ 30% relative to FusionRed, when expressed in yeast it showed $\sim$ 3.5-fold and $\sim$1.7-fold higher brightness than FusionRed and mCherry respectively (Figure 6.8b & 6.9b). As the *in-vitro* brightness of FR-1 is $\sim$1.8 fold higher than mCherry (Table 6.1) which is consistent with the *in-vivo* measurements ($\sim$ 1.7-fold higher brightness), we speculate that the slow maturation in FusionRed is remedied in FR-1. The reported maturation half-time for mCherry and FusionRed are 15 minutes and 130 minutes, respectively [12, 54].

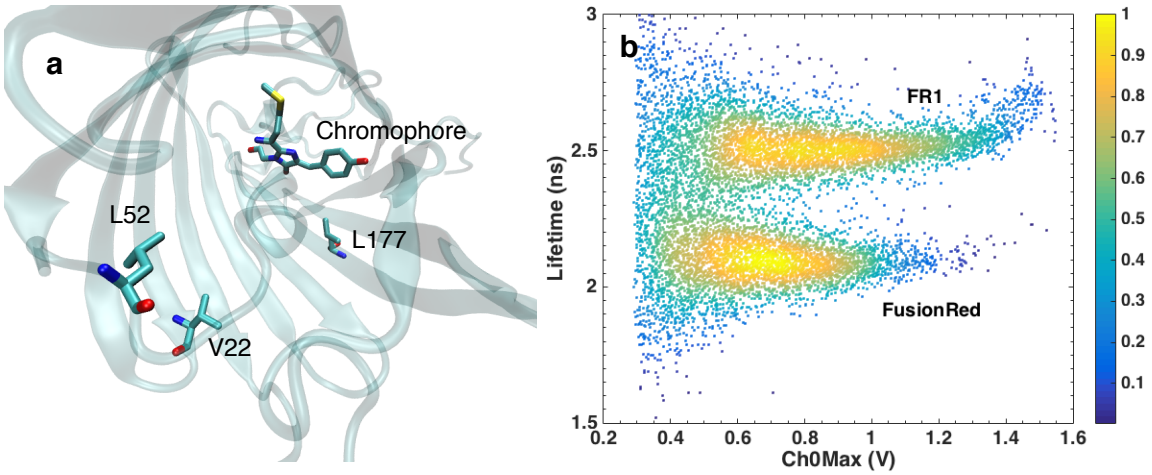

Figure 6.8: (a) FR-1 was found to have V22I, L52P & L177M mutations (avGFP numbering). Positions of these residues are displayed in mKate (3BXB) crystal structure. (b) Microfluidic screening results showed improved lifetime and brightness of the FR-1 mutant relative to FusionRed.

The FR-1 mutant was characterized with the following mutations relative to FusionRed: V22I, L52P and L177M. L177 pointed inside the β-barrel, close to the chromophore. On the other hand, L52 & V22 were in the loop region (Figure 6.8a). From our previous experience with FR-13 mutants, we speculated that the residue at position 177 might be crucial in modifying the photo-physical properties in FR-1. To confirm this notion, we generated FusionRed L177M (abbreviated as FR L177M). Table 6.1 compares the photo-physical properties of FusionRed, FR-1 and FR L177M. Although the ϕ of FR-1 and FR L177M mutants were same, the ϵ_{max} of FR L177M was slightly lower. However, we observed faster maturation in FR L177M upon bacterial expression. Hence, we concluded the L177M mutation improved the ϕ and maturation speed in FR1, while V22I and L52P mutations helped to maintain the high ϵ_{max} of FusionRed.

6.6 FusionRed Site-Directed Library

As described in the previous Chapter, by using mCherry as a template we generated several mutants with high quantum yield and brightness through site-directed mutagenesis. For instance, SLT-11, an mCherry mutant, was generated by targeting 143, 161, 163 & 197 residues (numbering based on mCherry crystal structure, PBD 2H5Q), showed a ϕ of 71%. Inspired by these results, we targeted the analogous residues in FusionRed to generate a site-directed library: 165, 167, 201 & 203 (avGFP numbering) which correspond to 161, 163, 195 & 197 in mCherry-based numbering. Figure 6.9a displays the brightness (Ch0Max) and lifetime profiles of the resulting site-directed library which contained a significant population with shorter lifetime ($\sim$1.2 ns) and lower brightness of a higher lifetime population. We enriched the bright population from this library (population enclosed in the pink box) through FACS-based selection. After several rounds of microfluidic and FACS-based sorting, we selected a few mutants from this library and called them FusionRed Site-Directed mutants or simply FSD mutants.

Figure 6.9b demonstrates the screening results of the FSD mutants along with FusionRed, FR1, SDC-5 and mCherry. The x- and y-axes represents the red and green fluorescence intensity

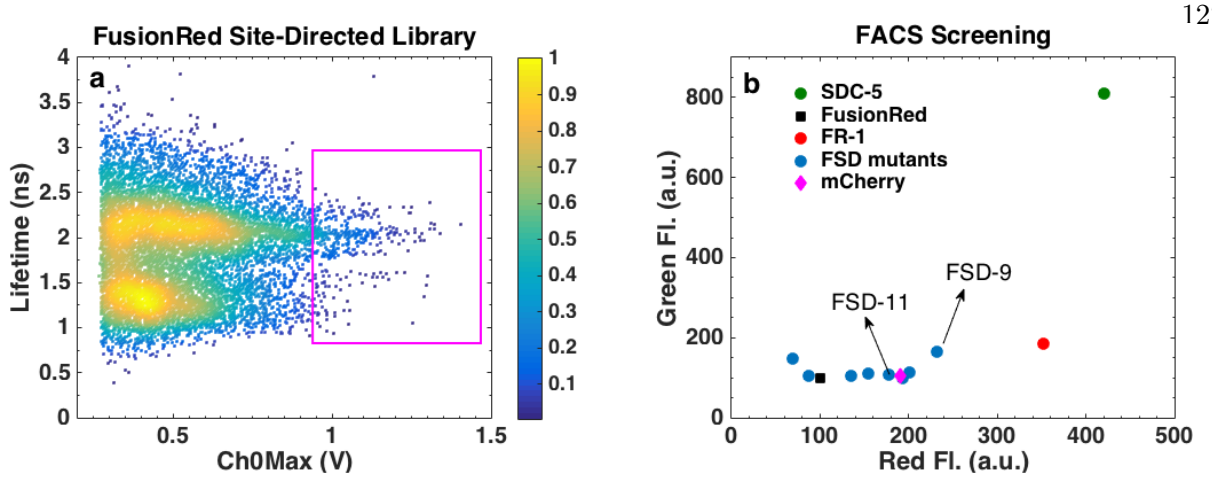

Figure 6.9: (a) Microfluidic screening results displaying the brightness (Ch0Max) and lifetime profile of FusionRed site-directed library generated by targeting residues at 165, 167, 201 and 203. The population with improved brightness (within the pink box) was enriched using FACS. Multiple rounds of subsequent microfluidic and FACS-based sorting generated FusionRed Site-Directed (FSD) mutants. (b) FACS screening results displaying mean red (561-nm excitation) and green (488-nm excitation) fluorescence intensities of the FSD mutants along with mCherry, SDC-5, FusionRed and FR-1.

of the mutants obtained by the excitation of 561-nm and 488-nm laser respectively. As evident from the Figure, several mutants showed higher brightness than FusionRed. For example, FSD-9 & FSD-11 show a single mutation from the wild-type FusionRed and were brighter or comparable to mCherry. The FR-1 variant, as discussed previously, showed higher brightness than both mCherry and FusionRed. All the mutants displayed lower green fluorescence than SDC-5, indicating the likely absence of GFP-like chromophore and therefore complete maturation.

The sequence analysis of FSD-9 and FSD-11 revealed the C165V and C165L mutations, respectively. Figure 6.10a shows that position 165 is very close to the phenolate-end of the chromophore and therefore it is unsurprising that modifications at this position modulate the photophysical properties. Figure 6.10b shows the fluorescence decays of FusionRed, FSD-9 and FSD-11 measured using yeast cell-lysate in TCSPC with tail-fitting. It is interesting to note that substitution of cysteine with valine at this position leads to significant increase in lifetime (1.67 ns in FusionRed *vs.* 2.03 ns in FSD-9) while leucine at this position reduced the fluorescence lifetime (1.21 ns in FSD-11).

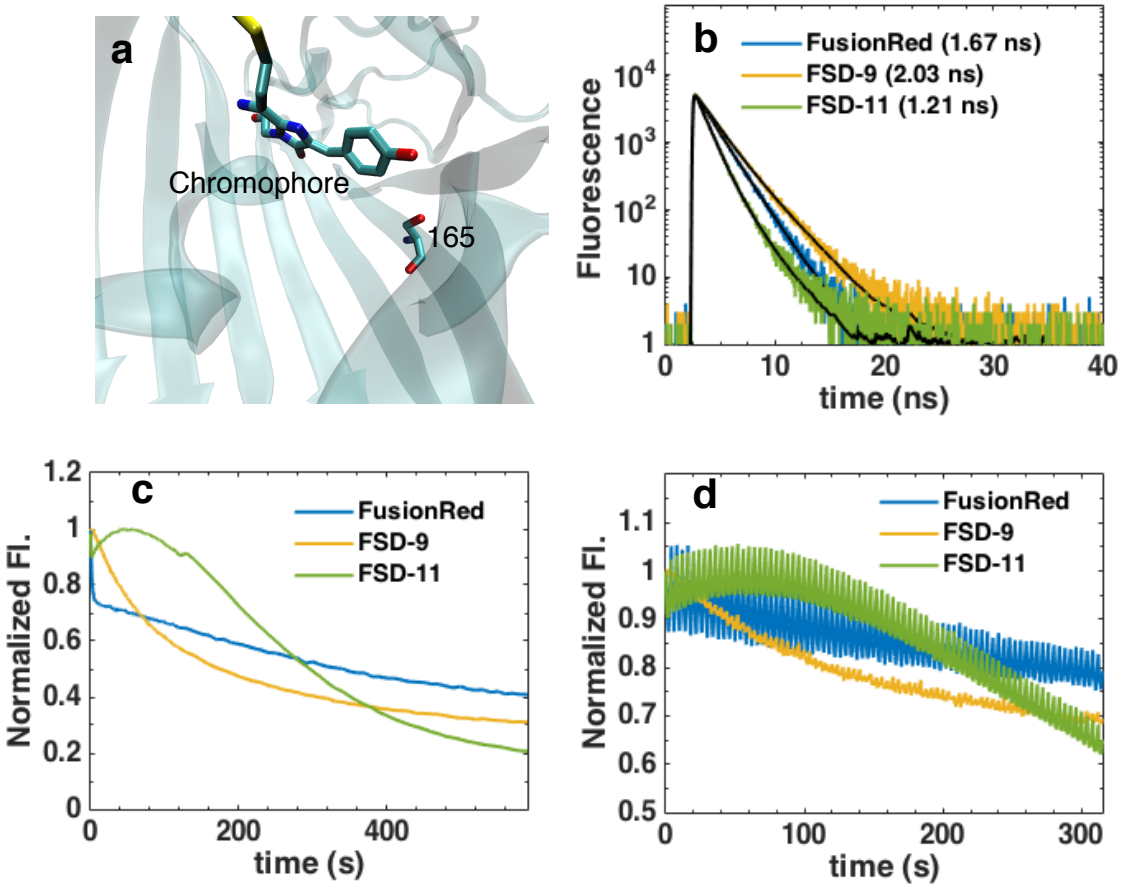

Figure 6.10: (a) Position 165 (161 in mCherry numbering) is displayed in mKate crystal structure (PBD 3X3B). Mutations at this positons controls the excited state lifetime, photobleaching and photoswitching properties of FusionRed (wild-type) FSD-9 and FSD-11. (b) FSD-9 & FSD-11 showed longer and shorter excited state lifetimes compared to FusionRed respectively. (c) Photobleaching decays of FusionRed mutants with 560-nm LED illumination at ~ 4 W/cm^2. Excitation intensities were not normalized according to the extinction coefficient of each mutant for these photobleaching experiments. (d) Photoswitching behavior of the FusionRed, FSD-9 & FSD-11 with alternate 560-nm and 438-nm LED illumination.

Figure 6.10c demonstrates the photobleaching decays of the mutants expressed in yeast upon 560-nm LED illumination from a commercial inverted microscope (Olympus) at ~ 4 W/cm^2. Both FusionRed and FSD-11 display a rapid drop in fluorescence in a short time-scale (2-4 s) indicating a significant amount of dark state conversion (DSC). This rapid decay of fluorescence in a short time-scale is absent in FSD-9 mutant and the photobleaching decay was nearly mono-exponential. This suggests that FSD-9 has reduced dark state conversion tendency compared to FusionRed. FSD-11 shows photoactivation followed by photobleaching upon 560-nm LED illumination. Please

note that excitation intensity was not normalized to give the same excitation rate while performing these bleaching experiments. All the mutants were irradiated with uniform ∼4 W/cm^2 LED light.

The photoswitching properties of these mutants have been captured in Figure 6.10d. Yeast cells expressing the FSD mutants were excited with 560-nm LED light for 2 s followed by a 2 s 438-nm LED illumination (with 561-nm LED off) and the whole cycle was repeated for 80 times. Along with inducing fluorescence, 560-nm illumination drives some population into photo-induced dark or OFF states. High-energy 438-nm illumination converts the population from the OFF state back to the ON state. Thus, alternative 560-nm and 438-nm illumination in FPs can reveal their ON-OFF state dynamics or photoswitching. Both FusionRed and FSD-11 show photoswitching while FSD-11 displays photoactivation similar to that observed in photobleaching decay (Figure 6.10c). Unlike FusionRed and FSD-11, photoswitching is nearly absent in FSD-9.

6.7 Discussion

Random mutagenesis on FusionRed generated FR-13 and FR-1 mutants. Photo-physical analyses of FR-13 mutants revealed that the A224T mutation was responsible for its improved lifetime/quantum yield as well as its reduced *in-vivo* brightness. Reduction in brightness of FR-13 upon cellular expression may be explained by its slow maturation observed in the bacterial expressions. We hypothesize that a polar threonine residue at 224 improved the rigidity of the chromophore through electrostatic or H-bonding interactions improving the lifetime and quantum yield but interfered with the chromophore formation process by slowing it down.

Multiple rounds of error-prone mutagenesis improved the brightness of FR-13 in yeast but the brightness was sub-optimal in mammalian cells. Although the M4V mutation improved the brightness in HeLa cells transiently expressing the mutants, the brightness was still lower than its promised ϵ_{max} and ϕ. For instance, from the *in-vitro* analyses, XH should be $\sim$ 2.4 times brighter than mCherry but as Table 6.2 shows, XH is slightly dimmer than mCherry. When the FRX mutants were stably expressed in MCF10A cell-line, the brightness was even lower than the

wild-type FusionRed. We interpret these inconsistencies in brightness as FRX mutants suffering from slow chromophore maturation as observed during their bacterial expression.

A custom-made image analysis program was used to quantify results of the OSER assay, which in turn was used to quantify the in-vivo dimerization efficiency. This technique enabled us to obtain the OSER score free of human subjectivity and in a high-throughput manner. As the Figure 6.6c indicates, to obtain a statistically reliable OSER score, $\sim$ 400 cells need to be analyzed. The original OSER article [100] and Bindels *et al.* [104] used $\sim$ 50 and $\sim$ 200 cells for OSER analyses which might be insufficient to get a robust score. On the other hand, Cranfill *et al.* used $\sim$ 10,000 cells to obtain the OSER score which we think was over-kill. The image analysis program developed by us could provide an objective OSER score for the FPs, eliminating large fluctuations in the score found in the literature [104, 101].

A single mutation (L177M) was able to improve the lifetime and quantum yield in FR-1. The L177M mutation was beneficial for the fast chromophore maturation in this mutant as observed by its fast expression in *E.coli*. Probably due to the faster maturation of FR-1, its *in-vitro* and *in-vivo* brightness were consistently higher than mCherry mutant by $\sim$1.8 and $\sim$ 1.7-fold respectively. To determine if improvement of brightness in FR-1 is due to the aggregation or dimerization, we measured fluorescence anisotropy decays of purified proteins and observed the rotational time-constant of FR-1 and FusionRed. The rotational time constants of FusionRed and FR-1 were found to be 15 ns and 17 ns, respectively. The *in-vivo* oligomerization tendency can be investigated by the OSER assay as described in Section 6.4. As the two other mutational positions of FR-1 (V22I & L52P) are in the loop region and the nature of mutations are similar *i.e.* non-polar group changed to non-polar, we anticipate that the good labeling efficiency of FusionRed would be retained in FR-1 upon mammalian cell expression.

Mutants derived from the FusionRed site-directed library showed interesting photo-physics. A single mutation in FSD-9 (*i.e.* C165V), reduced its dark state conversion (DSC) and increased the excited state lifetime. On the other hand, C165L mutation in FSD-11 reduced its lifetime and induced photoactivation. These results can shed light into the DSC and other non-radiative

pathways in FusionRed and its derivatives. The 165 position in FusionRed is equivalent to the 161 position in rsCherry. The authors in the rsCherry article [177] argued that by replacing a bulky isoleucine with a smaller serine residue at position 161, the chromophore is allowed to undergo a *cis-trans* isomerization enabling the photoswitching in rsCherry. This argument may explain replacing a cysteine with a bulkier valine at position 165 resulted in decreased DSC, which can be interpreted as decreased *cis-trans* isomerization of the chromophore in FSD-9. A reduced *cis-trans* isomerization in FSD-9 can decrease the possible non-radiative processes which is in agreement with its longer lifetime. However, replacing cysteine with a leucine at position 165 in FusionRed to form FSD-11 does not eliminate the reversible photoswitching property. Perhaps the bulkier leucine at 165 reduces the planarity of the chromophore, enhancing the non-radiative rate and thereby decreasing the fluorescence lifetime. A detailed investigation is necessary to explain these photo-physical behaviors of the FSD mutants.

Intrigued by the beneficial mutations at 177 (L177M in FR1) and 165 (C165V in FSD-9), we generated the mutant FR-1 C165V that contained both L177M and C165V mutations. FR-1 C165V showed higher quantum yield and extinction coefficient than FR-1 resulting a high *in-vitro* brightness (Table 6.1). However, the mutant was characterized by reduced bacterial expression. These results indicate that targeting 177 and 165 positions and subsequent selection of mutants with longer lifetime and brightness can generate improved version of FusionRed. Our future work will include these library generations.

6.8 Conclusion

Evolution of brighter FusionRed mutants through engineering of excited state lifetime was discussed in this Chapter. Several rounds of random mutagenesis on FusionRed generated FR-13 and FRX mutants which displayed higher *in-vitro* brightness, low oligomerization tendency and superb fusion efficiency. However, the brightness in mammalian cell-lines of those mutants remained sub-optimal, which we hypothesize is due to their slower chromophore maturation. On the other

hand, the FR-1 mutant showed improved expression in bacteria which we interpret as improved chromophore maturation. With its improved quantum yield, lifetime and robust expression, FR-1 is an improvement over FusionRed. Site-directed mutagenesis libraries of FusionRed, produced mutants with interesting photo-physics. Dark state conversion was nearly eliminated in FSD-9, resulting in mono-exponential fluorescence decay and reduced photoswitching. The FSD-11 mutant was characterized with photoactivation. These mutants can serve the templates for future library generation to improve the photostability or photoswitching properties of FusionRed or related FPs.

Chapter 7

Engineering of Radiative Lifetime in Red Fluorescent Proteins

7.1 Introduction

In our previous attempts to improve the fluorescence quantum yield (ϕ) in red fluorescent protein (RFP) mutants, we opted for increasing their excited state lifetime (τ). The rationale for this approach is that ϕ and τ are proportional to each other according to the equation below.

$$\phi = k_r * \tau \tag{7.1}$$

$$\tau = \frac{1}{k_r + k_{nr}} \tag{7.2}$$

where, k_r and k_{nr} are the rate-constants for radiative and non-radiative decays, respectively. Therefore, an increase in τ ensures an improvement in ϕ, as long as the radiative rate remains constant for a FP, resulting in a brighter FP variant. Based on this concept, several FusionRed and mCherry mutants were developed with fluorescence quantum yields up to 71%. However, as we discovered, the radiative rate may change with mutagenesis. For instance, C4PB-12 (described in Chapter 5) had a 29% improvement in lifetime compared to mCherry but that resulted in a marginal (8%) increase in ϕ compared to its precursor. Further analyses revealed that the reason behind this apparent inconsistency was a decline in radiative rates in C4PB mutants (see Chapter 5). This suggested that radiative rate is not an intrinsic property of the FP chromophore and is subject to change upon mutations.

As the Eqn. 7.1 and 7.2 show, enhancement of k_r leads to an increase in ϕ and a corresponding decrease in τ if the non-radiative rate remains unchanged. Although the engineering of molecular structure to increase radiative rate has not yet been reported, the effect of the metal surface on radiative rates of the fluorophores and the subsequent effects on their lifetimes and quantum yields have been described in the literature [178]. It was shown that fluorescence intensity of Eu^{3+} ions increased ~5 -fold in the presence of a Ag surface with a concomitant 100-fold decrease in fluorescence lifetime [179]. These observations were explained by the enhancement of the radiative rates in Eu^{3+} due to its electromagnetic coupling with Ag. Similar effects were also observed in erythrosin and rhodamine dyes on surface [180, 181].

Improvement in the radiative rate of a fluorophore is generally associated with an increase in its extinction coefficient (ϵ). As the Strickler-Berg equation shows, the radiative rate of a chromophore is inherently related to its ϵ as follows [168]:

$$A_{21} = k_r = \frac{8 \times 2303\pi n^2}{c^2} < \nu_f^{-3} >^{-1} \int \epsilon_\nu d ln\nu \tag{7.3}$$

where, c, n, ν and ϵ_ν are the speed of light, refractive index of the media, frequency of light and extinction coefficient at the frequency ν, respectively. ν. $< \nu_f^{-3} >$ is given by:

$$< \nu_f^{-3} > = \frac{\int \nu^{-3} I(\nu) d\nu}{\int I(\nu) d\nu} \tag{7.4}$$

where, $I(\nu)$ is the fluorescence intensity spectrum. According to Eqn. 7.3, an improvement in k_r can be achieved by increasing ϵ or *vice versa*. This inter-relation of extinction coefficient and the radiative rate-constant is illustrated by a number of FP engineering efforts. For instance, C4PB-12 had 17% reduction in k_r resulting in 26% decrease in ϵ_{max} compared to mCherry (Chapter 5). In another example, our analyses revealed that mRuby3 [102] had 13% increase in its radiative rate-constant (1.51×108 s^{-1} *vs.* 1.71×108 s^{-1}) which is associated with 13% enhancement (113,000 $M^{-1}cm^{-1}$ *vs.* 128 $M^{-1}cm^{-1}$) in ϵ_{max} relative to its precursor mRuby2 [165]. Similarly, mScarlet [104] was found to have 14% increase in ϵ_{max} relative to mCherry (88,000 $M^{-1}cm^{-1}$ *vs.* 100,000 $M^{-1}cm^{-1}$)

with a concomitant 18% increase in k_r (1.53×108 s^{-1} *vs.* 1.80×108 s^{-1}).

Based on these observations and analyses, we hypothesized that improving radiative rates of fluorescent proteins holds promise for simultaneous enhancement in extinction coefficients and quantum yields. This would improve overall theoretical brightness ($\epsilon * \phi$) of the FPs. Although improvement in brightness of the FPs by increasing the excited state lifetime or *via* error-prone mutagenesis are reported in the literature [155, 104, 102], to the best of our knowledge, rational approach to enhance the extinction coefficient of the FPs have not been achieved so far [88].

In Chapter 5, we developed SLT-11 through the engineering of its excited state lifetime. The SLT-11 mutant was found to have a high quantum yield (71%) and complete chromophore formation. However, due to its reduced ϵ, both *in-vitro* and *in-vivo* brightness of SLT-11 were observed to be lower than mScarlet (ϕ, 70%) [104]. Therefore, we attempted to improve the brightness of this mutant by explicitly engineering its radiative rate. Several large libraries (library size $\sim$ 800,000) were generated from SLT-11 by targeting the outward pointing residues. Multiple bright mutants were selected from the FACS-enriched libraries.

7.2 Library Design for the Radiative Rate Engineering

For improving extinction coefficient or radiative rate in a FP, we set out to modulate the transition dipole moment (μ_{12}) of the chromophore. This concept is based on the following set of equations:

$$B_{12} \propto \int \epsilon_\nu d ln\nu \tag{7.5}$$

$$B_{12} \propto \left|\langle \Psi_1 | \hat{M} | \Psi_2 \rangle\right|^2 \tag{7.6}$$

$$\propto \mu_{12} \tag{7.7}$$

where, B_{12} is the probability of a transition from state 1 to state 2, ϵ_ν is the extinction coefficient at the frequency ν, μ_{12} is the transition dipole moment, Ψ_1 and Ψ_2 are the electronic state wave-

functions of state 1 and state 2, respectively. $\hat{M}$ is the dipole moment operator ($\hat{M} = \sum_i er_i$, where r_i is the vector joining the electron i to the origin of a coordinate system linked to the molecule).

From Eqn. 7.6 and 7.7 it is obvious that increasing transition dipole moment can enhance the transition probability from state 1 to state 2 (B_{12}) which in turn can improve the extinction coefficient of the molecule. We propose that μ_{12} can be modulated by tuning the electric field in the three-dimensional space where the chromophore of the FP is located *i.e.* inside the β-barrel. This in essence, can change the intrinsic radiative rate of a chromophore [178]. We argue that the electric field of the space inside the β-barrel of a FP can be modulated with charged amino acids. Amino acids with charged side-chains can increase the electric field of the space, thereby increasing the effective excitation intensity, absorption cross-section or radiative rates of the chromophore [178].

Ideally, to change the radiative rate of FPs, we want to target the residues which do not influence the non-radiative rates, folding, maturations, monomericity *etc.* of FPs. In this regard, we hypothesized that mutations that point outwards of the β-barrel could effectively position charges in a such way as to influence the transition dipole, without adversely affecting properties such as chromophore maturation and folding. We further hypothesized that the residues located on the plane of transition dipole moment (μ_{12}) vector would be most effective in tuning the amplitude of μ_{12}. Hence, we propose that outward pointing residues on the plane of transition dipole moment vector can be targeted with charged residues to enhance the radiative rate of FPs.

The analysis of mutations involved in the evolution of mRuby3, mScarlet and C4PB-12 support our hypothesis. For instance, during enhancement of the brightness of C4 through random mutagenesis, N98K and K166R mutations appeared in some of the mutants (*e.g.* C4PB-12). Both the residues are located at the phenolate-end of the chromophore and lie around the plane of the μ_{12} vector (Figure 7.1a, b and Figure 7.4). In fact, all C4PB mutants generated through random mutagenesis contain the K166R mutation. The K166R mutation appeared during the evolution of mScarlet in the course of enhancement of brightness through random mutagenesis. We believe this outward-pointing mutation may be involved in enhancing the amplitude of μ_{12} and thereby

increasing the ϵ_{max} or brightness of the related FPs. We found similar mutations in mRuby3. For example, the residue at position 114 is located at the imidazolinone-end of the chromophore pointing outward was changed from a polar cysteine to a negatively charged glutamic acid (C114E) during the evolution of mRuby3 from mRuby2 [102]. Positively charged residues were also introduced at the phenolate-end of the barrel (S171H) during evolution of mRuby3.

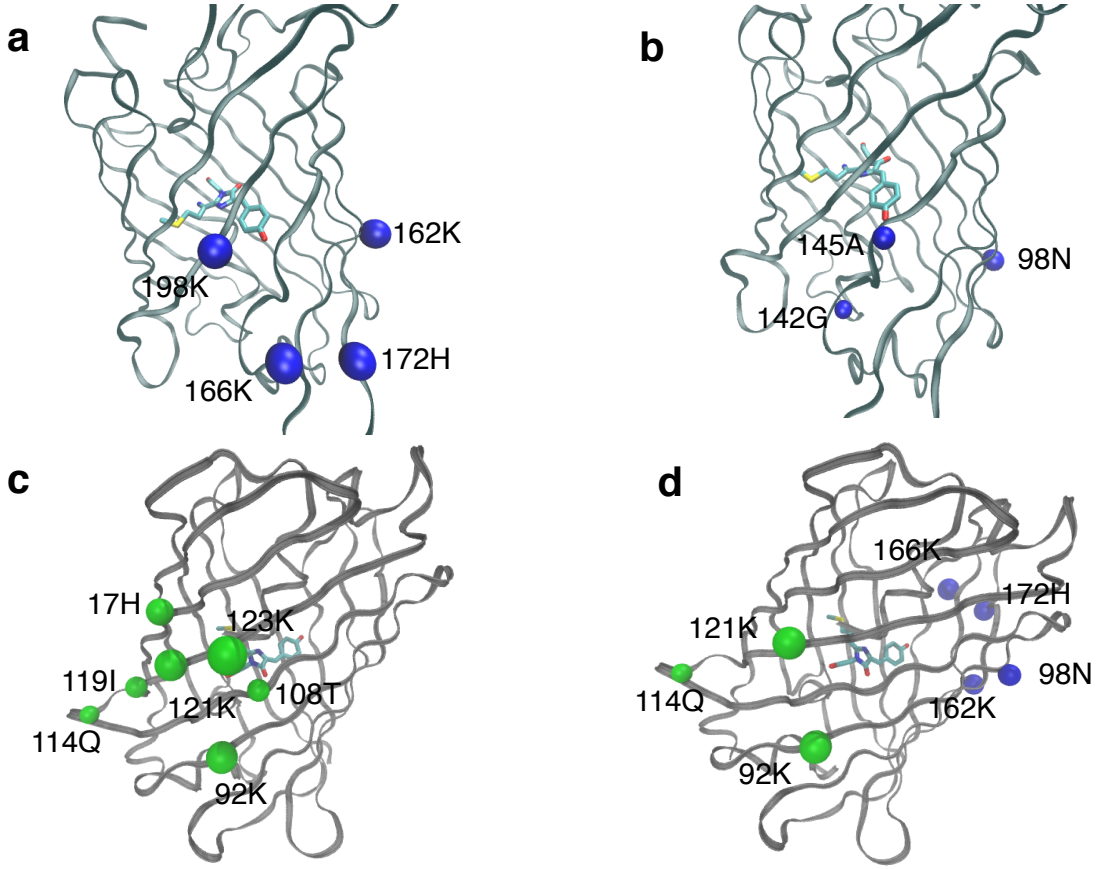

Figure 7.1: **Residues targeted to generate radiative rate libraries**: Site-directed mutagenesis with charged amino acid residues (arginine, lysine, aspartic acid and glutamic acid) at the phenolate-end (a, b) and imidazolinone-end (c) of the chromophore produced Ph libraries and Im library respectively. (d) A combined radiative rate library (Combined library) was generated by targeting both phenolate- and imidazolinone-end of the chromophore. Residues located at the phenolate- and imidazolinone-end of the chromophore are shown with blue and green sphere respectively. Targets are shown in a crystal structure of mCherry (PDB: 2H5Q).

Our analyses suggest that outward-pointing mutations in the vicinity of the phenolate- and imidazolinone-end of the chromophore might be effective at tuning the radiative rate of

the chromophore. Therefore, we designed two libraries targeting either the phenolate-end or the imidazolinone-end of the chromophore. We also recognized that the transition dipole moment is a complex function of charge re-distribution between the ground state and excited state of the chromophore. Therefore, we generated another library targeting both ends of the chromophore. We called these libraries as "Ph-library", "Im-library" and "Combined library", respectively. However, as the residues designed for Ph-library were very close to each other, we had to split the targets into two separate libraries for effective library construction: Ph-1 and Ph-2 library.

Table 7.1 demonstrates the residues we targeted and the rationale behind choosing them.

Table 7.1: Targets for the radiative rate libraries and the rationales. Numbering is based on mCherry crystal structure (PDB: 2H5Q).

Residues	Position	Rationale
166	Phenolate-end	appeared in mScarlet, C4PB clones which improves the brightness. Preferred mutation K166R
172	Phenolate-end	appeared in mScarlet and mRuby3. H in mCherry, mRuby3. R in mScarlet.
162	Phenolate-end	appeared in mRuby3.
98	Phenolate-end	appeared in C4PB mutants. Improves brightness.
145	Phenolate-end	Non-polar, close to phenolate-end.
142	Phenolate-end	Non-polar, close to phenolate-end.
198	Phenolate-end	Similar position as K166, close to phenolate-end.
114	Imidazolinone-end	appeared in mRuby3 (C114E), close to imidazolinone-end.
121	Imidazolinone-end	appeared in mRuby3 (H121N).
92	Imidazolinone-end	appeared in mApple (K92R), which is brighter than mCherry.
108	Imidazolinone-end	Close to imidazolinone-end.
17	Imidazolinone-end	appeared in C4PB clones.
119	Imidazolinone-end	Non-polar, close to imidazolinone-end.
123	Imidazolinone-end	Close to imidazolinone-end.

For selection of residues we considered the following criteria:

- Residues close to either end of the chromophore and previously reported to improve the brightness. For example, in our C4PB mutants and in mScarlet we found the mutation

K166R to improve the brightness. Similarly, 114Q in mRuby3 and 92K in mApple reported to enhance the brightness.

- Residues close to either phenolate- or imidazolinone-end of the chromophore that are non-polar.

Table 7.2 shows the residues we targeted to generate radiative-rate libraries.

Table 7.2: Proposed residues for targeting the four radiative rate libraries.

Library	Targets
Ph-1 Library	166, 172, 162, 198
Ph-2 Library	98, 145, 142
Im Library	114, 121, 92, 108, 17, 119, 123
Combined Library	114, 121, 92, 166, 172, 162, 98

Ideally, we wanted to saturate the phenolate- and imidazolinone-end of the chromophore with charged residues (K, H, R, E, D). After analyzing the codons that encode these amino acids, it appeared that we could not saturate our targets only with charged residues without adding some uncharged ones. Two possible codons and the resulting amino acids are shown in Table 7.3.

Table 7.3: **Choice of codon for the charged residues.** Amino acid residues in black are the desired ones whereas the AAs in reds are the uncharged residues. V=A/C/G, R=A/G, S=C/G, N=A/C/T/G. The number in the parentheses are the frequency of the residue occurrence.

Codon	Amino acid residues
VRS	K(*1*), H(*1*), R(*3*), E(*1*), D(*1*), S(*1*), N(*1*), Q(*1*), G(*2*)
RRN	K(*1*), R(*1*), E(*1*), D(*1*), S(*1*), N(*1*), G(*2*)

Unlike lysine (K) and arginine (R), histidine is positively charged only when the pH is below 6, so we can effectively target the amino acids with just K, R, E and D. As the Table 7.3 suggests using the RRN codon we can have K, R, E and D along with fewer uncharged residues (S, N, G) and with more uniform frequencies of occurrences of the amino acids. We therefore chose to employ the RRN codon. For the Combined and Im libraries, we targeted 7 residues (Table 7.2) with 7 amino acids using RRN codon (Table 7.3). So, the library size was $7^7 \sim$ 800,000. The size of Ph-1 and Ph-2 libraries were 2401 (7^4) and 343 (7^3), respectively.

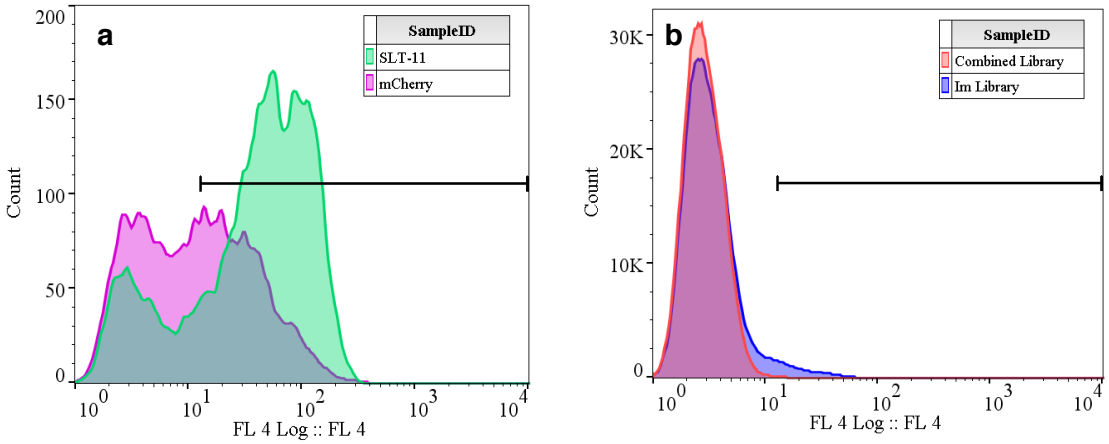

Figure 7.2: Distribution of the red fluorescence intensities (FL4Log::FL4) of mCherry/SLT-11 (a) and Im/Combined (b) libraries upon expression in yeast. The mean fluorescence intensities of mCherry and SLT-11 were measured as 38 and 66 respectively. $> 10^6$ cells expressing the libraries were screened through the FACS. The brightest 3% and 0.3% of the screened populations were selected from the Im and Combined libraries, respectively.

7.3 Screening of the Radiative Rate Libraries and the Mutants

Due to the large size of the radiative rate libraries, FACS-sorting was carried out to select only the fluorescent mutants. Figure 7.2 shows the FACS screening results of mCherry, SLT-11, Im and Combined libraries. Although the sizes of Im and Combined libraries were similar, we observed a larger number of fluorescent mutants in the Im library compared to the Combined library. Using FACS, we sorted the brightest 3% and 0.3% of the populations from Im and Combined libraries, respectively and subsequently grew them up.

Following the initial FACS-enrichment, the libraries were screened in the microfluidic system. Microfluidic screening revealed very low brightness of the mutants and consequently another FACS-enrichment was performed. Figure 7.3 displays the brightness and lifetime profiles of the libraries measured in microfluidic after two rounds of FASC-enrichment . Screening results of the libraries revealed two main populations: one with $\sim$ 2 ns lifetime (mCherry-like) and another with $\sim$4 ns lifetime (SLT-11-like).

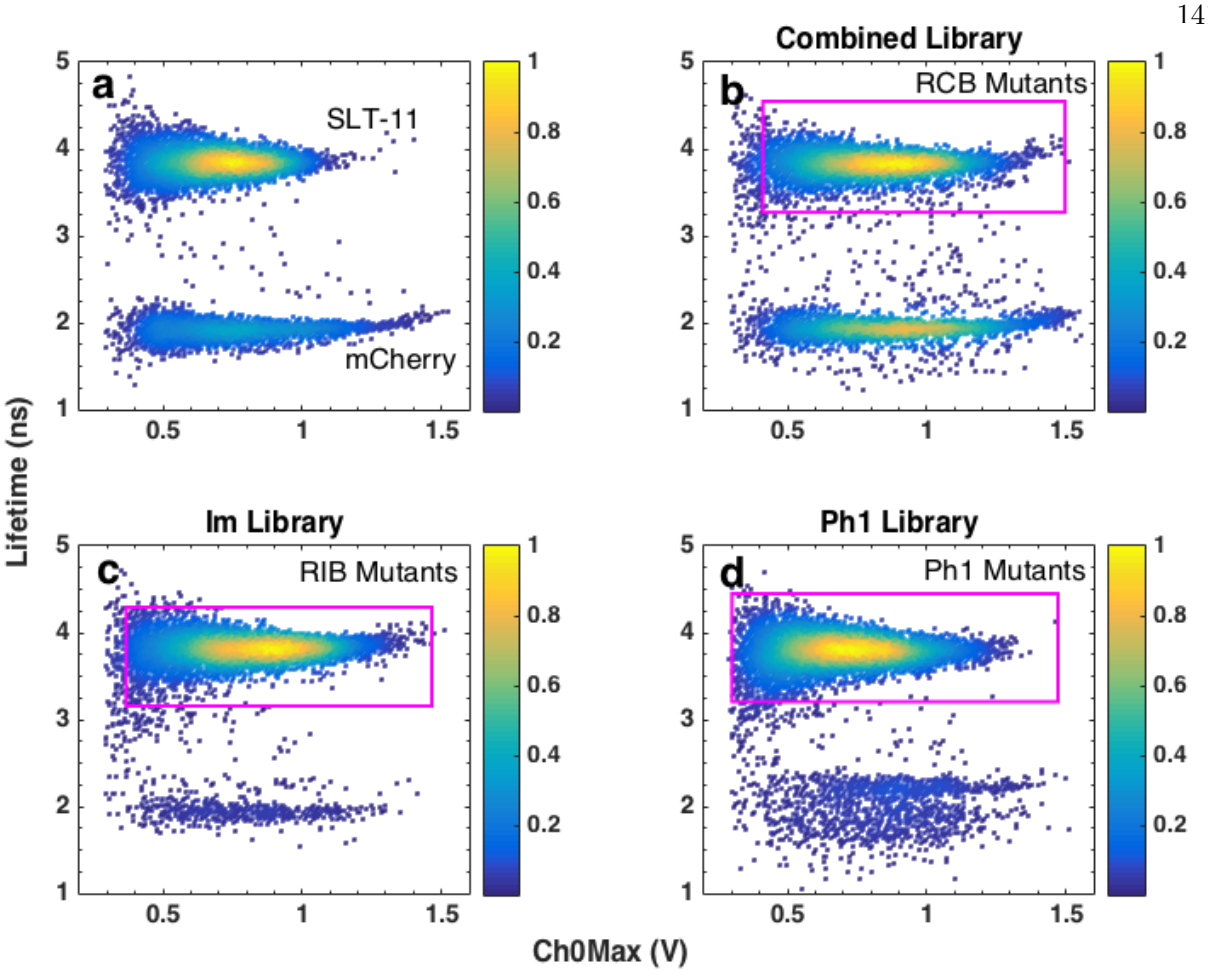

Figure 7.3: Screening results of radiative rate libraries after two rounds of FACS-enrichment eliminating the dim mutants. (a) Screening results of mCherry and SLT-11 mutant. SLT-11 is the immediate precursor of the radiative rate libraries (b, c, d).

These FACS-enriched libraries were expressed on galactose-containing plates and several mutants were selected based on their brightness and approximate lifetimes. Mutants selected from the Combined library with ∼4 ns lifetime were called RCB mutants (R=Radiative, C=Combined, B= selected based on Brightness). Similarly, mutants selected from Im library were called RIB. Ph1 and Ph2 mutants were selected from Ph1 and Ph2 libraries, respectively. DNA sequences of mutants with ∼2 ns lifetimes revealed unwanted R197I mutations that occurred inadvertently during library constructions. I197R mutation was introduced in the mCherry mutants at the very beginning of the directed evolution. This mutation was observed to play beneficial roles in the enhancement

of excited state lifetime and fluorescence quantum yield of the mutants. Therefore, the mutants having $\sim$ 2 ns lifetime where the reversal of I197R mutation occurred, were not pursued further.

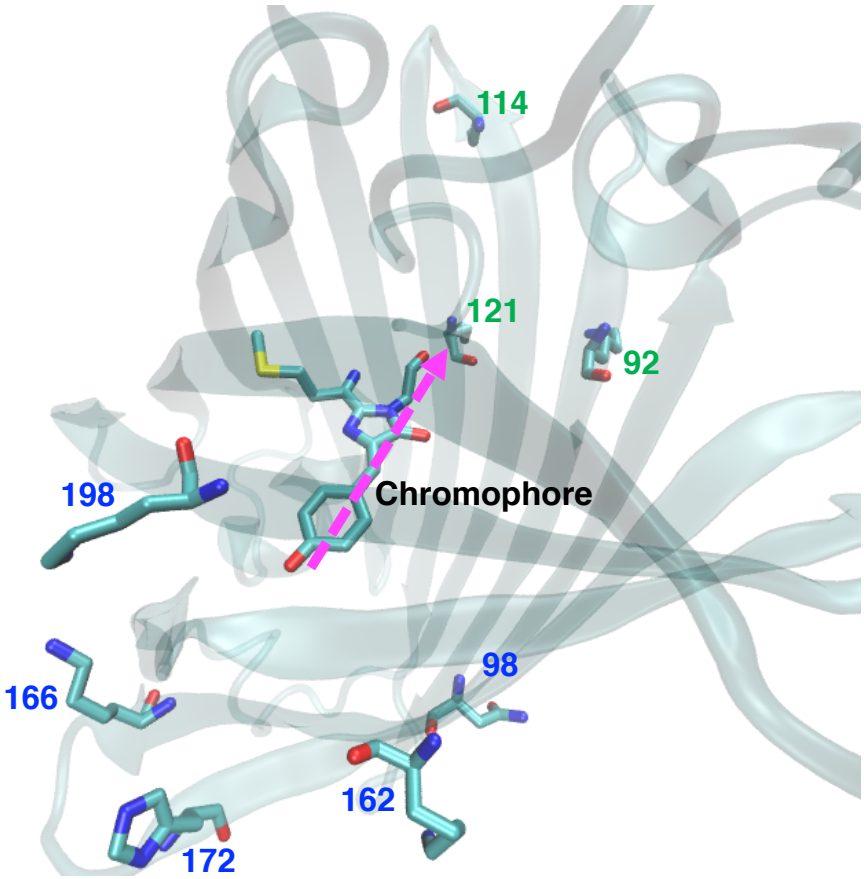

Figure 7.4: Mutations that appeared in the variants derived from the radiative rate libraries. Residues at positions 98, 162, 166, 172 and 198 are located at the phenolate-end of the chromophore while residues at positions 92, 121 and 114 are in the imidazolinone-end of the chromophore. The pink arrow shows the approximate direction of the transition dipole moment in a DsRed-like chromophore [182].

Table 7.4 depicts the mutations identified after screening the radiative rate libraries and selecting mutants with improved brightness compared to the precursor, SLT-11. There was no definitive pattern of charge placement for these mutations. However, we found a re-distribution of the charged residues in the phenolate- and imidazolinone-ends of the chromophore. We also found several mutations that were also observed in mRuby3, mScarlet or mApple FPs. For instance, K166R appeared in RCB-6, and was also found during the evolution of C4PB and mScarlet [104].

The K92R mutation was found to enhance the brightness of mApple [11], and was identified in RCB-2. During the evolution from mRuby2 to mRuby3 [102], C114E (*i.e.* polar to negatively charged) mutation was observed. However, in both RCB-2 and RCB-6, glutamines (polar) at this position were substituted with positively charged lysine or arginine, respectively.

Table 7.4: Amino acid mutations identified in the radiative rate mutants. The numbering of the residues is based on a reported mCherry crystal structure (PBD: 2H5Q).

RFPs	92	114	121	98	162	166	172	198
mCherry	K	Q	K	N	K	K	H	K
SLT-11				S				
RCB-2	R	K	E			N	K	
RCB-6	S	R	S	S	D	R	R	
Ph1-3				S		N	K	S
mScarlet		E				R	R	
mRuby2	T	C	H	R	H			R
mRuby3	T	E	N	R	D			R
FusionRed	T		N	T	D			R

7.4 *In-vivo* Brightness of the Radiative Rate mutants

FACS screening results displaying the *in-vivo* brightness of the radiative rate mutants upon expression in yeast and mammalian (HeLa) cells are presented in Figure 7.5. To obtain the red and green fluorescence, 561-nm (610/20-nm emission filter) and 488-nm (530/30-nm emission filter) excitations were used, respectively. Mean red and green fluorescence intensities of the mutants were measured from the FACS screening and described in Table 7.5. All of the radiative rate variants showed significant improvement in brightness relative to their precursor SLT-11 upon expression in yeast cells. In particular, RCB-2 and 6 displayed $\sim$ 3.5-fold and $\sim$ 5-fold higher brightness relative to mCherry and were brighter than previously published improved RFPs: mScarlet and mRuby3. All the mutants were characterized with low green fluorescence intensities compared to SDC-5, indicating likely complete chromophore formation. Indeed, the absorption spectra of the mutants did not have prominent 'green peak' (discussed below). A slight increase in green fluorescence in RCB-2 and 6 relative to SLT-11 might be due to bleed-through from the red fluorescence channel

into the green fluorescence channel.

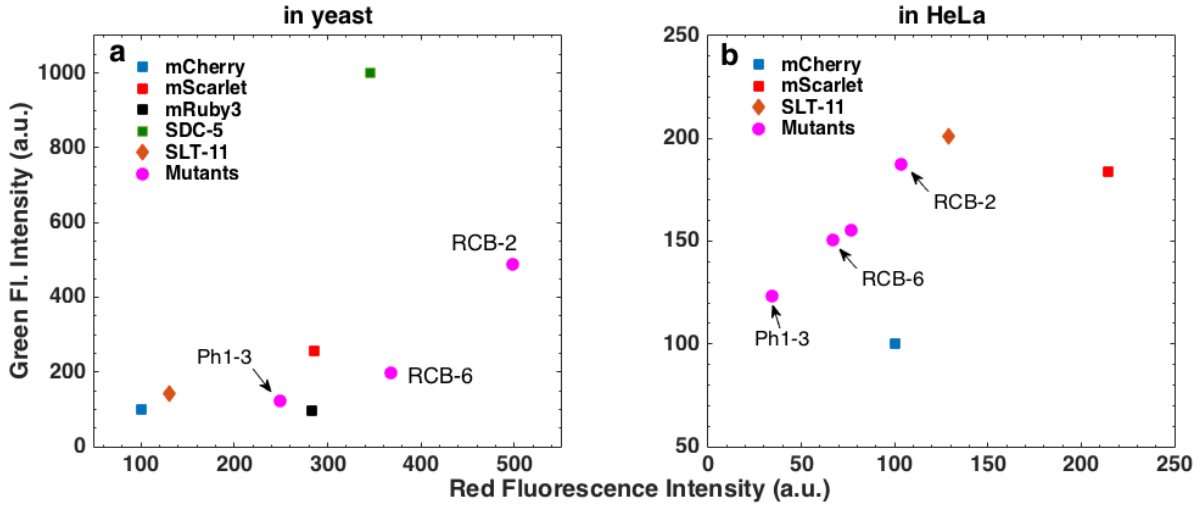

Figure 7.5: (a) Screening results of the radiative rate mutants along with mCherry, mScarlet, SDC-5, mRuby3 and SLT-11 displaying their red and green fluorescence intensities upon expression in yeast. RCB-6 and RCB-2 show increased red fluorescence compared to mScarlet and mRuby3. (b) FACS screening results of the radiative rate mutants upon expression in HeLa cells as a fusion to histone 2B, which restricts fluorescence to the nucleus . Mutants showed reduced red fluorescence intensity presumably due to their slow maturation in mammalian cells.

Although the radiative rate mutants showed enhanced brightness in yeast cells, upon expression in HeLa cells, the brightness of all mutants was lower than SLT-11 and mScarlet. This is probably due to their slow maturation or inefficient expression in the mammalian cells. The inefficient expression in the mammalian cells might be due to the incorporation of yeast-preferred codons in the mutants during their evolution in yeast. Currently, we are in the process of codon-optimization of the mutants for their efficient expression in mammalian cell-lines.

7.5 *In-vitro* Photo-physical Measurements

Inspired by the increased brightness in yeast cells, a few promising radiative rate mutants were expressed in *E.coli* for purification and subsequent photo-physical investigations. In particular, RCB-2 & RCB-6 were selected for their improved brightness relative to mScarlet and mRuby2. Although Ph1-3 was characterized with lower brightness than mScarlet/mRuby3, cell-lysate and

Table 7.5: FACS screening results displaying mean green and red fluorescence intensity of the mutants upon yeast and mammalian (HeLa) cell expressions. For each run, 10000 cells were screened to quantify their green and red fluorescence intensities.

Mutants	Green Fl. (in yeast)	Red Fl. (in yeast)	Green Fl. (in HeLa)	Red Fl. (in HeLa)
mCherry	100	100	100	100
mScarlet	257	286	184	214
mRuby3	95	283	-	-
SDC-5	1000	346	-	-
SLT-11	141	130	201	129
Ph1-3	123	249	123	34
RCB-2	489	498	187	103
RCB-6	197	368	150	67

microfluidic-based measurements revealed a significant decrease in its excited state lifetime. As a decrease in lifetime might be associated with increased radiative rate in the FPs, we also selected the Ph1-3 mutant for further characterization. However, the expression of these mutants was sub-optimal in *E.coli*, thus requiring longer growth time to show the characteristic color of the RFPs. Consequently, yield of the expressed proteins from *E.coli* cultures was low. Measurements of absorption spectra of these mutants showed unusually high background at wavelength <400 nm (Figure 7.6a), indicating the presence of impurities such as non-functional FPs. Due to this unusual background at shorter wavelengths, measurements requiring quantitative absorption spectra, *i.e.*, extinction coefficient and quantum yield could not be measured reliably. However, the emission-based *in-vitro* measurements (pKa, fluorescence lifetime, rotational time-constant) of those mutants were performed.

Figure 7.6 and Table 7.6 display *in-vitro* measurements of the radiative rate mutants. The absorption spectra revealed that the absorption maxima of the mutants remained unchanged compared to the precursor SLT-11. However, the shoulder at $\sim$ 490 nm was slightly increased in RCB-2 and it was totally absent in Ph1-3 (Figure 7.6a). Interestingly, pKa values of the mutants were significantly higher than SLT-11 indicating a decrease in pH resistance. The pKa of RCB-2 was close to that of mScarlet (5.3 in RCB-2 *vs.* 5.4 in mScarlet). The excited state lifetimes of all

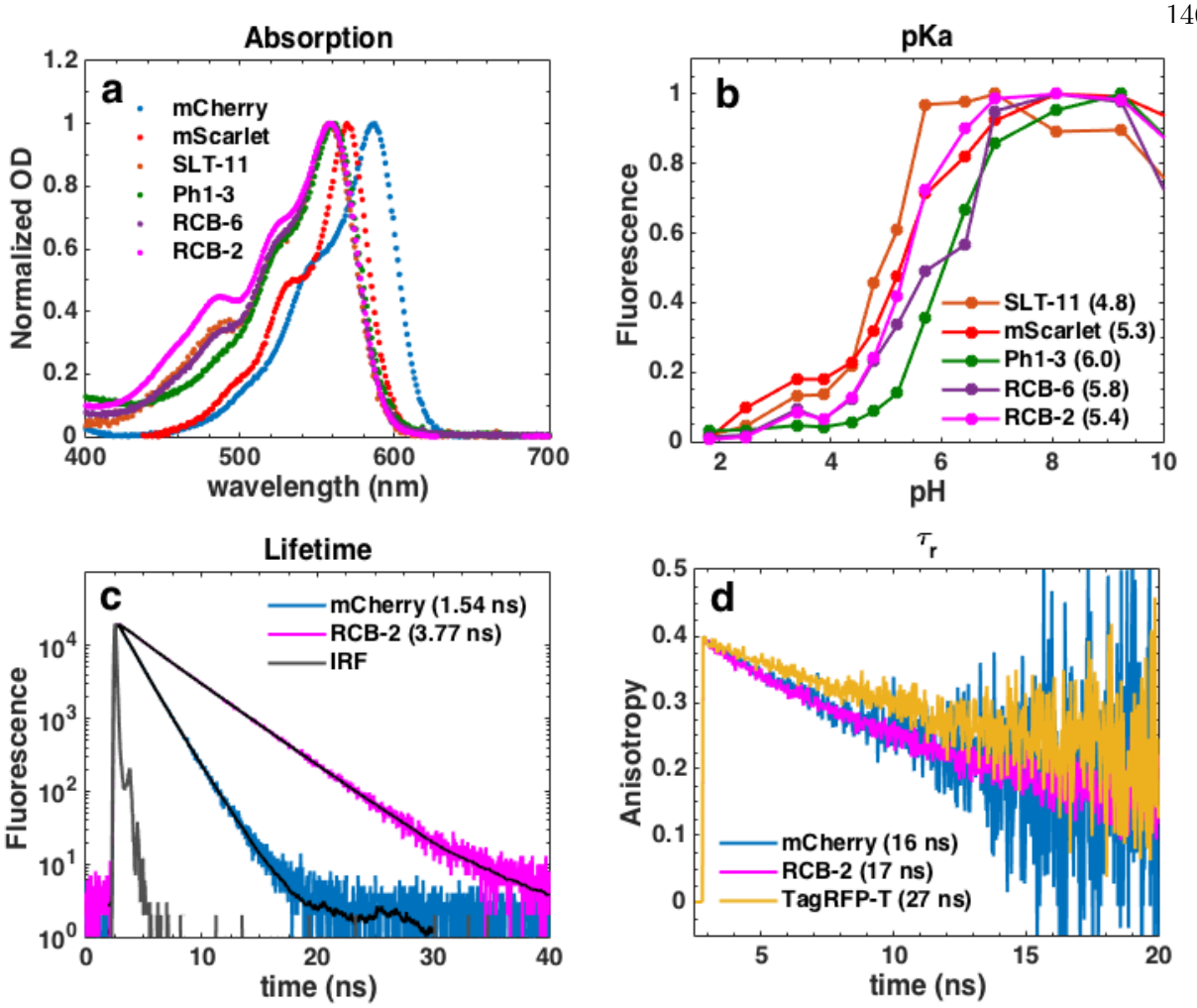

Figure 7.6: *In-vitro* photophysical measurements displaying (a) absorption spectra, (b) pH-dependence of fluorescence (c) excited state lifetimes and (d) anisotropy decays of the radiative rate mutants.

the mutants, particularly Ph1-3, were shorter compared to the precursor SLT-11 (Table 7.6). This might be a signature of increase in radiative rates in these mutants. The fluorescence transients of the mutants were fitted with iterative reconvolution with a bi-exponential function using the measured instrument response function (IRF) of the system. The rotational time-constant (τ_r) of the mutants was obtained by fitting their fluorescence anisotropy decays with a single exponential function. As Table 7.6 describes, all the radiative rate mutants were found to have similar τ_r as mCherry, suggesting they likely retained *in-vitro* monomeric character. TagRFP-T was characterized with slower τ_r, relative to the other mutants. This is consistent with its reported pronounced

in-vivo oligomerization tendencies [100, 101].

Table 7.6: *In-vitro* photo-physical measurements of the radiative rate mutants. pKa of mCherry and TagRFP-T were obtained from reference.

Mutants	λ_{max} (nm)	λ_{max} (nm)	pKa	τ (ns)	τ_r (ns)
mCherry	587	611	< 4.5	1.55	16
TagRFP-T	555	584	4.6	2.31	27
SLT-11	558	588	4.8	3.82	16
Ph1-3	561	591	6.0	3.57	17
RCB-6	559	588	5.8	3.72	17
RCB-2	559	591	5.4	3.77	17

7.6 Discussion

We have employed a novel rational design for the directed evolution of brightness in red fluorescent proteins. Based on fundamental principles, we hypothesized that the transition dipole moment (μ_{12}) involved in the chromophore excitation or emission can be effectively tuned to enhance extinction coefficient or radiative rates of the FPs, respectively, leading to their improved brightness. We argued that this tuning of μ_{12} can be achieved by the rearrangement of the charged residues along the direction of the transition dipole moment vector *i.e.* the residues located at the phenolate- and imidazolinone-end of the chromophore. Rearrangement of the charge residues at these locations can potentially modify the electric field of the three-dimensional space around the chromophore, thereby altering the electromagnetic coupling between its ground state and excited state. We opted for the outward-pointing residues as it was known from our previous investigations and others [12, 11] that the internal residues at these locations were associated with the proper folding and maturation of the chromophore *etc.*

Based on this hypothesis, we generated 4 site-directed libraries using SLT-11 as a template. Subsequent enrichments and selections of bright mutants resulted in three improved RFPs: Ph1-3, RCB-2 and RCB-6. While all of the mutants were characterized with higher brightness relative to their precursor (SLT-11), RCB-2 and RCB-6 also displayed higher red fluorescence intensity com-

pared to two bright RFPs, mRuby3 and mScarlet, upon expression in yeast. However, brightness of these mutants was sub-optimal upon expression in bacteria and mammalian cell-lines. Further modifications of the radiative rate mutants are underway for their efficient expressions in these organisms.

It is interesting to observe that the outward-pointing residues in the radiative rate mutants cause subtle changes in their absorption spectra (Figure 7.6a). While the spectra of RCB-6 was similar to the precursor SLT-11, the shoulder at ∼490 nm was slightly increased and totally absent in RCB-2 and Ph1-3, respectively. The radiative rate mutants were characterized by lower pH resistance or higher pKa than SLT-11. A similar reduction of the 'green peak' and change in pKa were observed in the generation of mGarnet2, an mRuby2 variant [183]. With the introduction of S171H and V121L mutations, pKa of mGarnet2 reduced to 6.8 from 7.4 with concomitant decrease in the peak at ∼480 nm. The residue at 171 (174 in mCherry numbering) points outward of the β-barrel and close to the phenolate-end of the chromophore.

All the radiative rate mutants showed shorter excited state lifetimes compared to their precursor, SLT-11 (Table 7.6). This might be a signature of their improvement in radiative rate-constants (Eqn. 7.2). Measurements of ϕ and ϵ_{max} of the mutants are required to support this claim unequivocally. The rotational time-constants of the radiative rate, measured from their anisotropy decays, were similar to mCherry. This might indicate that the increased brightness of the mutants is less likely due to aggregation or dimerization. However, *in-vivo* dimerization assay (*i.e.* OSER assay, Chapter 6) is required to quantify the dimerization tendencies of the mutants in cellular environments. Currently, we believe that the improvement in brightness of these mutants is due to their enhanced radiative rates or increased ϵ_{max} or the combination of both. However, improved folding or maturation efficiency of the radiative rate mutants leading to a larger amount of protein production in yeast cells, could also be a viable reason for the observed increase in brightness associated with mutants expressed in yeast cells. More *in-vitro* measurements (ϕ, ϵ_{max}, maturation rate *etc.*) and theoretical calculations *e.g.* mapping of the electric field inside the β-barrel, are needed for the complete understanding of the photo-physical behaviors of these mutants.

Recently, a quantum mechanics/molecular dynamics study by Park *et al.* described the improvement of fluorescence quantum yield for GFP variants through the re-distribution of the electric field inside the chromophore [184]. The authors of the article argued that improvement in ϕ of the GFP mutants was due to the hindrance in twisting (non-radiative) pathway of the chromophore induced by the electric field of the protein β-barrel. Their simulations predicted that increased electric field in the phenolate-end and decreased field in the imidazolinone-end of the chromophore was beneficial for improved ϕ in the GFP mutants. The authors also found that the residues in the phenolate-end were more influential in controlling the electrostatic potential of the FPs. This is in line with our observations of the mutations appeared in the radiative rate mutants (Figure 7.4) and also from the analyses of mScarlet, mRuby3, and C4PB mutations. However, there was no clear pattern of positively and negatively charged residues in the context of their respective locations at phenolate- and imidazolinone-end of the chromophore. Instead we found a re-distribution of the charged residues at the different ends of the chromophore (Table 7.4).

Improving the fluorescence quantum yield of FPs by decreasing the non-radiative pathways has a deleterious effect in their photostabilities. In previous work, we observed the fluorescence lifetimes and photostabilities of the RFP mutants were inversely-correlated [55]. This can be explained by the fact that, upon increasing the lifetime, the molecule spends a longer time in the excited states, which can increase the likelihood of various chemical changes (*e.g.* dark sate conversions, forming of radical species *etc.*) which ultimately leads to higher photobleaching. On the other hand, increasing radiative rates of the FPs can lead to an improvement in ϕ (beneficial for brightness) and reduction in lifetime (beneficial for photostability). Therefore, simultaneous improvement in brightness and photostability can be achieved by enhancing the radiative rates of the FPs. Suppression of photobleaching was observed in GFP and mCherry by increasing their radiative rates in nanofibers or nanostructures [185, 186].

Throughout our engineering effort of the radiative rate mutants and the FusionRed mutants (FR-13 and FRX mutants) described in Chapter 6, a resounding inconsistency of brightness of the FPs in yeast and mammalian cells was observed. Radiative rate mutants, similar to the FRX

mutants, were evolved in yeast and indeed the brightness in yeast was superb. However, this higher brightness of the mutants was not reproducible in the mammalian cell lines. While this indicates the complexity of the expression of FPs in different organisms, it is a clear message of "you get what you select". At this point, it is not clear why the FPs express differentially in yeast and mammalian cell-lines. The possible explanation would be different pH- & temperature-resistance, choice of codons in yeast and mammalian cells or combination of these factors. Detailed and careful investigations need to be carried out to find the answer.

7.7 Conclusion

In this Chapter, enhancement of brightness in RFPs based on a novel approach was discussed. We hypothesized that amino acid residues that point outward of the β-barrel and located near the phenolate- and imidazolinone-end of the chromophore can be substituted with charged residues to modulate the transition dipole moments of the chromophore involving its excitation or emission. This can be harnessed to increase the radiative rate or oscillator strength of the transition leading to enhancement of fluorescence quantum yield or extinction coefficient of the FPs. Based on this hypothesis, four site-directed libraries were generated and multiple bright mutants were selected. Some of the mutants displayed significant improvement in brightness upon expression in yeast relative to the previously published bright RFPs *e.g.* mRuby3 or mScarlet. However, expression efficiency of these mutants was sub-optimal in bacteria and mammalian cell-lines presumably due to slow maturation in these organisms. Current effort involves further mutagenesis of these mutants for efficient expression in mammalian cells. Detailed *in-vitro* measurements and theoretical investigations are needed for in-depth understanding of the improvement in brightness of these mutants. We speculate that the strategy described in this Chapter can be readily employed in improving the brightness of other sub-optimal FPs, *e.g.*, infra-red FPs.

Chapter 8

Future Directions

With site-directed mutagenesis of C12 targeting 143, 161 and 163 residues, several of mutants were produced with lifetime ranging from ∼1 ns to ∼4 ns. The measurement of their fluorescence quantum yield revealed a set mutants having fluorescence quantum yields ranging from 10% to 71%. The analyses of lifetime and fluorescence quantum yield of the mutants revealed a linear trend indicating similar radiative rate-constants of the mutants. Detailed *in-vitro* measurements of these closely related mutants can reveal the inter-relation of different photo-physical parameters with enhancement of ϕ. From these mutants, underlying mechanism(s) behind the improvement in the quantum yield of the RFPs can be studied in a systematic manner. The contribution of planarity, electric field, electrostatic interactions *etc.* can be investigated in the context of improvement in ϕ.

It is well-known in the literature that chromophore formation in RFPs occurs through a branched pathway. After the initial cyclization of the chromophore-forming residues, a fraction of the FP can form a GFP-like chromophore (*via* GFP pathway), while rest of the fraction forms an RFP-like chromophore through a blue-emitting intermediate (*via* RFP pathway). Some RFPs, *e.g.* mCherry, show a single peak around ∼ 560-580 nm in their absorption spectra indicating the chromophore formation pathway is heavily biased towards the formation of red-emitting chromophore. On the other hand, absorption spectra of some of the mCherry mutants, *e.g.*, SLT-1, were characterized with two peaks ∼490 nm (green peak) and ∼560 nm (red peak). This suggests that these mutants have propensities to go either GFP or RFP pathway forming a mixture of red and green-emitting FPs. Currently it is not known what molecular environments around the

chromophore-forming tri-peptide drives some reactions to GFP or RFP pathways. In our course of mutagenesis, we have generated multiple mCherry mutants with varying degree of 'green peak' intensities. Mutational analyses, time-resolved absorption-emission spectra *etc.* coupled with molecular dynamics simulations involving these mutants can reveal the molecular origin of the branching pathways in the formation of RFP chromophores. This can help the rational designing of the FPs with complete chromophore maturation.

In the course of evolving FusionRed, we generated FR-1, FR-13, FSD-9 and FSD-11 mutants which show interesting and contrasting photophysical properties. In FR-1, a single mutation L177M improves its maturation speed. On the other hand, FR-13 was characterized with very slow maturation. Further analyses involving FR-1 and FR-13 can reveal the molecular origin of the diverse maturation kinetics in these mutants. While photoswitching in FSD-9 is eliminated with a single mutation (C165V), photoactivation is induced in FSD-11 with C165L mutation upon 561-nm illumination. Detailed photo-physical and structural investigations including DSC, GSR, single molecule fluorescence trajectories of these mutants can elucidate the underlying mechanism of the light-induced behaviors in these mutants. These understandings can be used to generate photostable, photoswitching and photoactivatable version of FusionRed.

Bibliography

[1] Osamu Shimomura, Frank H Johnson, and Yo Saiga. Extraction, purification and properties of aequorin, a bioluminescent protein from the luminous hydromedusan, aequorea. Journal of Cellular Physiology, 59(3):223–239, 1962.

[2] Chris W Cody, Douglas C Prasher, William M Westler, Franklyn G Prendergast, and William W Ward. Chemical structure of the hexapeptide chromophore of the aequorea green-fluorescent protein. Biochemistry, 32(5):1212–1218, 1993.

[3] Osamu Shimomura. Structure of the chromophore of aequorea green fluorescent protein. FEBS letters, 104(2):220–222, 1979.

[4] Douglas C Prasher, Virginia K Eckenrode, William W Ward, Frank G Prendergast, and Milton J Cormier. Primary structure of the aequorea victoria green-fluorescent protein. Gene, 111(2):229–233, 1992.

[5] M Chalfie, Y Tu, G Euskirchen, WW Ward, and DC Prasher. Green fluorescent protein as a marker for gene expression. Science, 263(5148):802–805, 1994.

[6] Roger Heim, Douglas C Prasher, and Roger Y Tsien. Wavelength mutations and posttranslational autoxidation of green fluorescent protein. Proceedings of the National Academy of Sciences, 91(26):12501–12504, 1994.

[7] Roger Heim and Roger Y Tsien. Engineering green fluorescent protein for improved brightness, longer wavelengths and fluorescence resonance energy transfer. Current biology, 6(2):178–182, 1996.

[8] Takeharu Nagai, Keiji Ibata, Eun Sun Park, Mie Kubota, Katsuhiko Mikoshiba, and Atsushi Miyawaki. A variant of yellow fluorescent protein with fast and efficient maturation for cell-biological applications. Nature biotechnology, 20(1):87–90, 2002.

[9] Mikhail V Matz, Arkady F Fradkov, Yulii A Labas, Aleksandr P Savitsky, Andrey G Zaraisky, Mikhail L Markelov, and Sergey A Lukyanov. Fluorescent proteins from nonbioluminescent anthozoa species. Nature biotechnology, 17(10), 1999.

[10] Geoffrey S Baird, David A Zacharias, and Roger Y Tsien. Biochemistry, mutagenesis, and oligomerization of dsred, a red fluorescent protein from coral. Proceedings of the National Academy of Sciences, 97(22):11984–11989, 2000.

[11] Nathan C Shaner, Michael Z Lin, Michael R McKeown, Paul A Steinbach, Kristin L Hazelwood, Michael W Davidson, and Roger Y Tsien. Improving the photostability of bright monomeric orange and red fluorescent proteins. Nat Meth, 5(6):545–551, 06 2008.

[12] Nathan C Shaner, Robert E Campbell, Paul A Steinbach, Ben NG Giepmans, Amy E Palmer, and Roger Y Tsien. Improved monomeric red, orange and yellow fluorescent proteins derived from discosoma sp. red fluorescent protein. Nature biotechnology, 22(12):1567, 2004.

[13] Robert E Campbell, Oded Tour, Amy E Palmer, Paul A Steinbach, Geoffrey S Baird, David A Zacharias, and Roger Y Tsien. A monomeric red fluorescent protein. Proceedings of the National Academy of Sciences, 99(12):7877–7882, 2002.

[14] Roger Y. Tsien. The green fluorescent protein. Annual Review of Biochemistry, 67(1):509–544, 1998. PMID: 9759496.

[15] Eric Betzig, George H Patterson, Rachid Sougrat, O Wolf Lindwasser, Scott Olenych, Juan S Bonifacino, Michael W Davidson, Jennifer Lippincott-Schwartz, and Harald F Hess. Imaging intracellular fluorescent proteins at nanometer resolution. Science, 313(5793):1642–1645, 2006.

[16] Jan Vogelsang, Christian Steinhauer, Carsten Forthmann, Ingo H. Stein, Britta Person-Skegro, Thorben Cordes, and Philip Tinnefeld. Make them blink: Probes for super-resolution microscopy. ChemPhysChem, 11(12):2475–2490, 2010.

[17] Michael Hofmann, Christian Eggeling, Stefan Jakobs, and Stefan W Hell. Breaking the diffraction barrier in fluorescence microscopy at low light intensities by using reversibly photoswitchable proteins. Proceedings of the National Academy of Sciences of the United States of America, 102(49):17565–17569, 2005.

[18] Fan Yang. The molecular structure of green fluorescent protein. PhD thesis, Rice University, 1997.

[19] Peter Dedecker, Frans C. De Schryver, and Johan Hofkens. Fluorescent proteins: Shine on, you crazy diamond. Journal of the American Chemical Society, 135(7):2387–2402, 2013.

[20] Prem P Chapagain, Chola K Regmi, and William Castillo. Fluorescent protein barrel fluctuations and oxygen diffusion pathways in mcherry. The Journal of chemical physics, 135(23):12B613, 2011.

[21] Timothy I Wood, David P Barondeau, Chiharu Hitomi, Carey J Kassmann, John A Tainer, and Elizabeth D Getzoff. Defining the role of arginine 96 in green fluorescent protein fluorophore biosynthesis. Biochemistry, 44(49):16211–16220, 2005.

[22] Brian G Reid and Gregory C Flynn. Chromophore formation in green fluorescent protein. Biochemistry, 36(22):6786–6791, 1997.

[23] Timothy D Craggs. Green fluorescent protein: structure, folding and chromophore maturation. Chemical Society Reviews, 38(10):2865–2875, 2009.

[24] Rebekka M Wachter, Jennifer L Watkins, and Hanseong Kim. Mechanistic diversity of red fluorescence acquisition by gfp-like proteins. Biochemistry, 49(35):7417–7427, 2010.

[25] Larry A Gross, Geoffrey S Baird, Ross C Hoffman, Kim K Baldridge, and Roger Y Tsien. The structure of the chromophore within dsred, a red fluorescent protein from coral. Proceedings of the National Academy of Sciences, 97(22):11990–11995, 2000.

[26] Vladislav V Verkhusha, Dmitry M Chudakov, Nadya G Gurskaya, Sergey Lukyanov, and Konstantin A Lukyanov. Common pathway for the red chromophore formation in fluorescent proteins and chromoproteins. Chemistry & biology, 11(6):845–854, 2004.

[27] Rita L Strack, Daniel E Strongin, Laurens Mets, Benjamin S Glick, and Robert J Keenan. Chromophore formation in dsred occurs by a branched pathway. Journal of the American Chemical Society, 132(24):8496–8505, 2010.

[28] Ksenia B Bravaya, Oksana M Subach, Nadezhda Korovina, Vladislav V Verkhusha, and Anna I Krylov. Insight into the common mechanism of the chromophore formation in the red fluorescent proteins: the elusive blue intermediate revealed. Journal of the American Chemical Society, 134(5):2807–2814, 2012.

[29] Sergei Pletnev, Fedor V Subach, Zbigniew Dauter, Alexander Wlodawer, and Vladislav V Verkhusha. Understanding blue-to-red conversion in monomeric fluorescent timers and hydrolytic degradation of their chromophores. Journal of the American Chemical Society, 132(7):2243–2253, 2010.

[30] Oksana M Subach, Vladimir N Malashkevich, Wendy D Zencheck, Kateryna S Morozova, Kiryl D Piatkevich, Steven C Almo, and Vladislav V Verkhusha. Structural characterization of acylimine-containing blue and red chromophores in mtagbfp and tagrfp fluorescent proteins. Chemistry & biology, 17(4):333–341, 2010.

[31] Fedor V Subach, Vladimir N Malashkevich, Wendy D Zencheck, Hui Xiao, Grigory S Filonov, Steven C Almo, and Vladislav V Verkhusha. Photoactivation mechanism of pamcherry based on crystal structures of the protein in the dark and fluorescent states. Proceedings of the National Academy of Sciences, 106(50):21097–21102, 2009.

[32] Robert M. Dickson, Andrew B. Cubitt, Roger Y. Tsien, and W. E. Moerner. On/off blinking and switching behaviour of single molecules of green fluorescent protein. Nature, 388(6640):355–358, 07 1997.

[33] Premashis Manna and Ralph Jimenez. Time and frequency-domain measurement of ground-state recovery times in red fluorescent proteins. The Journal of Physical Chemistry B, 119(15):4944–4954, 2015.

[34] Peter Dedecker, Jun-ichi Hotta, Ryoko Ando, Atsushi Miyawaki, Yves Engelborghs, and Johan Hofkens. Fast and reversible photoswitching of the fluorescent protein dronpa as evidenced by fluorescence correlation spectroscopy. Biophysical journal, 91(5):L45–L47, 2006.

[35] Andreas Schenk, Sergey Ivanchenko, Carlheinz Röcker, Jörg Wiedenmann, and G Ulrich Nienhaus. Photodynamics of red fluorescent proteins studied by fluorescence correlation spectroscopy. Biophysical journal, 86(1):384–394, 2004.

[36] Petra Schwille, Susanne Kummer, Ahmed A Heikal, WE Moerner, and Watt W Webb. Fluorescence correlation spectroscopy reveals fast optical excitation-driven intramolecular dynamics of yellow fluorescent proteins. Proceedings of the National Academy of Sciences, 97(1):151–156, 2000.

[37] Martin Andresen, Andre C. Stiel, Simon Trowitzsch, Gert Weber, Christian Eggeling, Markus C. Wahl, Stefan W. Hell, and Stefan Jakobs. Structural basis for reversible photoswitching in dronpa. Proceedings of the National Academy of Sciences, 104(32):13005–13009, 2007.

[38] Russell B. Vegh, Ksenia B. Bravaya, Dmitry A. Bloch, Andreas S. Bommarius, Laren M. Tolbert, Michael Verkhovsky, Anna I. Krylov, and Kyril M. Solntsev. Chromophore photoreduction in red fluorescent proteins is responsible for bleaching and phototoxicity. The Journal of Physical Chemistry B, 118(17):4527–4534, 2014. PMID: 24712386.

[39] Ryoko Ando, Hideaki Mizuno, and Atsushi Miyawaki. Regulated fast nucleocytoplasmic shuttling observed by reversible protein highlighting. Science, 306(5700):1370–1373, 2004.

[40] Fedor V Subach, Lijuan Zhang, Theodorus WJ Gadella, Nadya G Gurskaya, Konstantin A Lukyanov, and Vladislav V Verkhusha. Red fluorescent protein with reversibly photoswitchable absorbance for photochromic fret. Chemistry & biology, 17(7):745–755, 2010.

[41] Konstantin A Lukyanov, Arkady F Fradkov, Nadya G Gurskaya, Mikhail V Matz, Yulii A Labas, Aleksandr P Savitsky, Mikhail L Markelov, Andrey G Zaraisky, Xiaoning Zhao, Yu Fang, et al. Natural animal coloration can be determined by a nonfluorescent green fluorescent protein homolog. Journal of Biological Chemistry, 275(34):25879–25882, 2000.

[42] Xi Zhang, Mingshu Zhang, Dong Li, Wenting He, Jianxin Peng, Eric Betzig, and Pingyong Xu. Highly photostable, reversibly photoswitchable fluorescent protein with high contrast ratio for live-cell superresolution microscopy. Proceedings of the National Academy of Sciences, 113(37):10364–10369, 2016.

[43] Ngan Nguyen Bich, Benjamien Moeyaert, Kristof Van Hecke, Peter Dedecker, Hideaki Mizuno, Johan Hofkens, and Luc Van Meervelt. Structural basis for the influence of a single mutation k145n on the oligomerization and photoswitching rate of dronpa. Acta Crystallographica Section D: Biological Crystallography, 68(12):1653–1659, 2012.

[44] Andre C Stiel, Simon Trowitzsch, Gert Weber, Martin Andresen, Christian Eggeling, Stefan W Hell, Stefan Jakobs, and Markus C Wahl. 1.8 å bright-state structure of the reversibly switchable fluorescent protein dronpa guides the generation of fast switching variants. Biochemical Journal, 402(1):35–42, 2007.

[45] Samuel LC Moors, Servaas Michielssens, Cristina Flors, Peter Dedecker, Johan Hofkens, and Arnout Ceulemans. How is cis- trans isomerization controlled in dronpa mutants? a replica exchange molecular dynamics study. Journal of chemical theory and computation, 4(6):1012–1020, 2008.

[46] George H Patterson and Jennifer Lippincott-Schwartz. A photoactivatable gfp for selective photolabeling of proteins and cells. Science, 297(5588):1873–1877, 2002.

[47] Fedor V Subach, George H Patterson, Suliana Manley, Jennifer M Gillette, Jennifer Lippincott-Schwartz, and Vladislav V Verkhusha. Photoactivatable mcherry for high-resolution two-color fluorescence microscopy. Nature methods, 6(2):153–159, 2009.

[48] Samuel T Hess, Thanu PK Girirajan, and Michael D Mason. Ultra-high resolution imaging by fluorescence photoactivation localization microscopy. Biophysical journal, 91(11):4258–4272, 2006.

[49] Nadya G Gurskaya, Vladislav V Verkhusha, Alexander S Shcheglov, Dmitry B Staroverov, Tatyana V Chepurnykh, Arkady F Fradkov, Sergey Lukyanov, and Konstantin A Lukyanov. Engineering of a monomeric green-to-red photoactivatable fluorescent protein induced by blue light. Nature biotechnology, 24(4):461, 2006.

[50] Ryoko Ando, Hiroshi Hama, Miki Yamamoto-Hino, Hideaki Mizuno, and Atsushi Miyawaki. An optical marker based on the uv-induced green-to-red photoconversion of a fluorescent protein. Proceedings of the National Academy of Sciences, 99(20):12651–12656, 2002.

[51] Jörg Wiedenmann, Sergey Ivanchenko, Franz Oswald, Florian Schmitt, Carlheinz Röcker, Anya Salih, Klaus-Dieter Spindler, and G Ulrich Nienhaus. Eosfp, a fluorescent marker protein with uv-inducible green-to-red fluorescence conversion. Proceedings of the National Academy of Sciences of the United States of America, 101(45):15905–15910, 2004.

[52] Michael J Rust, Mark Bates, and Xiaowei Zhuang. Sub-diffraction-limit imaging by stochastic optical reconstruction microscopy (storm). Nature methods, 3(10):793–796, 2006.

[53] Chenxi Duan, Virgile Adam, Martin Byrdin, Jacqueline Ridard, Sylvie Kieffer-Jaquinod, Cécile Morlot, Delphine Arcizet, Isabelle Demachy, and Dominique Bourgeois. Structural evidence for a two-regime photobleaching mechanism in a reversibly switchable fluorescent protein. Journal of the American Chemical Society, 135(42):15841–15850, 2013.

[54] I. I. Shemiakina, G. V. Ermakova, P. J. Cranfill, M. A. Baird, R. A. Evans, E. A. Souslova, D. B. Staroverov, A. Y. Gorokhovatsky, E. V. Putintseva, T. V. Gorodnicheva, T. V. Chepurnykh, L. Strukova, S. Lukyanov, A. G. Zaraisky, M. W. Davidson, D. M. Chudakov, and D. Shcherbo. A monomeric red fluorescent protein with low cytotoxicity. Nat Commun, 3:1204, 11 2012.

[55] Kevin M Dean, Lloyd M Davis, Jennifer L Lubbeck, Premashis Manna, Pia Friis, Amy E Palmer, and Ralph Jimenez. High-speed multiparameter photophysical analyses of fluorophore libraries. Analytical chemistry, 87(10):5026–5030, 2015.

[56] Kevin M. Dean, Jennifer L. Lubbeck, Jennifer K. Binder, Linda R. Schwall, Ralph Jimenez, and Amy E. Palmer. Analysis of red-fluorescent proteins provides insight into dark-state conversion and photodegradation. Biophysical Journal, 101(4):961–969, 8 2011.

[57] Kevin M. Dean, Jennifer L. Lubbeck, Lloyd M. Davis, Chola K. Regmi, Prem P. Chapagain, Bernard S. Gerstman, Ralph Jimenez, and Amy E. Palmer. Microfluidics-based selection of red-fluorescent proteins with decreased rates of photobleaching. Integr. Biol., 7:263–273, 2015.

[58] Mayu Sugiyama, Asako Sakaue-Sawano, Tadahiro Iimura, Kiyoko Fukami, Tetsuya Kitaguchi, Koichi Kawakami, Hitoshi Okamoto, Shin-ichi Higashijima, and Atsushi Miyawaki. Illuminating cell-cycle progression in the developing zebrafish embryo. Proceedings of the National Academy of Sciences, 106(49):20812–20817, 2009.

[59] Fedor V Subach, Oksana M Subach, Illia S Gundorov, Kateryna S Morozova, Kiryl D Piatkevich, Ana Maria Cuervo, and Vladislav V Verkhusha. Monomeric fluorescent timers that change color from blue to red report on cellular trafficking. Nature chemical biology, 5(2):118–126, 2009.

[60] Kevin M Dean and Amy E Palmer. Advances in fluorescence labeling strategies for dynamic cellular imaging. Nature chemical biology, 10(7):512–523, 2014.

[61] Steffen J Sahl, Stefan W Hell, and Stefan Jakobs. Fluorescence nanoscopy in cell biology. Nature reviews. Molecular cell biology, 2017.

[62] Sina Wäldchen, Julian Lehmann, Teresa Klein, Sebastian Van De Linde, and Markus Sauer. Light-induced cell damage in live-cell super-resolution microscopy. Scientific reports, 5, 2015.

[63] Erik A Rodriguez, Geraldine N Tran, Larry A Gross, Jessica L Crisp, Xiaokun Shu, John Y Lin, and Roger Y Tsien. A far-red fluorescent protein evolved from a cyanobacterial phycobiliprotein. Nature methods, 13(9):763–769, 2016.

[64] Fabian Hertel, Gary CH Mo, Sam Duwé, Peter Dedecker, and Jin Zhang. Refsofi for mapping nanoscale organization of protein-protein interactions in living cells. Cell reports, 14(2):390–400, 2016.

[65] Gary CH Mo, Brian Ross, Fabian Hertel, Premashis Manna, Xinxing Yang, Eric Greenwald, Chris Booth, Ashlee M Plummer, Brian Tenner, Zan Chen, et al. Genetically encoded biosensors for visualizing live-cell biochemical activity at super-resolution. Nature methods, 14(4):427–434, 2017.

[66] Elias M Puchner, Jessica M Walter, Robert Kasper, Bo Huang, and Wendell A Lim. Counting molecules in single organelles with superresolution microscopy allows tracking of the endosome maturation trajectory. Proceedings of the National Academy of Sciences, 110(40):16015–16020, 2013.

[67] Geoffrey S Baird, David A Zacharias, and Roger Y Tsien. Circular permutation and receptor insertion within green fluorescent proteins. Proceedings of the National Academy of Sciences, 96(20):11241–11246, 1999.

[68] Arno Germond, Hideaki Fujita, Taro Ichimura, and Tomonobu M Watanabe. Design and development of genetically encoded fluorescent sensors to monitor intracellular chemical and physical parameters. Biophysical reviews, 8(2):121–138, 2016.

[69] Atsushi Miyawaki and Yusuke Niino. Molecular spies for bioimaging—fluorescent protein-based probes. Molecular cell, 58(4):632–643, 2015.

[70] Allison M Dennis, Won Jong Rhee, David Sotto, Steven N Dublin, and Gang Bao. Quantum dot–fluorescent protein fret probes for sensing intracellular ph. ACS nano, 6(4):2917–2924, 2012.

[71] Jon S Donner, Sebastian A Thompson, Mark P Kreuzer, Guillaume Baffou, and Romain Quidant. Mapping intracellular temperature using green fluorescent protein. Nano letters, 12(4):2107–2111, 2012.

[72] Kazuki Harada, Motoki Ito, Xiaowen Wang, Mika Tanaka, Devina Wongso, Ayumu Konno, Hirokazu Hirai, Hajime Hirase, Takashi Tsuboi, and Tetsuya Kitaguchi. Red fluorescent protein-based camp indicator applicable to optogenetics and in vivo imaging. Scientific Reports, 7, 2017.

[73] Lin Tian, S Andrew Hires, Tianyi Mao, Daniel Huber, M Eugenia Chiappe, Sreekanth H Chalasani, Leopoldo Petreanu, Jasper Akerboom, Sean A McKinney, Eric R Schreiter, et al. Imaging neural activity in worms, flies and mice with improved gcamp calcium indicators. Nature methods, 6(12):875–881, 2009.

[74] Hatim A Zariwala, Bart G Borghuis, Tycho M Hoogland, Linda Madisen, Lin Tian, Chris I De Zeeuw, Hongkui Zeng, Loren L Looger, Karel Svoboda, and Tsai-Wen Chen. A cre-dependent gcamp3 reporter mouse for neuronal imaging in vivo. Journal of Neuroscience, 32(9):3131–3141, 2012.

[75] Tsai-Wen Chen, Trevor J Wardill, Yi Sun, Stefan R Pulver, Sabine L Renninger, Amy Baohan, Eric R Schreiter, Rex A Kerr, Michael B Orger, Vivek Jayaraman, et al. Ultra-sensitive fluorescent proteins for imaging neuronal activity. Nature, 499(7458):295, 2013.

[76] Philip J Dittmer, Jose G Miranda, Jessica A Gorski, and Amy E Palmer. Genetically encoded sensors to elucidate spatial distribution of cellular zinc. Journal of Biological Chemistry, 284(24):16289–16297, 2009.

[77] Jose G Miranda, Amanda L Weaver, Yan Qin, J Genevieve Park, Caitlin I Stoddard, Michael Z Lin, and Amy E Palmer. New alternately colored fret sensors for simultaneous monitoring of zn2+ in multiple cellular locations. PloS one, 7(11):e49371, 2012.

[78] Laurens H Lindenburg, Jan L Vinkenborg, Jorn Oortwijn, Stijn JA Aper, and Maarten Merkx. Magfret: the first genetically encoded fluorescent mg2+ sensor. PloS one, 8(12):e82009, 2013.

[79] Jan L Vinkenborg, Sander MJ van Duijnhoven, and Maarten Merkx. Reengineering of a fluorescent zinc sensor protein yields the first genetically encoded cadmium probe. Chemical Communications, 47(43):11879–11881, 2011.

[80] Erik A Rodriguez, Robert E Campbell, John Y Lin, Michael Z Lin, Atsushi Miyawaki, Amy E Palmer, Xiaokun Shu, Jin Zhang, and Roger Y Tsien. The growing and glowing toolbox of fluorescent and photoactive proteins. Trends in biochemical sciences, 42(2):111–129, 2017.

[81] Brett L Fiedler, Steven Van Buskirk, Kyle P Carter, Yan Qin, Margaret C Carpenter, Amy E Palmer, and Ralph Jimenez. Droplet microfluidic flow cytometer for sorting on transient cellular responses of genetically-encoded sensors. Analytical chemistry, 89(1):711–719, 2016.

[82] Daniel G Jay. Selective destruction of protein function by chromophore-assisted laser inactivation. Proceedings of the National Academy of Sciences, 85(15):5454–5458, 1988.

[83] Maria E Bulina, Dmitriy M Chudakov, Olga V Britanova, Yurii G Yanushevich, Dmitry B Staroverov, Tatyana V Chepurnykh, Ekaterina M Merzlyak, Maria A Shkrob, Sergey Lukyanov, and Konstantin A Lukyanov. A genetically encoded photosensitizer. Nature biotechnology, 24(1):95, 2006.

[84] Kiwamu Takemoto, Tomoki Matsuda, Naoki Sakai, Donald Fu, Masanori Noda, Susumu Uchiyama, Ippei Kotera, Yoshiyuki Arai, Masataka Horiuchi, Kiichi Fukui, et al. Supernova, a monomeric photosensitizing fluorescent protein for chromophore-assisted light inactivation. Scientific reports, 3:2629, 2013.

[85] Xin X Zhou, Hokyung K Chung, Amy J Lam, and Michael Z Lin. Optical control of protein activity by fluorescent protein domains. Science, 338(6108):810–814, 2012.

[86] Lindsey M Costantini, Mikhail Baloban, Michele L Markwardt, Mark Rizzo, Feng Guo, Vladislav V Verkhusha, and Erik L Snapp. A palette of fluorescent proteins optimized for diverse cellular environments. Nature communications, 6:7670, 2015.

[87] Ralph Weissleder et al. A clearer vision for in vivo imaging. Nature biotechnology, 19(4):316–316, 2001.

[88] Matthew G Eason, Adam M Damry, and Roberto A Chica. Structure-guided rational design of red fluorescent proteins: towards designer genetically-encoded fluorophores. Current opinion in structural biology, 45:91–99, 2017.

[89] Fedor V Subach, Kiryl D Piatkevich, and Vladislav V Verkhusha. Directed molecular evolution to design advanced red fluorescent proteins. Nature methods, 8(12):1019–1026, 2011.

[90] Hui-wang Ai, Michelle A Baird, Yi Shen, Michael W Davidson, and Robert E Campbell. Engineering and characterizing monomeric fluorescent proteins for live-cell imaging applications. Nature protocols, 9(4):910, 2014.

[91] Benjamin D Allen and Stephen L Mayo. Dramatic performance enhancements for the faster optimization algorithm. Journal of computational chemistry, 27(10):1071 –1075, 2006.

[92] Roberto A Chica, Matthew M Moore, Benjamin D Allen, and Stephen L Mayo. Generation of longer emission wavelength red fluorescent proteins using computationally designed libraries. Proceedings of the National Academy of Sciences, 107(47):20257–20262, 2010.

[93] John N Davis and Anthony N van den Pol. Viral mutagenesis as a means for generating novel proteins. Journal of virology, 84(3):1625–1630, 2010.

[94] Hiroshi Arakawa, Hiroaki Kudo, Vera Batrak, Randolph B Caldwell, Michael A Rieger, Joachim W Ellwart, and Jean-Marie Buerstedde. Protein evolution by hypermutation and selection in the b cell line dt40. Nucleic acids research, 36(1):e1–e1, 2007.

[95] Lei Wang, W Coyt Jackson, Paul A Steinbach, and Roger Y Tsien. Evolution of new nonantibody proteins via iterative somatic hypermutation. Proceedings of the National Academy of Sciences of the United States of America, 101(48):16745–16749, 2004.

[96] Jessica P Houston, Mark A Naivar, and James P Freyer. Digital analysis and sorting of fluorescence lifetime by flow cytometry. Cytometry Part A, 77(9):861–872, 2010.

[97] Ruofan Cao, Varayini Pankayatselvan, and Jessica P. Houston. Cytometric sorting based on the fluorescence lifetime of spectrally overlapping signals. Opt. Express, 21(12):14816–14831, Jun 2013.

[98] Lloyd M. Davis, Jennifer L. Lubbeck, Kevin M. Dean, Amy E. Palmer, and Ralph Jimenez. Microfluidic cell sorter for use in developing red fluorescent proteins with improved photostability. Lab Chip, 13:2320–2327, 2013.

[99] Ekaterina M Merzlyak, Joachim Goedhart, Dmitry Shcherbo, Mariya E Bulina, Aleksandr S Shcheglov, Arkady F Fradkov, Anna Gaintzeva, Konstantin A Lukyanov, Sergey Lukyanov, Theodorus WJ Gadella, et al. Bright monomeric red fluorescent protein with an extended fluorescence lifetime. Nature methods, 4(7):555, 2007.

[100] Lindsey M Costantini, Matteo Fossati, Maura Francolini, and Erik Lee Snapp. Assessing the tendency of fluorescent proteins to oligomerize under physiologic conditions. Traffic, 13(5):643–649, 2012.

[101] Paula J Cranfill, Brittney R Sell, Michelle A Baird, John R Allen, Zeno Lavagnino, H Martijn de Gruiter, Gert-Jan Kremers, Michael W Davidson, Alessandro Ustione, and David W Piston. Quantitative assessment of fluorescent proteins. Nature methods, 13(7):557–562, 2016.

[102] Bryce T Bajar, Emily S Wang, Amy J Lam, Bongjae B Kim, Conor L Jacobs, Elizabeth S Howe, Michael W Davidson, Michael Z Lin, and Jun Chu. Improving brightness and photostability of green and red fluorescent proteins for live cell imaging and fret reporting. Scientific reports, 6:20889, 2016.

[103] Antonia T Pandelieva, Miranda J Baran, Guido F Calderini, Jenna L McCann, Véronique Tremblay, Sabina Sarvan, James A Davey, Jean-François Couture, and Roberto A Chica. Brighter red fluorescent proteins by rational design of triple-decker motif. ACS chemical biology, 11(2):508–517, 2016.

[104] Daphne S Bindels, Lindsay Haarbosch, Laura Van Weeren, Marten Postma, Katrin E Wiese, Marieke Mastop, Sylvain Aumonier, Guillaume Gotthard, Antoine Royant, Mark A Hink, et al. mscarlet: a bright monomeric red fluorescent protein for cellular imaging. Nature methods, 14(1):53–56, 2017.

[105] Rui Liu, Qing-Nan Liang, Shu-Qi Du, Xiao-Jian Hu, and Yu Ding. The crystal structure of red fluorescent protein tagrfp-t reveals the mechanism of its superior photostability. Biochemical and biophysical research communications, 477(2):229–234, 2016.

[106] Haiyan Ren, Bing Yang, Cheng Ma, Ying S Hu, Peng George Wang, and Lei Wang. Cysteine sulfoxidation increases the photostability of red fluorescent proteins. ACS chemical biology, 11(10):2679 –2684, 2016.

[107] Anika Hense, Karin Nienhaus, and G Ulrich Nienhaus. Exploring color tuning strategies in red fluorescent proteins. Photochemical & Photobiological Sciences, 14(2):200–212, 2015.

[108] Ho-Leung Ng and Michael Z Lin. Structure-guided wavelength tuning in far-red fluorescent proteins. Current opinion in structural biology, 39:124–133, 2016.

[109] Rebekka M Wachter, Marc-André Elsliger, Karen Kallio, George T Hanson, and S James Remington. Structural basis of spectral shifts in the yellow-emission variants of green fluorescent protein. Structure, 6(10):1267–1277, 1998.

[110] Bella L Grigorenko, Alexander V Nemukhin, Igor V Polyakov, and Anna I Krylov. Triple-decker motif for red-shifted fluorescent protein mutants. The journal of physical chemistry letters, 4(10):1743–1747, 2013.

[111] Matthew M Moore, Samuel K Oteng-Pabi, Antonia T Pandelieva, Stephen L Mayo, and Roberto A Chica. Recovery of red fluorescent protein chromophore maturation deficiency through rational design. PloS one, 7(12):e52463, 2012.

[112] Ahmed A. Heikal, Samuel T. Hess, Geoffrey S. Baird, Roger Y. Tsien, and Watt W. Webb. Molecular spectroscopy and dynamics of intrinsically fluorescent proteins: Coral red (dsred) and yellow (citrine). Proceedings of the National Academy of Sciences, 97(22):11996–12001, 2000.

[113] Satoshi Habuchi, Ryoko Ando, Peter Dedecker, Wendy Verheijen, Hideaki Mizuno, Atsushi Miyawaki, and Johan Hofkens. Reversible single-molecule photoswitching in the gfp-like fluorescent protein dronpa. Proceedings of the National Academy of Sciences of the United States of America, 102(27):9511–9516, 2005.

[114] B Lounis, J Deich, FI Rosell, Steven G Boxer, and WE Moerner. Photophysics of ds red, a red fluorescent protein, from the ensemble to the single-molecule level. The Journal of Physical Chemistry B, 105(21):5048–5054, 2001.

[115] Jelle Hendrix, Cristina Flors, Peter Dedecker, Johan Hofkens, and Yves Engelborghs. Dark states in monomeric red fluorescent proteins studied by fluorescence correlation and single molecule spectroscopy. Biophysical Journal, 94(10):4103–4113, 5 2008.

[116] Mikhail Drobizhev, Caleb Stoltzfus, Igor Topol, Jack Collins, Geoffrey Wicks, Alexander Mikhaylov, Lauren Barnett, Thomas E Hughes, and Aleksander Rebane. Multiphoton photochemistry of red fluorescent proteins in solution and live cells. The Journal of Physical Chemistry B, 118(31):9167–9179, 2014.

[117] Sergei Pletnev, Dmitry Shcherbo, Dmitry M. Chudakov, Nadezhda Pletneva, Ekaterina M. Merzlyak, Alexander Wlodawer, Zbigniew Dauter, and Vladimir Pletnev. A crystallographic study of bright far-red fluorescent protein mkate reveals ph-induced cis-trans isomerization of the chromophore. Journal of Biological Chemistry, 283(43):28980–28987, 2008.

[118] Gerardo Abbandonato, Giovanni Signore, Riccardo Nifosì, Valerio Voliani, Ranieri Bizzarri, and Fabio Beltram. Cis–trans photoisomerization properties of gfp chromophore analogs. European Biophysics Journal, 40(11):1205–1214, 2011.

[119] Gerald Donnert, Christian Eggeling, and Stefan W Hell. Major signal increase in fluorescence microscopy through dark-state relaxation. Nat. Methods, 4(81):86, 2007.

[120] Jan Vogelsang, Christian Steinhauer, Carsten Forthmann, Ingo H Stein, Britta Person-Skegro, Thorben Cordes, and Philip Tinnefeld. Make them blink: Probes for super-resolution microscopy. ChemPhysChem, 11(12):2475–2490, 2010.

[121] Ulrike Endesfelder, Sebastian Malkusch, Benjamin Flottmann, Justine Mondry, Piotr Liguzinski, Peter J Verveer, and Mike Heilemann. Chemically induced photoswitching of fluorescent probes—a general concept for super-resolution microscopy. Molecules, 16(4):3106–3118, 2011.

[122] Thomas Dertinger, Mike Heilemann, Robert Vogel, Markus Sauer, and Shimon Weiss. Super-resolution optical fluctuation imaging with organic dyes. Angewandte Chemie, 122(49):9631–9633, 2010.

[123] Fedor V Subach, George H Patterson, Malte Renz, Jennifer Lippincott-Schwartz, and Vladislav V Verkhusha. Bright monomeric photoactivatable red fluorescent protein for two-color super-resolution sptpalm of live cells. Journal of the American Chemical Society, 132(18):6481–6491, 2010.

[124] Tanja Brakemann, Andre C Stiel, Gert Weber, Martin Andresen, Ilaria Testa, Tim Grotjohann, Marcel Leutenegger, Uwe Plessmann, Henning Urlaub, Christian Eggeling, et al. A reversibly photoswitchable gfp-like protein with fluorescence excitation decoupled from switching. Nature biotechnology, 29(10):942–947, 2011.

[125] Jennifer L. Lubbeck, Kevin M. Dean, Hairong Ma, Amy E. Palmer, and Ralph Jimenez. Microfluidic flow cytometer for quantifying photobleaching of fluorescent proteins in cells. Analytical Chemistry, 84(9):3929–3937, 2012.

[126] Flaminia Malvezzi-Campeggi, Michael Jahnz, Katrin G Heinze, Petra Dittrich, and Petra Schwille. Light-induced flickering of dsred provides evidence for distinct and interconvertible fluorescent states. Biophysical journal, 81(3):1776–1785, 2001.

[127] Evangelos Gatzogiannis, Xinxin Zhu, Ya-Ting Kao, and Wei Min. Observation of frequency-domain fluorescence anomalous phase advance due to dark-state hysteresis. The Journal of Physical Chemistry Letters, 2(5):461–466, 2011.

[128] Evangelos Gatzogiannis, Xinxin Zhu, Ya-Ting Kao, and Wei Min. Observation of frequency-domain fluorescence anomalous phase advance due to dark-state hysteresis. The Journal of Physical Chemistry Letters, 2(5):461–466, 2011.

[129] Joseph R. Lakowicz. Principles of Fluorescence Spectroscopy. Springer, 3 rd edition, 2006.

[130] G. H. Patterson, S. M. Knobel, W. D. Sharif, S. R. Kain, and D. W. Piston. Use of the green fluorescent protein and its mutants in quantitative fluorescence microscopy. Biophysical Journal, 73(5):2782–2790, 11 1997.

[131] Valerio Voliani, Ranieri Bizzarri, Riccardo Nifosì, Stefania Abbruzzetti, Elena Grandi, Cristiano Viappiani, and Fabio Beltram. Cis- trans photoisomerization of fluorescent-protein chromophores. The Journal of Physical Chemistry B, 112(34):10714–10722, 2008.

[132] Katjuša Brejc, Titia K Sixma, Paul A Kitts, Steven R Kain, Roger Y Tsien, Mats Ormö, and S James Remington. Structural basis for dual excitation and photoisomerization of the aequorea victoria green fluorescent protein. Proceedings of the National Academy of Sciences, 94(6):2306–2311, 1997.

[133] Aline Regis Faro, Philippe Carpentier, Gabriella Jonasson, Guillaume Pompidor, Delphine Arcizet, Isabelle Demachy, and Dominique Bourgeois. Low-temperature chromophore isomerization reveals the photoswitching mechanism of the fluorescent protein padron. Journal of the American Chemical Society, 133(41):16362–16365, 2011.

[134] Hideaki Mizuno, Tapas Kumar Mal, Markus Wälchli, Akihiro Kikuchi, Takashi Fukano, Ryoko Ando, Jeyaraman Jeyakanthan, Junichiro Taka, Yoshitsugu Shiro, Mitsuhiko Ikura, et al. Light-dependent regulation of structural flexibility in a photochromic fluorescent protein. Proceedings of the National Academy of Sciences, 105(27):9227–9232, 2008.

[135] Ya-Ting Kao, Xinxin Zhu, and Wei Min. Protein-flexibility mediated coupling between photoswitching kinetics and surrounding viscosity of a photochromic fluorescent protein. Proceedings of the National Academy of Sciences, 109(9):3220–3225, 2012.

[136] Arijit Roy, Martin J Field, Virgile Adam, and Dominique Bourgeois. The nature of transient dark states in a photoactivatable fluorescent protein. Journal of the American Chemical Society, 133(46):18586–18589, 2011.

[137] Virgile Adam, Philippe Carpentier, Sebastien Violot, Mickaël Lelimousin, Claudine Darnault, G Ulrich Nienhaus, and Dominique Bourgeois. Structural basis of x-ray-induced transient photobleaching in a photoactivatable green fluorescent protein. Journal of the American Chemical Society, 131(50):18063–18065, 2009.

[138] WE Moerner. A dozen years of single-molecule spectroscopy in physics, chemistry, and biophysics, 2002.

[139] Wai-Tak Yip, Dehong Hu, Ji Yu, David A Vanden Bout, and Paul F Barbara. Classifying the photophysical dynamics of single-and multiple-chromophoric molecules by single molecule spectroscopy. The Journal of Physical Chemistry A, 102(39):7564–7575, 1998.

[140] Philip Tinnefeld and Markus Sauer. Branching out of single-molecule fluorescence spectroscopy: Challenges for chemistry and influence on biology. Angewandte Chemie International Edition, 44(18):2642–2671, 2005.

[141] Shimon Weiss. Fluorescence spectroscopy of single biomolecules. Science, 283(5408):1676–1683, 1999.

[142] MF Garcia-Parajo, Gezina MJ Segers-Nolten, J-A Veerman, Jan Greve, and NF Van Hulst. Real-time light-driven dynamics of the fluorescence emission in single green fluorescent protein molecules. Proceedings of the National Academy of Sciences, 97(13):7237–7242, 2000.

[143] Erwin JG Peterman, Sophie Brasselet, and WE Moerner. The fluorescence dynamics of single molecules of green fluorescent protein. The Journal of Physical Chemistry A, 103(49):10553–10560, 1999.

[144] MF Garcia-Parajo, M Koopman, EMHP Van Dijk, Vinod Subramaniam, and NF Van Hulst. The nature of fluorescence emission in the red fluorescent protein dsred, revealed by single-molecule detection. Proceedings of the National Academy of Sciences, 98(25):14392–14397, 2001.

[145] Britta Seefeldt, Robert Kasper, Thorsten Seidel, Philip Tinnefeld, Karl-Josef Dietz, Mike Heilemann, and Markus Sauer. Fluorescent proteins for single-molecule fluorescence applications. Journal of biophotonics, 1(1):74–82, 2008.

[146] Christian Blum and Vinod Subramaniam. Single-molecule spectroscopy of fluorescent proteins. Analytical and bioanalytical chemistry, 393(2):527, 2009.

[147] B. Lounis, J. Deich, F. I. Rosell, Steven G. Boxer, and W. E. Moerner. Photophysics of dsred, a red fluorescent protein, from the ensemble to the single-molecule level. The Journal of Physical Chemistry B, 105(21):5048–5054, 2001.

[148] Thijs Roebroek, Sam Duwé, Wim Vandenberg, and Peter Dedecker. Reduced fluorescent protein switching fatigue by binding-induced emissive state stabilization. International Journal of Molecular Sciences, 18(9):2015–, 2017.

[149] Natalia V Klementieva, Anton I Pavlikov, Alexander A Moiseev, Nina G Bozhanova, Natalie M Mishina, Sergey A Lukyanov, Elena V Zagaynova, Konstantin A Lukyanov, and Alexander S Mishin. Intrinsic blinking of red fluorescent proteins for super-resolution microscopy. Chemical communications, 53(5):949–951, 2017.

[150] Charlotte C David, Peter Dedecker, Gert De Cremer, Natalie Verstraeten, Cyrielle Kint, Jan Michiels, and Johan Hofkens. Spectroscopic characterization of venus at the single molecule level. Photochemical & Photobiological Sciences, 11(2):358–363, 2012.

[151] Ryoichi Arai, Hiroshi Ueda, Atsushi Kitayama, Noriho Kamiya, and Teruyuki Nagamune. Design of the linkers which effectively separate domains of a bifunctional fusion protein. Protein engineering, 14(8):529–532, 2001.

[152] Daniel P Mahoney, Eric A Owens, Chaoyang Fan, Jung-Cheng Hsiang, Maged M Henary, and Robert M Dickson. Tailoring cyanine dark states for improved optically modulated fluorescence recovery. The Journal of Physical Chemistry B, 119(13):4637–4643, 2015.

[153] Joachim Goedhart, Laura Van Weeren, Mark A Hink, Norbert OE Vischer, Kees Jalink, and Theodorus WJ Gadella. Bright cyan fluorescent protein variants identified by fluorescence lifetime screening. Nature methods, 7(2):137–139, 2010.

[154] Jun Chu, Russell D Haynes, Stéphane Y Corbel, Pengpeng Li, Emilio González-González, John S Burg, Niloufar J Ataie, Amy J Lam, Paula J Cranfill, Michelle A Baird, et al. Non-invasive intravital imaging of cellular differentiation with a bright red-excitable fluorescent protein. Nature methods, 11(5):572–578, 2014.

[155] Joachim Goedhart, David Von Stetten, Marjolaine Noirclerc-Savoye, Mickaël Lelimousin, Linda Joosen, Mark A Hink, Laura Van Weeren, Theodorus WJ Gadella Jr, and Antoine Royant. Structure-guided evolution of cyan fluorescent proteins towards a quantum yield of 93%. Nature communications, 3:751, 2012.

[156] T Franke, S Braunmüller, L Schmid, A Wixforth, and DA Weitz. Surface acoustic wave actuated cell sorting (sawacs). Lab on a Chip, 10(6):789–794, 2010.

[157] Ting-Hsiang Wu, Yue Chen, Sung-Yong Park, Jason Hong, Tara Teslaa, Jiang F Zhong, Dino Di Carlo, Michael A Teitell, and Pei-Yu Chiou. Pulsed laser triggered high speed microfluidic fluorescence activated cell sorter. Lab on a Chip, 12(7):1378–1383, 2012.

[158] Thomas D Perroud, Julia N Kaiser, Jay C Sy, Todd W Lane, Catherine S Branda, Anup K Singh, and Kamlesh D Patel. Microfluidic-based cell sorting of francisella tularensis infected macrophages using optical forces. Analytical chemistry, 80(16):6365–6372, 2008.

[159] Sung Hwan Cho, Chun H Chen, Frank S Tsai, Jessica M Godin, and Yu-Hwa Lo. Human mammalian cell sorting using a highly integrated micro-fabricated fluorescence-activated cell sorter (μfacs). Lab on a Chip, 10(12):1567–1573, 2010.

[160] Mark M Wang, Eugene Tu, Daniel E Raymond, Joon Mo Yang, Haichuan Zhang, Norbert Hagen, Bob Dees, Elinore M Mercer, Anita H Forster, Ilona Kariv, et al. Microfluidic sorting of mammalian cells by optical force switching. Nature biotechnology, 23(1):83, 2005.

[161] Maulik V Patel, Armando R Tovar, and Abraham P Lee. Lateral cavity acoustic transducer as an on-chip cell/particle microfluidic switch. Lab on a Chip, 12(1):139–145, 2012.

[162] MJ Booth and T Wilson. Low-cost, frequency-domain, fluorescence lifetime confocal microscopy. Journal of microscopy, 214(1):36–42, 2004.

[163] Nathan C Shaner, Gerard G Lambert, Andrew Chammas, Yuhui Ni, Paula J Cranfill, Michelle A Baird, Brittney R Sell, John R Allen, Richard N Day, Maria Israelsson, et al. A bright monomeric green fluorescent protein derived from branchiostoma lanceolatum. Nature methods, 10(5):407–409, 2013.

[164] Dmitry Shcherbo, Christopher S Murphy, Galina V Ermakova, Elena A Solovieva, Tatiana V Chepurnykh, Aleksandr S Shcheglov, Vladislav V Verkhusha, Vladimir Z Pletnev, Kristin L Hazelwood, Patrick M Roche, et al. Far-red fluorescent tags for protein imaging in living tissues. Biochemical journal, 418(3):567–574, 2009.

[165] Amy J Lam, Francois St-Pierre, Yiyang Gong, Jesse D Marshall, Paula J Cranfill, Michelle A Baird, Michael R McKeown, Jorg Wiedenmann, Michael W Davidson, Mark J Schnitzer, Roger Y Tsien, and Michael Z Lin. Improving fret dynamic range with bright green and red fluorescent proteins. Nat Meth, 9(10):1005–1012, 10 2012.

[166] Xiaokun Shu, Nathan C Shaner, Corinne A Yarbrough, Roger Y Tsien, and S James Remington. Novel chromophores and buried charges control color in mfruits. Biochemistry, 45(32):9639–9647, 2006.

[167] Chola K Regmi, Yuba R Bhandari, Bernard S Gerstman, and Prem P Chapagain. Exploring the diffusion of molecular oxygen in the red fluorescent protein mcherry using explicit oxygen molecular dynamics simulations. The journal of physical chemistry B, 117(8):2247–2253, 2013.

[168] SJ Strickler and Robert A Berg. Relationship between absorption intensity and fluorescence lifetime of molecules. The Journal of chemical physics, 37(4):814–822, 1962.

[169] David A Zacharias, Jonathan D Violin, Alexandra C Newton, and Roger Y Tsien. Partitioning of lipid-modified monomeric gfps into membrane microdomains of live cells. Science, 296(5569):913–916, 2002.

[170] Erik L Snapp, Ramanujan S Hegde, Maura Francolini, Francesca Lombardo, Sara Colombo, Emanuela Pedrazzini, Nica Borgese, and Jennifer Lippincott-Schwartz. Formation of stacked er cisternae by low affinity protein interactions. J Cell Biol, 163(2):257–269, 2003.

[171] Hilary A Snaith, Andreas Anders, Itaru Samejima, and Kenneth E Sawin. New and old reagents for fluorescent protein tagging of microtubules in fission yeast: experimental and critical evaluation. Methods in cell biology, 97:147–172, 2010.

[172] Liubov A Kost, Evgeny S Nikitin, Violetta O Ivanova, Uhna Sung, Ekaterina V Putintseva, Dmitry M Chudakov, Pavel M Balaban, Konstantin A Lukyanov, and Alexey M Bogdanov. Insertion of the voltage-sensitive domain into circularly permuted red fluorescent protein as a design for genetically encoded voltage sensor. PloS one, 12(9):e0184225, 2017.

[173] Nina G Bozhanova, Mikhail S Baranov, Karen S Sarkisyan, Roman Gritenko, Konstantin V Mineev, Svetlana V Golodukhina, Nadezhda S Baleeva, Konstantin A Lukyanov, and Alexander S Mishin. Yellow and orange fluorescent proteins with tryptophan-based chromophores. ACS Chemical Biology, 2017.

[174] William L Noderer, Ross J Flockhart, Aparna Bhaduri, Alexander J Diaz de Arce, Jiajing Zhang, Paul A Khavari, and Clifford L Wang. Quantitative analysis of mammalian translation initiation sites by facs-seq. Molecular systems biology, 10(8):748, 2014.

[175] Lee Kamentsky, Thouis R Jones, Adam Fraser, Mark-Anthony Bray, David J Logan, Katherine L Madden, Vebjorn Ljosa, Curtis Rueden, Kevin W Eliceiri, and Anne E Carpenter. Improved structure, function and compatibility for cellprofiler: modular high-throughput image analysis software. Bioinformatics, 27(8):1179–1180, 2011.

[176] Erik LeeáSnapp et al. moxdendra2: an inert photoswitchable protein for oxidizing environments. Chemical Communications, 53(13):2106–2109, 2017.

[177] Andre C Stiel, Martin Andresen, Hannes Bock, Michael Hilbert, Jessica Schilde, Andreas Schönle, Christian Eggeling, Alexander Egner, Stefan W Hell, and Stefan Jakobs. Generation of monomeric reversibly switchable red fluorescent proteins for far-field fluorescence nanoscopy. Biophysical journal, 95(6):2989–2997, 2008.

[178] Joseph R Lakowicz. Radiative decay engineering: biophysical and biomedical applications. Analytical biochemistry, 298(1):1–24, 2001.

[179] DA Weitz, JI Gersten, S Garoff, CD Hanson, and TJ Gramila. Fluorescent lifetimes of molecules on silver-island films. Optics Letters, 7(2):89–91, 1982.

[180] A Leitner, ME Lippitsch, S Draxler, M Riegler, and FR Aussenegg. Fluorescence properties of dyes adsorbed to silver islands, investigated by picosecond techniques. Applied Physics B: Lasers and Optics, 36(2):105–109, 1985.

[181] FR Aussenegg, A Leitner, ME Lippitsch, H Reinisch, and M Riegler. Novel aspects of fluorescence lifetime for molecules positioned close to metal surfaces. Surface Science, 189:935–945, 1987.

[182] Tamar Ansbacher, Hemant Kumar Srivastava, Tamar Stein, Roi Baer, Maarten Merkx, and Avital Shurki. Calculation of transition dipole moment in fluorescent proteins—towards efficient energy transfer. Physical Chemistry Chemical Physics, 14(12):4109–4117, 2012.

[183] Gabriela Matela, Peng Gao, Gernot Guigas, Antonia F Eckert, Karin Nienhaus, and G Ulrich Nienhaus. A far-red emitting fluorescent marker protein, mgarnet2, for microscopy and sted nanoscopy. Chemical Communications, 53(5):979–982, 2017.

[184] Jae Woo Park and Young Min Rhee. Electric field keeps chromophore planar and produces high yield fluorescence in green fluorescent protein. Journal of the American Chemical Society, 138(41):13619–13629, 2016.

[185] Sabriye Acikgoz, Yakup Ulusu, Hasan Yungevis, Faruk Ozel, Abdurrahman Özen, Isa Gokce, Koray Kara, and Mahmut Kuş. Enhanced radiative decay rate of confined green fluorescent protein in polyvinylpyrrolidone-based nanofiber. The Journal of Physical Chemistry C, 120(31):17739–17744, 2016.

[186] Hu Cang, Yongmin Liu, Yuan Wang, Xiaobo Yin, and Xiang Zhang. Giant suppression of photobleaching for single molecule detection via the purcell effect. Technical report, CALIFORNIA UNIV BERKELEY NANOSCALE SCIENCE AND ENGINEERING CENTER, 2013.

[187] Paul CH Li and D Jed Harrison. Transport, manipulation, and reaction of biological cells on-chip using electrokinetic effects. Analytical Chemistry, 69(8):1564–1568, 1997.

[188] Shirin Faraji and Anna I Krylov. On the nature of an extended stokes shift in the mplum fluorescent protein. The Journal of Physical Chemistry B, 119(41):13052–13062, 2015.

[189] Emre Dikici and Sylvia Daunert. Fluorescent timers shine a light on protein trafficking. Nature chemical biology, 5(2):70–71, 2009.

[190] Andreas Crameri, Erik A Whitehorn, Emily Tate, and Willem PC Stemmer. Improved green fluorescent protein by molecular evolution using dna shuffling. Nature biotechnology, 14(3):315–319, 1996.

[191] Alexey Terskikh, Arkady Fradkov, Galina Ermakova, Andrey Zaraisky, Patrick Tan, Andrey V Kajava, Xiaoning Zhao, Sergey Lukyanov, Mikhail Matz, Stuart Kim, et al. " fluorescent timer": protein that changes color with time. Science, 290(5496):1585–1588, 2000.

[192] Stefan Beck, Takashi Sakurai, Brenda K Eustace, Gerald Beste, Robert Schier, Fritz Rudert, and Daniel G Jay. Fluorophore-assisted light inactivation: A high-throughput tool for direct target validation of proteins. Proteomics, 2(3):247–255, 2002.

[193] Jun-ya Hasegawa, Takehiko Ise, Kazuhiro J Fujimoto, Akihiro Kikuchi, Eiko Fukumura, Atsushi Miyawaki, and Yoshitsugu Shiro. Excited states of fluorescent proteins, mko and dsred: Chromophore- protein electrostatic interaction behind the color variations. The Journal of Physical Chemistry B, 114(8):2971–2979, 2010.

[194] AV Nemukhin, BL Grigorenko, and AP Savitsky. Computer modeling of the structure and spectra of fluorescent proteins. Acta Naturae ( ), 1(2 (2)), 2009.

[195] Michael Z Lin, Michael R McKeown, Ho-Leung Ng, Todd A Aguilera, Nathan C Shaner, Robert E Campbell, Stephen R Adams, Larry A Gross, Wendy Ma, Tom Alber, et al. Autofluorescent proteins with excitation in the optical window for intravital imaging in mammals. Chemistry & biology, 16(11):1169–1179, 2009.

[196] Kiryl D Piatkevich, James Hulit, Oksana M Subach, Bin Wu, Arian Abdulla, Jeffrey E Segall, and Vladislav V Verkhusha. Monomeric red fluorescent proteins with a large stokes shift. Proceedings of the National Academy of Sciences, 107(12):5369–5374, 2010.

[197] Dmitry Shcherbo, Ekaterina M Merzlyak, Tatiana V Chepurnykh, Arkady F Fradkov, Galina V Ermakova, Elena A Solovieva, Konstantin A Lukyanov, Ekaterina A Bogdanova, Andrey G Zaraisky, Sergey Lukyanov, et al. Bright far-red fluorescent protein for whole-body imaging. Nature methods, 4(9):741, 2007.

[198] Jörg Wiedenmann, Andreas Schenk, Carlheinz Röcker, Andreas Girod, Klaus-Dieter Spindler, and G Ulrich Nienhaus. A far-red fluorescent protein with fast maturation and reduced oligomerization tendency from entacmaea quadricolor (anthozoa, actinaria). Proceedings of the National Academy of Sciences, 99(18):11646–11651, 2002.

[199] Kirill Dmitrievich Piatkevich, Elena Nikolaevna Efremenko, Vladislav V Verkhusha, and Sergei D Varfolomeev. Red fluorescent proteins and their properties. Russian Chemical Reviews, 79(3):243, 2010.

[200] Simone Kredel, Franz Oswald, Karin Nienhaus, Karen Deuschle, Carlheinz Röcker, Michael Wolff, Ralf Heilker, G. Ulrich Nienhaus, and Jörg Wiedenmann. mruby, a bright monomeric red fluorescent protein for labeling of subcellular structures. PLoS ONE, 4(2):e4391, 02 2009.

[201] María Elena Martin, Fabrizia Negri, and Massimo Olivucci. Origin, nature, and fate of the fluorescent state of the green fluorescent protein chromophore at the caspt2//casscf resolution. Journal of the American Chemical Society, 126(17):5452–5464, 2004. PMID: 15113217.

[202] Thomas Dertinger, Mike Heilemann, Robert Vogel, Markus Sauer, and Shimon Weiss. Super-resolution optical fluctuation imaging with organic dyes. Angewandte Chemie, 122(49):9631–9633, 2010.

[203] Ulrike Endesfelder, Sebastian Malkusch, Benjamin Flottmann, Justine Mondry, Piotr Liguzinski, Peter J. Verveer, and Mike Heilemann. Chemically induced photoswitching of fluorescent probes—a general concept for super-resolution microscopy. Molecules, 16(4):3106–3118, 2011.

[204] Mikhail Drobizhev, Caleb Stoltzfus, Igor Topol, Jack Collins, Geoffrey Wicks, Alexander Mikhaylov, Lauren Barnett, Thomas E. Hughes, and Aleksander Rebane. Multiphoton photochemistry of red fluorescent proteins in solution and live cells. The Journal of Physical Chemistry B, 118(31):9167–9179, 2014. PMID: 25004113.

[205] Hui-wang Ai, Michelle A Baird, Yi Shen, Michael W Davidson, and Robert E Campbell. Engineering and characterizing monomeric fluorescent proteins for live-cell imaging applications. Nat. Protocols, 9(4):910–928, 04 2014.

[206] Xinxin Zhu and Wei Min. Frequency-domain phase fluorometry in the presence of dark states: A numerical study. Chemical Physics Letters, 516(1â“3):40 – 44, 2011.

Appendix A

Matlab Codes

A.1 Phase advance Computation

The Matlab code used to compute phase shifts of the system described by a 3 state model (2.6a) that was described in Chapter 2:

```
function PhaseFreq3State % phase calculation based on a 3 state model.
tic; % clock for measuring the computation time
clc; clear;
dataName = input('Save data as..?: ', 's');

    function dy=freq3State(t,y,nu)

   % photo physical Parameters

    h=6.626*e 34;c=2.998*e8; NA=6.022e23;% universal constants
    I0=25e7; % Laser Intensity; W/m^2
    epsilon=72e3; % Molar exctinction coefficient in M^ 1cm^ 1;
    sigma=2.303*epsilon*1e3*1e 4/NA; % Absorption cross section
    lambda=532*e 9; % excitation wavelength; 532 nm
    kEx0=I0*sigma*lambda/(h*c); % peak excitation rate
```

```
16      kEx=kEx0*(sin(2*pi*nu*t)+1); % excitation rate
17      tau=1.87; % excited state lifetime; ns
18      QY= 0.22; % quantum yield
19      kEm=(1e9*QY)/tau; % emission rate constant
20      kS1B=100; % bleaching rate constant from bright state, S1
21      kDB=0; % bleaching rate constant from dark state, D
22      kS1D=10e3; % DSC rate constant
23      kGSR=2e3; % GSR rate constant
24
25    % kinetics
26      dy=zeros(3,1);
27      dy(1) = kEx*y(1)+kEm*y(2)+kGSR*y(3);
28      dy(2)=kEx*y(1) (kEm+kS1B+kS1D)*y(2);
29      dy(3)=kS1D*y(2) (kGSR+kDB)*y(3);
30      end
31
32  nu=1e3:5e3:51e3; % Frequency Range
33  phi=zeros(size(nu));
34  period=10; % number of full period used for phase calculations
35
36  for ind=1:length(nu);
37
38      time_step=1e 8; % time step; 10 ns
39      Tspan=0:time_step:period/nu(ind); % time span to integrate
40      [T,Y]=ode45(@(t,y) freq3State(t,y,nu(ind)),Tspan,[1,0,0]); % Solve
            the kinetics
41      P=transpose(I0*sin(2*pi*nu(ind)*T));
```

```
42      Q=transpose(I0*sin(2*pi*nu(ind)*T+(pi/2)));
43      x=sum(P*Y(1:length(Tspan),2)); % in phase component (I)
44      y=sum(Q*Y(1:length(Tspan),2)); % in quadrature component(Q)
45      phi(ind)=atan(y/x)*180/pi; % phase in degree
46
47  end
48  toc; % computation done!
49  save(dataName,'nu','phi','I0','tau','kS1B','kS1D','kDB','time_step','
        period'); % save the data
50  end
```

A.2 Single Molecule Fluorescence

Matlab code that generates single molecule fluorescence traces based on a modified 3 state model (Figure 3.10b)described in the Chapter 3:

```
1  clc; clear
2
3  step_size=1e 6; %step size of the simulation; micro second
4  time=100000; % total duration of the simulation in second;
5  N=round(time/step_size,0); % total number of steps
6  turnover=300; % total number of turnover from on to off states
7
8  %photo physical parameters
9
10 kGSR=14; %kb, GSR rate constant
11 kDSC=42e3; %ka2, DSC rate constant
12 ka1=0; % no transition to dark state from S0
```

```
13 QY=0.41; % quanutm yield
14 tau=2.45e 9; %excited state lifetime
15 kEm=QY/tau; % ga2, radiative emission rate constant
16 k_ic=(kEm/QY) kEm kDSC; % internal conversion rate constant
17
18 h=6.626*e 34;c=2.998*e8; NA=6.022e23;% universal constants
19 I0=24e4; % Laser Intensity in W/m^2
20 epsilon=71e3; % Molar exctinction coefficient in M^ 1cm^ 1 at lambda;
21 sigma=2.303*epsilon*1e3*1e 4/NA; % Absorption cross section
22 lambda=561*e 9; % excitation wavelength
23 kEx=(I0*sigma*lambda)/(h*c); % ga1, excitation rate
24
25 p11=(0+0)*step_size; p21=(0+0)*step_size;
26 p12=(ka1+kEx)*step_size; p22=1 exp( (kDSC+kEm+k_ic)*step_size);
27 prob=[p11 p12; p21 p22]; % probality of leaving state B and A;
28 prob_B=kGSR*step_size; % probality of leaving B state
29 c11=0; c21=0;
30 c12=kEx/(kEx+ka1); c22=(kEm+k_ic)/(kEm+kDSC+k_ic);
31 cProb=[c11 c12; c21 c22];
32
33 signal=1;
34 t=1;
35 j=1;
36 k=1;
37
38 trace=zeros(N,1);
39 on=zeros(length(turnover),1);
```

```
40 off=zeros(length(turnover),1);
41
42 c=1;
43 ct=1;
44 m=1;
45 n=1;
46
47 conformation=zeros(N,1);
48 c1=zeros(length(N),1);
49 c2=zeros(length(N),1);
50
51
52 for i=1:N;
53
54     trace(i)=signal;
55     conformation(i)=c;
56     if signal==1;
57         if rand> prob(c,signal+1)
58         t=t+1; % continue with the present state
59         ct=ct+1;
60         else if rand>=cProb(c,signal+1)
61                     ct=ct+1; % change the fluorescent state
62                     on(j)=t*step_size;
63                     j=j+1;
64                     signal=rem(signal+1,2);
65                     t=1;
66               else   t=t+1; % change the conformation
```

```
67                      if     c==1;
68                             c1(m)=ct;
69                             m=m+1;
70                      else   c2(n)=ct;
71                             n=n+1;
72                      end
73                          c=rem(c,2)+1;
74                          ct=1;
75                  end
76              end
77          else   if rand>prob_B; % molecule in the dark state
78                  t=t+1; ct=ct+1;
79              else  off(k)=t*step_size;
80                  k=k+1;
81                  signal=rem(signal+1,2);
82                  t=1;
83              end
84          end
85  end
86  tim=0:step_size:(length(trace) 1)*step_size;
87
88  save('TagT_3Smodified2','tim','trace','kEx','kEm','kGSR','kDSC','
        step_size') % save data
```

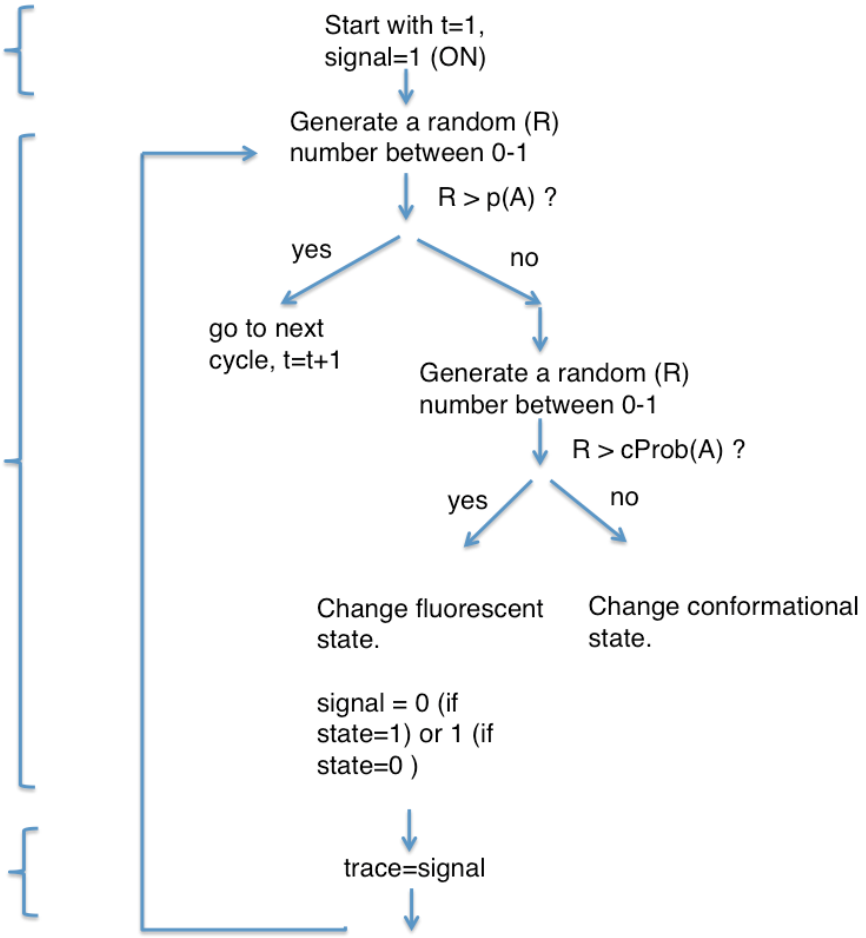

Figure A.1: Algorithm to generate single molecule fluorescence traces with multiple bright and dark states.

Appendix B

Setting up and Cleaning of the Microfluidic System for Screening and Sorting

B.1 General Rules

- No microfluidics or any part of the device holder can leave the optics table tent without being sealed in a jar. They can never be exposed to ambient air.
- Never touch any microfluidics or any parts of the device manifold (white manifold, "o" rings, and orange rubber stoppers) with anything other than tweezers.
- Make sure that the water level of the sonicator is never higher than the lids of the containers since they are not water-proof jars. However, keep the water at the minimum level indicated on the sonicator tank.
- Try to never use high pressure (>20 psi). With high pressure more debris will likely to appear.
- Every liquid (except cells) goes through 0.2 μm filter.
- Ultrapure water does not need to be filtered for cleaning purposes but does need to be filtered if being pumped through the microfluidic.
- Refrigerate any solutions other than bleach and water.
- Use a new syringe and filter each day.

- Never store anything other than glass chips in bleach solutions.
- If you need to use new tubes or want to clean the tubes, cut them to the required length and sonicate them in ultrapure water for > 40 minutes in a sealed jug. Then, attach them to the 20 psi air (on microscope) and run air through them to dry them out for > 20 minutes.
- Fill reservoirs with 150 μl of solution.
- Fill and empty reservoirs using micropipettes.

B.2 Setting up the Microfluidic for Screening and Sorting

- Sonicate the device in the same $\sim$10% bleach solution that it was stored in overnight for 60 minutes.
- Simultaneously sonicate the jar of "o" rings and orange rubber stoppers with adding a small amount of detergent (alconox). The manifold does not need to be sonicated.
- Rinse white manifold three times with ultrapure water. Leave third rinse water in container to store manifold in when experiments are over.
- Rinse the "o" rings and stoppers three times with ultrapure water and then leave them in third aliquot of water.
- Remove the microfluidic from the jar with tweezers and hold it over the waste bucket to rinse with the ultrapure water.
- Put microfluidic into bottom of metal device holder.
- Place "o" rings on manifold with tweezers.
- Place manifold on top of microfluidic.

- Screw manifold retaining ring on.
- Fill side reservoirs with 150 μl with filtered (with 2 μm filter) ultrapure water. In the middle reservoir add cell media (blank media ((yeast nitrogen base, ammonium sulphate)) + 14% OptiPrep). The OptiPrep help to distinguish the sheath channels and the sample channel.
- Place stoppers into holes with tweezers.
- Attach metal lid with two screws (can be done without tweezers).
- Pump water through the device at 10 psi for 10 minutes. This would clear up any dirt or cell-debris that is present from the previous run. The flow would be symmetric. If not, there might be some clogging upstream of the channel. Try to flow the media with inserting the pressure tubes into the two outlets (back-pressure). This usually clear the clogging and makes the flow symmetric again.
- Run the microfluidic with adding 150 μl blank media through all of the three channels at 2 psi. This step eliminate any bubble/air that is present in the channel and stabilizes the stream.
- Now the microfluidic is ready run for screening or sorting. Add blank media into the two sheath channel and filtered sample containing cells into the middle/sample channel. It is very important to filter the sample with 40 μm filter. Otherwise, the cell-debris clogs the channel.
- Use the pressure controller to control the flow in the microlfuidic.
- If you want to recover the cells after the experiment, load the collection reservoir with some amount of ($\sim$150 μl) blank media.

B.3 Cleaning Procedure

- Empty all the reservoirs.
- Run $\sim$ 20 % bleach through all the reservoirs.
- Empty inlets and outlets.
- Disassemble device holder and all parts of manifold except stainless steel quick connects
- Put microfluidic into its conical tube with new 20% bleach solution (filtered bleach and ultrapure water, neither of which need to be re-filtered at this point).
- Sonicate for 40 minutes (can put on timer and leave overnight in sonication bath).
- Everything else is stored in water overnight with possible addition of alconox. Bleach will cause rust to metal and degrade rubber so never leave these parts in bleach for any length of time longer than 10 min.

Appendix C

Protocol for Microfluidic Screening and Sorting & Operation of the LabView Software

After the flow is stable and symmetric in the microfluidic, screening & sorting can be performed. Here is the detailed step-by-step protocol for screening and sorting with the operation of the custom-made LabView Software.

- For screening, load the buffer (blank media) in the sheath reservoirs and filtered sample in the middle reservoir. Run the microfluidic in low pressure so that sample stream goes through the middle of the channel and transit through the middle of the elliptical beams focused on the chip. However, for sorting, before turning on the pressure make sure the flow is biased towards to the waste channel otherwise there would be contamination.

- For sorting purpose, flow speed of all the channels should be below 1 psi.

- Mark the positions where the cells are passing through the beams (only lifetime beams and photobleaching beams). This will help you to monitor if there is any fluctuation of flow during the screening. It will give the coordinates of the lifetime and photobleaching beams that are required to compute the speed of the cells through the channel. Speed of the cells will be used for setting-up the timing for sorting.

- Turn on the PMT with $\sim$-750 V. This voltage may vary depending on the brightness of the sample. I have used the voltage (gain) from -700 V to -800 V.

- Turn on the Lock-in amplifier (Zurich Instruments) and open the associate LabOne software. Choose the modulation frequency (29.5 MHz), filters and the gain of the I & Q channels.

- Open the LabView software. There are three components of the software: Target Program (Target-41.vi; real-time control of the sorter *etc.*), Host Program (Host-41.vi; control of sort and data representation) and Test program (Test AO and DO.vi; for setting-up the trap laser).

- First, turn on the Target.vi and then Host.vi.

- From the Host.vi, adjust the threshold for Channel 0 (Ch0; signal from lifetime PMT) and Channel 1 (Ch1; signal from photobleaching PMT), so that you get equal count on both channels. You can adjust the threshold from 'Pulse' panel of the program.

- Adjust the 'transit time' from the panel 'Matching' in the Host.vi program.

- Calibrate the lifetime of the sample adjusting 'N-Delta' control from the 'PMT1' panel in the Host.vi program. I used mCherry for this calibration process (τ = 1.87 ns in the phase-fluorimetry).

- Now, the microfluidic is ready for screening. Re-start the Host.vi program and continue to obtain data with your desired counts. For screening single mutants, I screen $\sim$ 7,000 - 10,000 counts. For the counts I refer to the number of cells that is pair-matched ('MatchedToCh0'; Panel 'Run'; Host.vi program).

- If you plan to sort, now stop both the Target.vi & Host.vi programs.

- Turn on the trap laser with 30 % power.

- Add a neutral density (ND) filter (OD $>$ 2.0 ?) in front of the entrance of the trap-laser box.

- Open 'Test AO and DO.vi' program and run it. It will show the trajectory of the trap laser beam in the camera. Place the trajectory at little upstream of the junction for the waste and collection channel (see Chapter 4 Figure 4.7).
- Focus the trap laser on the microfluidic. This is very crucial part. This will determine whether you would effectively sort or burn the chip.
- Take out the ND filter in front of the trap laser box.
- Stop the 'Test AO and DO.vi' program. Run the Target.vi and Host.vi, in that sequence.
- Next step is the setting-up of the timing for efficient sorting. In principle, we need to enter the Switch factor (SwitchF), Delay factor (DelayF) and adjust the Extra Delay in the program for efficient sorting (Figure C.1) [98]. In a previous avatar of this sorter, we had multiple beams to measure these parameters (SwitchF & DelayF) and the measured parameters were entered into the program. However, I follow these protocols for setting-up the timing:
    - Enter the position of lifetime and PostBleach beams into the 'Switch' panel of the Host.vi program.
    - Use a previously found SwitchF (~ 0.7) and DelayF (~ 0.3).
    - Adjust the ExtraDelay parameter in combination with visual inspection of trap-laser firing and consequent sorting of the cells.
    - Adjust the ExtraDelay in a systematic way until you get the desired efficiency, .
- Once you have good sorting efficiency (> 50 %), you can select a population you want to sort in the 'Select' panel of the Host.vi program.
- Sort the population to obtain the desired number of the cells.

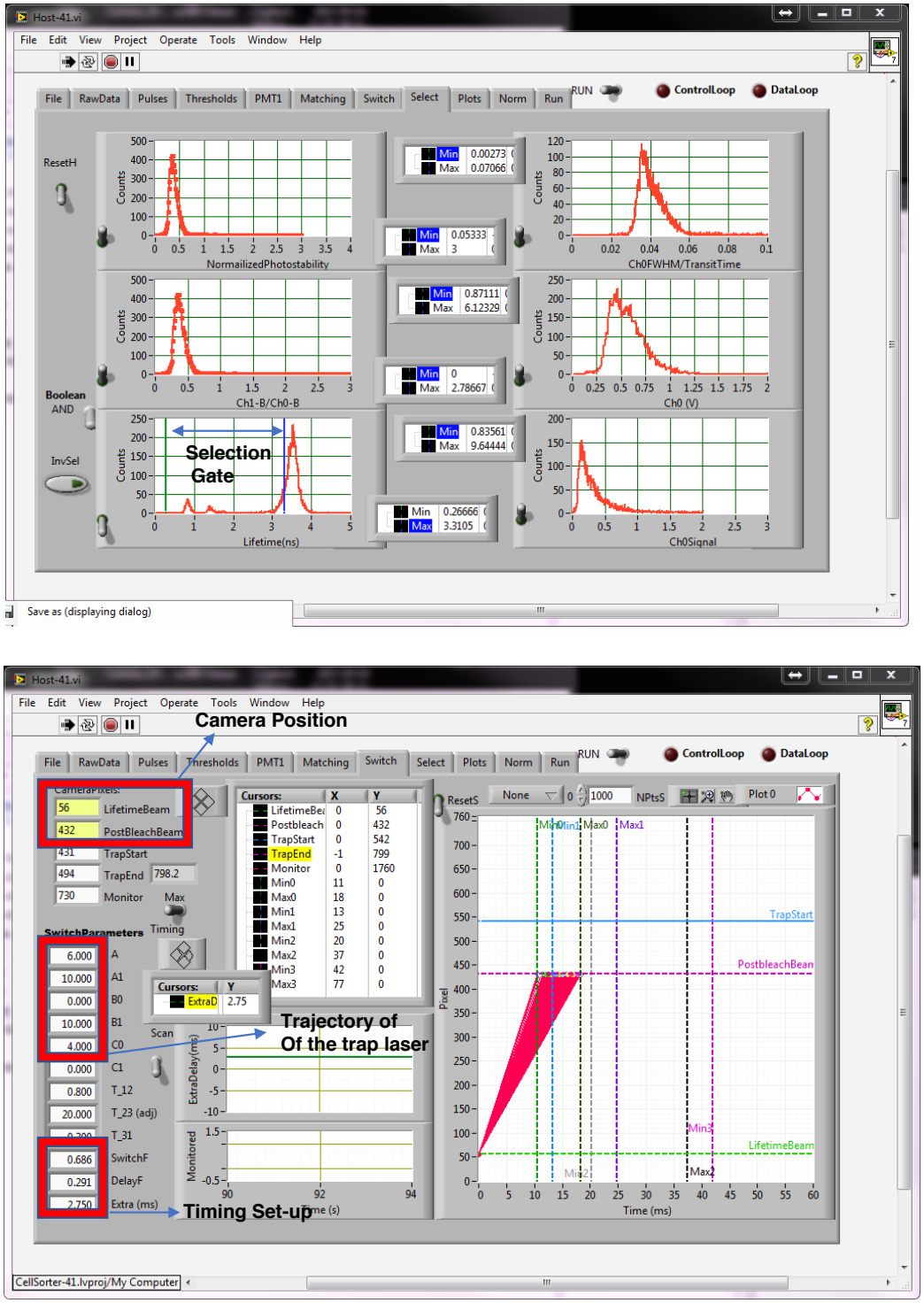

Figure C.1: **Sorting protocol:** (above) Selection gate shown in the LabView program. (below) The parameters required to add for the timing set-up during sorting: lifetime and post-bleach beam positions, SwitchF, DelayF, Extra.

Appendix D

Protocol for Site-directed & Random Mutagenesis

D.1 Library construction

The original DNA templates for mCherry and other FPs were amplified with gene-specific primers and cloned into pDonr221 using Gateway recombination system (Life Technologies) and sequenced. The forward primer for each FP included a recombination recognition sequence (attB1), a Shine-Dalgarno sequence for prokaryotic expression, a BamH1 restriction endonuclease site, a Kozak sequence for mammalian expression and an $\sim$ 30 nucleotide sequence complementary to the FP. The reverse primer for each FP included $\sim$ 30 nucleotide complementary to the FP, a stop codon, an EcoR1 restriction endonuclease site and an attB2 recombination recognition sequence. Still using the Gateway recombination system an LR reaction was performed to clone the FP into pYestDest52 vector (Life technologies). After sequence was confirmed the FP/pYestDest52 plasmids were used as template for library construction.

D.2 Error-prone libraries:

GeneMorph II Random Mutagenesis kit (Agilent Cat No. 200550) was used to create the error-prone libraries. The kit protocol was followed with different amount of template and cycles depending on the error rate. T7 and V5 universal primers (both located on pYesDest52 vector) were used for the amplification. After first round of PCR, the PCR product was run on a gel and gel-

extracted. The gel-extracted PCR product was used for a second round of PCR to create enough DNA for homologous recombination. After PCR purification the library DNA was isopropanol-precipitated and eluted in a few μl of water.

D.3 Site directed libraries:

QuikChange site-directed mutagenesis method was used to make point mutations or switch single amino acids using PfuTurboDNA polymerase and a Thermo cycler. PfuTurboDNA polymerase replicates both plasmid strands with high fidelity and without displacing the mutant oligonucleotide primers. The basic procedure utilizes a supercoiled double-stranded DNA (dsDNA) vector with the FP of interest and two synthetic oligonucleotide primers containing the desired mutation. The oligonucleotide primers, each complementary to opposite strands of the vector, are extended during temperature cycling by PfuTurboDNA polymerase. Incorporation of the oligonucleotide primers generates a mutated plasmid containing staggered nicks. Following temperature cycling, the product is treated with DpnI. The DpnI endonuclease digest the parental DNA template and makes it possible to select for mutation-containing synthesized DNA. The nicked vector DNA containing the desired mutations is then transformed into *E.coli* (Top10).

Libraries with multiple site-directed targets were created using SOE reaction (Splicing overlap extension). Primers were designed to introduce the desired mutations and the initial PCR s generate overlapping gene segments that are used as template DNA for another PCR to create a full-length product. The internal primers generate overlapping, complementary 3′ends on the intermediate segments and introduce the desired nucleotide changes for site-directed mutagenesis. Overlapping strands of these intermediate products hybridize at this 3′region in a subsequent PCR and are extended to generate the full-length product amplified by flanking primers. The full length product is gel-extracted and isopropanol-precipitated and eluted in a few μl water.

D.4 Electroporation:

Fresh Competent yeast cells (*Saccaromyces cerevisiae* BY4741) were prepared prior to electroporation.

Cells, DNA and cut pYestDest52 vector were combined and left on ice for 5 min. Electroporation conditions (Bio-Rad Gene Pulser Xcell): C = 25 μF, PC = 200 ohm, V = 1.5 kV (in 0.2 cm cuvettes).

Cells were passed twice prior to expression.

Interesting mutants were transferred to pBad-His vector for expression/Ni-Nta protein purification.

D.5 Site-directed mutagenesis using Gblock:

- Design the desired open reading frame (ORF) of the mutants *in silico*.
    - Include entire ORF (from 'start' to 'stop' codon)
    - Add restriction enzyme cloning sites to the 5′and 3′ends (5′-BamHI, 3′-NotI)
    - Add single bp 'A' just downstream of 5′-BamHI site to keep things in frame
- Digest Gblock(s) w/ BamHI-HF/NotI ($\sim$ 2hrs at 37°C) and perform reaction clean up (Qiagen MinElute kit - Cat no. 28004).
- Ligate BamHI/NotI-cut Gblock into BamHI/NotI-cut PiggyBac-H2B vector.
    - $\sim$ 60ng vector
    - $\sim$ 25ng Gblock
    - 1μl T4 ligase (from NEB)
    - 15 μl reaction volume total
    - room temperature/$\sim$2hrs
- Transform competent *E.coli* (Stellar cells from Takara Bio) w/ 2.5 μl of ligation mixture.

- Pick single colonies, grow up in LB/Amp100 (37°C O/N), and miniprep (Omega Biotek kit - Cat no. D6942).

- Sequence over inserted Gblock (including cloning sites) to ensure fidelity.

Appendix E

Photo-physical Characterization of the Fluorescent Proteins

E.1 Extinction Coefficient

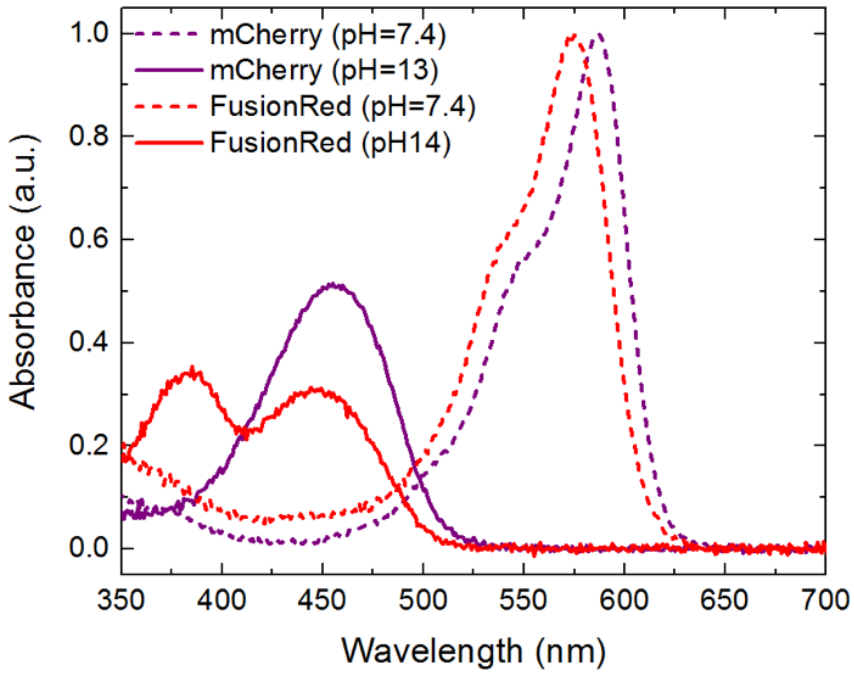

Figure E.1: Absorption spectra of mCherry and FusionRed in Tris-HCl buffer (pH=7.4) and NaOH solution (pH=13 or pH=14).

The extinction coefficient of mCherry, FusionRed and their mutants are calculated using the alkali-denaturation method described in the literature [54]. We measured absorption spectrum of the fresh RFP in Tris-HCl buffer (pH=7.4), and repeated the same measurement with same

amount of fresh RFP in NaOH solution with same volume as previously used Tris-HCl buffer in the same quartz cuvette. The NaOH solution had pH=13 for mCherry and its mutants and pH=14 for FusionRed and its mutants. The spectra were obtained using Cary 500 Scan UV-Vis-NIR spectrometer.

The absorption spectra of mCherry and FusionRed were normalized according to the absorption peak of each RFP in Tris-HCl buffer and plotted in Figure E.1. The extinction coefficients of the alkali-denatured chromophore near 380 nm (ϵ_{380nm}) and 450 nm (ϵ_{450nm}) are 70,000 $M^{-1}cm^{-1}$ and 44,000 $M^{-1}cm^{-1}$, respectively [54]. Using these extinction coefficient values, the extinction coefficient of RFPs (ϵ_{RFP}) can be calculated:

$$\epsilon_{RFP} = \frac{A_{RFP}}{A_{380nm}/\epsilon_{380nm} + A_{450nm}/\epsilon_{450nm}} \tag{E.1}$$

where ϵ is the extinction coefficient and A is the absorbance.

E.2 Quantum Yield

For the measurement of fluorescence quantum yield, we use the following protocol:

- A series of samples containing purified fluorescent proteins (in Tris-HCl buffer, pH=7.4) is prepared with 4-5 different concentrations. Maximum OD of the most concentrated sample should be around 0.2-0.3, measured in a cuvette of 4 cm path length.

- Absorption spectra of the samples are measured in a spectrophotometer. Baseline corrections are performed for the spectra. For measuring the absorption spectra, we use a cuvette of 4 cm path length rather than the usual 1 cm path length cuvette. This gives more robust and error-free absorption spectra.

- The emission spectra of the same samples are measured in a fluorimeter. Baseline corrections are performed for the spectra. Cuvette with 1 cm path length is fine for these measurements.

- Integrated fluorescence of the samples are quantified by measuring the area under the emission spectra.

- Integrated fluorescence of the spectra are plotted against the OD at the wavelength the samples are excited the to obtain the emission spectra. Usually we excite the samples at 520 nm to obtain the emission spectra of the RFPs. Figure E.2 displays the Integrated fluorescence *vs.* OD@520 nm of some FPs.

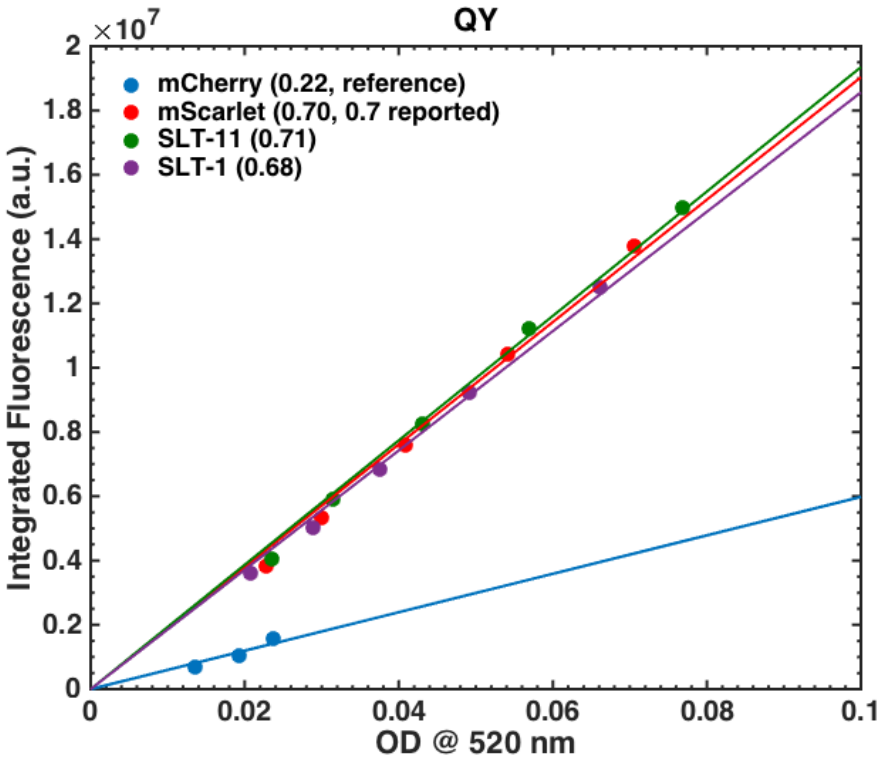

Figure E.2: Integrated fluorescence *vs.* OD at 520 for few red fluorescent proteins.

- Integrated fluorescence *vs.* OD plot can be fitted with a straight line of the form: $y = slope * x$, where y= integrated fluorescence and x = OD. Please note that the fitted line should go through (x=0, y=0) point. If the fitted line deviates from the (0,0) point, this indicates some errors in the measurements.

- Fluorescence quantum yield of the sampel (ϕ_{sample}) is then computed as:

$$\phi_{sample} = \frac{\phi_{ref} * slope_{sample} * \eta^2_{sample}}{slope_{ref} * \eta^2_{ref}} \tag{E.2}$$

  where η_{sample} and η_{ref} are the refractive index of the sample and the reference, respectively.

- mCherry (ϕ, 0.22 in Tris-HCl, pH=7.4) or Cresyl violet (ϕ, 0.54 in EtOH) is used as a reference.

- Tris-HCl buffer (pH=7.4) is used for all the dilutions.

E.3 pKa

For the measurement of pKa, we follow the method described by Cranfill *et al.* [101].

- A set of buffers with pH ranging from 2-10 is prepared. The composition of the buffers are displayed in Table E.1, E.2 and E.3. The buffer with pH 2.2 (Buffer A) is prepared by diluting 2.5 ml of 0.2M glycine-HCl to 10 ml.

Table E.1: pH = 3-6

Buffers	Calculated pH	0.1 M citric acid (ml)	0.1 M Na-citrate (ml)	Diluted to (ml)
B	3.0	4.7	0.3	10
C	3.6	3.7	1.3	10
D	4.0	3.3	1.7	10
E	4.6	2.6	2.4	10
F	5.0	2.1	2.9	10
G	5.4	1.6	3.4	10
H	6.0	0.95	4.0	10

Table E.2: pH = 6.5-8.0

Buffers	Calculated pH	0.2 M KH_2PO_4 (ml)	0.2 M Na_2HPO_4 (ml)	Diluted to (ml)
I	6.5	6.9	3.1	-
J	7.0	3.9	6.1	-
K	8.0	0.5	9.5	-

Table E.3: pH = 9.0-10

Buffers	Calculated pH	0.2M Glycine (ml)	0.2M NaOH (ml)	Diluted to (ml)
L	9.0	2.5	0.44	10
M	10.0	2.5	2.3	10

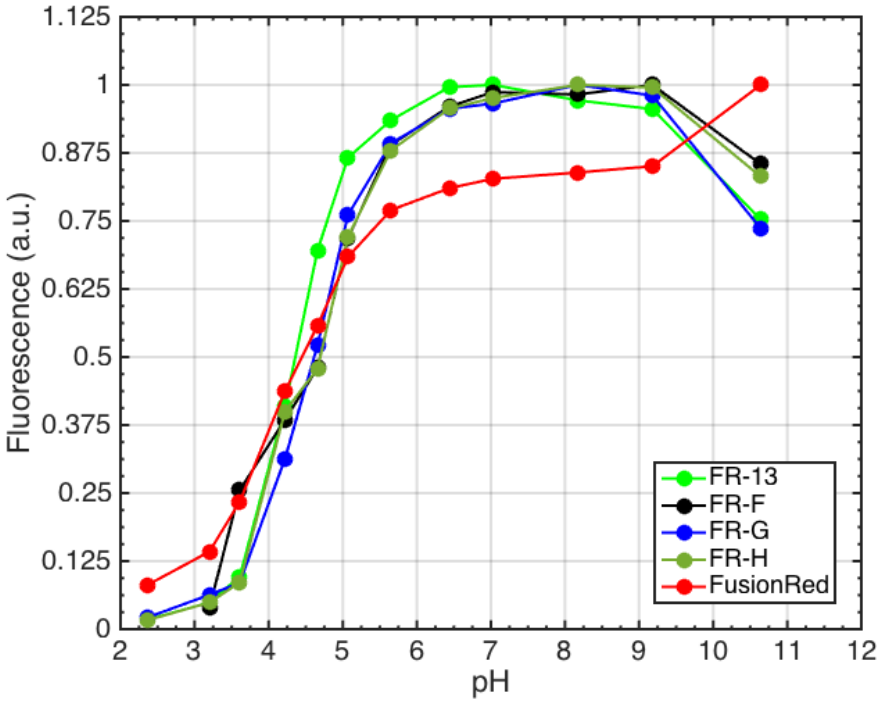

Figure E.3: pH-resistance of the FusionRed mutants. pKa is defined as the pH where the fluorescence is 50% of the maximum value.

- The actual pH of the buffers are measured using a pH-meter.
- Same amount of purified FP is added in all the buffers and left at room temperature for an hour.
- The emission spectra of the buffer solutions containing FPs are measured using a plate-reader.
- Fluorescence of the samples are quantified by the maxima of the emission peaks or the area under the emission spectra. Both method gives similar results.
- Fluorescence of the sample and the corresponding measured pH values are plotted. Figure

E.3 displays a typical pH *vs.* Fluorescence for a set of fluorescent proteins.

- pKa of the FP is defined as the pH where the fluorescence is half of the maximum fluorescence.

Appendix F

Electronic Circults

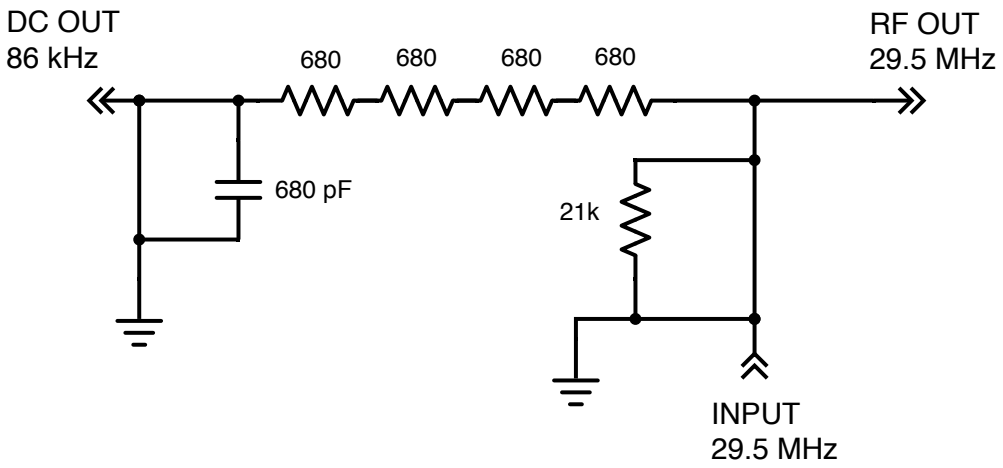

Figure F.1: Circuit diagram of the bias tee used in the microfluidic sorter.

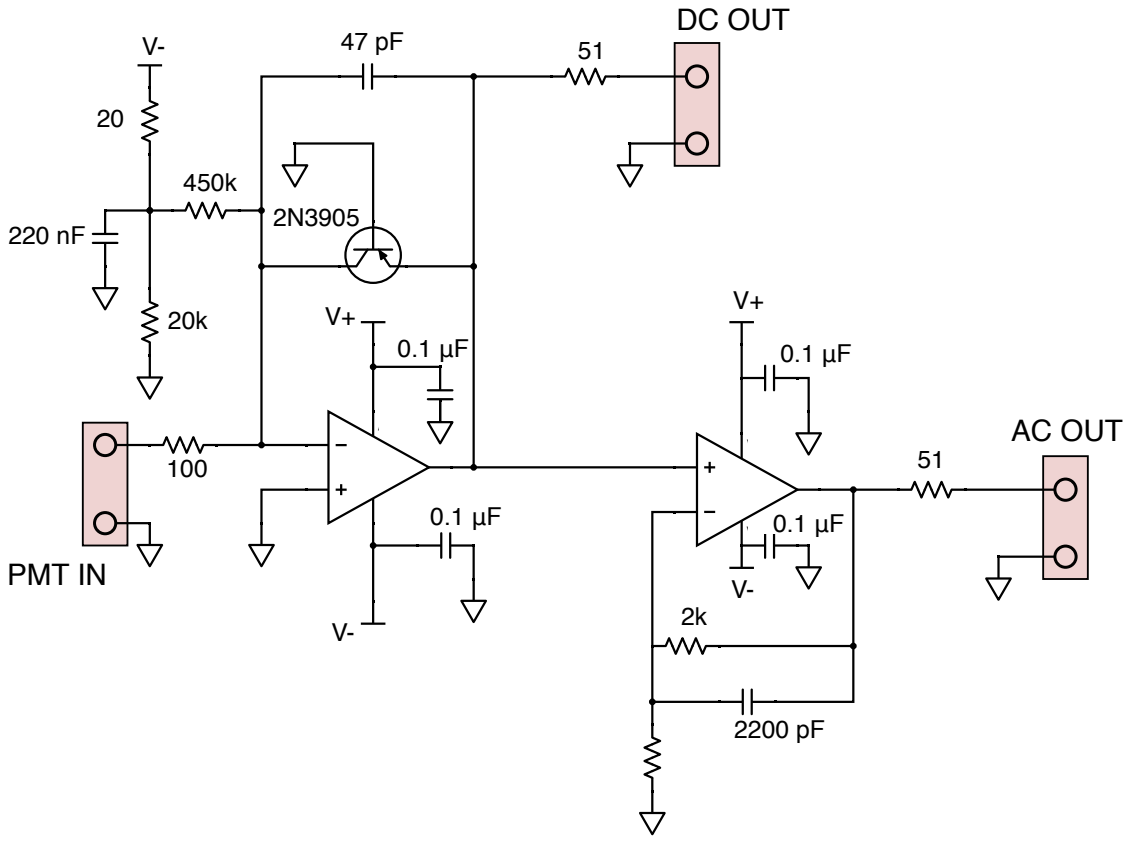

Figure F.2: Circuit diagram of the log amplifier used for the signal amplification.

Appendix G

Sequence Alignment for FusionRed mutants

Sequence alignment of FusionRed mutants:Residue numbering is based on alignment with avGFP sequence. Residues highlighting blue and yellow are associated with folding and monomerization of FusionRed clones. Mutations accumulated in first, second and third round of EP-PCR mutagenesis libraries are highlighted in orange, magenta and cyan respectively. Internal residues are highlighted in grey.

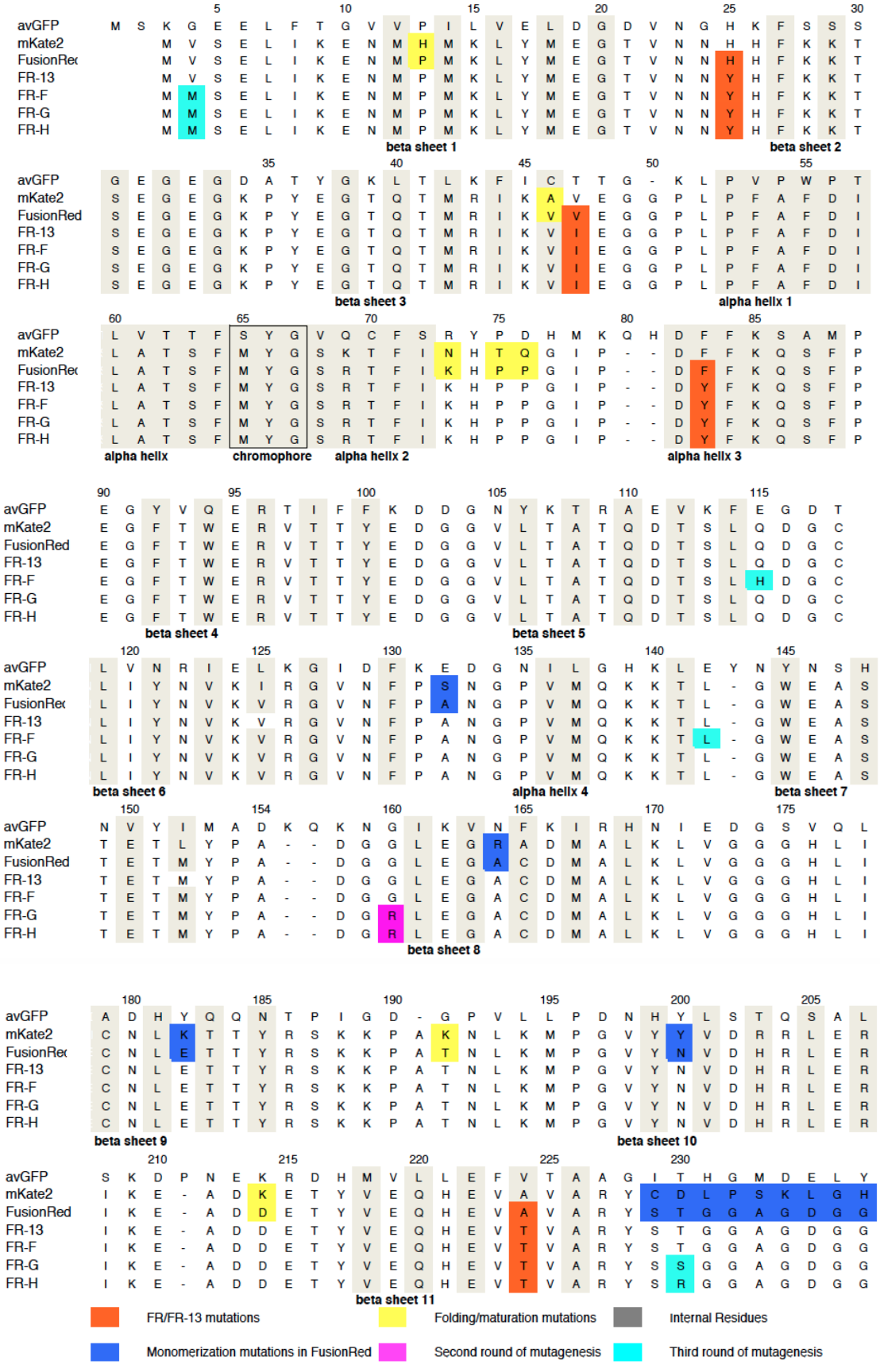
avGFP
mKate2
FusionRed
FR-13
FR-F
FR-G
FR-H
beta sheet 1
beta sheet 2
beta sheet 3
alpha helix 1
alpha helix
chromophore
alpha helix 2
alpha helix 3
beta sheet 4
beta sheet 5
beta sheet 6
alpha helix 4
beta sheet 7
beta sheet 8
beta sheet 9
beta sheet 10
beta sheet 11
FR/FR-13 mutations
Folding/maturation mutations
Internal Residues
Monomerization mutations in FusionRed
Second round of mutagenesis
Third round of mutagenesis

Appendix H

Program for Analyzing OSER Structures

Here are the details of the analysis program that we have developed for an objective quantification of OSER score (see Chapter 6). The analysis pipeline can be summarized as follows:

Raw Images

⇓

Identification of cells based on a global thresholding & size

⇓

Identification of bright structures (whorls) inside cells based on intensity & size

⇓

Filtering the bright structures to identify whorls based on shape of the structures

⇓

Relate cells & whorls based on location

⇓

Analysis

For the identification of cells, a binary image was generated by a global thresholding that discriminate fluorescence from the image background (Figure H.1b). In the next step, the cells were identified by:

- using the previously generated binary image as a guide &
- size of the identified objects.

10-50 μm window was used as a size criterion for the cells. Median size of the cells was $\sim$ 20 μm. The program correctly identified cells (green outlines) and rejected the tiny dots (pink outlines) based on size (Figure H.1c).

The intensity distribution of the identified cells were measured. Another binary image was generated with using a threshold of: $\mu_{cell} + n * \sigma_{cell}$, where, μ_{cell} and σ_{cell} are the mean and standard deviation of the intensity distribution of the cells. n is an adjustable parameter. n= 1-2 works well in our purpose for the identification of bright structures in the cells. n=1.5 was used to generate the binary image 2 (Figure H.1d). Bright structures in the cells were identified using the binary image generated in the previous pipeline & based on size criterion. $\sim$1-7 μm was used as a size criterion for the OSER structures. The program correctly identifies the bright structures (green outlines) inside the cells H.1e.

In the original OSER article [100], part of the nucleus having "karmellae" was not considered as whorls. These are nuclear-associated paired membranes produced by over-expression of the enzymes. As "karmellae" s have different shapes than the whorls, they can be easily filtered out using either eccentricity the form factor (f) of the identified objects. Form factor is defined as follows:

$$f = 4\pi * A/p^2 \tag{H.1}$$

where, A and p are the area and perimeter of the structure. A "karmellae" from the cells have been filtered out (shape with pink outline) using a criterion of form factor $>$ 0.25 (Figure H.1f).

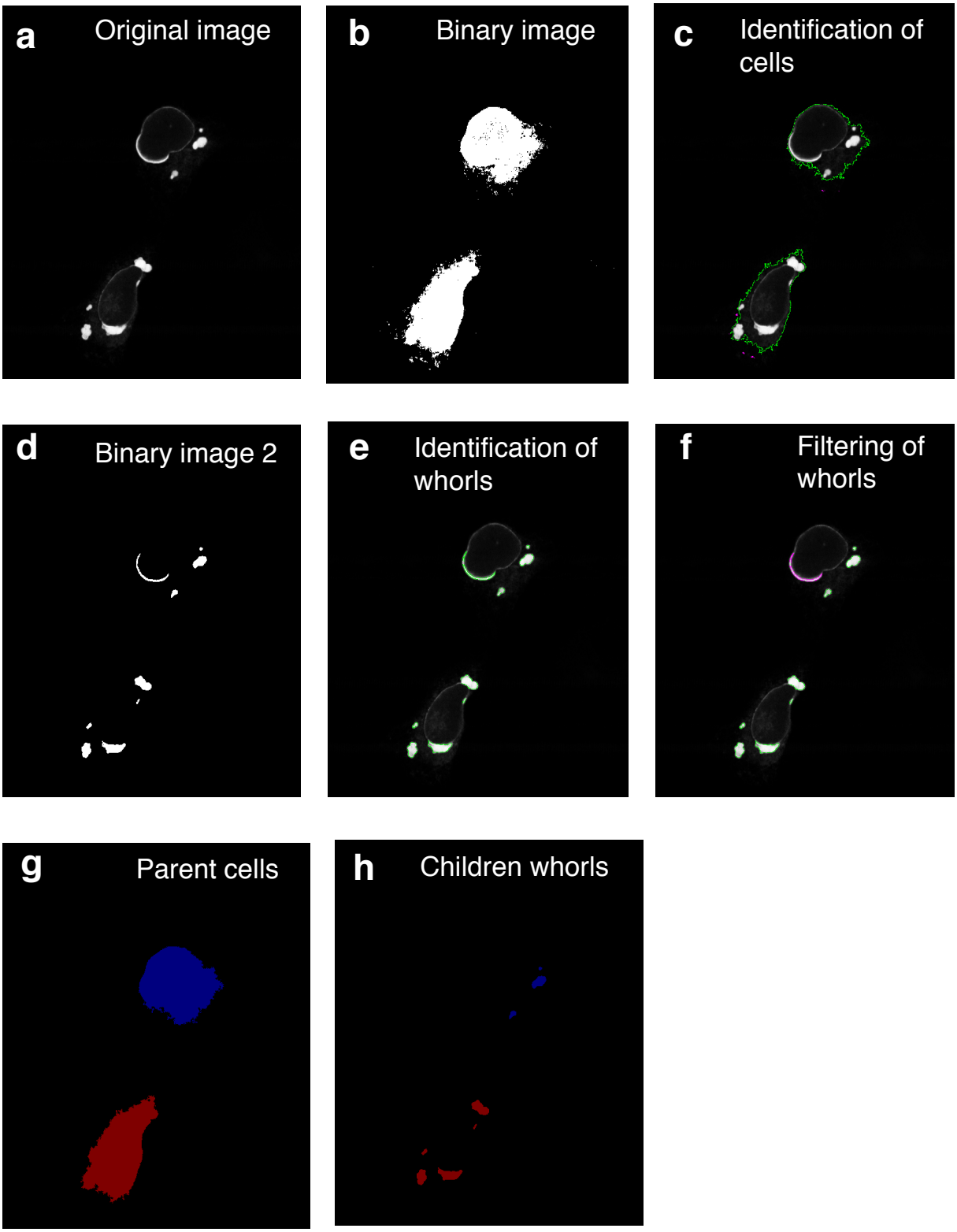

Figure H.1: The analysis of the OSER structures. Detailed description is given in the text.

Structures with roundish shape have been identified as whorls (green outlines). Filtering of whorl based on form factor also eliminates some false positive structures *e.g.* nice reticular network. Finally, identified whorls & cells are related based on their location. In Figure H.1g and H.1h cells were color-labeled with the whorls associated with them.